An Assessment of the Effects of Cloud Inhomogeneity on Ice Cloud Radiative Properties

by
Paul W. Stackhouse Jr. and Graeme L. Stephens

Department of Atmospheric Science
Colorado State University
Fort Collins, Colorado

Research Supported by NSF Grants ATMS-9100795 and ATM-8812353

Colorado State University

Department of Atmospheric Science

Paper No. 595

AN ASSESSMENT OF THE EFFECTS OF CLOUD INHOMOGENEITY ON ICE CLOUD RADIATIVE PROPERTIES

Paul W. Stackhouse, Jr. and Graeme L. Stephens

Research supported by the Department of Energy Contract #DE-FG03-94ER61748 and the National Science Foundation Grant #ATM-9100795.

Principal Investigator: Graeme L. Stephens

Department of Atmospheric Science
Colorado State University
Fort Collins, CO 80523

January, 1996

Atmospheric Science Paper No. 595

ABSTRACT

This research focuses on understanding and quantifying the effects of microphysics and cloud inhomogeneity on the radiative properties of cirrus clouds. To realize these goals, the Spherical Harmonic Spatial Grid method of radiative transfer (SHSG) is used to simulate the radiances and fluxes of cirrus with horizontal variability. The clouds in these simulations are inferred from ground based radar and lidar measurements by one of two new methods. The first produces a two-dimensional cloud field that has a variable extinction but has a constant single-scattering albedo and phase function. The second method gives cloud fields that vary in both the extinction and the single-scattering albedo, but have a constant phase function.

Using both types of clouds, the two-dimensional (2D) and independent pixel (IP) radiative properties of horizontally inhomogeneous cirrus are computed using SHSG. The sensitivities of radiances to variability and cloud optical properties are quantified using a bispectral plane-parallel retrieval grid to estimate the known cloud microphysical properties. The results are analyzed to determine the conditions that give the largest error in the retrievals. The fluxes are analyzed in terms of the differences between 2D and IP albedos, transmittances and absorptances. Both radiances and fluxes show greater sensitivity to horizontal inhomogeneity as the solar zenith angle, the domain averaged optical depth and cloud brokenness are increased. However, the domain averaged differences due to cloud variability in unbroken clouds tended to cancel, but do not in the case of the broken cloud. Sensitivities to the form of the phase function are significant for radiances at certain scattering angles in thin clouds. The errors in the retrievals in these instances can dominate over horizontal inhomogeniety in unbroken clouds and do not disappear in the domain average. Finally, varying the single-scattering albedo in unbroken cloud at an absorbing wavelength causes RMS errors for both radiances and fluxes that are similar in size to error caused by internal inhomogeneity alone.

The sensitivity studies are used as a framework to interpret the radiative observations of cirrus clouds made during the FIRE Cirrus IFO II experiment from the afternoon Sabreliner flight on 26 November 1991. New methods are developed to infer spectral optical depths, direct-to-total ratios, and transmittances at large solar zenith angles. The estimates of these quantities and plane-parallel theory are used in a new method to infer the asymmetry parameter of cirrus. Although no conclusions about the value of g are possible in this case, the plane-parallel theory provides an envelope within which most observations

lie. A co-location between the radar and aircraft during the Sabreliner flight provides an unique opportunity to directly compare observed and simulated reflected radiances and fluxes. The results show that the two-dimensional cloud structure is required to account for measured radiances and plane-parallel theory is applicable only over a large spatial distance. In contrast to the observed radiances, the variability of the measured albedos are explained adequately using the independent pixel approximation. The results of this research identify unresolved issues for future work and suggest changes in the design of future field experiments to address these issues.

ACKNOWLEDGEMENTS

We are indebted to a number of people who have given their time, expertise, and data to make this research possible. We are indebted to Dr. David Randall, Dr. Thomas VonderHaar and Dr. Chiaoyao She all of Colorado State University for their evaluation of the manuscript. We are also thankful to the following researchers: Dr. Frank Evans who provided SHSG, the 2D Monte-Carlo model and the expertise to run these programs; Dr. Andrew Heymsfield and Steve Aulenbach for providing the reduced microphysical data; Francisco Valero and Peter Pilewskie in providing the reduced TDDR data; Taniel Uttal and Janet Intrieri for providing the radar and lidar data; the Research Aviation Facility at the National Center for Atmospheric Research for providing the cold chamber facilicites; and Ted Cannon at the Renewable Energy Laboratories for allowing us to use his lab for pre-experimental calibration. We also gratefully acknowledge the invaluble assistance of Robert McCoy who designed the data acquisition system for CSU radiation instrumention on board the Saberliner aircraft and who gave countless hours toward the calibration of SPERAD. Finally, we wish to thank Sue Lini and Heather Jensen, who helped to prepare the manuscript.

This research was supported by NSF grants ATM-9100795 and ATM-8812353. Much of data used in the case study research was retrieved from the Langley Research Center Distributed Active Archive Center (DAAC). Some of the two-dimensional radiative transfer model computations were performed using the super computer facilities at Colorado State University Computer Center.

CONTENTS

LIST OF FIGURES

LIST OF TABLES

Chapter 1

INTRODUCTION

The subject of this research brings together two large areas of intensive research that have considerable effect upon our understanding of the way in which both solar and infrared radiation are transferred through clouds. The radiative processes not only have ramifications in the short term development and dissipation of cloud systems, but also on the regulation and maintenance of climate. The effect of cloud inhomogeneity upon the way in which radiation is transferred through the atmosphere and the impacts by this process on the Earth's climate are only now beginning to be understood. Cirrus clouds are especially important in this respect. Consisting of nonspherical particles whose optical properties alone are not well understood, cirrus clouds are very prevalent and persistent in the earth's atmosphere. These clouds contain inhomogeneities generally ignored in the estimation of their bulk radiative properties and in the remote sensing of their microphysical properties. This research seeks to increase our understanding of the potential impacts of inhomogeneity upon the measurement of cirrus cloud radiative properties and upon the determination of bulk cloud properties.

1.1 Inhomogeneous Clouds and Radiative Transfer

The fact that cloud inhomogeneity can have a large effect upon the way in which radiation is transferred through the atmosphere is only now starting to be appreciated. The effect of such inhomogeneity has been assumed to be small in the domain averages and as a result has been ignored in most cloud and climate modeling efforts to date. Yet it has not been demonstrated that the effects of cloud inhomogeneities are small (e.g., Stephens, 1988). A further problem that faces the atmospheric science community is the interpretation of radiance and flux measurements obtained in real inhomogeneous cloud situations. Radiative measurements are usually made on much smaller scales than those computed in a climate model. On these smaller scales the effect of inhomogeneity can be significant. For example, Figure 1.1 presents a photograph of an inhomogeneous cumulus cloud field over the ocean. Clearly visible in the picture are three bright areas on the surface of the ocean beneath small cumulus clouds. These bright areas on the ocean occur as a result of the reflection of light off the cloud sides. The measurement of downwelling fluxes over these bright spots might give anomalous values for the transmittances (see,

Welch et al., 1980). These type of effects cannot be treated in the traditional plane-parallel models currently used in cloud models, yet these effects significantly impact estimates of absorption in clouds. Note also in Figure 1.1 the bright and dark areas on the surface of the clouds. A sensor with a narrow field of view would measure radiances that vary significantly across these areas. A plane-parallel retrieval scheme used for these radiances gives estimates of microphysical properties that are not necessarily real.

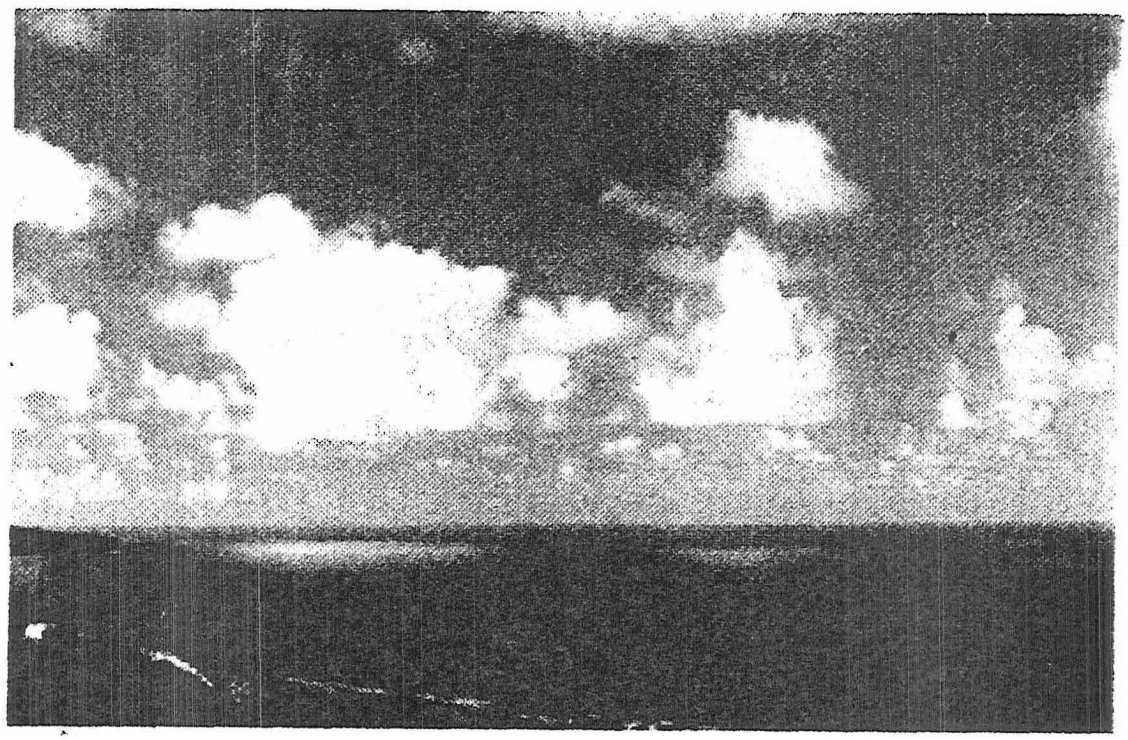

Figure 1.1: A photograph demonstrating the effects of cloud inhomogeneities on solar radiation.

In recognition of the potential effects of inhomogeneities on the interpretation of radiative measurements and the possible climatic effects of these processes, a number of studies have recently attempted to shed light on the effects of the cloud inhomogeneities on radiative transfer. The first of these studies investigated the effects of cloud structure on the radiative properties of clouds by studying geometric distributions of finite clouds with internal homogeneity (i.e., McKee and Cox, 1974). The McKee and Cox study was the forerunner of many such studies using a Monte Carlo model to study the effects of such finite clouds on radiative transfer. Welch and Wielicki (1989) show that the albedo of a distribution of broken clouds can be reduced by as much as 8% depending upon the cloud fraction, surface albedo and solar zenith angle. Another investigator, Barker (1992), used Monte Carlo techniques to investigate the effects of internal variability within an unbroken statistically isotropic cloud. From this study it is found that internal variability

can also decrease the albedo in the neighborhood of $2-5\%$ relative to plane-parallel calculations for clouds of visible optical depth greater than 2 at a solar zenith angle of $60°$. It was also found that inhomogeneity increased the solar energy absorption of thick clouds and decreased the absorption of thin clouds. The effects of both broken and internal cloud inhomogeneity found in these studies are relevant to the study of cirrus cloudiness, especially the middle latitude cirrus studied in recent field programs. This study endeavors to characterize the effects of both types of inhomogeneities in cirrus.

1.2 Why Cirrus Clouds?

The uncertainties associated with the radiative effect of cirrus clouds upon the earth-atmosphere system constitute one of the major cloud-radiation issues in our quest to understand our climate system. The large areal coverage and persistence of cirrus cloud systems especially in the tropical regions, are reasons to believe that these significantly affect the radiation budget of the Earth (i.e., Cox, 1973; Stephens and Webster, 1981; Liou, 1986). To assess the impact of cirrus cloudiness on the global climate system it is essential to better understand the mechanisms which produce cirrus clouds and how these clouds interact with solar and infrared radiation (Starr, 1987). However, the characteristics of cirrus cloudiness cause considerable difficulty in deriving this understanding. Cirrus clouds are located at very high altitudes making them generally inaccessible to most *in situ* observing platforms. Additionally, cirrus systems tend to be composed of thin cloud layers the structure of which varies considerably in the horizontal and vertical. Finally, cirrus clouds are composed of nonspherical ice particles, the single scattering properties of which are not very well understood (for a review see, Stephens, 1995). These confounding characteristics provide the impetus to study these clouds in a much more systematic and thorough way culminating in several field programs dedicated to the study cirrus clouds (e.g., Starr, 1987, Raschke, 1988).

1.2.1 Past Cirrus Studies

Cirrus clouds have been studied using penetrating aircraft that attempt to acquire information regarding their microphysical and radiative properties (i.e., Griffith et al., 1980; Paltridge and Platt., 1981; Paltridge, 1988; Foot, 1988; Stackhouse, Jr. and Stephens, 1991; Kinne et al., 1992; and Francis et al., 1994). Microphysical measurements of the cirrus size distributions are usually obtained with a 1-D or 2-D particle probe to infer distributions of equivalent volume or area spheres and/or hexagonal crystals. From these quantities Ice Water Content and "effective radius" are defined and are related directly to the radiative measurements (i.e., Paltridge and Platt., 1981; Paltridge, 1988). Single scattering properties from either Lorentz-Mie theory (spheres and cylinders) and geometric optics (hexagonal columns) are derived from the inferred ice crystals and are used in plane-parallel radiative transfer models to derive cloud properties which are then compared to

the observed cloud radiative properties (i.e., Foot, 1988; Stackhouse, Jr. and Stephens, 1991; and Kinne et al., 1992). Although providing much better insight into the relationship between the microphysical and radiative properties of cirrus, these studies identify various uncertainties found in the observations to account for discrepancies between theory and measurements. These uncertainties include the microphysical measurements, the inference of single scattering properties from these measurements, and the temporal and spatial sampling problems associated with the radiative measurements caused by large vertical and horizontal inhomogeneities.

1.2.2 Unresolved Issues in Cirrus Cloud Radiation Interactions

Of the uncertainties mentioned above perhaps most recent progress has occurred in microphysical measurements. Some of the uncertainty that exists regarding the possible significant concentrations of small ice crystals in the clouds is now beginning to be clarified. Platt et al. (1989) cite evidence for the existence of small particles which are believed to enhance cloud albedos. Several recent advances in instrumentation in the measurement of small particles. The new instruments have been flown on aircraft (i.e., the Desert Research Institute ice particle replicator and the NCAR Video Particle Sampler) and balloons (the NCAR balloonsonde replicator) in more recent field experiments, such as FIRE Cirrus II. Some of these data are already available to the scientific community.

Another uncertainty associated with the microphysical measurements involves the determination of crystal shape. Cirrus crystals are known to exhibit a very large range of irregularity and since most probe measurements are one or two dimensional in nature, assumptions must be made concerning the remaining dimensions and densities to infer size distributions and mass characteristics. This uncertainty concerning the shape becomes very important when attempting to estimate the single scattering and absorption properties of cirrus ice crystals. Present scattering theories like geometric optics of Takano and Liou (1989) give asymmetry parameters ranging from 0.77 to 0.84 for various distributions of hexagonal crystals for a wavelength of 0.55 μm. Both Stackhouse, Jr. and Stephens (1991) and Kinne et al. (1992) show that asymmetry parameters of around 0.7 give better agreement between theory and observations. Kinne *et al.* point out that these lower asymmetry parameters can be caused by both underestimated concentrations of small particles and by the complicated shapes of the crystals.

Besides the inference of cirrus cloud single scattering properties, another major area of uncertainty involves the effects of horizontal and vertical inhomogeneities of clouds on the radiative transfer. In designing an experiment, it is useful to minimize the effects of horizontal inhomogeneities by selecting what seems to be more homogeneous cases and averaging over selected time intervals. Smith, Jr. et al. (1990) proposed a more statistical way to analyze the data by stratifying the broadband radiometric observations compared to the mean. Yet, this study and several others (i.e., Stackhouse, Jr. and

Stephens, 1991; Kinne et al., 1992) involved flight legs which had fixed ground positions so that the cloud top and bottom were not sampled simultaneously. Thus, not only do the radiometric observations themselves include information from the three-dimensional radiance field but sampling errors add considerable uncertainty to the interpretation of cloud radiative properties.

The FIRE (First ISCCP Regional Experiment) Cirrus IFO (Intensive Field Operation) II was held from mid November to mid December in 1991 and aimed to provide some clarification of these issues. The approach was to observe cirrus cloudiness simultaneously with a multitude of instruments. Data from this field program are used in this research in an effort to address the issue concerning the effect of inhomogeneity on the radiative properties of cirrus cloudiness.

1.3 Research Objectives

The purpose of this research is provide an assessment of the effects that dimensionality has on radiative transfer through these clouds. To this end the objectives of this research are three fold:

1. to develop a method of deriving distributions of cirrus cloud optical properties from ground based measurements;

2. to use these distributions in two-dimensional radiative transfer simulations to study the effects of inhomogeneity upon radiance and flux fields, to quantify these effects and provide an understanding of the conditions under which plane-parallel theory causes large error; and

3. to test these two-dimensional simulations by comparison with actual radiative measurements.

These objectives give insight into the information required to more accurately simulate the variability of radiative measurements. The most important topics addressed by this research are:

- the effect of inhomogeneity on cirrus cloud radiances and the ramifications of these sensitivities to the retrieval of cloud properties;

- the effect of inhomogeneity on cirrus cloud fluxes both on smaller scales and on the domain averaged cloud properties;

- the difference in sensitivity of radiances and fluxes to the same inhomogeneity;

- the conditions under which the effects of cloud structure dominate over the effects of cloud microphysics for radiances and fluxes;

- the information required to properly simulate the variability of measured optical properties in cloud radiances and fluxes; and finally
- the identification of those factors that are required to parameterize these effects in future work.

These topics are pursued by comparing two-dimensional radiative transfer to independent pixel plane-parallel calculations to ascertain the errors incurred when not considering the horizontal transfer of radiation within cloud. These types of simulations are also compared to aircraft observations of radiances and fluxes to infer the information regarding cloud structure required to explain the observations.

1.4 Research Outline and Description

This research demonstrates that the uncertainties in radiative properties associated with cloud structure are as significant as the uncertainties associated with the scattering properties of cirrus particles. This research attempts to quantify these uncertainties. The research here has three components that fulfill the objectives listed above and serve to outline this report. The three components are: the incorporation of cirrus clouds with realistic cloud structure into a multi-dimensional radiative transfer model, a theoretical study of effects of inhomogeneities and scattering properties on the radiation fields, and the comparison of observed radiances and fluxes with theory. Each component is described in detail below.

1.4.1 Deriving Cirrus Cloud Fields for Multi-dimensional Radiative Transfer

In the following chapter, two methods of deriving two-dimensional cirrus clouds are described. The first employs radar reflectivity data from a radar that has both horizon-to-horizon scan and vertically pointing radar modes. The radar is the NOAA ERL K_a-band 8.66 *mm* radar which was deployed and operated during the first half of the FIRE Cirrus II experiment. A method is introduced to convert the two-dimensional radar reflectivity fields to fields of extinction. For this method, the single-scattering albedo and phase function are held constant everywhere in the domain. This produces a cloud field that has the same effective radius everywhere with only the total concentration varying from point to point to account for the observed radar reflectances. Clouds produced using this method are referred to as "constant microphysics clouds".

The second method of producing a two-dimensional cloud field uses coincident radar and lidar data. These two coincident measurements are used to infer both total concentration and effective radius cloud fields (see, Intrieri et al., 1993). From these fields, and an assumed functional form of the size distribution, both extinction and single-scattering albedo fields are derived. This cloud field is referred to as the "variable microphysics

cloud" since the shape of the size distribution, as represented by the effective radius, changes throughout the cloud as well as the total concentration.

Chapter 2 also contains a description of the radiative transfer model used to simulate the radiative properties of these two-dimensional clouds. The model used here is the Spherical Harmonic Spatial Grid method (SHSG) that is presented by Evans (1993). The model is chosen for this research because of its ability to simulate radiative properties in arbitrary cloudiness. As such, it offers an advantage over many other multi-dimensional models in use today. In Chapter 2, this method is outlined and some developmental work is described relating to the accuracy and performance of the model.

1.4.2 Sensitivity Studies with Radiances and Fluxes

Chapters 3 and 4 address the second research objective and contain the results of a series of sensitivity studies characterizing the effect of variability on the determination of radiance and flux properties respectively. The goal is to provide insight into sensitivities of cirrus cloud radiative properties to the scattering properties of the cirrus ice crystals and to the structural inhomogeneities associated with these clouds. A variety of sensitivity studies are performed using the SHSG model. These studies are intended to characterize the types of sensitivities that radiative properties such as radiances and fluxes, and derived properties such as cloud reflectances, emittances, and albedos have to changes in the optical properties of the clouds. Of particular importance are the sensitivities of the radiation field to the shape of the scattering phase function, which is not well understood for nonspherical phase crystals. Presently optical properties, including the shape of the phase function, associated with spherical ice and to a lesser extent hexagonal ice crystals (i.e.,Takano and Liou, 1989) are commonly used to approximate the scattering and absorption properties of nonspherical ice. These assumptions are currently used to interpret cirrus cloud observations (e.g., Intrieri et al., 1993) and as a basis for the retrieval algorithms of cloud properties (e.g., Wielicki et al., 1990). Understanding the types of uncertainties associated with errors in the shape of the phase function especially in the light of multi-dimensional radiative transfer are essential to the understanding of remotely sensed cloud radiative properties and are meant to test the sensitivity of radiative transfer to ice crystal shape.

Additionally, sensitivity studies are conducted to investigate the effect of both the vertical and horizontal cloud inhomogeneities in the internal structure of cirrus clouds. Both clouds with constant microphysics and variable microphysics are used in the sensitivity study. The sensitivity studies in Chapter 3 examine the effects of inhomogeneities on radiances in terms of the impact upon retrieved cloud properties such as the optical depth and effective radius. The sensitivity study presented in Chapter 4 examines the effects of inhomogeneities in terms albedo, transmittances, and absorptances. The effects

are compared on both the grid point and domain average scales. The sensitivities are presented for absorbing and nonabsorbing solar wavelengths and for an infrared wavelength. Finally, the sensitivities of the radiances and fluxes due to internal cirrus variability are compared to those produced in the simulation of radiances and fluxes in broken cirrus clouds.

The subsequent analysis of these radiance and flux sensitivities gives insight into the conditions under which the use of plane-parallel theory leads to large error in the estimation of cloud radiative properties. The relative contributions to these errors from inhomogeneity and from the variation of microphysical properties such as the phase function shape and single-scattering albedo are compared. The conditions under which microphysical variation dominates over the cloud structure are identified. The results of chapters 3 and 4 are subsequently used to interpret the radiative observations obtained during the experiment.

1.4.3 Observational Component

The third and final objective of this research is fulfilled in the comparison of aircraft radiative observations to simulations using a two-dimensional cloud field as described above. During this field experiment the NCAR Sabreliner was equipped with several different instruments including those which give microphysical and radiative measurements. Microphysical measurements of size distribution, number concentration, and ice water content are used to determine cloud single-scattering properties. Radiative instruments from the aircraft give quantities such as broadband solar and thermal infrared fluxes, spectral downwelling fluxes and spectral upwelling radiances. The analysis is performed using the data set described above in two general components which are:

1. the retrieval of optical depths, the ratio of direct beam radiation to total radiation, and transmittances using flux measurements, and

2. a detailed case study comparing solar radiative flux and radiance observations with two-dimensional simulations of radiances and albedo.

Cirrus Cloud Flux Retrievals

Chapter 5 describes in detail the instrumentation included on the Sabreliner during the FIRE Cirrus II experiment. This chapter also describes the development a new retrieval scheme to estimate the cloud spectral optical depth, direct beam to total ratio and the cloud transmittances from spectral flux data. The scheme uses two different instruments and accounts for very large solar zenith angles. The results of the scheme are given for the afternoon Sabreliner flight on Nov. 26, 1991. If the clouds for this case were plane-parallel, then the asymmetry parameter of the cloud could be estimated for these data. Plane-parallel calculations for a variety of asymmetry parameters are contrasted against observations. The results are then compared to the sensitivities of downwelling transmittances as discussed in Chapter 4.

Detailed Case Study

Chapter 6 presents the results of a detailed case study involving one flight leg from 26 Nov. 1991 case. This detailed case study involves the co-location of the aircraft flight leg with time that the cloud passed over the radar. This co-location gives the unique opportunity to compare the observed radiance and flux measurements to the simulations of cloud radiative properties using the two-dimensional cloud field observed from the radar. The simulations of spectral radiances and flux albedos are compared to those measured by the aircraft. The comparisons give insight as to sensitivity differences between radiances and fluxes and to the amount of information required to account for the variability in the radiance and flux fields.

1.4.4 Summary, Conclusions and Recommendations

In the seventh and final chapter, the results from this work are summarized and conclusions are drawn from the results of the sensitivity studies and the comparison of theory to the observations. The conclusions of this work lead to many suggestions as to the type of future work required to understand these processes in a more complete way. Improvements to experimental procedures are suggested and the factors that may be required to parameterize the influence of inhomogeneities on cirrus cloud radiative properties are given.

Chapter 2

RADIATIVE TRANSFER IN TWO-DIMENSIONAL CIRRUS CLOUDS

There have been numerous studies aimed at understanding the effects of multiple dimensioned clouds on radiative transfer. Most of the earlier studies involved the simulation of the radiative properties with geometric distributions of finite clouds using Monte Carlo methods (eg., McKee and Cox, 1974). A few methods have been developed to study clouds having periodic or imposed functional inhomogeneities (eg., Stephens, 1986) and clouds containing fractal (eg., Davis et al., 1990) and random (eg., Barker, 1992) inhomogeneity. With the development of discrete grid models, more arbitrary clouds can be treated (eg., Gabriel et al., 1993). For this purpose, the Spherical Harmonic Spatial Grid (SHSG) method of radiative transfer was developed by Evans (1993) (hereafter referred to as Evans). This method is configured to treat two-dimensional clouds of arbitrary structure using a discrete grid and approximating the radiance field with a spherical harmonic expansion. In this study, the two-dimensional clouds are produced by using radar reflectivities to determine the cloud structure. This method gives clouds that contain a realistic representation of the horizontal inhomogeneity. A procedure for the derivation of two-dimensional cirrus clouds from radar observations is presented first in this chapter. This discussion is followed by a description of the SHSG radiative transfer model and issues pertaining to the accurate simulation of cloud radiative properties using the model.

2.1 Deriving Two Dimensional Cloud Fields

The problem of deriving multi-dimensional cloud optical properties is complex and is a topic of ongoing research. It requires the knowledge of microphysical information such as size distribution, shape, and density of cloud particles at a high enough resolution to capture the inhomogeneities in cloud structure. To date such information is impossible to attain without the use of numerical models that are subject to their own assumptions and constraints. Typically, the microphysical properties of clouds, specifically cirrus clouds, are obtained by averaging a time series of aircraft observations over a given path (see, Paltridge and Platt., 1981; Foot, 1988; Stackhouse, Jr. and Stephens, 1991; Kinne et al., 1992; and Francis et al., 1994 for examples). This type of analysis is required since a finite time average is needed to obtain a reasonable estimate of the size distribution from the 2D PMS probes, the instrument most commonly used to derive microphysical information.

Not only are these measurements subject to the uncertainty of under sampling small particles, but parameterizations are required to estimate cloud ice water content from the 2D probe information. The purpose of the averaging is to determine the "mean" cloud properties representative of that level of cloud and to combine these with mean properties at other levels to determine a mean cloud profile. However, the radiative properties of these mean clouds compared with radiative properties of more realistic clouds that include the natural inhomogeneity structure are not necessarily similar.

Since aircraft microphysical data cannot give the spatial resolution required to investigate the effects of cloud inhomogeneities and cannot give simultaneous cloud profiles, radar data are used to determine the horizontal and vertical cloud structure. For this study, cloud fields are obtained from two different types of radar scan modes using the Environmental Research Laboratory's K_a-band radar ($\lambda = 8.7mm$) (see Martner and Kropfli, 1993 for a more complete description of the radar). The two types of radar scan modes are the two-dimensional range-height indicator (RHI) display of a horizon to vertical to horizon scan and the vertically pointing scan mode. The RHI display gives the two-dimensional cloud structure along a particular direction at a particular time. Two-dimensional clouds are obtained from vertically pointing mode by using a time series of cloud vertical profiles. Both types of data are used to develop two-dimensional clouds in this research. All the selected cirrus clouds were observed on 26 November 1991 during the FIRE Cirrus II IFO (Taneil Uttal, personal communication).

The purpose of this sub-section is to outline a procedure that assigns optical properties to clouds observed by radar containing realistic horizontal inhomogeneities. To this end, clouds with two-dimensional structure are derived and used in radiative transfer calculations in two ways. First, given a cloud structure as described below, the particle size distribution is assumed fixed throughout with only particle number density varying. For this case, only extinction varies within the cloud. The second approach is referred to as a variable microphysics cloud case since the size distribution is allowed to vary producing changes in the extinction and the single scattering albedo throughout the cloud. The following two subsections describe the process of deriving these two types of clouds for subsequent use in two-dimensional radiative transfer calculations.

2.1.1 Clouds with Constant Microphysics

The first type of cloud derived from radar observations and subsequently used in radiative transfer calculations is the cloud of constant microphysics or constant effective radius. The RHI clouds or radar scan data is used to derive these clouds. Three of the RHI images from the 26 November 1991 case are used each giving cloud reflectivities at 50 meter resolution. The first cirrus cloud (cloud 1) is characterized by two generating cells with characteristic tails separated by a space of a few kilometers which is filled with thin cloudiness. A second cloud field (cloud 2) contains a thick generating cell in the

middle of the cloud and is horizontally stratified. Finally, the last cloud (cloud 3) contains two generating cells which are separated by an area of thin cloud of approximately 1 km. For illustrative purposes, this thin cloud area was set to the minimum extinction in order to emphasize the break in the cloud giving an approximate cloud cover of 90% for the cross-section.

Derivation of optical properties from radar data cannot be achieved without ambiguity and this remains a topic of ongoing research. This ambiguity is a result of the fact that reflectivity is a function of the sixth moment of the size distribution whereas the extinction is proportional to area. Radar reflectivities have been demonstrated to be insensitive to small particles in the presence of larger particles greater than 100 μm in characteristic size (Schneider and Stephens, 1995). However, it is well understood that smaller particles are important to albedo measurements in the visible wavelengths (e.g., Stackhouse, Jr. and Stephens, 1991). Sometimes overlooked is the uncertainty associated with the density of these cloud particles which can influence the index of refraction of the particle and thus alter the reflectivity. These factors add considerable uncertainty to the relation between radar reflectivity and the optical properties. Simplifying assumptions are made for the sensitivity analysis pursued here.

For the purposes of this study and for the sake of simplicity, the cloud reflectivities were converted to ice water content using the empirical relation of Sassen (1987),

$$IWC = 0.037 Z_i^{0.696}$$

where Z_i is the reflectivity factor of ice ($mm^6 \cdot m^{-3}$) and IWC is the ice water content ($g \cdot m^{-3}$). This relationship is controversial in itself (Brown et al., 1994) and has been derived from several previous studies relating radar reflectivity and crystal mass. Ice water content estimates derived from this relationship are used to produce a two-dimensional ice water content field. At this point, a modified gamma size distribution of equivalent area spheres was selected to represent the size distribution of the cloud at every grid point. The modified gamma size distribution has the form

$$n(r) = \frac{N_o}{\Gamma(p) r_m} \left(\frac{r}{r_m}\right)^{p-1} \exp\left(-\frac{r}{r_m}\right) \tag{2.1}$$

where

$$r_m = \frac{r_e}{p+2}$$

and $r_e = 80 \mu m$ is the effective radius, $N_o = 0.02\ cm^{-3}$ is the total concentration and $p = 4$. These parameters of the modified size distribution are selected to produce a distribution which roughly corresponded to a size distribution measured during FIRE Cirrus I (see Fig.2.1 as adapted from Stackhouse, Jr. and Stephens, 1991).The inferred IWC of this distribution is 0.0216 $g \cdot m^{-3}$. The extinctions and single scatter albedos

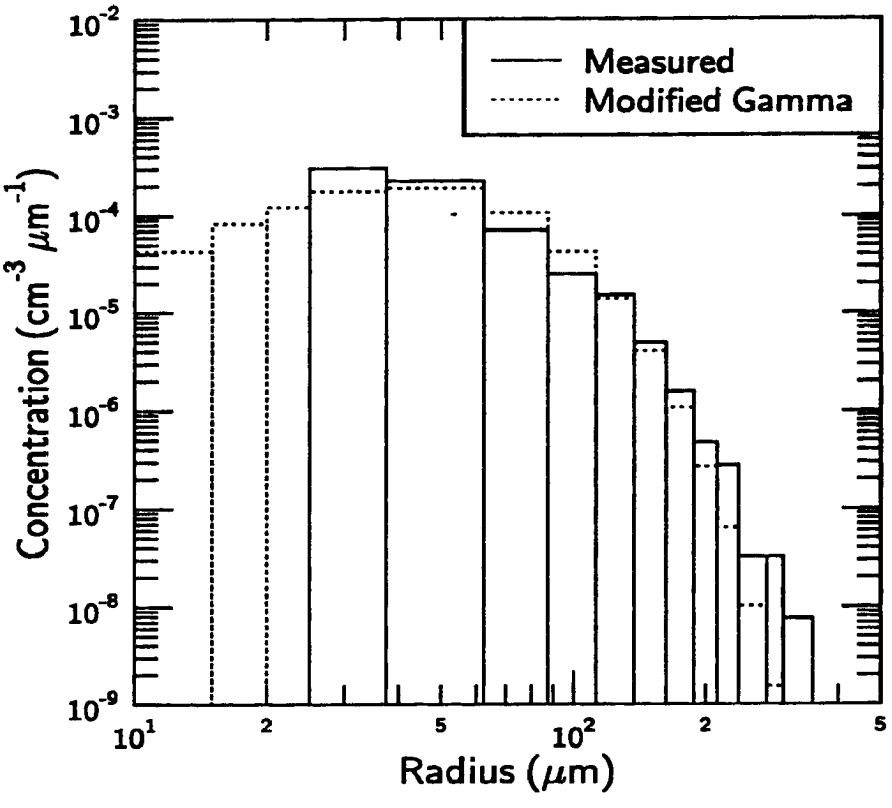

Figure 2.1: Comparison between the modified gamma distribution used to derive cloud field extinctions with $r_e = 80\mu m$ and $IWC = 0.0216\ g\,m^{-3}$ and a measured size distribution from a middle cloud level.

Table 2.1: Cirrus cloud optical properties as a function of wavelength (λ) for the size distribution described in the text.

λ (μm)	K_{ext} (km^{-1})	ω_0	b	g_1	g_2	g_{eff}
0.83	0.45863	0.9998	1.000	0.790	—	0.79
			0.970	0.833	-0.600	0.79
			0.920	0.911	-0.600	0.79
1.65	0.46264	0.8940	1.000	0.810	—	0.81
			0.970	0.852	-0.550	0.81
			0.920	0.928	-0.550	0.81
2.21	0.46521	0.9020	1.000	0.840	—	0.84
			0.970	0.880	-0.450	0.84
			0.920	0.952	-0.450	0.84
3.75	0.47075	0.5832	1.000	0.936	—	0.94
			0.970	0.968	-0.100	0.94
11.5	0.48086	0.5303	1.000	0.948	—	0.95
			0.970	0.981	-0.100	0.95

for this distribution of equivalent area spheres are computed using Lorentz-Mie theory. The computations were performed at several different wavelengths including the three Landsat channel wavelengths 0.83, 1.65 and 2.21 μm and the windows at wavelengths of 3.7 and 11.5 μm. The extinctions and single scattering albedos for this distribution and wavelengths are given in Table 2.1. Using the ice water content cloud field obtained from the radar measurements, a two-dimensional extinction field was derived according to

$$k_{ext} = k_o \frac{IWC}{IWC_o}$$

where the subscript $_o$ denotes the extinction (k) and ice water content (IWC) assumed for the modified gamma size distribution. This scaling effectively adjusts the total concentration of the particles at a particular grid point to a value consistent with the ice water content derived from the radar measurement. The resulting two-dimensional cross-section extinction fields at 0.83 μm for all three clouds are shown in Figures 2.2a,b,c. Figure 2.3 gives the horizontal variation and the number distribution of column optical depth for each of these three clouds that are normalized to a domain averaged column optical depth of unity. The three clouds represent varying degrees of variability that are used in the analysis of the radiative transfer simulations. Note that the distribution of the stratified cloud (cloud 2) is narrow, ranging from 0.5 to 1.5 optical depth compared to cirrus uncinus cloud (cloud 1) and the broken cloud (cloud 3) which have much broader distributions ranging from 0.0 to 2.3. The shapes of the distributions are vastly different. The stratified cloud has a distinct peak, but the broken cloud has several relative maxima, the most distinct of which appearing at minimum optical depths. Cloud 1 has one very distinct peak which occurs at the minimum optical depths. The domain averaged column optical depths from both of these clouds are scaled to obtain clouds of domain averaged

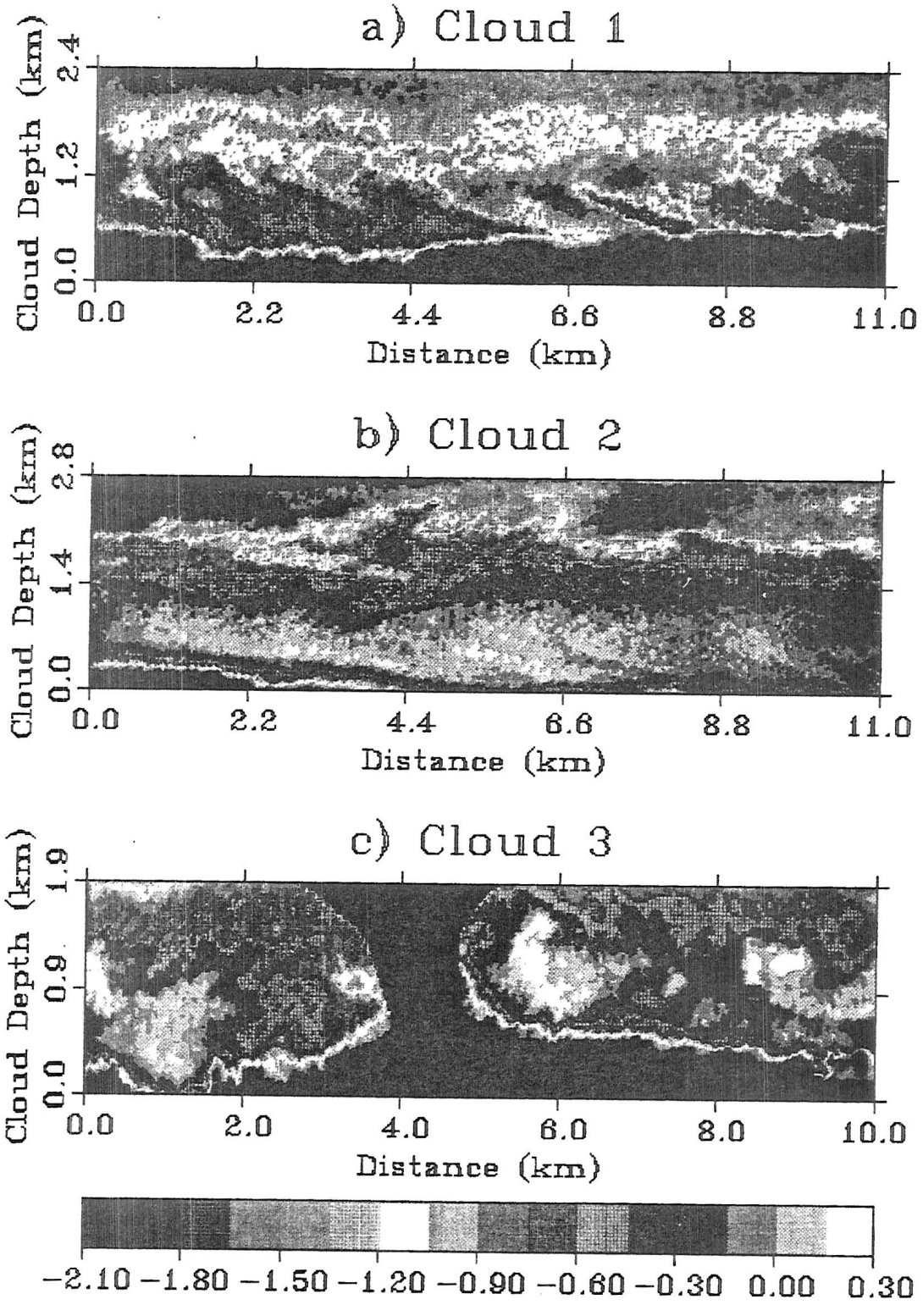

Figure 2.2: 2D extinction fields in $\log(km^{-1})$ for a) cloud 1 and b) cloud 2 and c) cloud3 as derived from the Ka-band radar reflectivity data from NOAA ERL collected during FIRE Cirrus II, Nov 26, 1991.

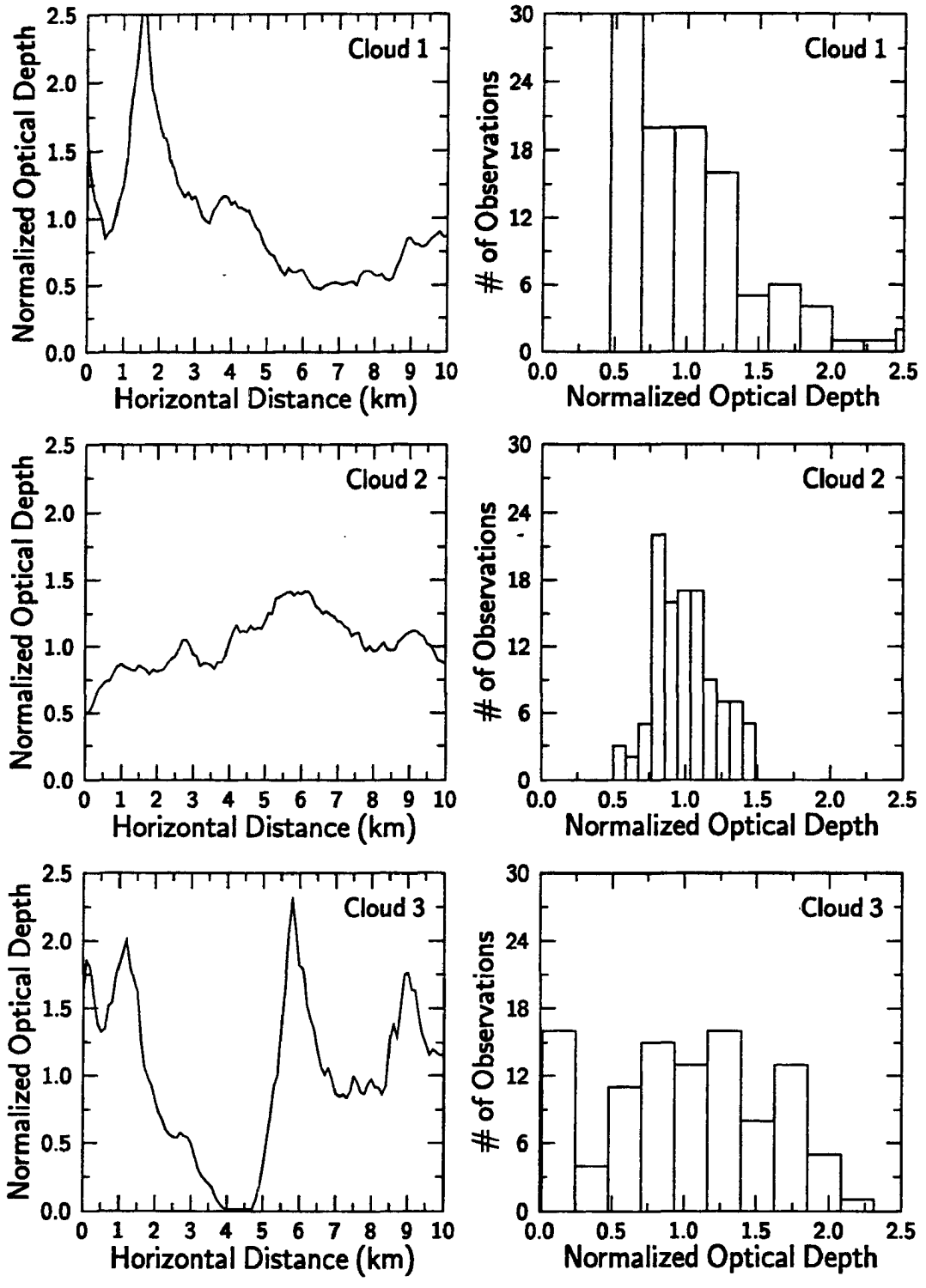

Figure 2.3: Column normalized optical depths as a function of distance and in terms of frequency for each of the three clouds described in the text at 0.83 μm. The domain averaged column optical depth is 1.0 for each cloud.

optical depths ranging from 0.5 to 8.0 in order to better understand the sensitivity of the radiative transfer to this quantity.

The single scatter albedos and phase functions of the ice were assumed to remain constant across the cloud domain but are varied with wavelength. The phase functions were chosen to have asymmetry parameters equivalent to those from the geometric optic computations of Takano and Liou (1989, and personal communication). These asymmetry parameters for each wavelength were used as g_{eff} in the double Henyey-Greenstein function (DHG) to prescribe the phase function. The double Henyey-Greenstein phase function has the form

$$P_{DHG}(\cos\Theta) = b\ P_{HG}(\cos\Theta, g_1) + (1-b)P_{HG}(\cos\Theta, g_2), \tag{2.2}$$

where g_1, g_2 and b are constants related by

$$g_{eff} = b\ g_1 + (1-b)\ g_2 \tag{2.3}$$

and where the single Henyey-Greenstein function is represented as a Legendre series by

$$P_{HG}(\cos\Theta, g) = \sum_{l=0}^{256}(2l+1)g^l P_l(\cos\Theta)$$

with P_l representing an associated Legendre polynomial. An example of the double Henyey-Greenstein phase function as compared to the phase function derived from Takano and Liou (1989) for several different parameters at a wavelength of 0.83 μm is given in Figure 2.4. The phase function parameters for each wavelength are shown in Table 2.1 for the modified gamma size distribution given above. The preceding assumptions produce a cloud field which varies in extinction (and thus structure) while holding the other optical properties of the cloud constant. As a result, a cloud is produced which has a constant size distribution shape and therefore a constant effective radius.

2.1.2 Clouds with Variable Effective Radius

An alternative way to define a two-dimensional cloud field where the effective radius of the size distribution is not assumed to be constant comes from the lidar and radar backscatter technique of Intrieri et al. (1993). This method takes advantage of the coincident backscattering properties of both the K_a-band radar and the CO_2 Lidar ($\lambda = 10\mu m$). Radar reflectivities from a vertically pointed scan mode are converted to backscatter coefficients (see Intrieri et al., 1993). The ratios of these coefficients to co-located lidar backscattering coefficients are computed. These observed ratios are then compared to theoretically produced ratios expressed as a function of the effective radius, r_e. The effective radius is defined as

$$r_e = \frac{\int n(r)\, r^3\, dr}{\int n(r)\, r^2\, dr} \tag{2.4}$$

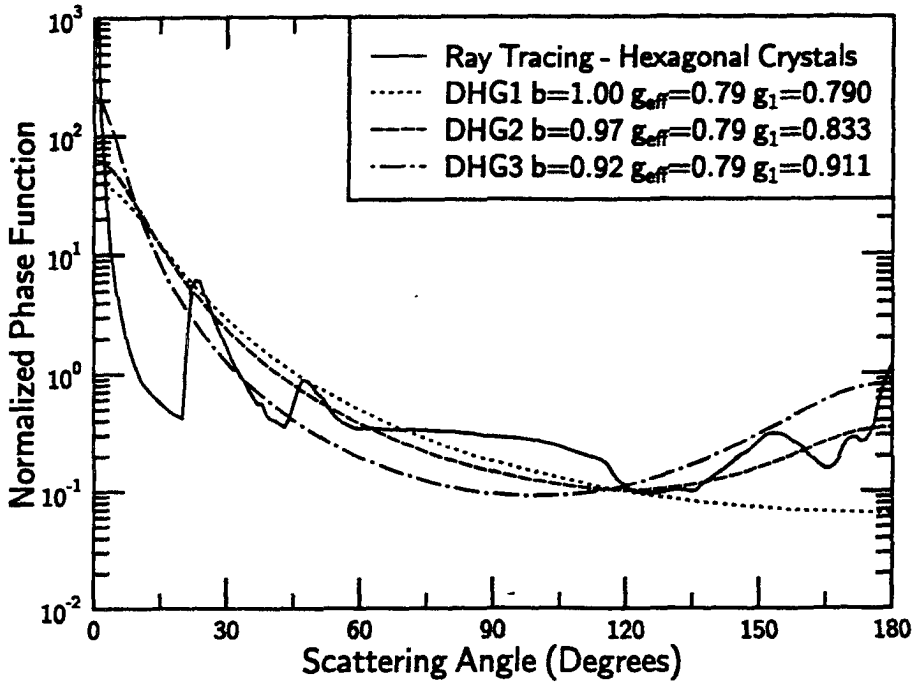

Figure 2.4: The double Henyey-Greenstein functions selected to approximate the phase functions generated for hexagonal crystals ice by Takano and Liou using the ray tracing approach.

where r is the equivalent volume sphere radius. The size distribution of the clouds was assumed to follow the modified gamma distribution shown in equation 2.1. Since in principle this ratio is independent of the total concentration of particles, this quantity can be retrieved using a method similar to that of Feingold and Levin (1987). Thus, two independent measures of the cirrus cloud microphysics r_e and N_o are derived by combining lidar and radar measurements of the same scene. It is important to note that this type of inter-comparison helps to narrow some of the ambiguities associated with inferring ice water content directly from radar reflectivities. This is true despite the coarse assumptions of equivalent volume spheres and an analytic form of the size distribution. For the purposes of this study, these uncertainties are not vital to the final results since only the sensitivities to cloud inhomogeneities are desired.

Deriving Extinction and Single-Scattering Albedo Fields

Figures 2.5a, b show two-dimensional fields of effective radius and total concentration using the lidar-radar backscattering technique (Intrieri, personal communication). Since these fields represent vertical profile data, they are actually derived in terms of time but have been converted to a horizontal distance by assuming cloud advection with the mean wind speed. The mean wind speed for the cloud case presented here as measured from aircraft is approximately 19 $m \cdot s^{-1}$. The cloud shown requires the assumption that the

changes in cloud structure due to its evolution are small compared to changes in horizontal advection for approximately 8 minutes. From the retrieved fields in Fig. 2.5, the volume extinction and scattering coefficients are derived from Lorentz-Mie computations at every size bin in a size distribution by first computing the optical properties for a normalized size distribution (denoted $k_{ext_{o_i}}$, $k_{sca_{o_i}}$ and n_{o_i}) and then using

$$k_{ext}(\lambda) = \sum_{i=1}^{N_b} k_{ext_{o_i}}(\lambda) \left[\frac{n_i \left(r_{e_{ix,iz}}, N_{ix,iz} \right)}{n_{o_i}} \right], \tag{2.5}$$

$$k_{sca}(\lambda) = \sum_{i=1}^{N_b} k_{sca_{o_i}}(\lambda) \left[\frac{n_i \left(r_{e_{ix,iz}}, N_{ix,iz} \right)}{n_{o_i}} \right], \tag{2.6}$$

with the single scatter albedo given by

$$\omega_o = \frac{k_{sca}(\lambda)}{k_{ext}(\lambda)}. \tag{2.7}$$

In the preceding equations, N_b is the number of equivalent volume size bins and $r_{e_{ix,iz}}$ and $N_{ix,iz}$ are the estimated effective radius and total concentration at the grid point ix, iz using the lidar–radar technique. These parameters are used in equation 2.1 to estimate the number density n_i. The normalized optical properties are computed using equation 2.1 with the parameters r_e, N_o and p set to 70 μm, 0.065 cm^{-3} and 2.0 respectively for the Mie computations. Figures 2.6a and b show the extinction and single scattering albedo fields derived for the sensitivity study presented here. The phase functions are imposed exactly as the constant microphysics cases above. The domain averaged optical depth for this cloud is 1.26. The distribution of optical depths and single scattering albedos are shown in Figure 2.7. Note that the optical depth histogram (center panel) is similar to that from cloud 2 of the constant effective radius clouds (see Fig. 2.3). For this reason, the flux and radiance simulations of cloud 2 are compared to those from this variable microphysics cloud. Assignment of cloud optical properties in this fashion allow investigation into the sensitivity of cloud radiative properties to more realistic cloud inhomogeneities.

Deriving the Domain Averaged Effective Radius and Single-Scattering Albedo

In order to ascertain the effects of the vertical inhomogeneities upon the flux and radiance quantities, the variable microphysics cloud simulations are compared with simulations using the same distribution of extinction but specifying a constant single scattering albedo analogous to the constant microphysics cases. This constant single scattering albedo is derived by computing the domain averaged effective radius and total concentration from the 2D fields estimated from the radar-lidar technique. The domain averaged total concentration is computed conventionally by

$$\left\langle \overline{N_o} \right\rangle_{domain} = \frac{1}{N_x N_z} \sum_{i=1}^{N_x} \sum_{j=1}^{N_z} N_{o_{i,j}}$$

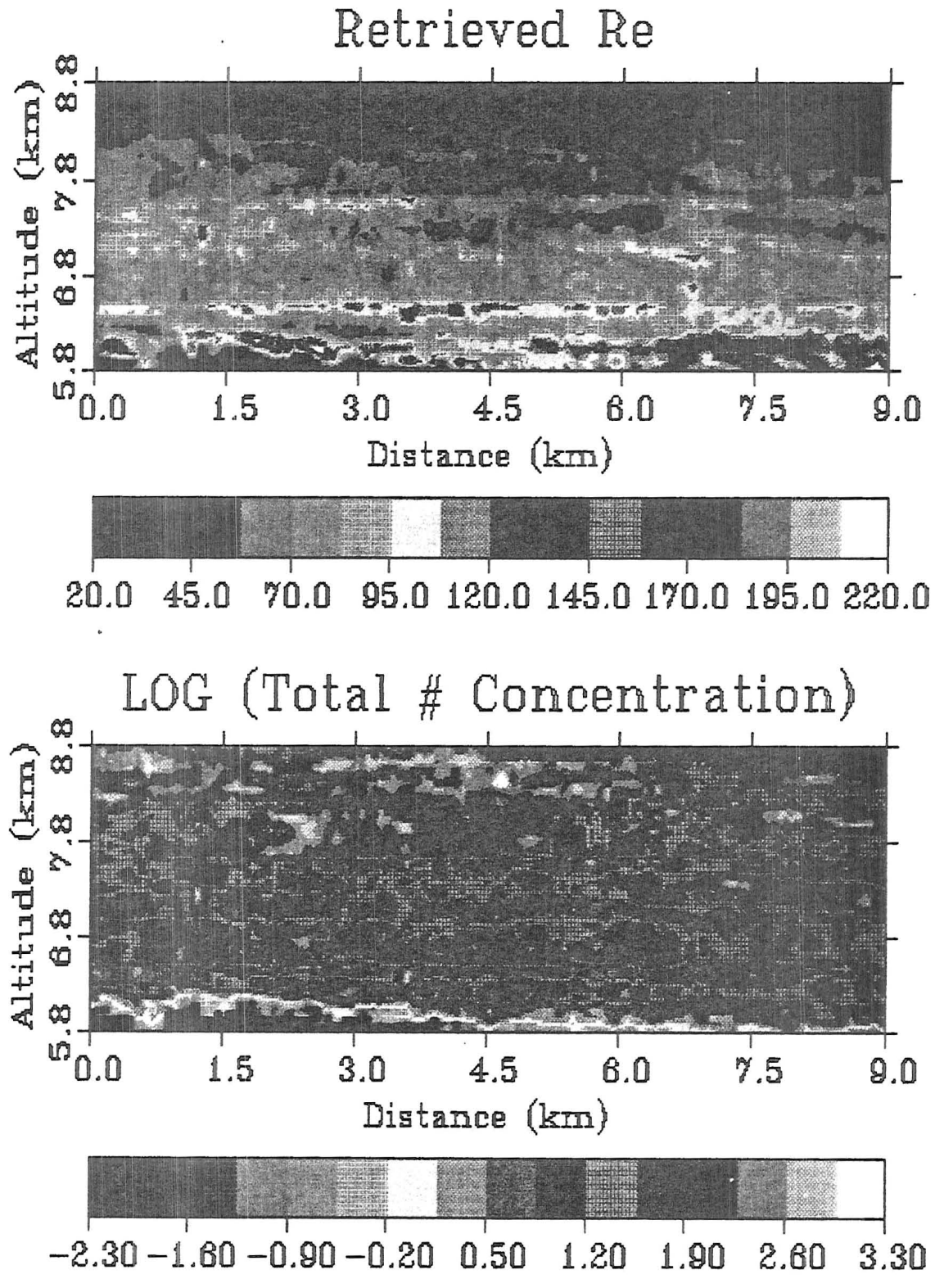

Figure 2.5: Retrieved 2D fields of a) effective radius in μm and b) the logarithm of total concentration in $\log(cm^{-3})$ as derived from the radar-lidar technique of Intrieri *et al.*, (1993).

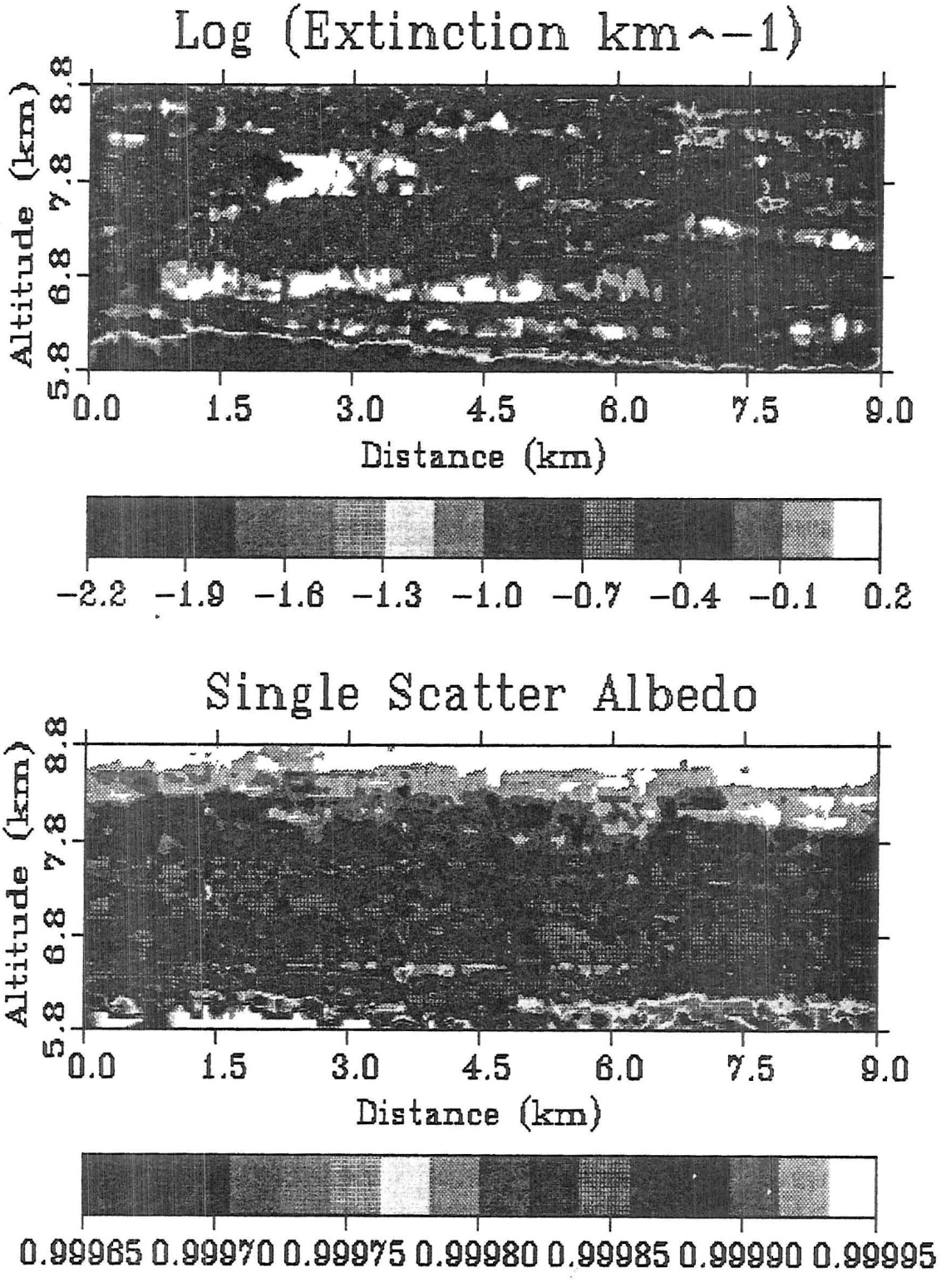

Figure 2.6: Derived 2D fields of a) the logarithm of extinction in $\log(km^{-1})$ and b) the single scatter albedo of the cloud derived from radar-lidar retrievals.

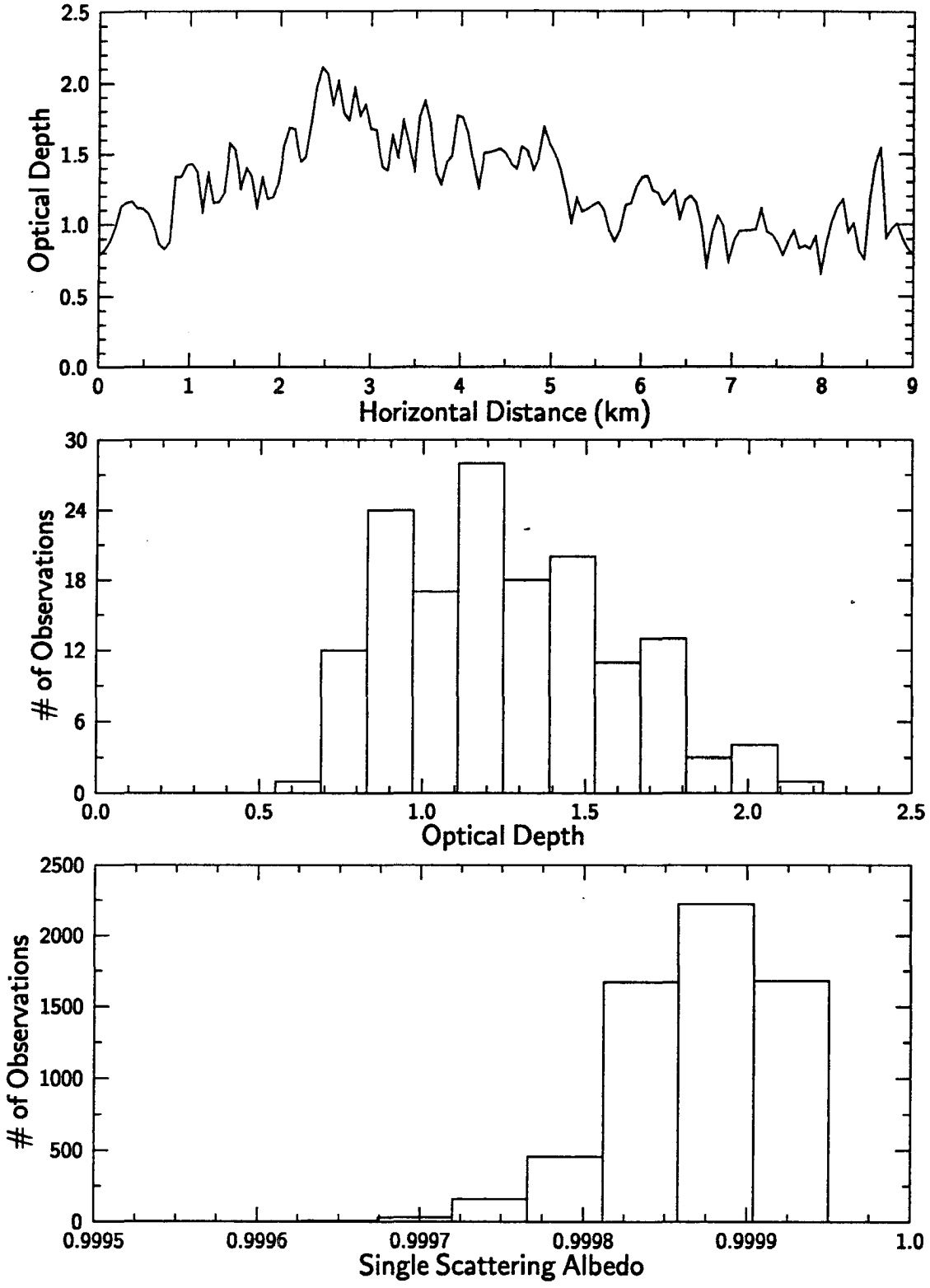

Figure 2.7: The distribution of optical depth (top two panels) and single scattering albedo (bottom panel) for the variable microphysics cloud.

where N_o is the total concentration and N_x and N_z are the total number of x and z grid points respectively. The domain averaged effective radius is computed somewhat differently. Using equations 2.1 and 2.4 the domain average effective radius reduces to

$$\langle \overline{r_e} \rangle_{domain} = \frac{\sum_{i=1}^{N_x} \sum_{j=1}^{N_z} N_{o_{i,j}} r_{e_{i,j}}^3}{\sum_{i=1}^{N_x} \sum_{j=1}^{N_z} N_{o_{i,j}} r_{e_{i,j}}^2} \tag{2.8}$$

where r_e is the effective radius from the modified gamma size distribution that is estimated at each point by the radar-lidar retrieval method. Using these definitions the domain averaged particle concentration and effective radius for the cloud are 0.0703 cm^{-3} and 63.2 μm respectively. The wavelength dependent domain averaged single scattering albedos are found by using equations 2.5, 2.6 and 2.7. For the wavelengths of 0.83 μm, 1.65 μm, 2.21 μm, and 11.5 μm the domain averaged single-scattering albedos are 0.99988, 0.91170, 0.92012 and 0.52347 respectively. Note that these values correspond to locations within the top half of the cloud (note the value for 0.83 μm and refer back to Fig. 2.6) where the largest concentrations of particles are located. Radiative transfer calculations using the domain averaged single-scattering albedos are compared to those of the variable single-scattering albedo field to ascertain the effects of such variability.

2.2 A Multi-Dimensional Radiative Transfer Model

To simulate the radiative properties of the two-dimensional clouds derived in the previous section, a multi-dimensional radiative transfer model is required that can accurately simulate radiance and flux fields in clouds with horizontal inhomogeneity. Such a method, the Spherical Harmonic Spatial Grid radiative transfer model (SHSG), is used in this research. This method solves the two-dimensional radiative transfer equation by approximating the radiance field as a spherical harmonic expansion for the angular dependencies and a discrete grid for the spatial properties. The discretization of the radiative transfer equation with the specified boundary conditions, produces a sparsely coupled linear system that can be solved iteratively using the conjugate gradient method. This representation of the radiative transfer leads to the following advantages of using SHSG, justifying its use in this study:

1. the ability to model clouds of arbitrary structure,

2. the relatively efficient computation costs for accurate solutions,

3. the ability to compute radiative properties at all grid points and angles with one solution, and finally

4. the computation of independent pixel calculations conveniently and consistently with two-dimensional results.

The remainder of this section gives a brief summary of the model formulation as developed by Evans. The last two sections of this chapter provide additional information about some important numerical issues and discuss the validation of SHSG with a two dimensional Monte Carlo model.

2.2.1 Radiative Transfer Equation

The form of the monochromatic radiative transfer equation in two dimensions is expressed as follows:

$$\mu\frac{\partial I}{\partial z}+\sqrt{1-\mu^2}\cos\phi\frac{\partial I}{\partial x}=-kI+\frac{k\tilde{\omega}}{4\pi}\int_0^{2\pi}\int_{-1}^{1}P(\mu,\mu',\phi,\phi')I(\mu',\phi')d\mu'd\phi'+S, \quad (2.9)$$

where μ is the cosine of the zenith angle (positive for upwelling angles), ϕ is the azimuthal angle, and z and x are the vertical and horizontal coordinates respectively. The radiance field I and the diffuse source term S are functions of angle and location. The phase function P depends on the scattering angle and location. Lastly, the extinction k and single scatter albedo $\tilde{\omega}$ depend only on location. The diffuse source term S in (2.9) represents either thermal or single scattered direct solar radiation and these are written respectively as,

$$S(x,z)=k(1-\tilde{\omega})B(T) \quad (2.10)$$

and

$$S(\mu,\phi,x,z)=\frac{k\tilde{\omega}F_o}{4\pi\mu_o}P(\mu,\phi,\mu_o,\phi_o)\exp[-\tau_s(x,z)] \quad (2.11)$$

where $B(T)$ is the Planck function of temperature T, F_o is the solar flux at the top of the domain with the solar beam having the direction (ϕ_o,μ_o), and $\tau_s(x,z)$ is the optical path of the collimated beam to (x,z). Beer-Bouget-Lambert law is used to compute the attenuation of the direct beam.

2.2.2 Angular Expansion

The angular part of the intensity fields is expanded as a truncated spherical harmonic series. This series is expressed in the following form:

$$I(\mu,\phi)=\sum_{m=0}^{M}\sum_{l=m}^{L+m}I_{lm}Y_{lm}(\mu,\phi), \quad (2.12)$$

where the spherical harmonic functions (Y_{lm}) are represented as

$$Y_{lm}(\mu,\phi)=\gamma_{lm}\mathcal{P}_l^m(\mu)\cos m\phi$$

and

$$\gamma_{lm} = \sqrt{\frac{(2l+1)}{2\pi(1+\delta_{0m})}\frac{(l-m)!}{(l+m)!}}$$

$$\delta_{lm} = \begin{cases} 1 \text{ for } l = m \\ 0 \text{ for } l \neq m \end{cases}$$

where $\mathcal{P}_l^m(\mu)$ are the associated Legendre functions. For simplification, the radiance in two dimensions is assumed to be an even function of the azimuth angle, thus eliminating the need for the sine terms of the expansion. This assumption limits the sun to a fixed azimuth that is set to $\phi_o = 180°$ for the simulations presented here.

According to Evans, the streaming terms of the radiative transfer equation for the z and x terms respectively are written as,

$$\left[\mu\frac{\partial I}{\partial z}\right]_{lm} = \alpha_{lm}^{-}\frac{\partial I_{l-1,m}}{\partial z} + \alpha_{lm}^{+}\frac{\partial I_{l+1,m}}{\partial z} \tag{2.13}$$

and

$$\left[\sqrt{(1-\mu^2)}\cos\phi\frac{\partial I}{\partial x}\right]_{lm} = b_{lm}^{--}\frac{\partial I_{l-1,m-1}}{\partial x} + b_{lm}^{+-}\frac{\partial I_{l+1,m-1}}{\partial x} + b_{lm}^{-+}\frac{\partial I_{l-1,m+1}}{\partial x} + b_{lm}^{++}\frac{\partial I_{l+1,m+1}}{\partial x}, \tag{2.14}$$

where

$$\alpha_{lm}^{-} = \sqrt{\frac{(l-m)(l+m)}{(2l-1)(2l+1)}}, \qquad \alpha_{lm}^{-} = \sqrt{\frac{(l-m+1)(l+m+1)}{(2l+1)(2l+3)}},$$

$$b_{lm}^{--} = -\sqrt{\frac{(1+\delta_{1m})(l+m)(l+m-1)}{4(2l-1)(2l+1)}}, \quad b_{lm}^{+-} = -\sqrt{\frac{(1+\delta_{1m})(l-m+1)(l-m+2)}{4(2l+1)(2l+3)}},$$

$$b_{lm}^{-+} = -\sqrt{\frac{(1+\delta_{0m})(l-m)(l-m+1)}{4(2l-1)(2l+1)}}, \quad b_{lm}^{++} = -\sqrt{\frac{(1+\delta_{0m})(l+m+1)(l+m+2)}{4(2l+1)(2l+3)}}.$$

For randomly oriented particles, the phase function may be expanded as a Legendre series in the scattering angle Θ as

$$P(\cos\Theta) = \sum_{l=0}^{L+M} \chi_l \mathcal{P}_l(\cos\Theta). \tag{2.15}$$

Applying the addition theorem of associated Legendre functions, integrating over angles (μ', ϕ'), and using the orthogonality relations of Y_{lm}'s, the scattering integral becomes

$$\left[\frac{1}{4\pi}\int_0^{2\pi}\int_{-1}^{1} P(\mu,\mu',\phi,\phi')I(\mu',\phi')d\mu' d\phi'\right]_{lm} = \frac{\chi_l}{2l+1}I_{lm}. \tag{2.16}$$

Inspection of (2.16) reveals that spherical harmonic terms of the scattering integral are not coupled. This is true if the phase function depends only upon the scattering angle Θ.

The thermal emission (2.10) and the single scattered solar sources (2.11) are also expanded in spherical harmonics as,

$$S_{lm}^{\mathrm{ir}} = k(1-\tilde{\omega})B(T)\sqrt{4\pi}\delta_{l0}\delta_{m0} \tag{2.17}$$

and

$$S_{lm}^{\mathrm{so}} = \frac{F_0}{\mu_0} Y_{lm}(\mu_0,\phi_0)\left(\frac{k\tilde{\omega}\chi_l}{2l+1}\right)\exp[-\tau_s(x,z)]. \tag{2.18}$$

In these equations the thermal source term (S_{lm}^{ir}) is isotropic and the solar source requires the computation of the direct collimated solar beam flux. The optical depth (τ_s) is computed by integrating the extinction field from each grid point toward the sun assuming that the extinction ($k(x,z)$) varies bilinearly within each grid cell.

2.2.3 Spatial Grid Discretization

The radiance fields and optical properties are represented on a discrete grid as discussed by Evans. The grid coordinates are assumed independent and thus the grid is rectangular. For the simulations reported here, the grid is evenly spaced, but this need not be the case in general. The finite difference approximations used to estimate the partial derivatives in x and z are the three-point centered scheme and a two-point trapezoidal scheme respectively. Both schemes are second-order, but the two-point scheme in z was chosen because of the difficulty encountered at the top and bottom boundaries of the grid. The optical properties of the cloud are defined at each grid point and are the extinction, single scatter albedo and a Legendre series representation of the phase function.

2.2.4 Boundary Conditions

Selection of boundary conditions for the spherical harmonic method has prevented this method from becoming more widely used. Evans has chosen periodic boundaries in x and modified Marshak (1947) boundary conditions in z. This method constrains the odd hemispheric moments of the radiance field at the boundaries according to,

$$\int_0^1 [I(\mu) - \Gamma(\mu)]\,\mathcal{P}_l(\mu)d\mu = 0 \quad l = 1,3,...L \tag{2.19}$$

which can be generalized to multiple dimensions by replacing the Legendre functions with Y_{lm}'s in (2.19) and integrating both angles over the hemisphere to get

$$\int_0^{2\pi}\int_0^1 [I(\mu,\phi) - \Gamma(\mu,\phi)]\,Y_{lm}(\mu,\phi)d\mu d\phi = 0 \quad \text{for } l-m \text{ odd}\ . \tag{2.20}$$

The conditions (2.20) constrain one hemisphere of radiance independent of the other since for $l-m$ odd, the Y_{lm}'s are odd functions of μ. Also, this condition also is assured of producing the correct number of constraint equations because the number of terms with $l-m$ odd is always less than or equal to half the total number of terms in the series. This method was used to specify isotropic thermal radiation at cloud top and emission

or reflection of radiation at cloud base. The upwelling radiance at the lower boundary is expressed as

$$\Gamma_b(\mu,\phi) = \Gamma_e + \int_0^{2\pi}\int_{-1}^{0} R(\mu,\phi,\mu',\phi')I(\mu',\phi')d\mu' d\phi', \tag{2.21}$$

where Γ_e is the surface source of diffuse radiation from either emission or direct solar radiation and R is the surface reflection function that can be a Lambertian or Fresnel specular surface. There is assumed to be no upwelling collimated radiation. These boundary conditions are expressed as a set of linear equations involving the spherical harmonic coefficients of the radiance field at each point on the boundaries and are written as,

$$\sum_{l'} U_{lm,l'}I_{l'm} = \Gamma_{lm} \quad l-m \text{ odd}, \tag{2.22}$$

the coefficients of which (i.e., U and Γ) are derived by substituting 2.21 into 2.20 and integrating over the azimuth angle.

2.2.5 Solution Method

According to Evans, the preceding equations form a coupled linear system of equations in terms of the radiance vector **I**, the source terms **S**, and the sparse matrix denoted as **D**. The discretized radiative transfer and boundary conditions constrain the problem to allow a unique solution. This solution is found using the iterative conjugate gradient method of solution by Kershaw (1978) which reduces the residuals of the equations given an initial guess. In matrix-vector notation, the problem is represented in terms of the radiance vector **I**, the residual vector **r**, and the step direction vector **p** as:

$$\lambda = \frac{|\mathbf{r}_n|^2}{|\mathbf{p}_n|^2}$$
$$\mathbf{I}_{n+1} = \mathbf{I}_n + \lambda \mathbf{p}_n$$
$$\mathbf{r}_{n+1} = \mathbf{D}\mathbf{I}_{n+1} - \mathbf{S}$$
$$\gamma = \frac{|\mathbf{r}_{n+1}|^2}{|\mathbf{r}_n|^2}$$
$$\mathbf{p}_{n+1} = -\mathbf{D}^{\mathrm{T}}\mathbf{r}_{n+1} + \gamma \mathbf{p}_n$$

with $\mathbf{r}_0$ as the initial residual vector and $\mathbf{p}_0 = -\mathbf{D}^{\mathrm{T}}\mathbf{r}_0$ as the initial step direction. The iterations are continued until $\mathrm{RMS}(\mathbf{r}_{n+1})/\mathrm{RMS}(\mathbf{I}_{n+1}) \leq tol$, where *tol* is a specified tolerance taken to be 0.001 for the simulations presented in this report. The size of the three vectors, **I**, **r**, and **p** determines the memory requirements of this method and is specified by the spherical harmonic expansion and grid discretization. The effects of changing the spherical harmonic expansion and the grid discretization on the solution accuracy, memory requirements, number of iterations and the duration of each iteration are explored in the next section. The SHSG model can be initialized using a spherical harmonic solution for $L = 1$, $M = 0$ truncation (i.e., a column two-stream solution) or with the input of a complete radiance field from a previous SHSG solution. The initialization of the model is discussed in more detail in Section 2.3.

2.2.6 Computation of Radiative Quantities

The resulting radiance fields, which satisfy the given tolerance specification, are weighted with a cosine and integrated using numerical quadrature over all angles to compute the upwelling and downwelling fluxes at a given level. The symmetry of the spherical harmonic series when multiplied by the cosine of the zenith angle (μ) and the integration over all azimuth angles requires that only the $m = 0$ terms be used. Thus, the fluxes are computed according to

$$F^{\uparrow,\downarrow} = \sum_{l=0}^{L} I_{l0} \left[2\pi \int_{0,-1}^{1,0} \mu Y_{l0}(\mu, 0) \mathrm{d}\mu \right].$$

The net flux in both the horizontal and vertical are computed for each grid box using only one term of the spherical harmonic series from the radiance field as follows:

$$F_x = -\left(\frac{4\pi}{3}\right)^{\frac{1}{2}} I_{11}$$

and

$$F_z = \left(\frac{4\pi}{3}\right)^{\frac{1}{2}} I_{10}.$$

Integrating the right side of the radiative transfer equation over all angles gives the net flux convergence that is proportional to the heating rate. This net flux convergence is given by

$$-\nabla \cdot \mathbf{F}_{net} = 4\pi k(1-\tilde{\omega}) \left[\overline{I} - B(T) \right]$$

for the thermal source term and

$$-\nabla \cdot \mathbf{F}_{net} = k(1-\tilde{\omega}) \left[4\pi \overline{I} + \frac{F_0}{\mu_0} e^{-\tau_s} \right]$$

for the solar source term where $\overline{I}$ is the mean intensity and $\overline{I} = (4\pi)^{1/2} I_{00}$.

The computation of the emerging radiances can be subject to large errors due to the truncations of the spherical harmonic series. These errors are reduced by computing the radiances in one of two ways. The first way is to generalize the Cesàro filter used by Dave and Armstrong (1974) to compute the radiances. Using this filter, the radiances at each level are computed by,

$$I(\mu, \phi) = \sum_{m=0}^{M} \sum_{l=m}^{L+m} \left[1 - \frac{(l-m)}{(L+1)} \right] \left[1 - \frac{m}{(M+1)} \right] I_{lm} Y_{lm}(\mu, \phi). \tag{2.23}$$

The advantage of this method is quick computation of the radiance at any level in the cloud field. Another method of computing radiances and avoiding computation errors, is

to compute only the radiances emerging from the top and bottom of the atmosphere grid by integrating the radiative transfer equation to get,

$$I(0) = e^{-\tau(s)} I(s) + \int_0^s \exp\left[-\int_0^{s'} k(t)dt\right] J(s')k(s')ds'. \tag{2.24}$$

The source function J is computed using the spherical harmonic expansion of the radiance field to compute the scattering integral (Kourganoff, 1952). Thus,

$$J_{scat}(\mu,\phi) = \frac{\tilde{\omega}}{4\pi}\int_0^{2\pi}\int_{-1}^{1} P(\mu,\phi,\mu',\phi')I(\mu',\phi')d\mu'd\phi' = \sum_{m=0}^{M}\sum_{l=m}^{L+m}\frac{\tilde{\omega}\chi_l}{2l+1}I_{lm}Y_{lm}(\mu,\phi), \tag{2.25}$$

which is added to thermal emission or the direct-to-diffuse source term to compute the total source term. These two methods of computing radiances are compared with exact 2-D Monte Carlo results in Section 2.4.

SHSG also includes an 'independent pixel approximation' which has no coupling in the x direction and computes solar beam and radiance path integrals in independent columns. This approximation is used to obtain the column plane-parallel estimations of radiant quantities from the cloud and are called independent pixel results (IPA).

2.3 Using SHSG to Compute Cloud Radiative Properties

To run SHSG, the spherical truncations L and M and the discretized optical properties must be specified appropriately. Choosing L, M and the proper grid size is a process that depends on the nature of the problem being studied and the complexities of the cloud system itself. Usually, one expects to require more L terms for problems dealing with more highly forward scattering phase functions and more M terms when the azimuthal properties become more important such as when using lower solar zenith angles. The size of the grid is important when considering the resolution of the cloud field, its optical thickness and homogeneity. In the following subsections, a portion of cloud 1, assigned optical properties as described above, is used in a series of calculations to test the parameters required for SHSG to converge to an accurate solution. These factors are considered within the overall context of the practical limits of the user's particular computing capabilities, which are discussed first in this section. This subsection is followed by subsections describing the process of selecting the spherical harmonic truncation and the grid size that result in the accurate simulation of the radiance field for the given cloud case.

2.3.1 Computational Issues

Although SHSG is used to simulate clouds of arbitrary structure, the total memory available and the computation time required to reach an accurate solution on a particular machine limits the grid size and spherical truncation that can be used to simulate a cloud

Table 2.2: Properties of example simulations of cloud 1 using three different grids and two different solar zenith angles.

Solar Zenith Angle	N_x	N_z	Iterations	Time (secs)	Time/Iteration (secs)
25	50	21	122	620	5.1
25	100	41	61	1171	19.2
25	200	61	29	2347	80.9
65	50	21	171	825	4.8
65	100	41	162	2812	17.4
65	200	61	62	4468	72.1

field. As noted above, three vectors required for the conjugate gradient method dominate the memory requirements of the SHSG model. The size of these vectors is represented as $N = N_x N_z N_{lm}$ where $N_{lm} = (L+1)(M+1)$ is the number terms in the spherical harmonic expansion and N_x and N_z are the grid sizes for the x and z domains respectively. The time required for the model to converge to an accurate solution also depends on N. It is simply a product of the time it takes for one iteration and the total number of iterations required for convergence to the specified tolerance. Consequently, Evans investigated how the total number of iterations required to reach convergence varied with increasing N. Evans found that: 1) for a constant grid size, the number of iterations required tended to an asymptote as N_{lm} increased, and 2) for a constant N_{lm}, the number of iterations increased about 30 and 20 for solar and thermal wavelengths respectively for every factor of two increase in vertical grid size (N_z), but is insensitive to horizontal grid increases (N_x). These properties can greatly increase the required memory and lengthen the computation time for increasingly complicated extinction fields and scattering geometries. However, Evans does note two different techniques of reducing the computation time required to obtain a meaningful solution.

The first of these techniques is called a course grid initialization. As noted above the model can be initialized with a column two-stream radiative transfer solution or with a previous solution. Table 2.2 gives the number of iterations and total computation times for a series of cases using the course grid initialization scheme for a cloud field having a domain averaged optical depth of eight, a spherical truncation of $L = 31$, $M = 11$, and two different solar zenith angles 25° and 65°. Note that the number of total iterations decreases with each case. This behavior not only can be used for finding the convergence to an accurate solution for a given optical medium, but also leads to a significant computational time savings for the higher resolution cases. As noted above from Evans, a doubling of the resolution and initializing with a two-stream leads to an increase in the number of iterations by a factor of 30. Since a doubling of the grid size also results in a fourfold increase in the time required for each iteration (see Table 2.2), the effect of doubling the grid size and initializing from a two-stream solution would increase the total computation time by

a factor of 120. As a result, the course grid initialization scheme becomes necessary as the grid sizes (i.e., N) become larger. Note also that the lower solar zenith angle required much more iterations and thus more computation time than the higher solar zenith angle cases. This shows that the total computational time is not only sensitive to N, but also to the particular scattering geometries of the simulations. These factors also must be taken into account when planning SHSG simulations.

Besides the course grid initialization scheme, another technique that reduces the number of iterations is to set a minimum extinction value. The specification of extremely low extinction values (i.e., $< 10^{-4}$) has been observed to increase greatly the number of iterations required for convergence of the conjugate gradient solution. Selecting the appropriate minimum extinction reduces this problem without significantly affecting the resultant radiative solution. For the simulations presented in this study, the minimum extinction is set to 0.005 km^{-1}.

These properties of SHSG show the viability of the method. However, the absolute accuracy of the solution, which has a specified grid size and spherical harmonic truncation, is important to understand given a particular extinction field. The absolute accuracy of the calculation depends upon the approximations to the angular and spatial resolution of the optical media that are inherent in the selection of the spherical truncations and the grid size.

2.3.2 Specification of the Spherical Truncation

The specification of the spherical harmonic truncation (i.e., L and M) limits the angular resolution of the radiance field. This limit introduces error into the resulting radiances dependant upon the optical thickness and scattering properties of an optical media. Also, the specification of L introduces error into the expression of the phase function (see equation 2.15). The goal then, is to select spherical truncations that limit the error of the resulting approximations. Assuming that SHSG will converge to more exact solutions as L and M are increased, the truncations of the series are selected based on a trial and error method. Thus, the radiance field computed at one set of truncations is compared with that computed at a higher set of truncations until a convergence to a particular solution is reached. As an illustration of this process, Figure 2.8 presents the upward radiances computed for several different L truncations given a M truncation of 7 for a cloud field that has a domain averaged optical depth of about 1.0 at a wavelength of 0.83 μm.Figure 2.8 shows that the difference between the radiances decreases significantly with the increase in L. Figure 2.9 shows the root mean square (RMS) relative differences between the increasing L terms.For this cloud case there is a convergence of the radiances for $L > 23$ as the relative changes decrease from an average of nearly 10% between $L = 7$ and $L = 15$ to less than 2% between $L = 23$ and $L = 31$ (see Table 2.3). For a thicker cloud with an average optical depth of 8.0, the L terms required in the harmonic series

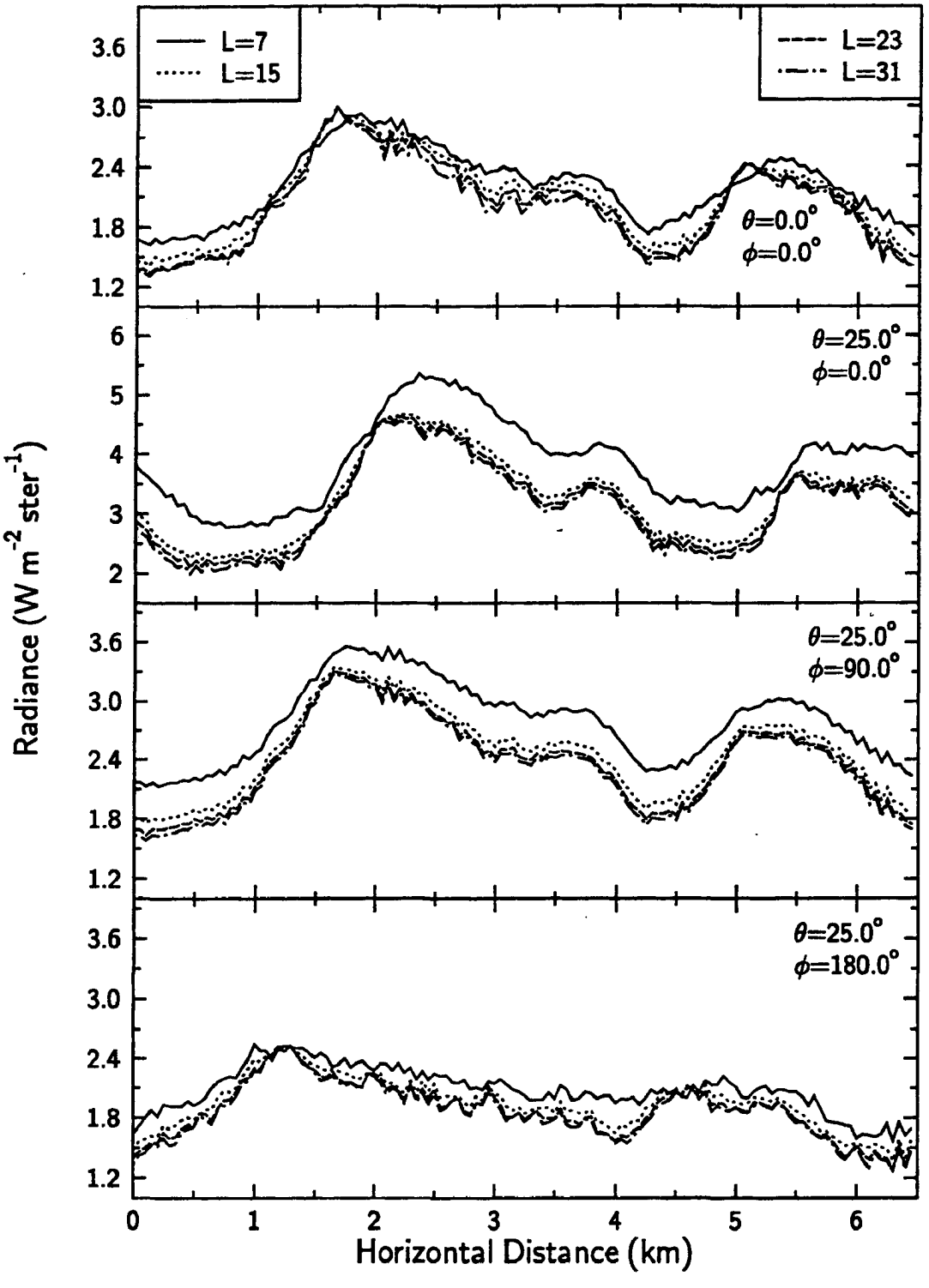

Figure 2.8: Two-dimensional upward radiances using various L truncations at the indicated viewing angles with $M = 7$ for cloud 1 with a domain averaged optical depth of 1.0 and a solar zenith angle of 50° .

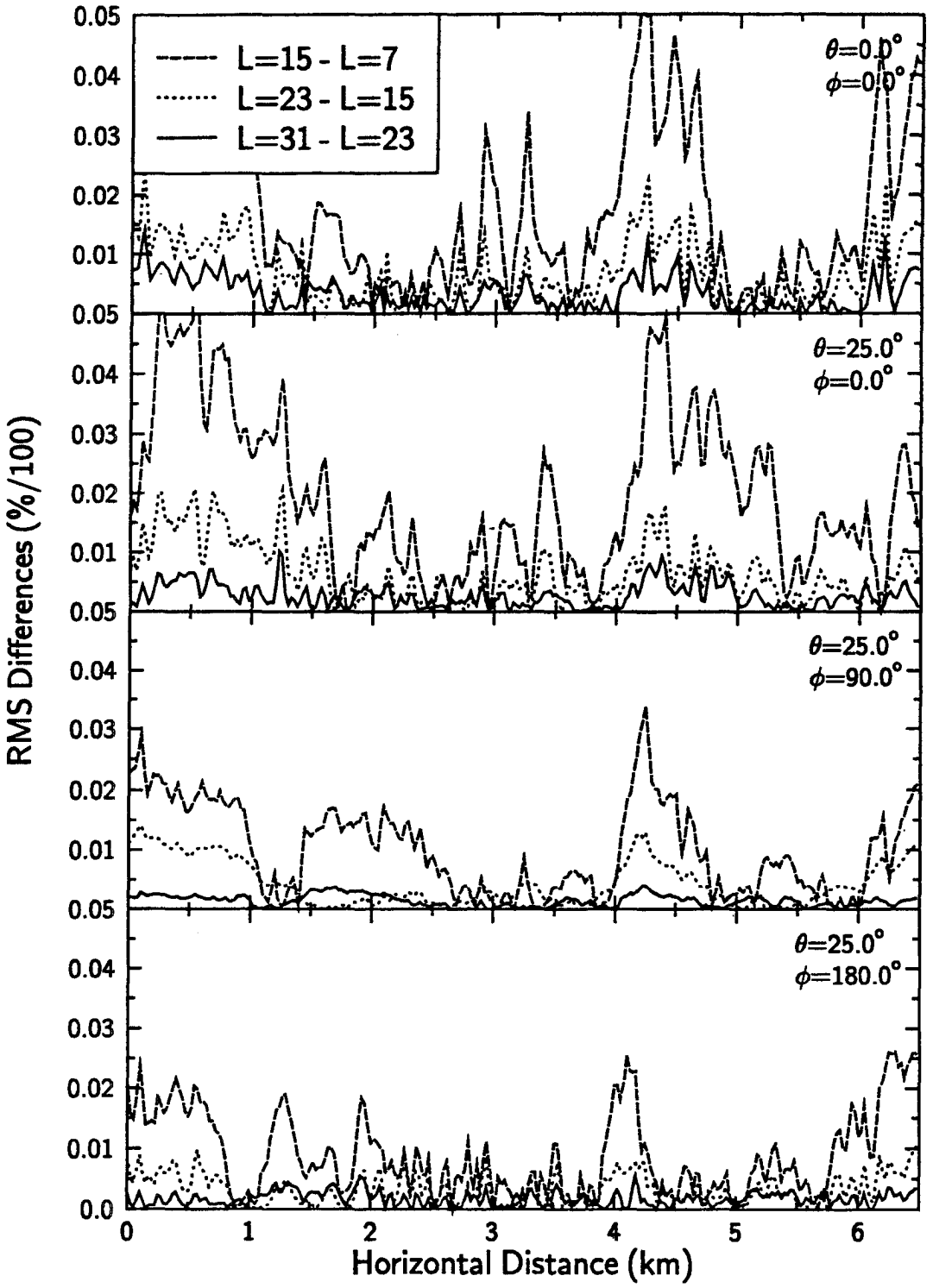

Figure 2.9: RMS relative differences of upward radiances for successive L truncations for the same cloud field as in Fig 2.1.

Table 2.3: Percent RMS relative differences in upward and downward radiances computed over the horizontal and all viewing angles for successive values of L for cloud 1 scaled to domain averaged optical depths of 1 and 8.

	$\tau = 1.0$		$\tau = 8.0$	
L Values	**Upward**	**Downward**	**Upward**	**Downward**
L=15 - L=7	9.87	10.69	2.04	4.24
L=23 - L=15	3.65	3.10	0.63	1.55
L=31 - L=23	2.32	1.68	0.34	0.77

for convergence is reduced to about 15. This is shown in Table 2.3 where the RMS % differences, averaged over the horizontal and all viewing angles between each successive value of L, are seen to be greatly reduced from the thin cloud case. A similar type of behavior occurs for the M modes shown again by RMS relative differences in Figure 2.10. This figure shows relative differences that decrease to less than 2% between the $M = 7$ and $M = 11$ cases representing a type of convergence. This behavior holds even at lower viewing angles where the overall relative difference is about 3% between these values of M.

One reason that so many terms are required is a direct result of the approximation of the truncated phase function. A coarse truncation of the Legendre series used to approximate the phase function introduces spurious oscillations.These types of oscillations, which become worse as the forward scattering is increased, affect the radiances of thin clouds where single scattering is the primary process determining the reflection. In these instances, especially for higher zenith angles, negative upward radiances resulted requiring larger L values to control. However, when multiple scattering dominates, as for thicker clouds, this problem is evidently reduced. To prevent the problems with negative radiances and reduce the L terms required to represent a phase function for thin clouds, the Δ-M method introduced by Wiscombe (1976) is incorporated in the model. Figure 2.12 shows the effect of using the Δ-M method with various L values for the same phase function presented in Fig 2.11. The amplitude of the oscillations is significantly reduced for a particular L using Δ-M than without the approximation. This allows for the reduction of spherical harmonic terms in the representation of the phase function and provides for the representation of more highly forward scattering phase functions.Implementation of the Δ-M method requires the scaling of extinction, single scatter albedo, and the phase function. However, in SHSG Evans notes that all the terms of the radiative transfer equation except the solar pseudo-source term are invariant to the scaling (see equation 2.18). Thus, the incorporation of the Δ-M method into SHSG is simple and greatly improves the ability of the model to use more realistic highly asymmetric phase functions. The results of using this scaling method are compared with two-dimensional Monte Carlo simulations in Section 2.4.

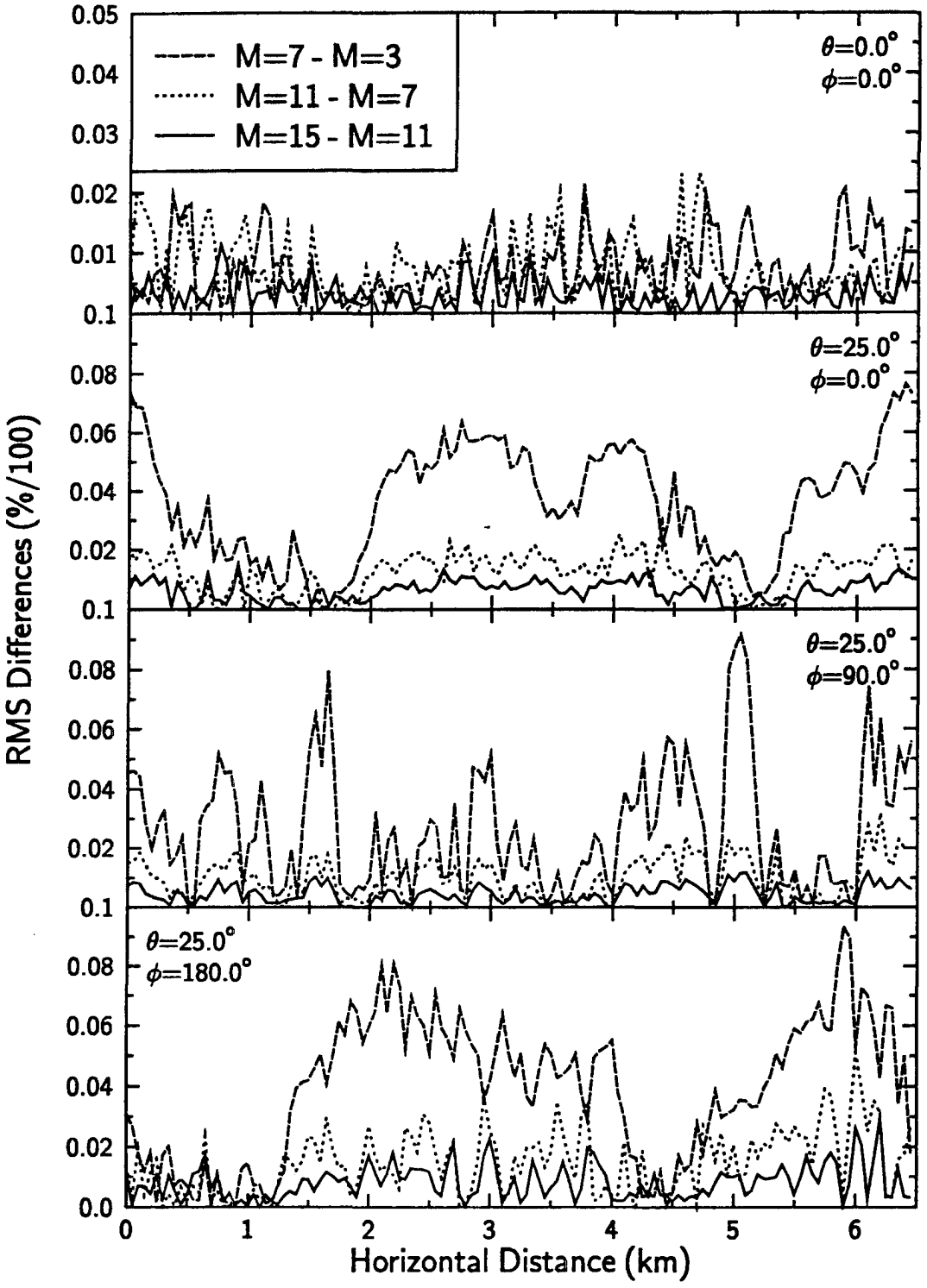

Figure 2.10: RMS relative differences of upward radiances for the cloud field of Fig. 2.1 but for successive M truncations at the indicated viewing angles and $L = 23$.

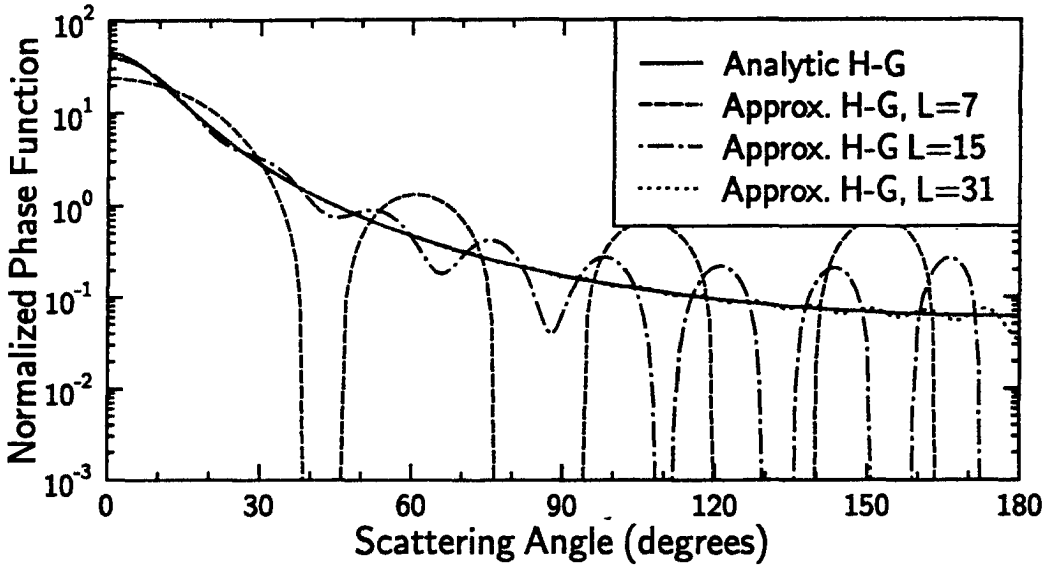

Figure 2.11: Analytic Henyey-Greenstein phase function for $g = 0.8$ compared with the same phase function produced from a Legendre series representation with the number of L terms indicated.

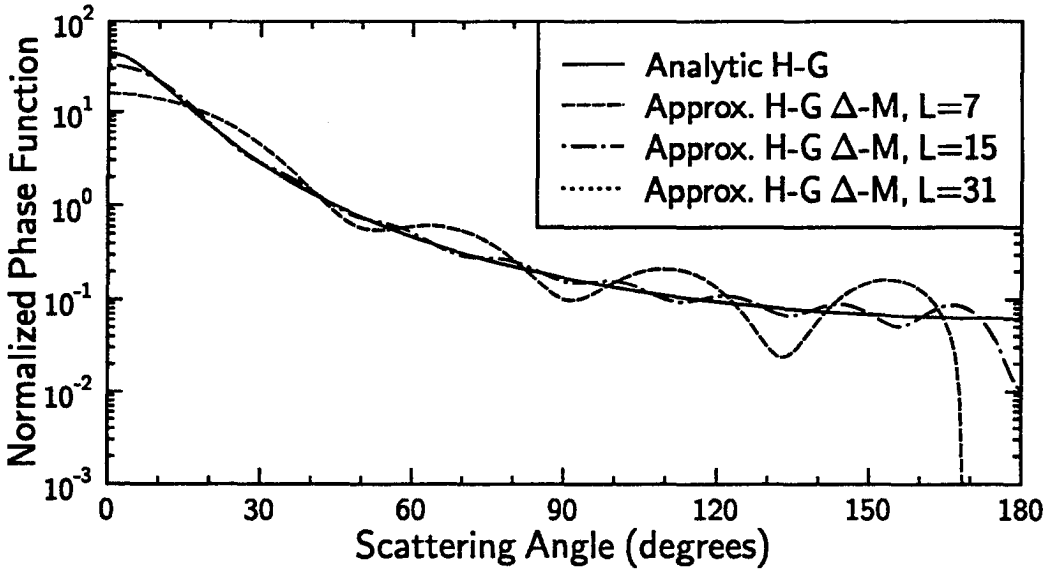

Figure 2.12: Analytic Henyey-Greenstein phase function for $g = 0.8$ compared with the same phase function produced from a Legendre series representation using the δ-M approximation with the number of L terms indicated.

Table 2.4: The relative RMS differences from the highest resolution grid for the cases presented in Table 2.1.

Solar Zenith Angle	N_x	N_z	Max τ	RMS Relative Differences (%)	
				Up	Down
25	50	21	1.1463	1.0	0.9
25	100	41	0.5939	0.2	0.2
25	200	61	0.2969	—	—
65	50	21	1.1463	3.1	2.3
65	100	41	0.5939	0.3	0.2
65	200	61	0.2969	—	—

2.3.3 Grid Selection

The selection of the grid size is not only a problem dependent upon the optical properties and spatial variability of the optical media, but also to the particular scattering geometry of the simulation. These properties of a radiance calculation require spatial resolutions sufficient to reduce the computation of spatial derivatives (see equations 2.13 and 2.14). As a result, the proper spatial resolution depends upon the extinction across a grid cell, the scattering properties of that grid cell and the variations of extinction relative to the maximum extinction within the medium. Since the radiance viewing angles and the solar zenith angle increase the path length, these parameters also influence the radiance gradients. In order to reduce these effects, only radiances at viewing angles $\leq 45°$ are used in this study. This defines a viewing geometry that is typical of scanning radiometers from space and aircraft. The remaining parameters are chosen based upon a trial and error process like the one used above for the spherical truncations.

As an example of this process, the maximum optical depth across a grid cell and the relative RMS differences from the highest resolution simulations of calculations presented in Table 2.2 are given in Table 2.4. Figure 2.13 presents the upward radiances at the nadir viewing angle for both zenith angle cases. Although the relative RMS difference values are small, the oscillatory nature of this course grid about the finer resolution solutions is evident in the figure. The order of magnitude decrease in the relative RMS values represents the kind of effect that doubling the grid resolution may have. Note that these relative RMS values are smaller for downward radiances than for upward radiances. It is also important to note that the solution to the course grid at the lower solar zenith angle produces larger relative RMS values than the solution at higher solar zenith angles. The effect of increasing the viewing angle was only very small for these calculations, but there seems to be an overall trend of relative error decreasing toward the backscattering angles. Finally, both Table 2.4 and Figure 2.13 show that there is a convergence of the solution about the $N_x = 100$, $N_z = 41$ grid.This grid has a maximum extinction across a grid cell of about 0.6, which agrees with the suggested criteria of Evans that this quantity be less

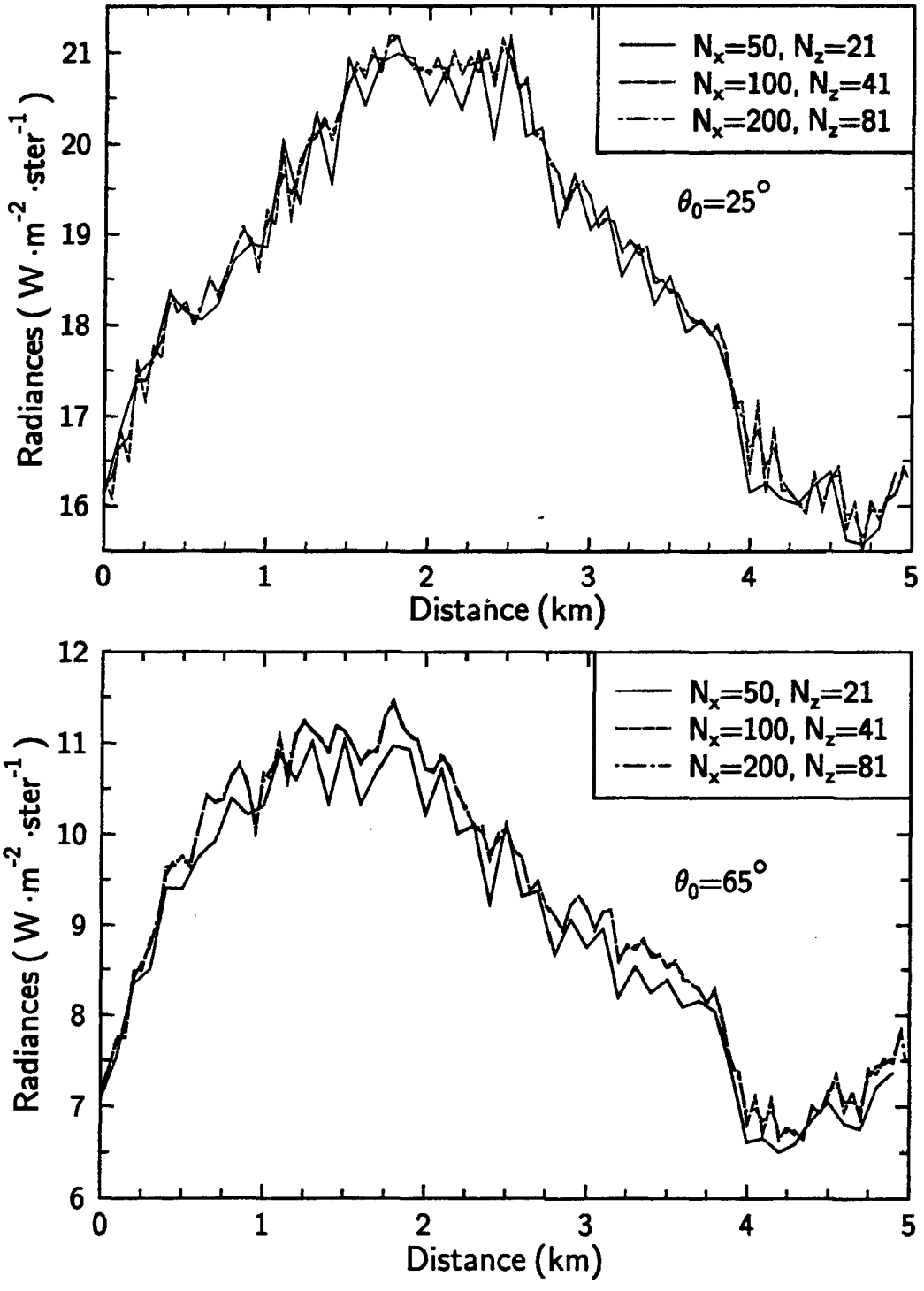

Figure 2.13: Upward radiances for the three different grid sizes and solar zenith angles as indicated for cloud 1 as described in the text.

than 1.0. However, in testing it was found that this criterion was too conservative for certain thick homogeneous clouds that contain very large radiance gradients in the solar wavelengths at cloud top (see, Duda, 1994). As a result, an additional test was prescribed for the radiance gradients. However, for cirrus clouds this is usually not a problem since the clouds are optically thin with the only locally large radiance gradients near an area of large extinction, which normally occurs near cloud base. Thus, for the simulations presented here, the grid resolution was selected by limiting the maximum grid cell optical depth to less than 0.5 and by testing for convergence of solution with increasing grid size at the lowest solar zenith angles.

2.4 SHSG Validation with Monte Carlo Simulations

To evaluate further the absolute accuracy of SHSG, a series of comparisons is made with a two-dimensional Monte Carlo model. The comparisons are made to test the Δ-M method and to evaluate the method of computing radiances (see equations 2.23 and 2.24) in a more quantitative way. A "backward" Monte Carlo employed by Evans to test the SHSG method is used here. This model has the same periodic boundary conditions in the horizontal as SHSG. Additionally, the inputs to the Monte Carlo model are analogous to the inputs accepted by SHSG, except for the order of scatter and the integration nodes (i.e., number of photons). After a series of tests, the order of scatter and the number of photons were set to 40 and 100,000 respectively. The phase function used in the Monte Carlo model is represented by 256 Legendre coefficients as opposed to that of SHSG that approximates the phase function with a truncated series and with the Δ-M method. The assignment of the order of scatter, integration nodes, and phase function in this manner, allow the Monte Carlo calculations to be considered "truth". These calculations are then compared with the SHSG solutions to ascertain the overall accuracy of SHSG and evaluate the Δ-M and radiance computational methods.

As noted previously, the double Henyey-Greenstein function is used to approximate the phase function of ice crystals. In this case, the constants are chosen to produce the most highly asymmetric phase function that is used in the course of this research. The constants g_1, g_2, and b as defined in equations 2.2 and 2.3 are set to 0.952, -0.45 and 0.92 respectively where $g_{eff} = 0.84$. The single scattering albedo was held constant at 0.9021. The asymmetry parameters and single scatter albedos typify a spherical ice cloud at 2.21 μm. This wavelength was chosen because of the difficulty encountered with negative radiances. SHSG was observed to do much better at shorter wavelengths and in the thermal emission regime. As a result, the comparisons here are thought to comprise a type of worst case. Cloud 1 is scaled to produce two different cloud fields having domain optical depths of 0.5 and 8.0. These optical depths represent a very thin and very thick cirrus cloud respectively. The solar zenith angle for these simulations is specified as 60°

Table 2.5: Average relative error in percent over all azimuth angles (ϕ) and viewing angles (θ) $\leq 45°$ (or $cos(\theta) \geq 0.7$) between SHSG and the Monte Carlo radiances.

Spherical Truncation	$\overline{\tau} = 0.5$				$\overline{\tau} = 8.0$			
	No $\Delta - M$		$\Delta - M$		No $\Delta - M$		$\Delta - M$	
	Kour.	Ces.	Kour.	Ces.	Kour.	Ces.	Kour.	Ces.
$L = 15, M = 7$	412.66	14.30	14.64	13.42	105 .12	6.89	5.51	4.49
$L = 23, M = 11$	371.53	12.19	14.57	11.17	86.80	3.20	7.00	3.14
$L = 31, M = 15$	180.33	13.76	11.65	9.69	40.82	3.30	3.59	2.91
$L = 47, M = 23$	166.02	13.05	7.79	6.84	41.16	4.88	4.76	3.34

and the grid size was $N_x = 64$, $N_z = 65$. Finally, the comparisons were made between upward radiances for 28 discrete angles at a centrally located horizontal grid point at cloud top.

A sample of the results is shown for the domain averaged optical depth cases of 0.5 and 8.0 in Figures 2.14 and 2.15.Each figure contains four panels that give the radiances from SHSG with increasing spherical truncations using the Cesàro filtering method, the Cesàro and Kourganoff methods with the Δ-M scaling and the Monte Carlo computations as a function of the cosine of the viewing angle at an azimuth angle of 0°. These figures also show the oscillatory nature of the Kourganoff method as opposed to the smoothing nature of the Cesàro method. The Kourganoff solutions without the Δ-M scaling are so extremely oscillatory that they are not plotted here. However, even in this case, the oscillations are observed to decrease in amplitude with increasing spherical truncation. These figures illustrate how SHSG solutions, using either method of radiance computation, converge to the correct solution with increasing truncations. Note that in Figure 2.14 the change in the solutions from $L = 15$, $M = 7$ to $L = 23$, $M = 11$ is very large, especially with the Kourganoff method. However, the change in the solutions from $L = 23$, $M = 11$ to $L = 31$, $M = 15$ is much less dramatic. This also holds for the domain averaged optical depth case of 8.0 except for the Cesàro Δ-M scheme, which shows excellent agreement even at the lowest truncation. Figures 2.16 and 2.17 compare the SHSG and the Monte Carlo method for all the angles at both the domain averaged optical depth clouds. Overall, the SHSG simulations agree well with the Monte Carlo results, especially for the viewing angles $\leq 45°$ (i.e., cosine of the viewing angle ≥ 0.7).An exception to this occurs for the 180° azimuth angle for the Cesàro method in the thick cloud. However, even here the agreement is good for viewing angles $\leq 45°$ and improves with increasing spherical truncation. Table 2.5 shows the average relative error of the SHSG calculations (in percent) as a function of truncation and radiance computation method for these viewing angles. The results indicate that thin clouds require a higher spherical truncation than thick clouds to attain the same absolute accuracy. Only the highest truncations presented here for the thin cloud reduce the average error in the radiances to less than 10%. However, since the thin cloud radiances represent a worst case, it is expected that thicker clouds or clouds

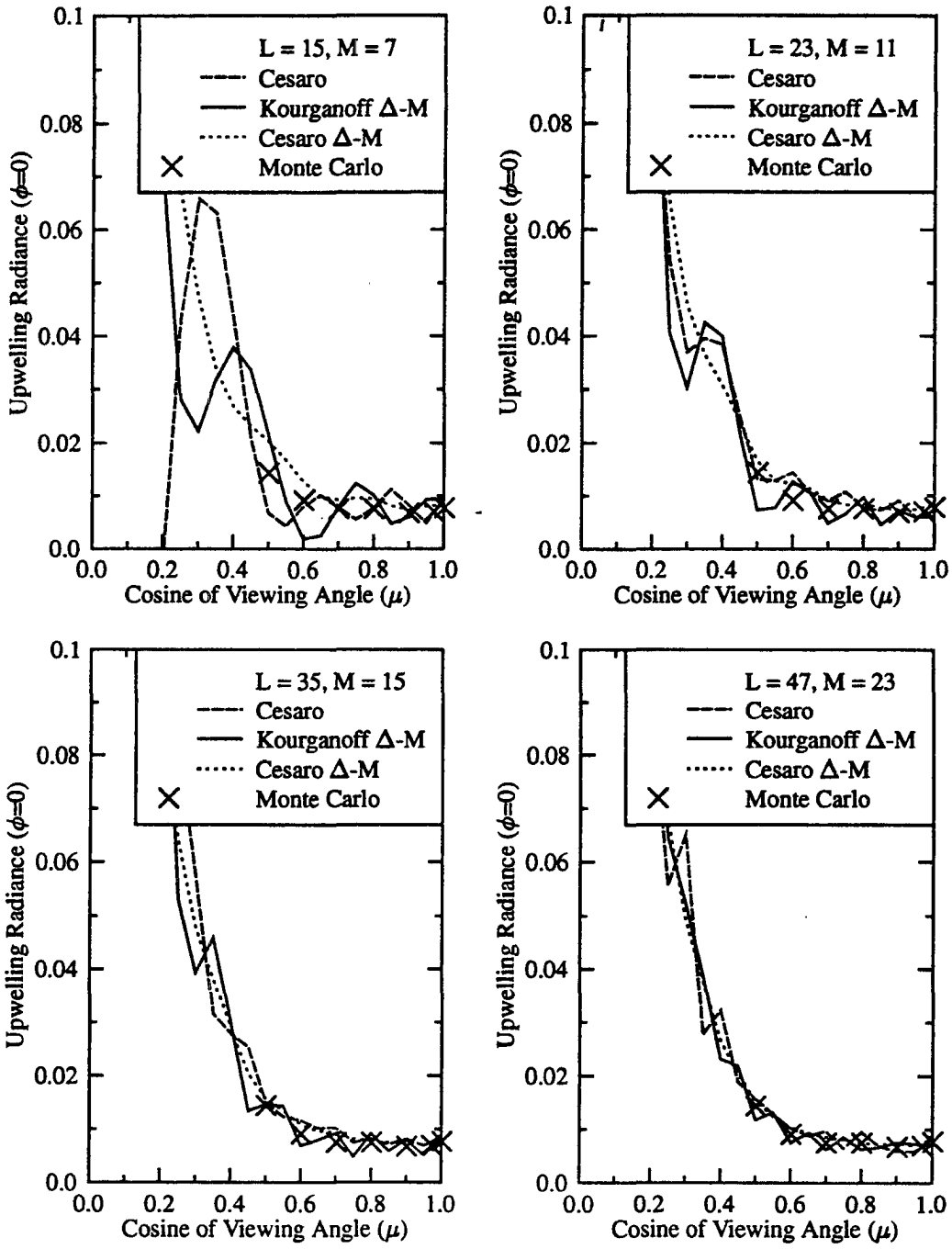

Figure 2.14: Upward radiances as a function of the cosine of the viewing angle (μ) at the azimuth angle $\phi = 0°$ from SHSG and the Monte Carlo methods with increasing spherical truncation of SHSG in cloud 1 with the domain averaged thickness of 0.5.

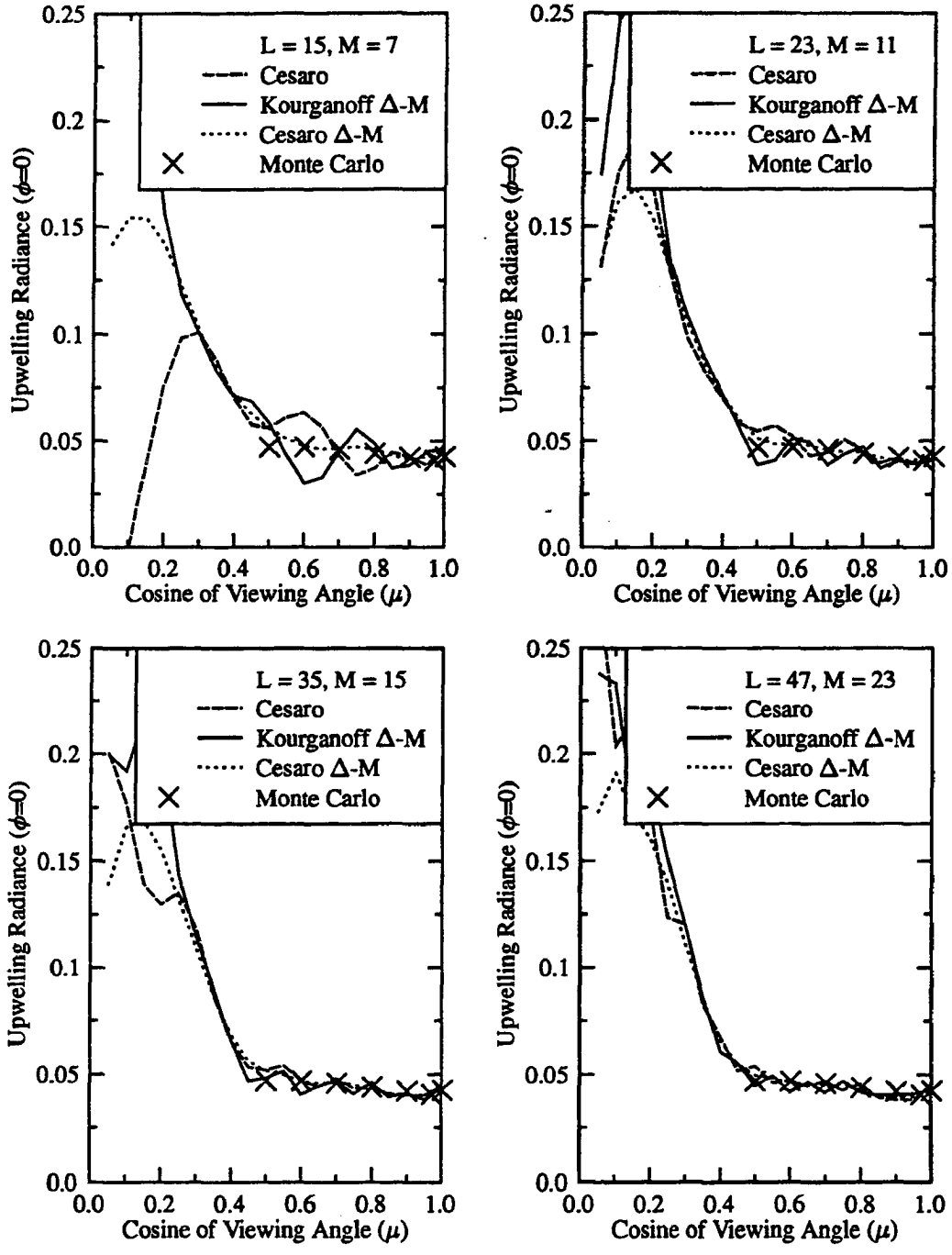

Figure 2.15: Upward radiances as a function of the cosine of the viewing angle (μ) at the azimuth angle $\phi = 0°$ from SHSG and the Monte Carlo methods with increasing spherical truncation of SHSG in cloud 1 with a domain averaged thickness of 8.0.

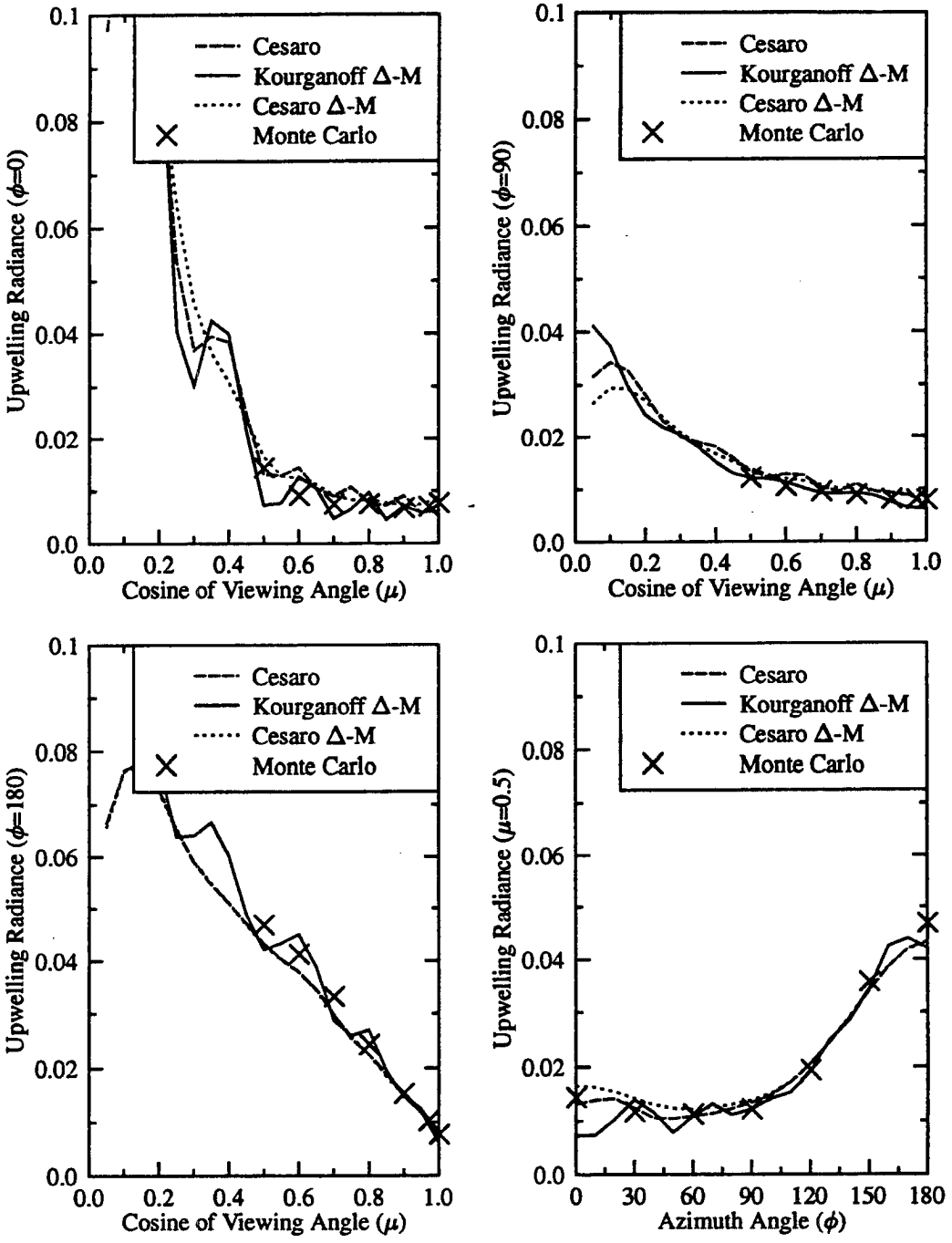

Figure 2.16: Upward radiances from SHSG and Monte Carlo methods with a spherical truncation of $L = 23, M = 11$ in SHSG for all the comparison angles in cloud 1 with domain averaged thickness of 0.5.

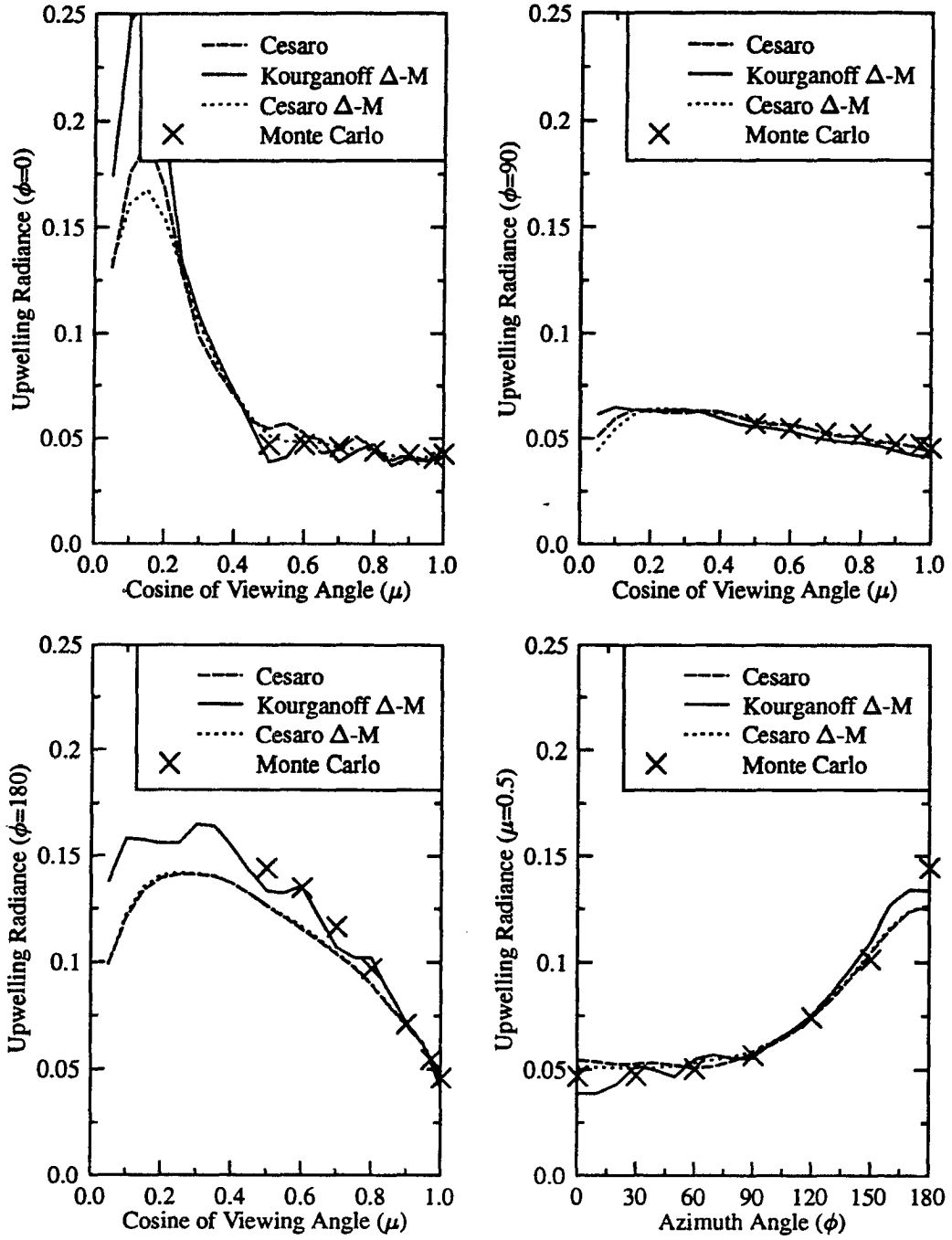

Figure 2.17: Upward radiances from SHSG and the Monte Carlo methods for a spherical truncation of $L = 23, M = 11$ in SHSG for all the comparison angles in cloud 1 with domain averaged thickness of 8.0.

with less asymmetrical phase functions will give absolute errors less than this. Based upon these results and the computational constraints of running SHSG, the spherical truncations between $L = 23$, $M = 11$ and $L = 31$, $M = 15$ with the Δ-M scaling method are used in this research for all the simulations. Although not explicitly discussed here, the computation of fluxes using this criteria will be much more accurate since only the $m = 0$ modes are required in the integration. Evans found that a truncation of $L = 15$, $M = 7$ produces agreement with Monte Carlo simulations well under 2%. Finally, the Cesàro filtering method of calculating the radiances generally produced less error than the Kourganoff method. Since this method also allows the computation of radiances at any given level, the Cesàro is used exclusively in the simulations presented in this report.

2.5 Chapter Summary

This chapter outlines a procedure to infer two-dimensional clouds from radar observations and describes the Spherical Harmonic Spatial Grid method of multi-dimensional radiative transfer (Evans, 1993) used to simulate the radiative properties of these clouds. The two-dimensional cloud fields are derived from radar observations in order to ascertain the effects of two-dimensional radiative transfer on the radiance fields within ice clouds. These two-dimensional ice cloud fields were derived in two different ways. The first cloud type used only radar measurements and a parameterization to produce clouds which had a variable extinction field but a constant single-scattering albedo and scattering phase function. These clouds are used to understand the effect of cloud structure on radiative transfer. The second cloud type is derived from a method using both radar and lidar data. This method gives two-dimensional fields of effective radius and total concentration which can be converted to two-dimensional fields of extinction and single-scattering albedo. This type of cloud is used to investigate the effects of varying the effective radius throughout the cloud upon the radiative transfer. Together both of these cloud types are used in the subsequent chapters to ascertain the relative importance of horizontal inhomogeneity and cloud microphysics in determining the radiative properties of cirrus clouds in given situations.

To complete such analysis a two-dimensional radiative transfer is used that can treat clouds as described above. The radiative transfer model selected for this purpose is the Spherical Harmonic Spatial Grid method developed by Evans (1993). The attributes of this method, which justify its use in the investigation of ice cloud radiative properties, are the ability to:

1. model arbitrarily shaped clouds;

2. determine the radiative quantities of the cloud at any horizontal or vertical grid point with only one solution; and

3. generate independent pixel radiative quantities easily by specifying one parameter within the model.

The use of SHSG to simulate the radiative properties of two-dimensional clouds required thorough testing of the method and the conditions under which the most accurate solutions could be obtained. This testing involved comparing the model solutions for increasing spherical harmonic truncation and decreasing grid resolution. The absolute accuracy of the method is tested by comparison to simulations using a two-dimensional Monte Carlo method. Practical limitations involving the memory capacity of the computer on which the calculations are performed were also considered. To ensure the most accurate solutions given these limitations the minimum spherical harmonic truncation for the calculation of radiances is taken to be $L = 23$, $M = 11$ for all the calculations here. Since this truncation leads to errors in the representation of the phase function in the model, the Δ-M method is used to partially compensate for this effect. The choice of the grid size is optimized to produce the most accurate results for a given cloud domain by requiring the maximum grid cell extinction to be less than 0.5. To reduce the number of iterations required for convergence, a minimum extinction of 0.005 km^{-1} is specified. Finally, the Cesàro method is introduced to compute the radiances from the spherical harmonic series since this method is more accurate and more convenient than the Kourganoff method.

Using the above criteria and guidelines to determine the conditions under which SHSG is used, a series of radiance calculations using SHSG on a two-dimensional cloud inferred from radar are compared to Monte Carlo calculations in the same cloud. The overall relative differences obtained between SHSG and the Monte Carlo for a worst case scenario with a highly forward scattering phase function and an absorbing wavelength are 3.1% for the thick cloud and 11.2% for the thin cloud. Comparisons for all other conditions were much better. The agreement between fluxes although not explicitly described in detail here is found by Evans to be better than 2% under spherical truncations much less stringent than used above for the calculation of radiance. It should be noted that these criteria provide the first guess at determining the grid size and spherical harmonic truncation for SHSG simulations that should be tested by the trial and error method for each particular case. An understanding of the limitations of this model and the use of the guidelines stated above ensure an accurate solution given the stable behavior of the SHSG method. The following two chapters use the clouds and the radiative transfer described in this chapter to conduct sensitivity studies of radiances and fluxes to the effects of horizontal cloud structure.

Chapter 3

THE SENSITIVITY OF RADIANCE FIELDS TO THE OPTICAL PROPERTIES AND SPATIAL INHOMOGENEITIES OF TWO-DIMENSIONAL ICE CLOUDS

The purpose of this chapter is to demonstrate the sensitivity of cirrus cloud radiance properties to variations in cloud structure and cloud microphysical properties in two dimensions. These sensitivities are investigated using the two types of two-dimensional cirrus cloud fields derived from radar observations as described in the previous chapter. The first type of cloud contains ice particles that vary in concentration only and have a constant microphysical distribution. These clouds isolate the influences of inhomogeneities in cloud structure upon the radiative properties of ice clouds. The second type of cloud contains ice particles described by size distributions that vary throughout the cloud. Radiative transfer calculations in these clouds represent the convolution of both the cloud structural effects and the variation of microphysical properties in two dimensions. In this chapter, the sensitivities of the radiance properties are discussed for both types of clouds. The implication of these sensitivities is illustrated by using plane-parallel remote sensing techniques to estimate the column optical depth and effective radius by comparing these estimations to the actual cloud properties. In this way, the relative importance of the cloud inhomogeneities and cloud microphysics in the form of both the single-scattering albedo and phase function is assessed.

3.1 Sensitivities of Radiances and Retrievals for Clouds with Constant Microphysics

By definition radiances are directional quantities and are strongly dependent upon the optical properties of the cloud encountered along a slant path. For this reason, the radiances computed from clouds with two-dimensional slant paths may differ significantly from radiances computed using plane-parallel theory. In this section, the implications of these differences are examined and then interpreted in terms of plane-parallel bispectral retrieval methods. Such methods are frequently used to estimate cloud properties from satellite radiance measurements. Here, the radiances from 2D calculations are used in conjunction with plane-parallel bispectral retrieval to estimate the optical depth and effective radius of the cloud. Since these quantities are specified by the assumptions described in Chapter 2 (Section 2.1.1), the differences between retrievals with two-dimensional and

independent pixel radiances may be attributed to the effects of the cloud inhomogeneities. Besides the cloud inhomogeneities, the sensitivities of the reflected radiances and the retrievals to small changes in the form of the phase function are also demonstrated in this section. These sensitivities imply the importance of using the proper form of the scattering phase function during the retrieval process. Since the clouds modeled in this section have constant microphysics, the sensitivities shown here to cloud inhomogeneities and phase function form highlight the uncertainties of the retrieval process under the best conditions.

3.1.1 Radiances

The sensitivities in the radiance fields are investigated using a number of simulations for the three clouds described in Section 2.1.1 (see Fig. 2.2 a,b,c). Two-dimensional radiance calculations are compared with independent pixel calculations to assess the effect of the two-dimensional radiative transfer. The calculations are performed for three different solar zenith angles; 10°, 50° and 75°. The cloud fields are scaled such that the domain average column optical depths are 0.5, 2.0 and 8.0. These optical depth permit the analysis of 2D and IPA radiance calculations for thin, medium, and thick cloudiness. The sensitivities of the reflected radiances are discussed first according to the effects of cloud structure and then to the effects of varying the shape of the phase function.

Sensitivities of Radiances to Cloud Structure

Examples of the types of sensitivities that reflected radiances exhibit are illustrated in Figures 3.1 and 3.2. These figures contrast the behavior of the IPA and 2D reflected and transmitted radiances for cloud 2 and cloud 3 at a wavelength of 0.83 μm, at a nadir viewing angle (i.e., $\theta = 0.0°$ and $\phi = 0.0°$) and the phase function DHG2 (see Table 2.1). The normalized column integrated optical depth for each cloud is shown for comparison in the bottom panel of each figure. The figures show the sensitivity of the radiances to changes in the solar zenith angle as the domain averaged optical depth of the cloud changes. Both figures show the dramatic increase in the reflected radiance with increasing optical depth. Note also that the difference between the radiances at solar zenith angles 10° and 75° increase from about a factor of two for the thinnest cloud to about a factor of 5 for the thickest cloud. These differences highlight the strong dependence of the radiance field to the solar zenith angle.

Figures 3.1 and 3.2 also show differences between the 2D and IPA radiances for clouds 2 and 3. In both figures, the agreement between the 2D and IPA radiances becomes worse as the domain optical depth increases. For the stratified and unbroken cloud 2 in Fig. 3.1, the agreement is very good. Note that 2D peak radiances are less than those for IPA and that 2D minimum radiances are greater than those for IPA. Thus, the 2D radiances are smoothed relative to the IPA. This smoothing is evidence of the effect that horizontal cloud inhomogeneities have upon the radiance field where the horizontal interaction of

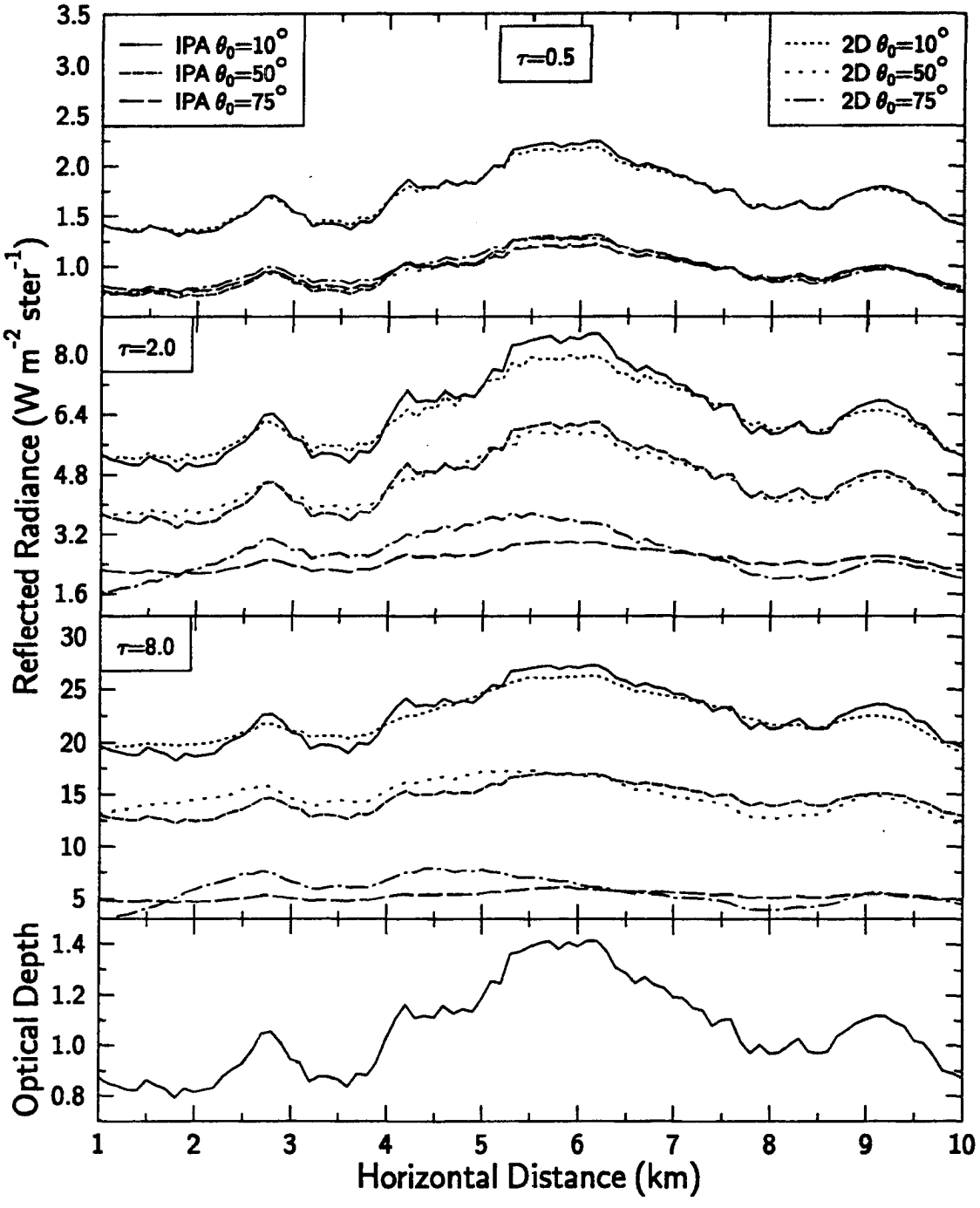

Figure 3.1: 2D and IPA reflected radiances at $0.83\mu m$ for cloud 2 and a nadir viewing angle. The solar zenith angles and domain averaged optical depths are indicated in the legend. The bottom panel gives the normalized column optical depth for the cloud.

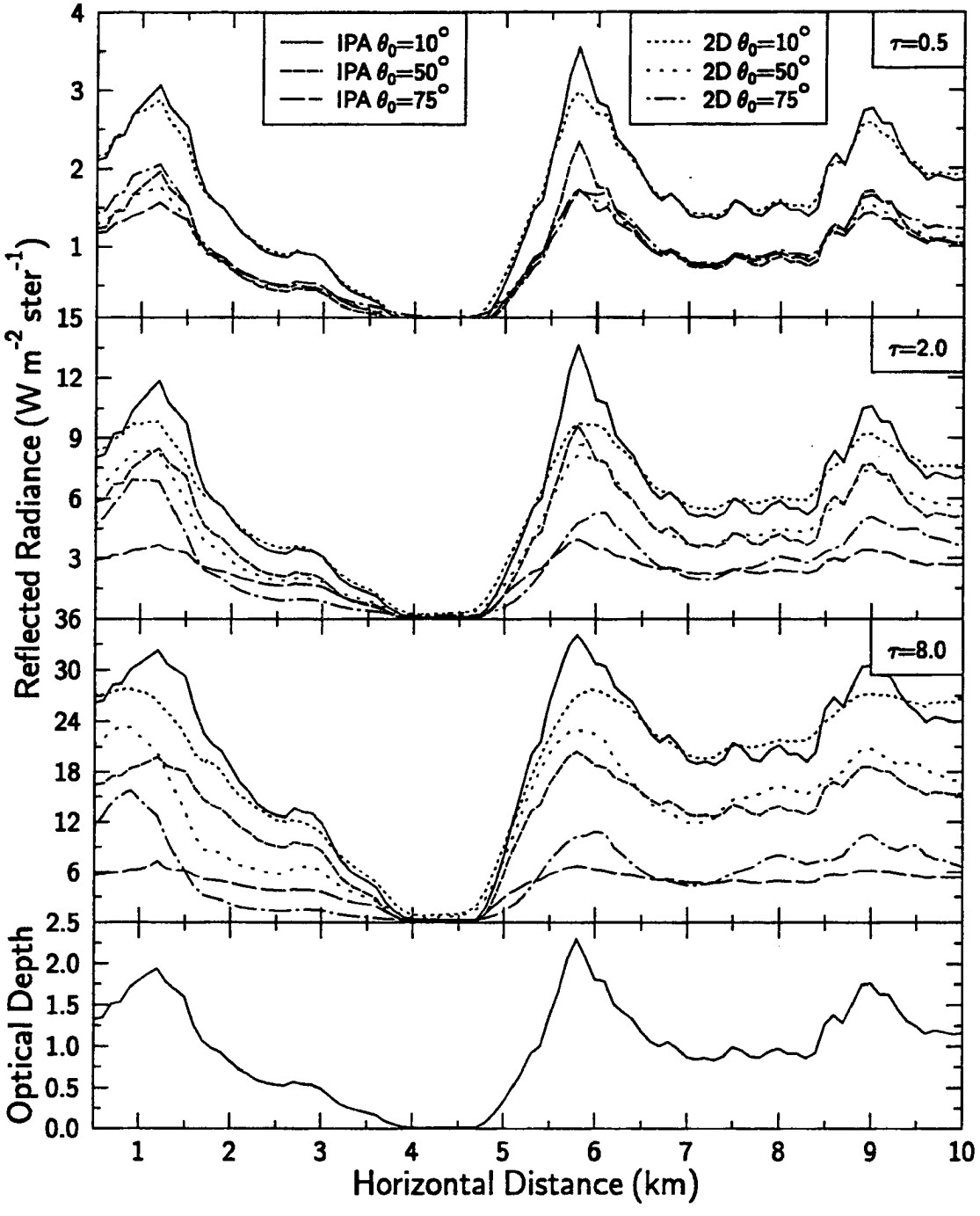

Figure 3.2: 2D and IPA reflected radiances at $0.83\mu m$ for cloud 3 and a nadir viewing angle. The solar zenith angles and domain averaged optical depths are indicated in the legend. The bottom panel gives the normalized column optical depth for the cloud.

radiation within the clouds begins to lessen the dependence of the radiance field on the column integrated optical depth. Figure 3.2 shows this behavior very clearly, especially for the high sun (small solar zenith angle) case.

At the large solar zenith angles a different behavior is observed. The IPA radiances at this viewing angle become more flat. This is caused by a reduction of the sensitivity of reflected radiances for increasing optical paths. The optical paths in cloud columns increase as the optical depth or the solar zenith angle increase. In these cases, the 2D radiances have higher maximums than the IPA. However, Figure 3.1 shows that these 2D radiance maximums at the largest solar zenith angle occur to the left of the optical depth maximums (see bottom panel). This "out of phase" appearance tends to increase as the domain average optical depth increases and is due to the horizontal inhomogeneities of the cloud. To understand this remember that the collimated beam in SHSG flows from the left to the right at the specified solar zenith angle. For the large solar zenith angle case, the radiances reflected in the nadir direction are enhanced to the sun side (left side) of the column optical depth maximum and reduced to the dark side (right side). This effect is analogous to the commonly observed phenomenon of "cloud shadowing". In the case of cloud 2, a concentrated area of extinction embedded within the cloud reflects energy to the sun side that eventually is scattered vertically out of the cloud.

The cloud shadowing effect is illustrated much more clearly once the viewing angle is changed from the nadir direction. Figures 3.3 and 3.4 show 2D and IPA reflected radiances at the domain averaged optical depth of 2.0 and at solar zenith angles of 10° and 75°. The top three panels give the radiances for $\theta = 30.0°, \phi = 0.0°; \theta = 0.0°, \phi = 0.0°$; and $\theta = 30.0°, \phi = 180.0°$ respectively. All three of these viewing angles are in the plane of the sun, the first in the forward scattering direction and the second in the backward scattering direction. The bottom panel gives the normalized column optical depth for comparison. Evident in both figures is the shift in the 2D maximum radiances from the right of the maximum column optical depth to the left as the viewing angle changes from the forward to the backward scattering direction. The difference in distance of these peaks is approximately 1.5 *km*. For cloud 3 (Fig. 3.4), there are 2D reflected radiances that occur at horizontal locations where there is virtually no cloud. This cloud shadowing is solely due to the interaction of radiation with the horizontal cloud inhomogeneity.

The comparisons of 2D and IPA reflected radiances reveal the effects of the horizontal transport of radiation within the cloud field. At the nadir viewing angle and at the small solar zenith angle the 2D radiances appear smoothed relative to the IPA radiances. As the domain averaged optical depth and solar zenith angle increase the effects of cloud structure through cloud shadowing are observed. The magnitude of these effects is dependent upon the viewing geometry but become larger in the cases examined here as the cloud optical depth and the solar zenith angle increase. In these cases, the optical path through the medium becomes longer and the horizontal interaction of radiation becomes more important in the determination of the reflected radiance.

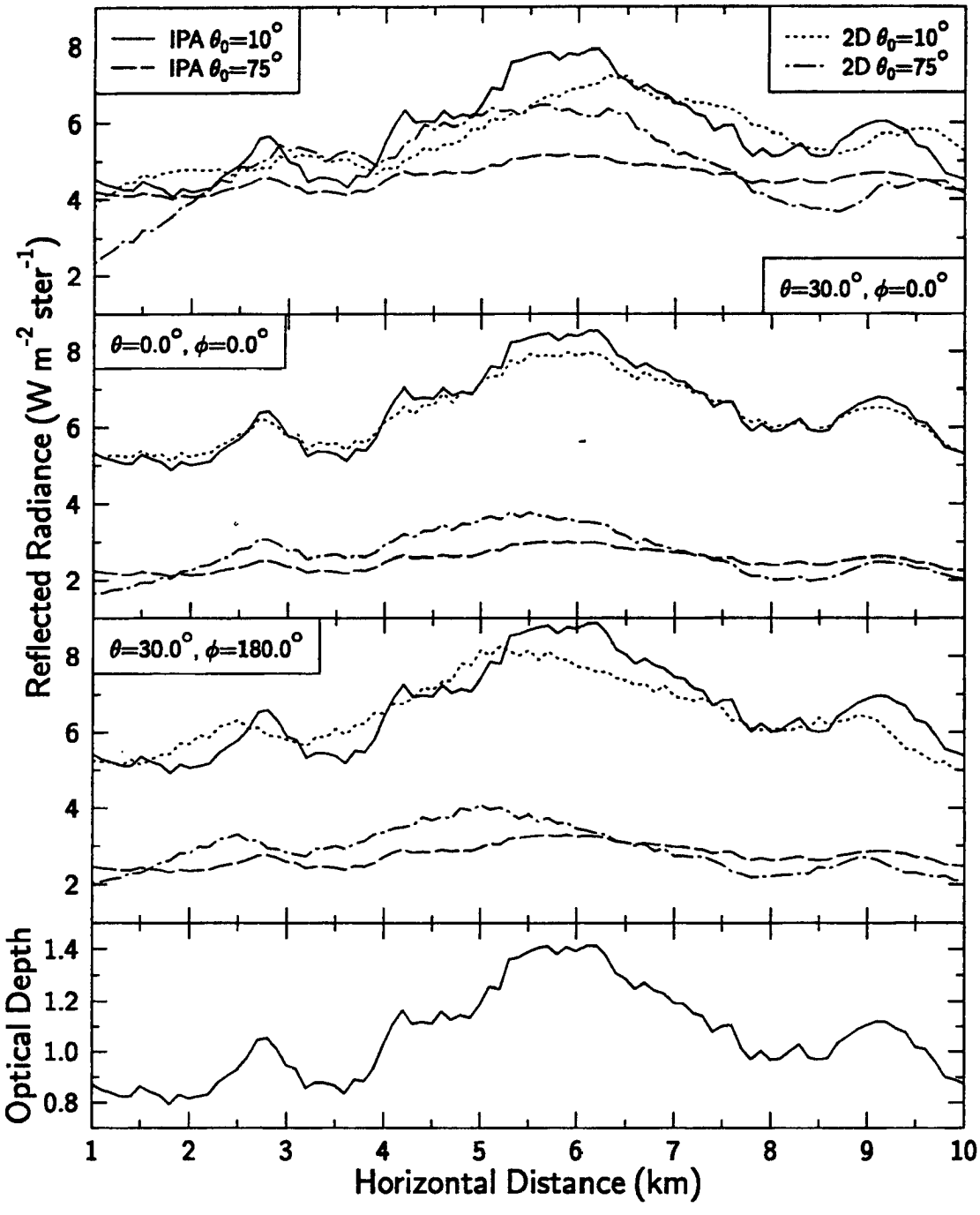

Figure 3.3: 2D and IPA reflected radiances at $0.83\mu m$ for cloud 2 and a domain averaged optical depth of 2. The solar zenith angles and the viewing angles are indicated in the legend. The bottom panel gives the normalized column optical depth for the cloud.

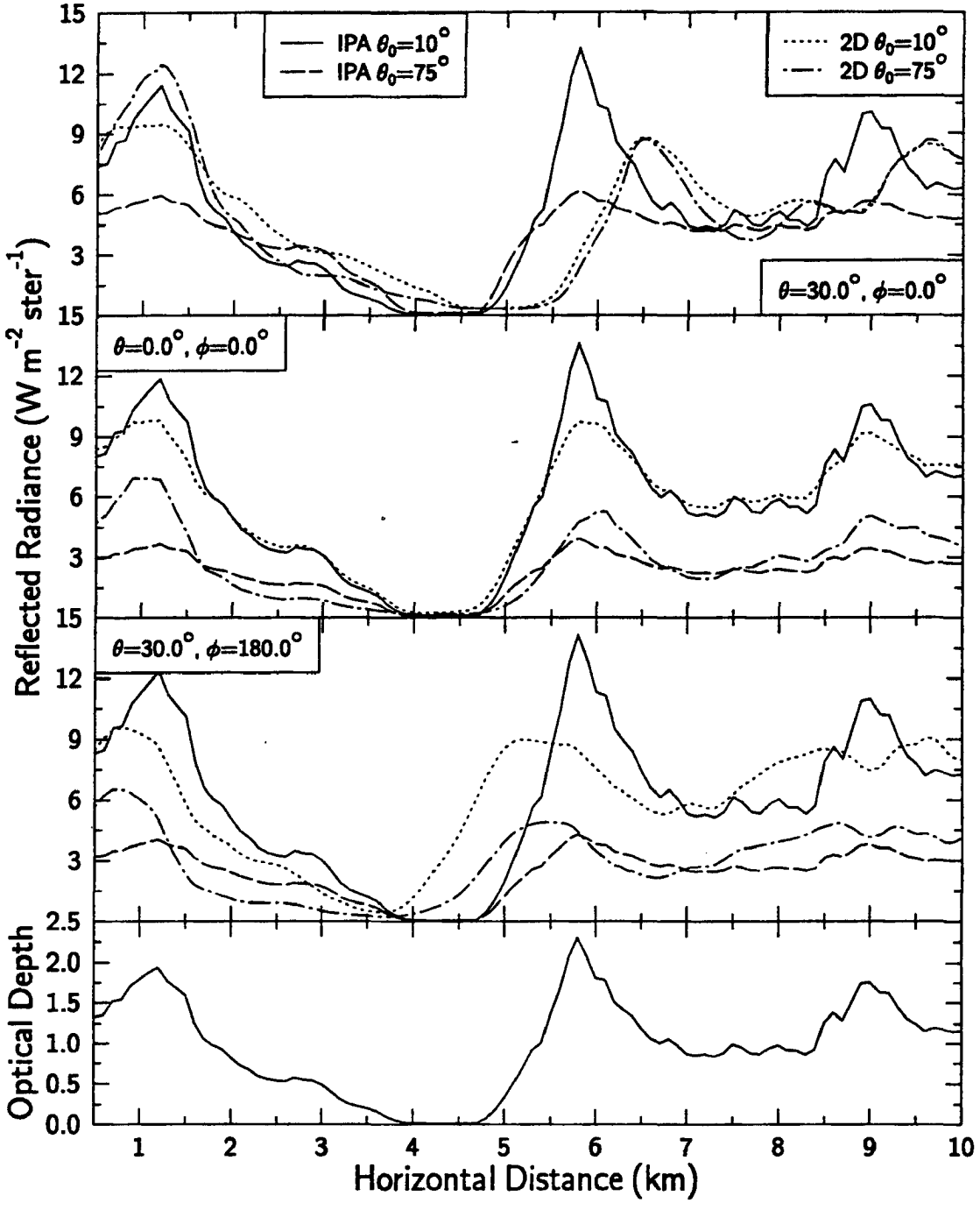

Figure 3.4: 2D and IPA reflected radiances at $0.83\mu m$ for cloud 3 and a domain averaged optical depth of 2. The solar zenith angles and the viewing angles are indicated in the legend. The bottom panel gives the normalized column optical depth for the cloud.

Sensitivities of Radiances to the Phase Function

Besides the effects of cloud structure, the sensitivities to changes in the shape of the phase function also can affect the radiance field in a significant fashion. Figures 3.5 and 3.6 present the 2D reflected radiances for the solar zenith angles of 10° and 50° respectively at $\lambda = 0.83\ \mu m$, a nadir viewing angle, and three domain averaged optical depths. Each panel in Figs. 3.5 and 3.6 gives the reflected radiances for the phase functions illustrated in Figure 2.4. Both figures show that biases in the radiances result from using the different forms of the phase function even though each phase function has the same effective asymmetry parameter. The biases in the reflected radiances for the solar zenith angle at 10° are much larger than those at 50°. The reason for this is understood by considering the differences in phase functions corresponding to these particular scattering geometries. Since both Figures 3.5 and 3.6 show radiances at the nadir viewing angle, the scattering angles at the solar zenith angles of 10° and 50° are 170° and 130° respectively. Figure 2.4 shows that the DHG3 phase function is more than a factor of ten larger than the DHG1 phase function at 170°. Thus, an increase in the magnitude of the phase function at one scattering angle (in this case $\Theta = 170°$) leads to an increase in the reflected radiance from the cloud. At the 130° scattering angle, DHG3 is only about 15% larger than DHG1 and as a result the biases in the reflected radiances are smaller as well.

Both the figures show that sensitivity of the radiances to the form of the phase function decreases as the domain averaged optical depth of the cloud increases. For instance, in Figure 3.5 the radiances using DHG3 are on average are roughly a factor of 6 greater than those using DHG1 at $\overline{\tau} = 0.5$ (top panel). However, the radiances at $\overline{\tau} = 8.0$ are only about a factor of 1/4 greater. Thus, in this case the radiances are about 24 times more sensitive to the phase function in the thin cloud than in the thick. At $\theta_o = 50°$, in Figure 3.6, relative differences between these two phase functions in the thin cloud is about 2 to 3 times larger than in the thick cloud. Clearly, these results imply that radiances are very sensitive to the shape of the phase function but that this sensitivity depends greatly on the scattering geometry and the relative differences decrease as the clouds become thicker. Since the form of the phase function (and for that matter the asymmetry parameter) for ice clouds is relatively unknown, these sensitivities have significant ramifications in the estimation of cloud properties, especially since the majority of cirrus clouds are optically thin.

3.1.2 Retrievals

In order to quantify the effects of the sensitivities of radiances to cloud structure and phase function shape, bispectral retrievals of optical depth and effective radius are simulated analogous to the retrievals presented by Wielicki et al. (1990). The object of this section is to evaluate the errors that result when the 2D radiances discussed above

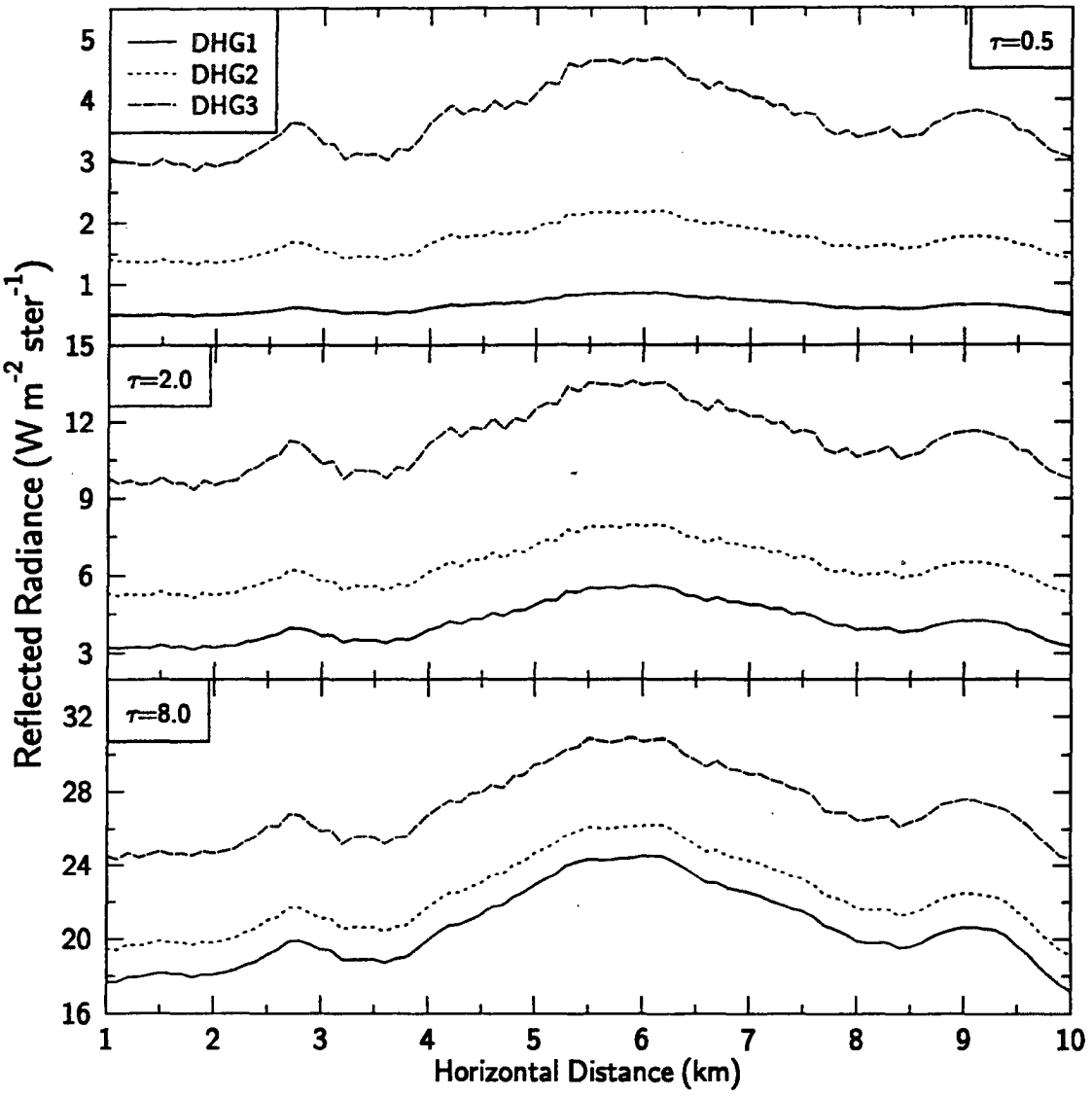

Figure 3.5: 2D reflected radiances at $0.83\mu m$ for cloud 2 and a solar zenith angle of 10°. The domain averaged optical depths and phase function forms are indicated.

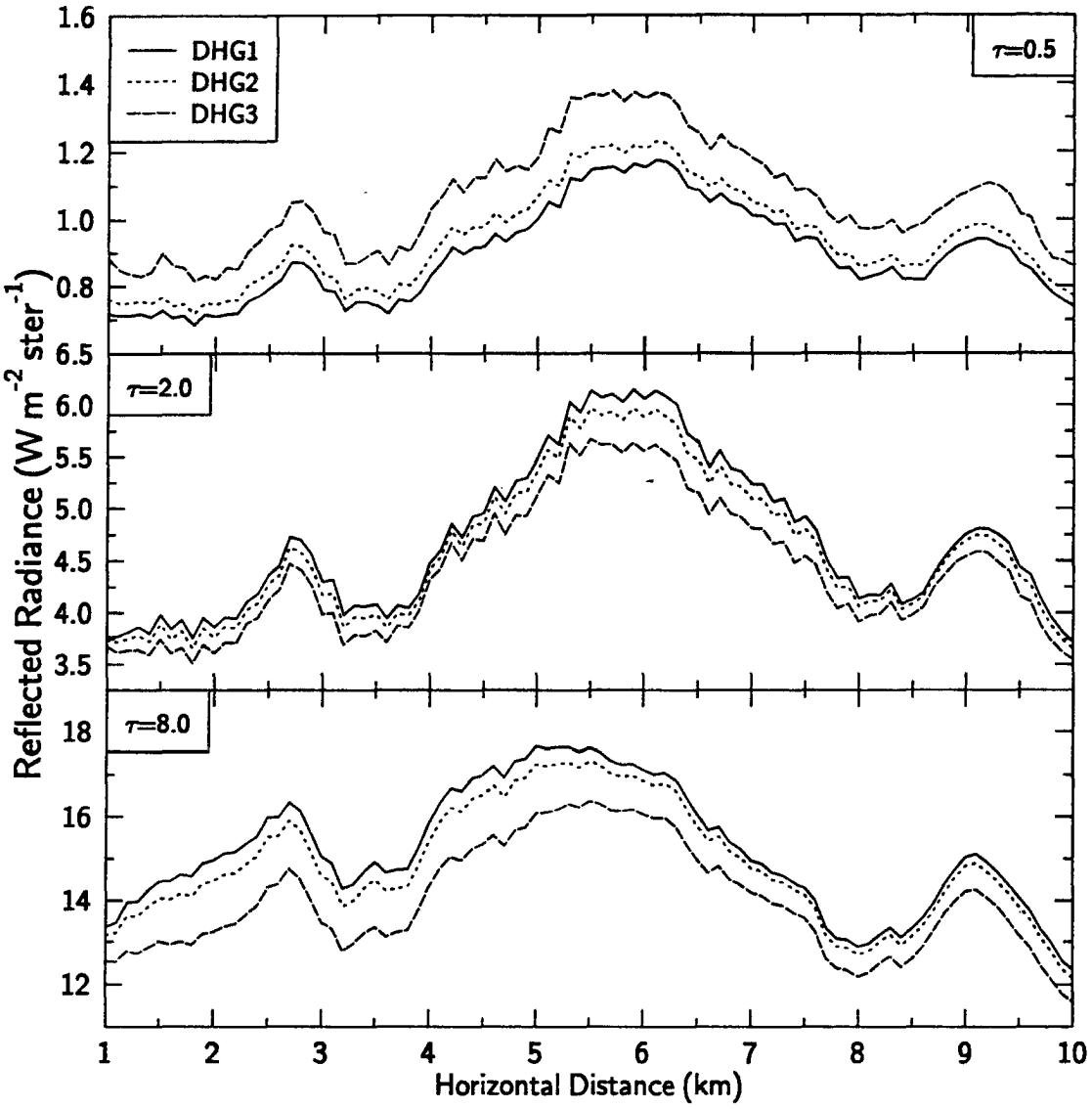

Figure 3.6: 2D reflected radiances at $0.83\mu m$ for cloud 2 and a solar zenith angle of 50°. The domain averaged optical depths and phase function forms are indicated.

are interpreted with plane-parallel independent pixel theory. Bispectral retrieval methods using independent pixel theory are the conventional method of retrieving cloud properties from observing platforms such as aircraft and satellite. Cloud properties retrieved using a bispectral method with 2D radiances are then compared to the specified cloud properties to ascertain the effects of cloud structure and the phase function upon the retrieval process.

One such bispectral method of satellite retrieval involves the use of radiance information at both an absorbing and nonabsorbing wavelength (see,Wielicki et al., 1990). At the nonabsorbing wavelengths, reflected radiances are strongly dependent upon the optical depth of the cloud. At the absorbing wavelengths, the reflected radiance is assumed to be not only dependent upon optical depth, but also upon the size of the particles inside the cloud itself. Plane-parallel radiance simulations at both wavelengths are used to construct a grid from which both the optical depth and the particle effective radius of a cloud is retrieved. The channels used for this study are the Landsat channels of 0.83 μm and 1.65 μm (see,Wielicki et al., 1990). Radiance values are converted to reflectance according to

$$R_\lambda(\theta,\phi) = \frac{\pi L_\lambda(\theta,\phi)}{\mu_o F_{o_\lambda}} \tag{3.1}$$

where $L_\lambda(\theta,\phi)$ is the observed radiance at the given wavelength λ, the viewing angle θ, and the azimuth angle ϕ. The 2D and IPA SHSG simulations are used to simulate the observed radiances denoted L. The constants μ_o and F_{o_λ} are the solar zenith angle and solar flux at the given wavelength respectively. Examples of the bispectral retrieval grids in terms of reflectance are given in Figure 3.7 for the solar zenith angles of 10° and 50° and a viewing and azimuth angle of 0°. The grid is composed of lines of constant effective radius and optical depth that are computed using the independent pixel approximation form of SHSG for vertically uniform clouds at a given scattering geometry (.i.e., θ_o, ϕ_o, θ, and ϕ). The grids are used as input to a routine which interpolates the 2D and IPA reflectances from the simulated cloud fields at both wavelengths to derive an optical depth and effective radius.

To demonstrate the bispectral relationships between cloud top reflectances at 0.83 μm and 1.65 μm, the radiances from Figs. 3.5 and 3.6 are converted to reflectances and plotted in Figure 3.8. The top two panels present the IPA bispectral reflectances for each of the three forms of the phase function at solar zenith angles 10° and 50° on the left and right respectively. The bottom two panels give the 2D bispectral reflectances of the same quantities. All four panels contain the cloud top reflectances at a nadir viewing angle from cloud 2 which has a specified value of $r_e = 80\,\mu m$. Also, the lines of constant effective radius, which are derived from the retrieval grid with phase function DHG1, are shown for clarity in all four panels. The top panels show that the IPA reflectances using the phase function DHG1 lie exactly on the 80 μm line of constant effective radius. Since $r_e = 80$ μm for this cloud, this result verifies the accuracy of the method using the

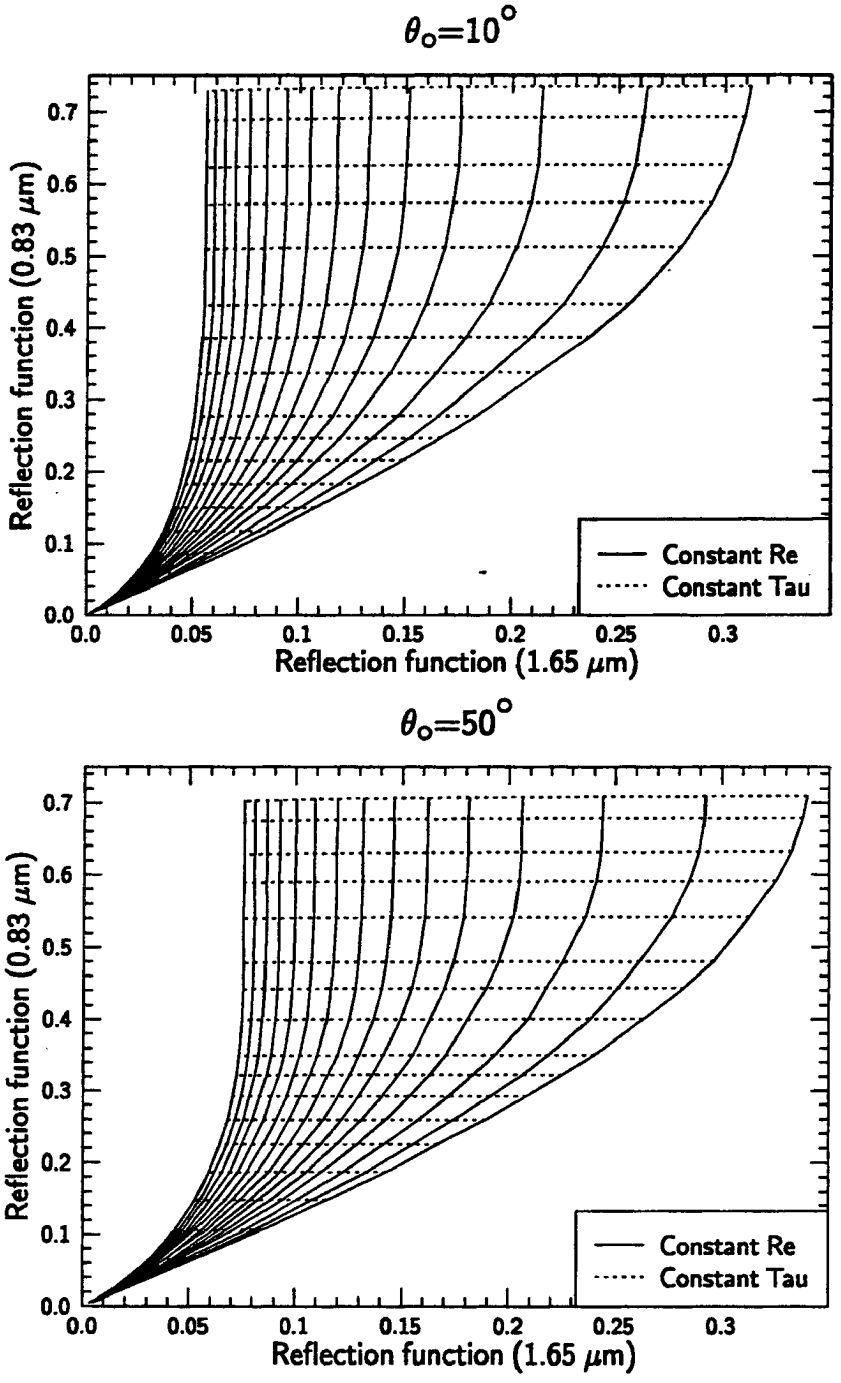

Figure 3.7: Sample retrieval grids generated from plane- parallel independent pixel calculations of uniform clouds at the solar zenith angles indicated and a viewing and azimuth angle of 0°.

plane-parallel assumption with the same phase function as the retrieval grid. However, immediately apparent from the IPA cloud top reflectances is the effect of using the other forms of the phase function. Note that bispectral radiances from the other phase functions lie along curves of effective radius much less than the actual size of the cloud particles. As discussed above, the magnitude of the DHG3 phase function exceeds that of DHG1 at the scattering angle for a nadir viewing angle and $\theta_o = 10°$. This enhanced scattering increases the DHG3 cloud reflectances relative to those computed using DHG1. These DHG3 cloud reflectances correspond to reflectances for a cloud about 20 μm using the DHG1 retrieval grid and retrievals using this grid would result in an underestimation of the actual particle size by a factor of 4. Also, as mentioned above, there is much less difference between the IPA reflectances at $\theta_o = 50°$ and this nadir viewing angle since the differences between the phase functions DHG1 and DHG3 are much less at this scattering angle. The IPA results from Figure 3.8 illustrate the importance of knowing the proper phase function in the retrieval process.

The 2D bispectral reflectances, which are more representative of observed radiances from Fig. 3.8 show the effects of the cloud geometry upon the bispectral relationships. The scatter about the lines of constant effective radius noticeably increases compared with the IPA reflectances. Also, the scatter of the 2D reflectances increases as the solar zenith angle increases from 10° to 50°. The most significant scatter is found for the cloud with the largest domain optical depth, shown by the cluster of points with the largest reflectances. Note that the minimum reflectances in this cluster do not follow the shape of the constant effective radius curves from plane-parallel theory, especially for $\theta_o = 50°$. These minimum reflectances are found at places in the cloud where cloud shadowing is present and do not necessarily correspond to locations of minimum column optical depth. This lack of correspondence between the minimum column optical depths and minimum reflectances illustrates the break down of the independent pixel technique and is a result of the increased horizontal radiative interaction that occurs as the sun lowers relative to the cloud. At $\theta_o = 50°$, the minimum reflectances of the upward cluster of points overestimate the actual effective radius by as much as 87.5%. Thus, both the horizontal interaction within a cloud field and the phase function uncertainty can result in large errors using the plane-parallel independent pixel retrieval technique. The characteristics of these errors for the clouds with constant microphysics are described more quantitatively in terms of the retrievals for both cloud optical depth and effective radius in the following subsections.

Optical Depth Retrievals

Figures 3.9 and 3.10 give examples of the retrieval of optical depth for cloud 2 from both the IPA and 2D reflectance for a nadir viewing angle and at solar zenith angles of 10° and 50° respectively. The retrieval grid is based upon the phase function DHG1 and the radiances were computed using this phase function as well. In each of the panels the

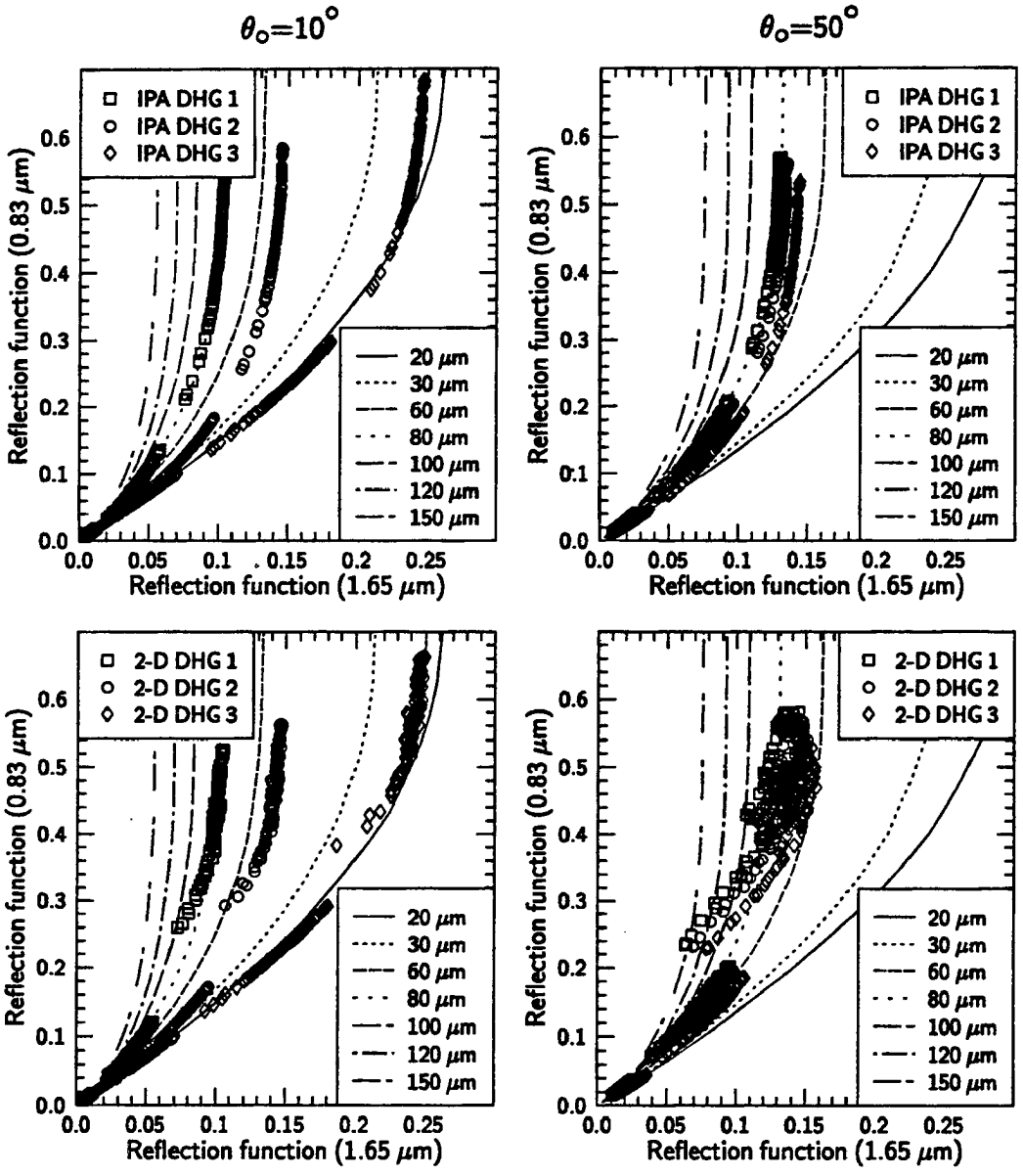

Figure 3.8: Bispectral plots of nadir reflectances for cloud 2 with the indicated solar zenith angles for each column and lines of constant effective radius as shown. Reflectances from all three forms of the phase function are plotted as well as reflectances from the three domain averaged optical depths as noted in the text.

thick solid line denotes the optical depth as integrated over each column of the cloud. All optical depths are for the wavelength 0.83 μm. The figures show that the IPA retrievals at both solar zenith angles agree closely with the actual integrated column optical depth. This indicates that the retrieval procedure is performing well for this idealized cloud.

However, the retrievals with the 2D radiances show local differences dependent upon the cloud structure and scattering geometry. These differences should not be interpreted as error due to the 2D reflectances, but as differences caused by using plane-parallel theory to analyze multi-dimensional radiances. For $\theta_o = 10°$, as depicted in Fig. 3.9, the 2D retrieval curves appear smoothed with comparison to the column by column optical depth. Areas of optical depth relative maximums are underestimated and areas of relative minimums are overestimated by the retrieval. These areas of local differences between the actual column optical depths and the 2D retrievals rarely exceed 10% for cloud 2 at this scattering geometry. Since the retrieval process underestimates relative maximums and overestimates relative minimums the domain average retrieved optical depths fall within 3% of the actual domain averaged optical depth.

A slightly different behavior occurs in Fig. 3.10 which depicts the retrievals at the nadir viewing angle for $\theta_o = 50°$. The retrievals for cloud 2 with domain averaged optical depths of 0.5 and 2.0 behave much like those at 10°, except that at $\overline{\tau} = 2.0$ the 2D retrievals seem to be slightly out of phase with the actual column optical depth curve. This is much more clearly seen at $\overline{\tau} = 8.0$. Here, higher 2D reflectances on the sun side of the optically thick part of the cloud are interpreted with plane-parallel theory to correspond to much larger optical depths than the actual columns contain. The magnitude of the relative difference approaches 25% in this region. This tendency toward the shifting of the reflectances relative to the actual column optical does not appreciably affect the domain average retrieved optical depth that is overestimated in the retrieval by 3.2%. This demonstrates that cloud structure, even when relatively stratified and homogeneous, can cause large local biases in the retrievals of optical depth. However, the magnitude of these biases are dependent upon the length scale of the cloud inhomogeneities, since the domain averages agree within a few percent.

Optical depth retrievals for the broken cloud 3 show much larger effects of the cloud inhomogeneities and these are shown in Figure 3.11. This figure depicts the results of the retrievals for a nadir viewing angle at a solar zenith angle of 50° using the DHG2 phase function and retrieval grid. At certain locations the 2D radiances are beyond the retrieval grid and a retrieval is not possible. However, where retrievals are obtained, the disagreements between the column integrated optical depth and 2D radiances interpreted using the plane-parallel grid are much like those for cloud 2, but more extreme, especially with increasing optical depths. At the largest optical depth considerable error is obtained at locations in the vicinity of column integrated optical depth maximums due to the cloud shadowing effect already discussed.

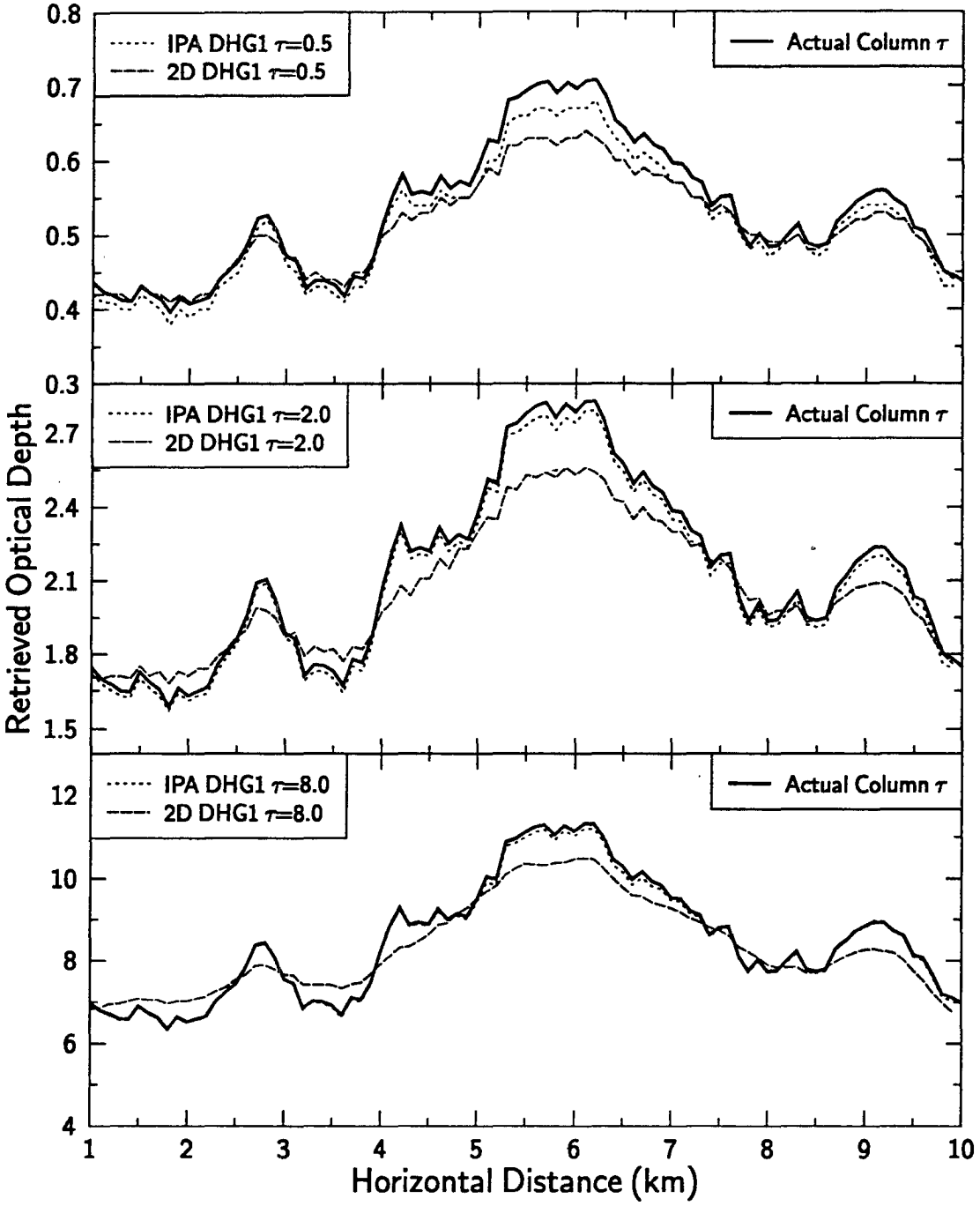

Figure 3.9: Retrieved optical depth as a function of horizontal distance from 2D and IPA reflectances using a retrieval grid with the DH1 used the phase function at a solar zenith angle of 10°. Each panel gives the retrievals for cloud 2 with a different domain optical depth as indicated. The actual column integrated optical depth of the cloud is given by the thick line.

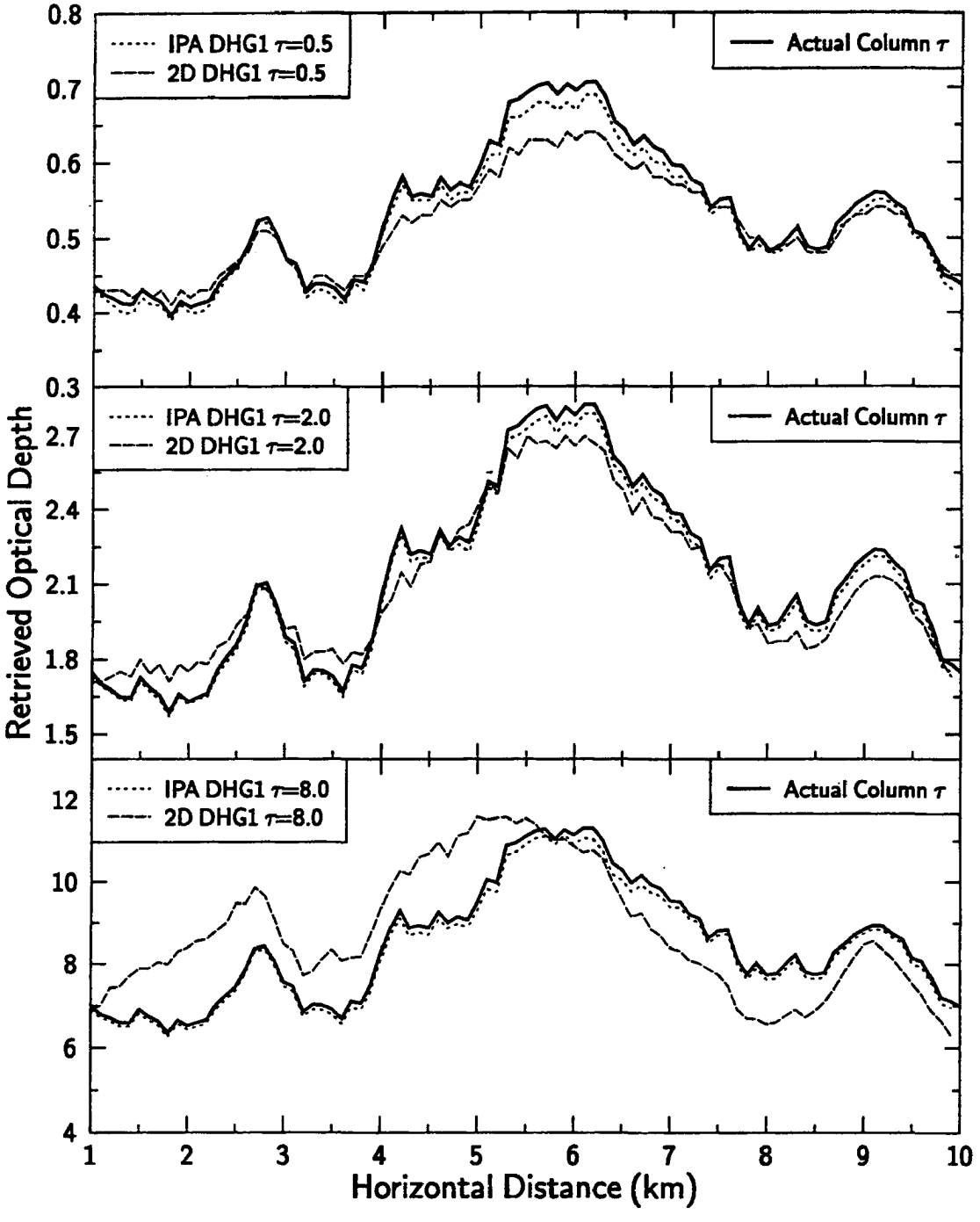

Figure 3.10: Retrieved optical depth as a function of horizontal distance from 2D and IPA reflectances using a retrieval grid with the DHG1 phase function at a solar zenith angle of 50°. Each panel gives the retrievals for cloud 2 with a different domain optical depth as indicated. The actual column integrated optical depth of the cloud is given by the thick line.

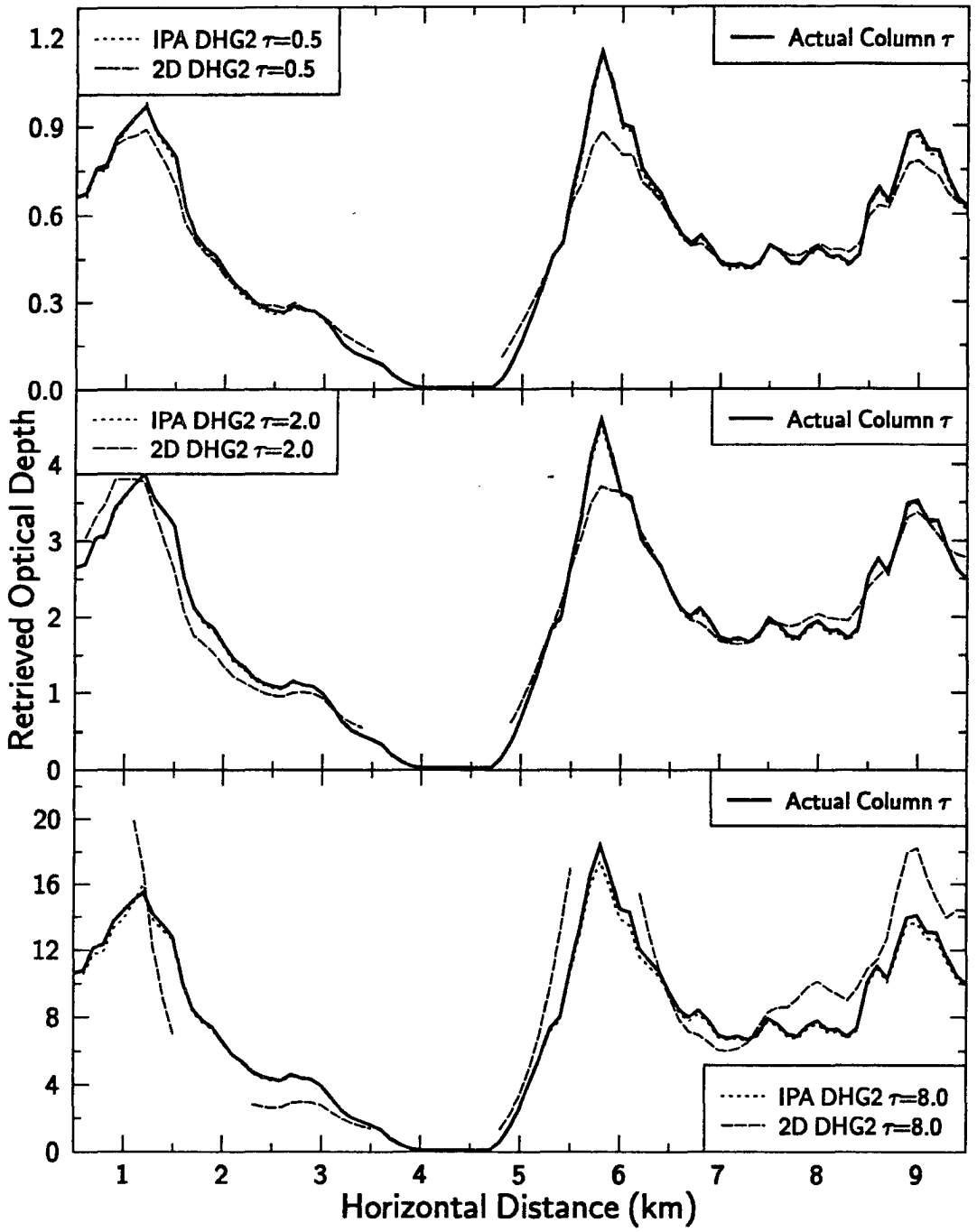

Figure 3.11: Retrieved optical depth as function of horizontal distance for IPA and 2D reflectances using a retrieval grid based upon phase function DHG1 at a solar zenith angle of 50°. Each panel gives the retrievals for cloud 3 with a different domain optical depth as indicated. The actual integrated column optical depth of the cloud is given by the thick line.

Figure 3.12 gives the RMS differences computed over all horizontal grid points between the retrieved optical depths using 2D reflected radiances and the actual column integrated optical depth as a function of the scattering angle. The scattering angle is defined as the angle between the sun and the viewing angle which is determined by θ and ϕ. The RMS differences are divided by the domain averaged optical depth for each case and expressed in terms of percent. Thus, the quantity represents a measure of the normalized absolute difference between the actual column averaged optical depth and plane-parallel retrievals of 2D reflectances. The curves with the solid shapes denote points generated using the DHG1 phase function in both the retrieval grid and 2D reflectance calculations. The curves with the open shapes represent relative RMS optical depth differences that result from using the DHG1 phase function in the retrieval grid calculations and the DHG2 phase function in the 2D calculations. The three different solar zenith angles are differentiated by shape and are denoted in the legend in the top panel of the figure.

Referring to the solid shapes for the thinnest cloud in Fig. 3.12 (top panel), the retrievals at each solar zenith angle are relatively similar with most RMS differences being less than 15% of the domain averaged optical depth. However, as the optical depth increases the RMS differences of the retrievals at 75° relative to the domain optical depth become much larger than those at the solar zenith angles of 10° and 50°. At these angles the RMS differences remain at a level that is less than 15% of their respective domain averaged optical depths. A general tendency exists for the lowest differences relative to the domain average optical depths to occur at the scattering angle which corresponds to a viewing angle at nadir (i.e., $\theta = 0°$ and $\phi = 0°$) which are 170°, 130° and 105° for solar zenith angles of 10°, 50° and 75° respectively. Thus, from these simulations it can be concluded that optical depth retrievals using a bispectral approach are best for solar zenith angles less than about 50° and a viewing angle at or near nadir.

The open shapes depicted of Fig. 3.12 show how error in the shape of the phase function affect the retrievals. Note the RMS differences for the thinnest cloud and the open shapes are closest to the solid shapes at about the 120° scattering angle. At this angle the difference between the DHG1 and DHG2 phase functions is close to its minimum. As the difference between the phase functions increase, especially towards the backscattering angle, the retrievals deteriorate dramatically. In these instances, the error in the phase functions overwhelms that due to the inhomogeneity. The domain averages also become substantially different. For instance, for the thin cloud case at $\theta_o = 10°$, the domain averaged retrieved optical depth at the nadir viewing angle is 1.07. This is more than a factor of 2 greater than the actual domain average. However, as optical depth increases the sensitivity to the phase function decreases such that the overestimation of optical depth at $\overline{\tau} = 8$, at $\theta_o = 10°$ and nadir is 9.26, a relative error of 15.8%.

Figure 3.13 depicts the RMS optical depth difference as a percent of the domain averaged cloud optical depth for the broken cloud 3. In this figure, the points at the solar

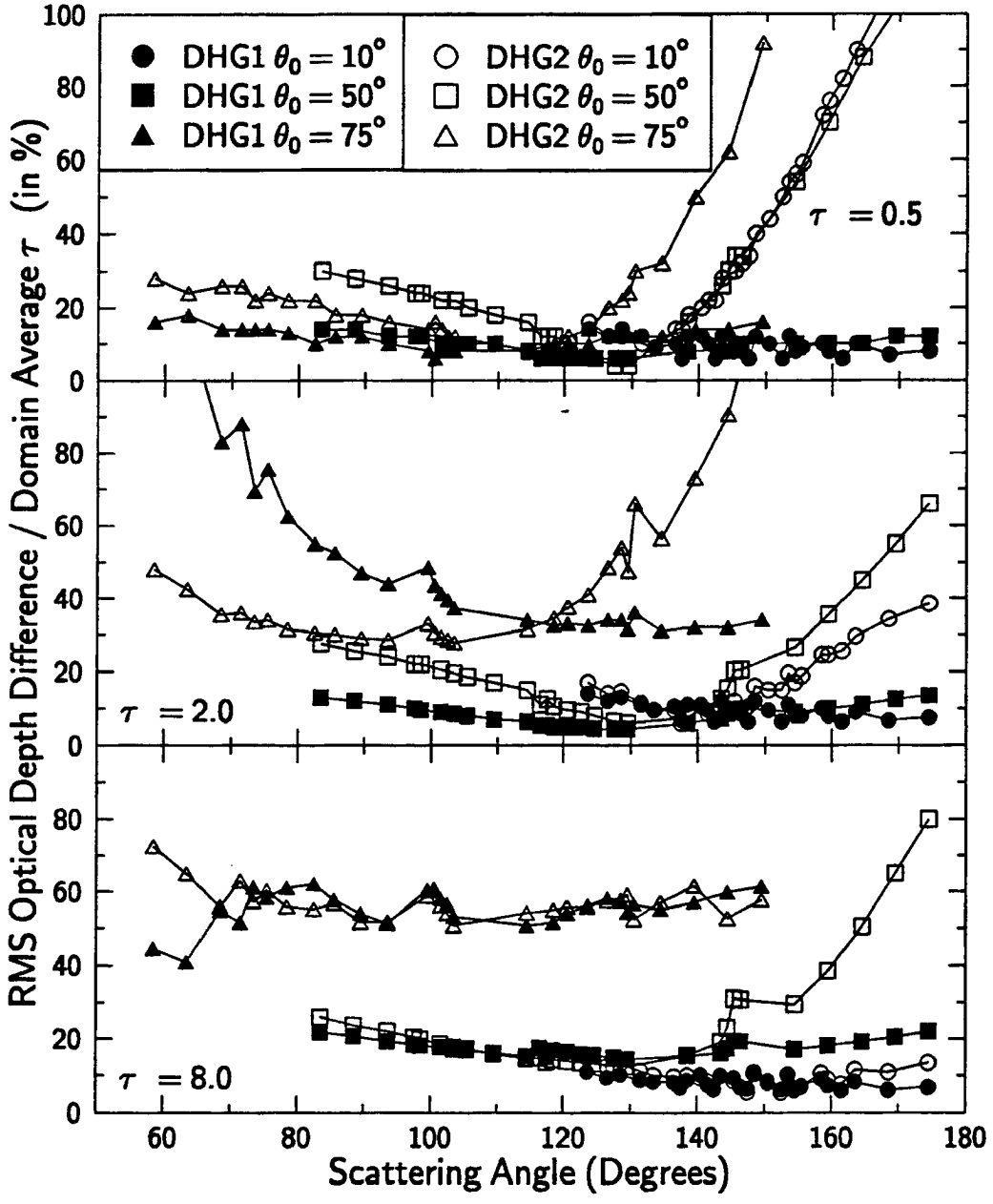

Figure 3.12: RMS differences between optical depth retrievals and the actual column optical depths as a function of the scattering angle for cloud 2. The differences are divided by the actual domain averaged optical depth and expressed in terms of a percentage. Solid shapes correspond to retrievals where DHG1 is used in both the 2D simulations and the retrieval grid. Open shapes refer to a retrieval grid with DHG1 and 2D calculations using DHG2.

zenith angle of 75° are not plotted due to the problem of the large number of 2D radiances that fell outside the retrieval grid. Inspection of this figure and comparison to the Figure 3.12 for cloud 2 reveals that RMS differences are higher by almost a factor of two. Many of the same features and solar zenith angles of 10° and 50°, observed for cloud 2 are also found for cloud 3. These include the tendency for the minimum RMS values at a particular solar zenith angle to occur at nadir. Furthermore, it is seen by comparing the open to the closed shapes that the differences due to phase function error are much less important at most scattering angles compared to the effects of the inhomogeneity. Unfortunately, the domain averaged retrieved optical depths for this cloud cannot be compared to the actual domain averaged optical depth since the retrievals at several grid points are unavailable. However, it is clear that the inhomogeneities associated with this broken cloud produce much larger localized errors than a stratified unbroken error.

Thus, these results indicate that cloud structure inhomogeneities cause localized error in the retrieval of optical depth that may be reduced in certain cases by averaging. However, error due to uncertainty in the phase function causes biases at scattering angles where the differences between the modeled and actual phase functions are the greatest. These biases are greatly emphasized for clouds with small domain averaged optical depths, but become less important in the case of the broken cloud.

Effective Radius Retrievals

Since the clouds simulated for this sensitivity study have a constant effective radius of 80 μm, the results of the retrieval process are compared to this value to determine the factors that affect the accuracy of the retrieval. Figure 3.14 presents the results for the retrieval of effective radius using the cloud top reflectances for cloud 2 and the retrieval grid based upon DHG1. Both the IPA and 2D reflected radiances from both the DHG1 and DHG2 phase functions are used in this retrieval at nadir with a solar zenith angle of 50°. A line is drawn corresponding to the value of 80 μm. As above, differences from this 80 μm line are caused by interpreting 2D fluxes with plane-parallel theory and thus are a measure of the error in the retrieval method. In the top panel corresponding to cloud 2 with $\overline{\tau} = 0.5$, the retrievals using the 2D reflectance compare favorably to the IPA retrievals. The bias shown in this panel by the curves marked DHG1 is most probably due to inaccuracies of the grid interpolation routine since the grid shrinks in size with decreasing optical depth.

Despite this problem, Figure 3.14 clearly shows that the sensitivity of retrieved effective radius to the phase function decreases with increasing optical depth. For the thin cloud in this case (top panel), the retrieval is extremely sensitive to the phase function. Using DHG1 to interpret 2D radiances with the phase function DHG2 results in an underestimation of the effective radius by almost 20 μm, an error of 25%. This difference represents a bias which remains in the domain average means. By contrast, the retrieval

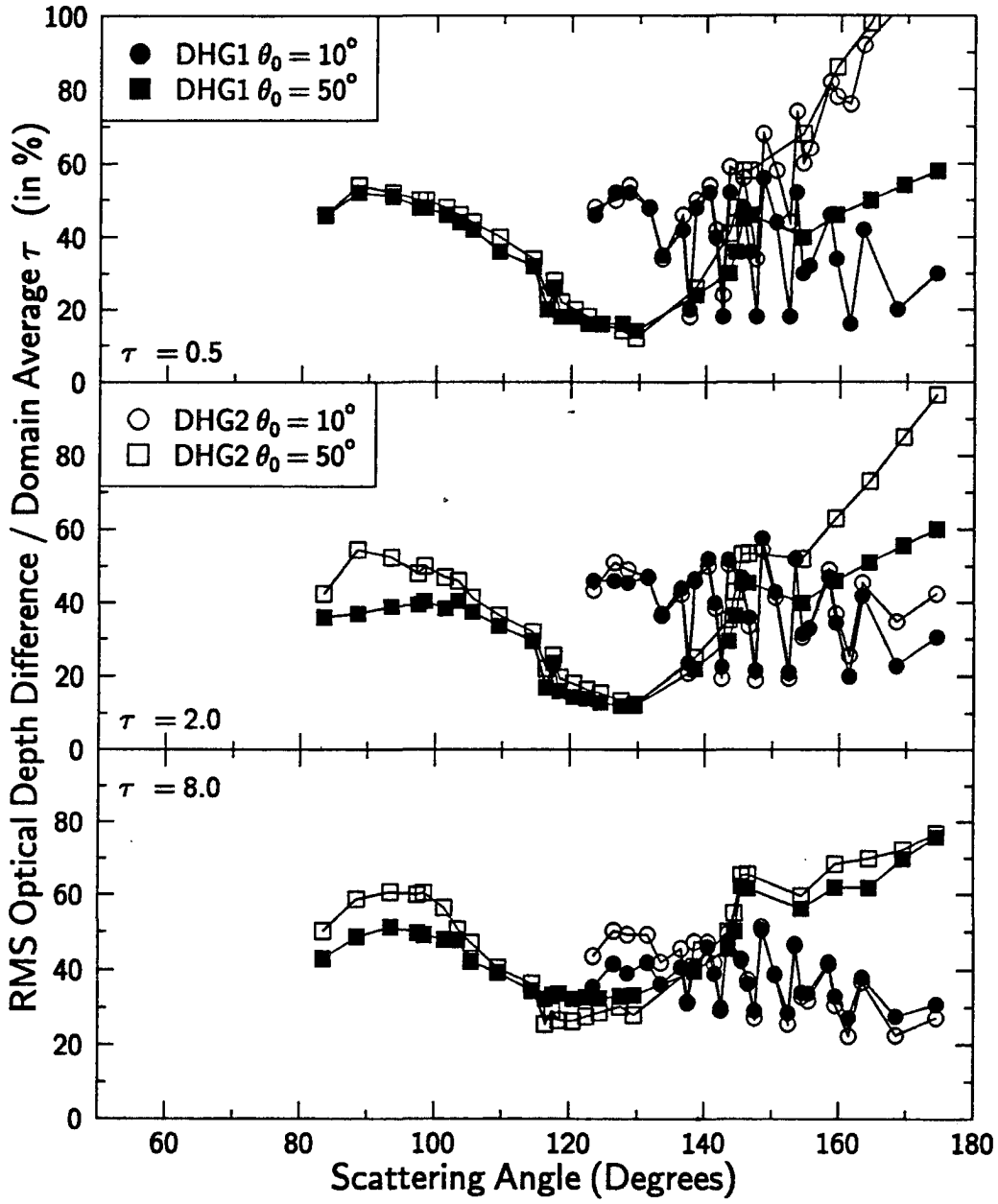

Figure 3.13: RMS differences between optical depth retrievals and actual column optical depths for cloud 3 as a function of the scattering angle. The differences are divided by the actual domain averaged optical depth and expressed in terms of a percentage. Solid shapes correspond to retrievals where DHG1 is used in both the 2D simulations and the retrieval grid. Open shapes refer to a retrieval grid with DHG1 and 2D calculations using DHG2.

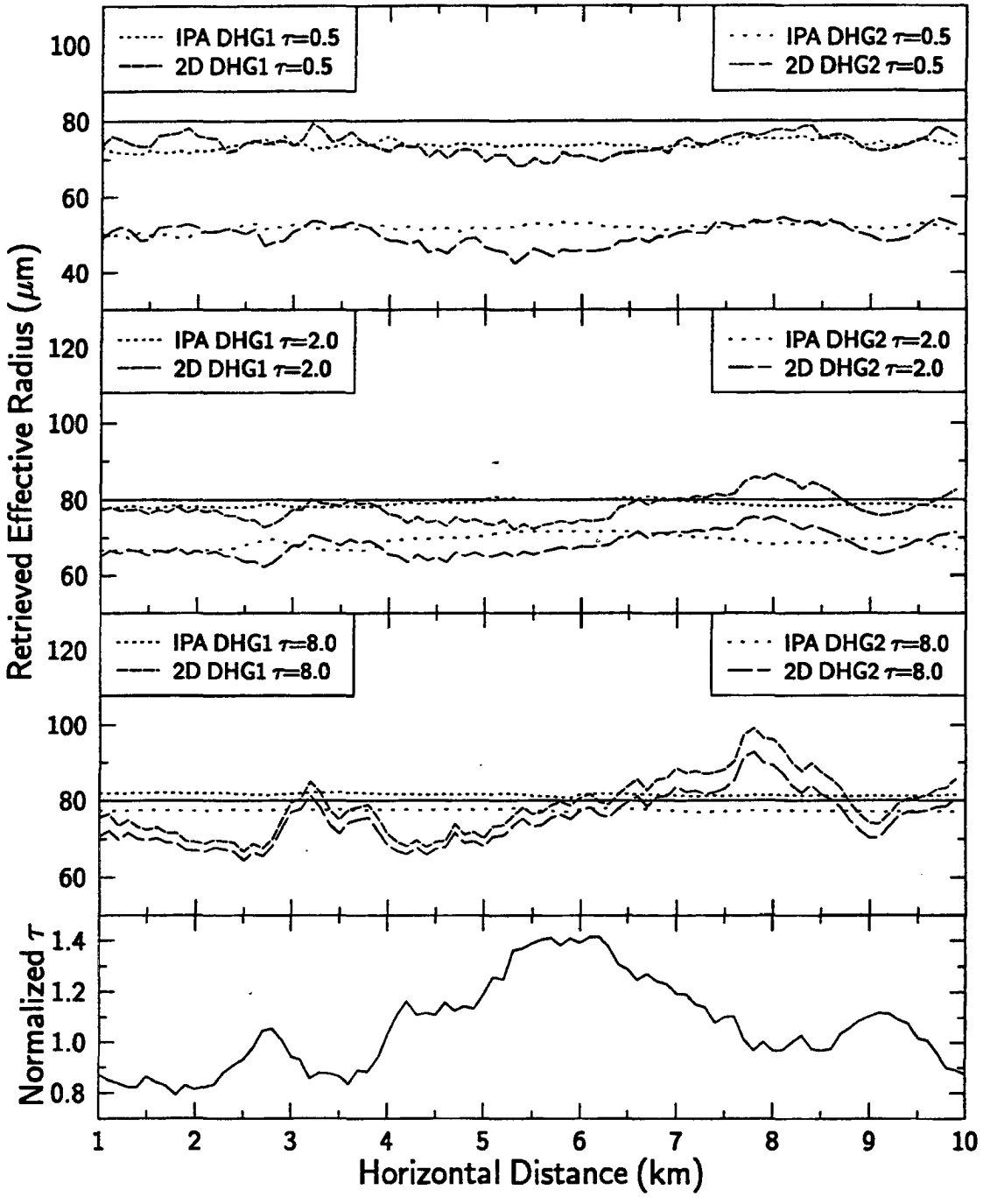

Figure 3.14: Retrieved effective radius as a function of horizontal distance from 2D reflectances and a retrieval grid which used the phase function DHG1 at a solar zenith angle of 50°. The top three panels give the retrievals for cloud 2 with the domain optical depth as indicated and a solid line drawn to designate the 80 μm effective radius. The bottom panel contains the actual column integrated optical depth for comparison.

of optical depth was much less sensitive to the phase function at $\overline{\tau} = 8.0$ where the difference between the two curves is only 3-5 μm, corresponding to a bias error that is at most about 6%. Figure 3.14 also shows that the sensitivity of the retrieved effective radius to the cloud inhomogeneities increases with optical depth. This is seen most clearly at $\overline{\tau} = 8.0$ where the effective radius to the sun side of the optically thick region in cloud 2 is underestimated and the effective radius on the opposite side of the cloud is overestimated. This is a direct result of the cloud structure where at $\theta_o = 50°$ the radiances on the sun side of the optically thick part of the cloud are enhanced which appear to the plane-parallel retrieval theory as smaller particles. However, for this particular cloud the domain averaged retrieved effective radius are within about 2.5% of 80 μm. The lone exception seems to be some of the retrievals at the 75° solar zenith angle where 2D retrievals of effective radius overestimated the true effective radius by about 10% (not shown). Once again, with the exception of retrieving effective radius at low sun angles, the effects of inhomogeneities at least for cloud 2 appear to be dependent upon the scale of the inhomogeneities embedded within the cloud. Averages tend to cancel out the small scale effects of the inhomogeneities.

The variation of the retrieved effective radius in the horizontal for the broken cloud 3 is shown in Figure 3.15. Although retrievals are not possible at each grid point, the localized errors are much larger than observed for cloud 2. In this case, the bias between the retrievals from DHG1 and DHG2 2D reflectances is not as large as the error resulting from the structural inhomogeneity. Without the retrievals from each grid point the overall domain averaged effective radius cannot be evaluated exactly, but the overestimations of the effective radius appear to dominate especially for the largest optical depth of 8.0. So, for this cloud, averages over the small scale effects may not cancel entirely the effects of inhomogeneities as observed in the case of cloud 2. Thus, error in this retrieval method is dependent upon not only the scale of the inhomogeneity, but also the magnitude of such inhomogeneity.

Figure 3.16 presents a summary of the results of the effective radius retrievals in terms of the scattering angle. The RMS effective radius differences computed over all horizontal grid points at a particular scattering angle are divided by the constant 80 μm and expressed in terms of a percent. Once again, the solid shapes are used for retrievals where the phase function DHG1 is used for both the 2D and the retrieval grid simulations and the open shapes correspond to points where 2D reflectances with DHG2 are interpreted with a retrieval grid based on DHG1. Overall, the RMS differences for the cases using the same phase functions are of the same relative magnitude of the optical depth retrievals shown in Fig. 3.12. Figure 3.16 shows, as in the case of the optical depth retrievals, that the sensitivity of the retrievals to solar zenith angles increase dramatically for angles greater than about 50°. This is especially true for domain averaged optical depths of 2 or greater. The figure also shows a general tendency for the effective radius retrievals to

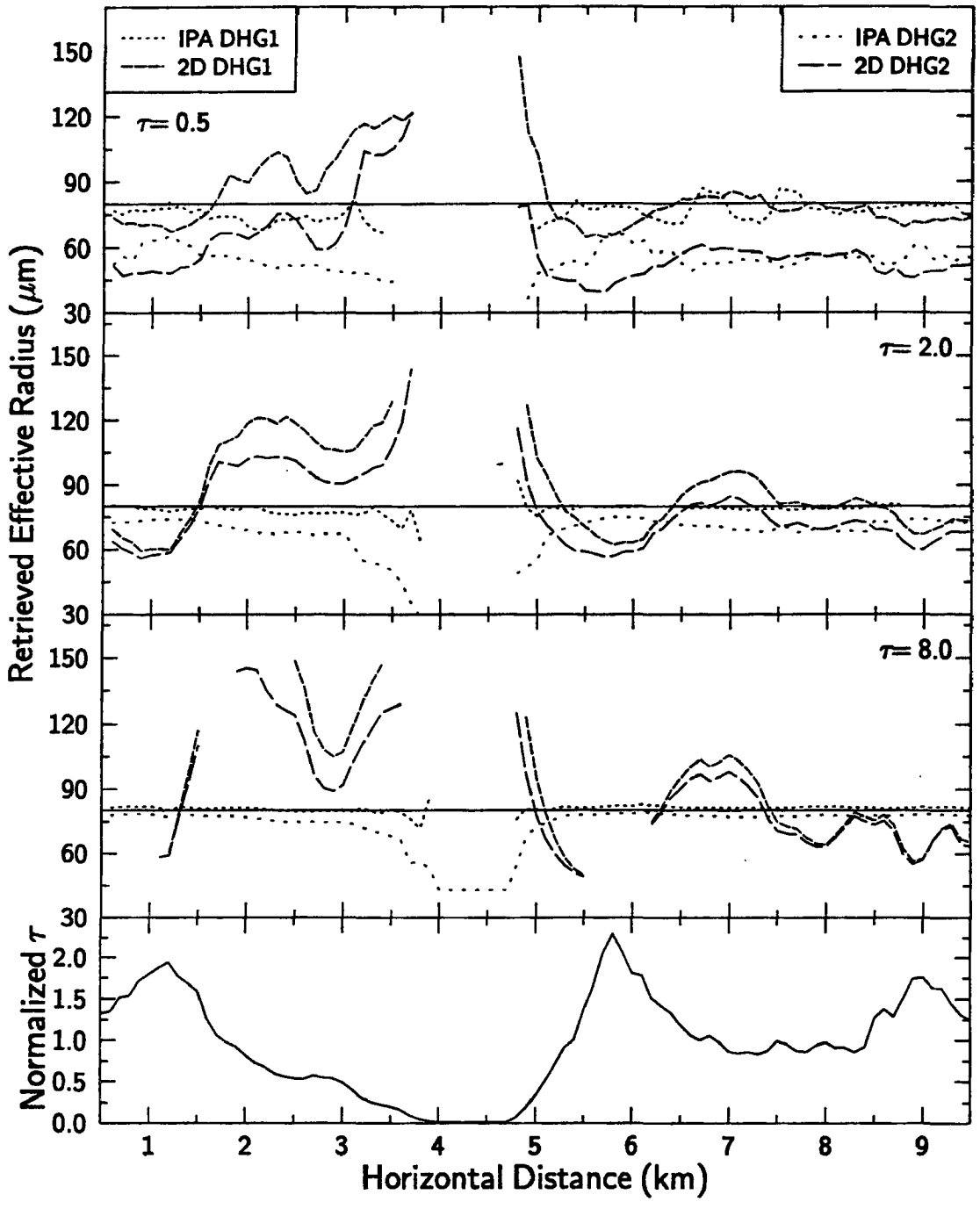

Figure 3.15: Retrieved effective radius as a function of horizontal distance from 2D reflectances and a retrieval grid which used the phase function DHG1 at a solar zenith angle of 50°. The top three panels give the retrievals for cloud 3 with the domain optical depth as indicated. The bottom panel contains the actual column integrated optical depth for comparison.

improve towards the backscattering direction. This tendency is shown in the solid shaped points by the general decrease of the percent RMS difference with increasing scattering angle and is emphasized for retrievals at large solar zenith angles.

The percent RMS differences for the effective radius retrieval for cloud 3 are shown in Figure 3.17. As in the case of Fig3.13, only the retrievals for the solar zenith angles of 10° and 50° are shown. Comparison of the solid shapes between Figures 3.16 and 3.17 show that the RMS differences for the broken cloud are much higher than those for the more stratified cloud. For cloud 2, the RMS percent differences are observed to be less than 10%, but for cloud 3 these values are 20% to 30%. Thus, the inhomogeneities of cloud 3 cause much larger localized error over all angles than the inhomogeneities of cloud 2. Also, the solid shapes show the same tendency for the retrieval to improve towards the backscattering angle as seen in Fig. 3.16. Figure 3.17 also shows that the RMS errors associated with using the DHG2 phase function in the DHG1 retrieval grid (open shapes) are much closer to the RMS errors from using the DHG1 radiances (solid shapes) than observed in Fig. 3.16. This may indicate that as the inhomogeneities increase the uncertainty in the phase function becomes less important, especially for large optical depths. However, Fig. 3.17 still shows that for thinner clouds the RMS differences are very sensitive to the phase function uncertainties at scattering angles where large differences exist between the assumed and actual phase function.

The results of the effective radius retrievals for a cloud that varies in extinction only, like that of the optical depth retrievals, indicate that the differences between actual and retrieval phase functions can lead to large bias error. These errors become very large especially for the thin cloud cases at the scattering angles where differences in the phase functions become large. Errors which are caused by the plane-parallel assumption are dependent upon the magnitude of the cloud inhomogeneity and upon the scale over which the measurement is made. At a fine scale (like 50 m as shown in the simulations), localized errors can be very large but may cancel out as larger area averages are computed. For the stratified cloud 2, this cancellation of localized error is quite apparent. However, for the broken cloud 3, this cancellation may not be complete and biases in the retrievals from only the inhomogeneity may result. Finally, regardless of the inhomogeneities, the effective radius retrievals for clouds with domain averaged optical depth greater than two improve towards the backscattering direction (i.e., $\Theta = 180°$), provided that the phase function used to generate the retrieval grid is representative of the actual cirrus cloud particles.

3.2 Radiance Field Sensitivities for Clouds with Variable Microphysics

The results in the previous section using ice clouds with constant microphysical distributions isolate the effects of horizontal inhomogeneities in an idealized way. In reality,

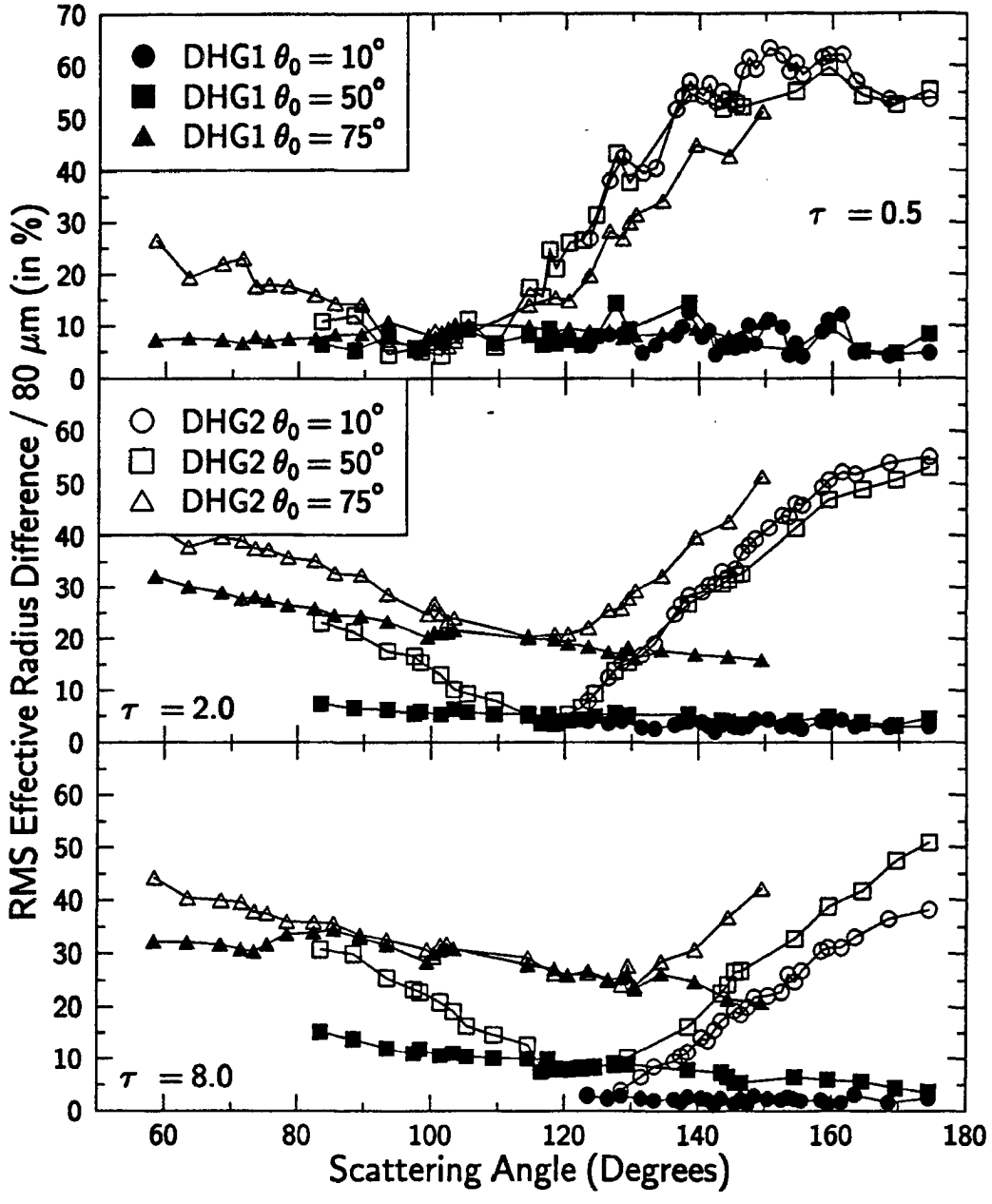

Figure 3.16: RMS differences for cloud 2 computed over all horizontal grid points between the effective radius retrievals and the actual effective radius 80.0 μm as a function of the scattering angle. The differences are divided by the actual effective radius and expressed in terms of a percent. Solid shapes correspond to retrievals where DHG1 is used in both the 2D simulations and the retrieval grid. Open shapes refer to retrievals using a retrieval grid with DHG1 and 2D calculations using DHG2.

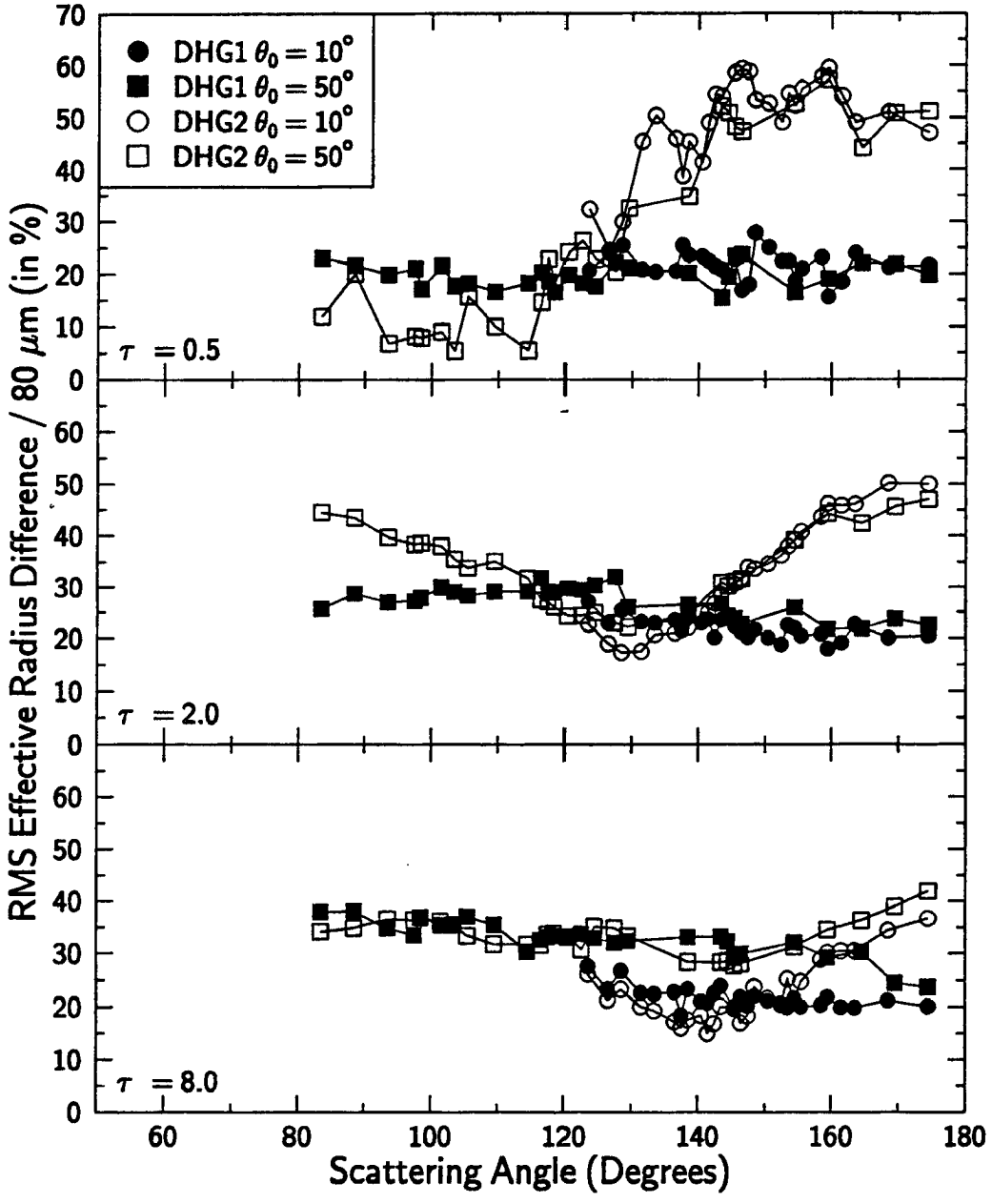

Figure 3.17: RMS differences for cloud 3 computed over all horizontal grid points between the effective radius retrievals and the actual effective radius 80.0 μm as a function of the scattering angle. The differences are divided by the actual effective radius and expressed in terms of a percent. Solid shapes correspond to retrievals where DHG1 is used in both the 2D simulations and the retrieval grid. Open shapes refer to retrievals using a retrieval grid with DHG1 and 2D calculations using DHG2.

the microphysical distributions of ice clouds vary both horizontally and vertically. This variability of the microphysical properties of ice clouds results not only in variability of the extinction properties of the cloud, but also in the single-scattering albedo and phase function as well. In an attempt to study this problem in two dimensions, the simulations in this section focus upon the sensitivities of the radiance field for clouds with both variable extinction and single-scattering albedo fields. The phase function for the simulations presented is assumed constant since its dependence on a size distribution of irregularly shaped ice particles is not well understood. The addition of the variable single-scattering albedo field, as described in detail in Section 2.1.2., will produce additional uncertainty in the retrieval process. This uncertainty occurs because the plane-parallel retrieval grid is based upon clouds with vertically uniform single-scattering albedo since each grid point is computed assuming a specified optical depth and effective radius. As a result, the retrievals will contain error using both 2D and IPA reflectances due to variation of extinction and single-scattering albedo throughout the cloud. For this reason, the 2D and IPA reflectances are compared to reflectances assuming a weighted average effective radius as defined in equation 2.8 that corresponds to a domain averaged single-scattering albedo. Based on comparison of these reflectances to 2D and IPA reflectances, the sensitivities of both the optical depth and effective radius retrievals to vertical and horizontal inhomogeneities are derived.

3.2.1 Reflectances

The reflected radiances at nadir for the cloud with variable extinction and albedo fields for wavelengths 0.83 μm and 1.65 μm are given in Figures 3.18 and 3.19. Each panel of the figures presents the nadir reflected radiances for 3 solar zenith angles (10°, 50° and 75°). At each solar zenith angle, the reflected radiances are shown using the variable extinction and single-scattering albedo fields in 2D calculations as well as independent pixel calculations using the domain averaged ω_0 (denoted IP1) and the variable ω_0 field (denoted IP2). The bottom panel of both figures gives the normalized optical depth as a function of horizontal distance as a reference. Note that this cloud, unlike the clouds of the previous section, has variability on much smaller scales. This is shown by the high frequency oscillations of the optical depth that result from the radar-lidar retrieval method. As a result, the IP1 and IP2 reflected radiances at both wavelengths show such oscillatory behavior. It is interesting to note that these oscillations are damped as the optical path is increased by increasing the domain average optical depth, increasing the solar zenith angle, or increasing the absorption. However, the 2D reflected radiances are smoothed relative to the IPA calculations for the solar zenith angles of 10° and 50° at both domain averaged optical depths and at both wavelengths. At 75°, the larger scale relative maximum from about 1 to 5 km causes cloud shadowing effects. The effects of inhomogeneities are seen in the optical depth and effective radius retrievals in the upcoming subsections.

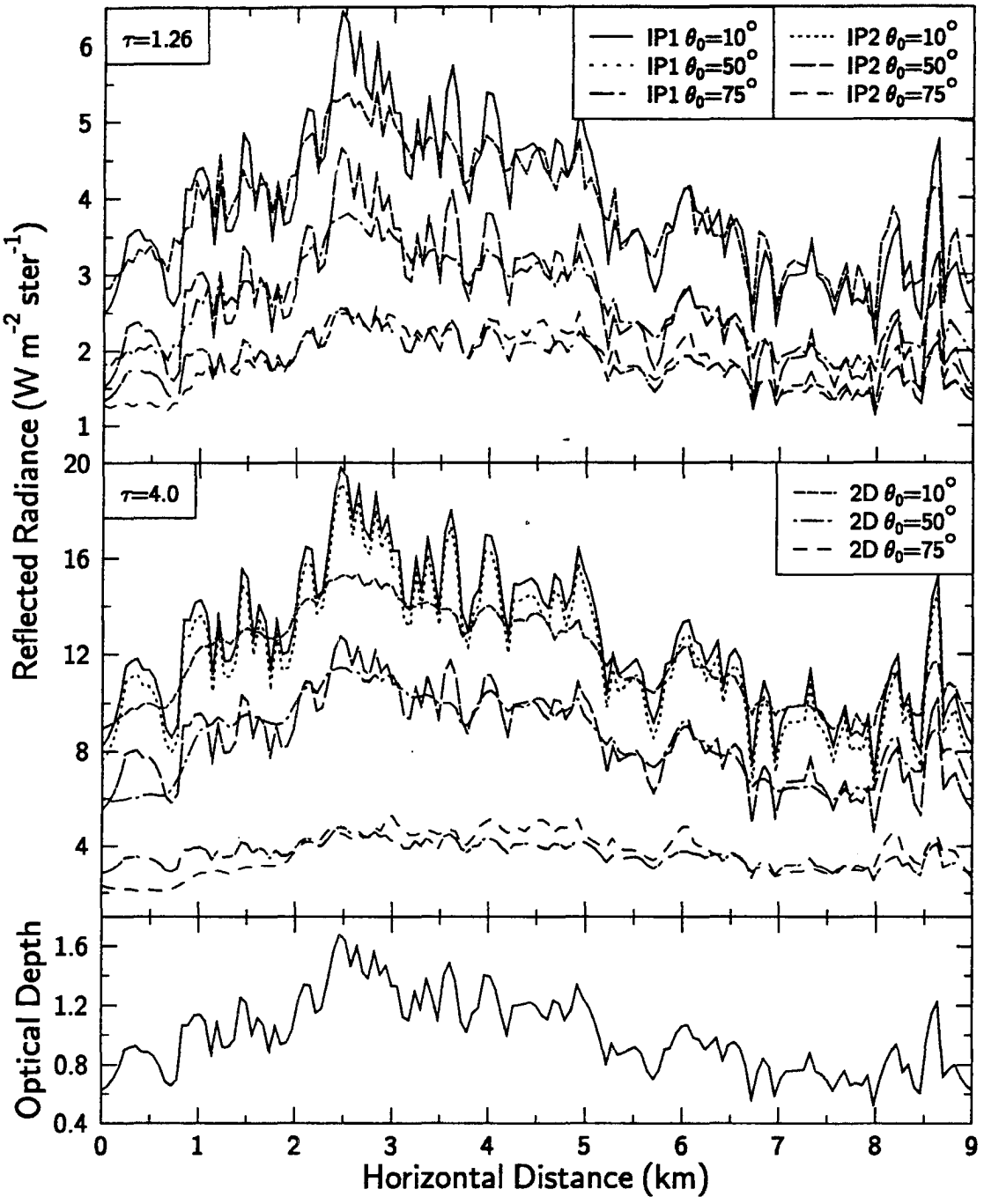

Figure 3.18: IP1, IP2 and 2D reflected radiances at 0.83 μm and a nadir viewing angle. The solar zenith angles and domain averaged optical depths are indicated in the legend. The bottom panel gives the normalized column optical depth for the cloud.

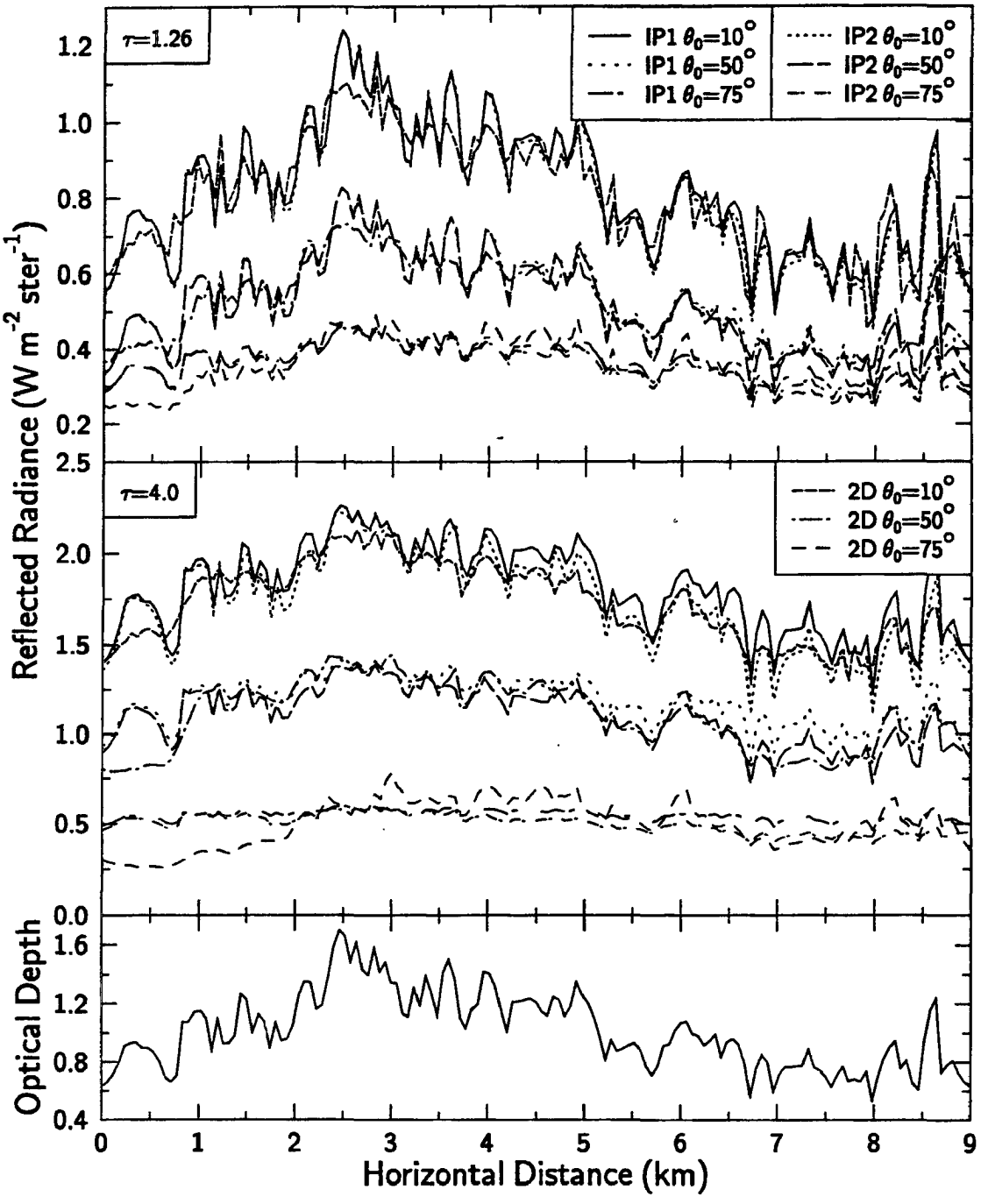

Figure 3.19: IP1, IP2 and 2D reflected radiances at 1.65 μm and a nadir viewing angle. The solar zenith angles and domain averaged optical depths are indicated in the legend. The bottom panel gives the normalized column optical depth for the cloud.

Also, Figure 3.18 shows that the IP2 calculations agree very closely to those calculations with the weighted average single-scattering albedo at 0.83 μm. This is especially true for the cloud with domain averaged optical depth of 1.26. There is some disagreement at the smallest solar zenith angle for the domain averaged optical depth of 4.0, but the agreement improves for increasing solar zenith angle. This agreement results from the insensitivity of the single-scattering albedo to particle size at this wavelength. However, at 1.65 μm, where there is much larger absorption, the single-scattering albedo is much more sensitive to the particle effective radius. This is seen in Fig.3.18 by the apparent disagreement the independent pixel radiances between the variable and constant single-scattering albedo. The figure shows that this disagreement increases with increasing domain averaged optical depth. These sensitivities are more quantitatively analyzed in the following sections.

3.2.2 Optical Depth Retrieval

As demonstrated in the previous section, the radiances at 0.83 μm are insensitive to the particle size. As a result, the inhomogeneities in particle size throughout this cloud may not affect the retrieval of optical depth significantly. Figure 3.20 shows the visible optical depth retrievals for domain averaged optical depths of 1.26 and 4.0 at a solar zenith of 50°. Retrievals using both the IP2 and 2D reflectances are plotted along with the actual column optical depths. The figure shows excellent agreement between the column optical depth and the retrieved optical depth when using the IP2 reflectances with the variable single-scattering albedo. This indicates that the vertical inhomogeneities of particle size do not affect the optical depth retrieval at this wavelength. The retrievals using the 2D reflectances do contain larger error when compared to the column integrated optical depth. The retrievals tend to be smoothed relative to the narrowly spaced maximum and minimum characteristic of the column optical depths. For the domain averaged optical depth of 4.0, the retrievals show a slight tendency towards cloud shadowing. As noted in the discussion of clouds with constant effective radius, these effects are caused by the interaction of radiation with cloud inhomogeneities.

A more complete overview of the magnitude of the errors found in the process of retrieving optical depth for this cloud is shown in Figure 3.21. This figure gives the average RMS difference over all grid points between the actual column integrated optical depth and the retrieved optical depth as a function of scattering angle. The points are differentiated by their solar zenith angles with each solar zenith angle plotted as a different shape and indicated in the legend. As well, the figure reveals that IP2 calculations with a variable single-scattering albedo have minimal effect on the plane-parallel retrieval. However, the RMS differences for the 2D reflectances and solar zenith angles less than 50° show consistent RMS differences from 10 to 30% of the domain averaged optical depth. The minimum RMS relative differences occur at the scattering angle corresponding to the

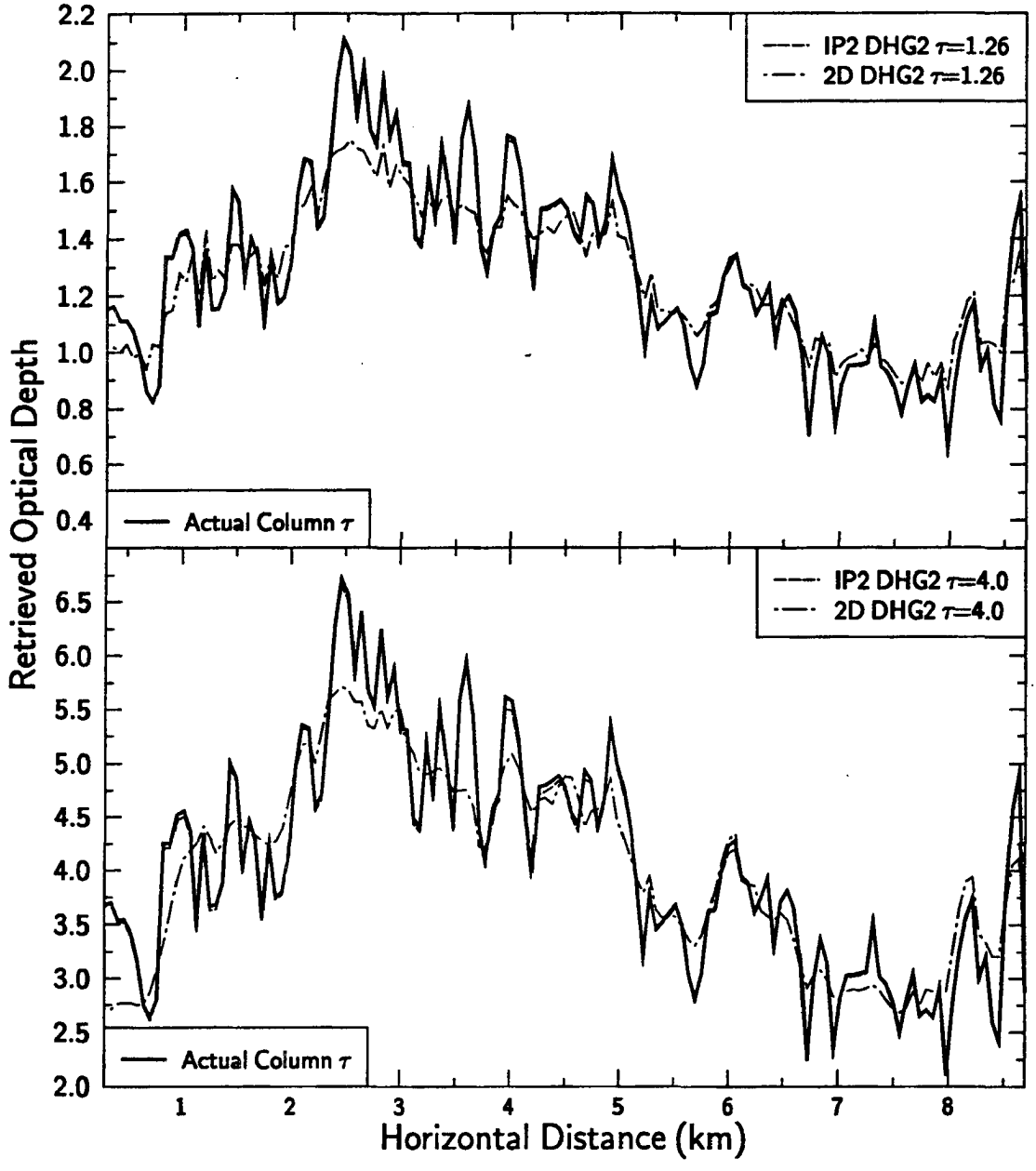

Figure 3.20: Retrieved optical depth from IPA and 2D reflectances as a function of horizontal distance and a retrieval grid which used the phase function DHG2 at a solar zenith angle of 50°. Each panel gives the retrievals with the indicated domain averaged optical depth for the cloud with a variable single-scattering albedo. The actual column integrated optical depths are given for comparison.

nadir viewing angle consistent with retrieval results from the constant microphysics cases. RMS errors for the solar zenith angle of 75° are much larger, especially at scattering angles that correspond to forward scattered radiation.

The error associated with the domain averaged IP2 and 2D retrievals of optical depth is shown in Figure 3.22. This figure presents the domain averaged retrieved optical depth relative errors as a function of the scattering angle for IP1, IP2, and 2D reflectance calculations . All three optical depths are shown at both the domain averaged optical depth clouds. The relative domain average errors are positive if the optical depth is overestimated and negative if it is underestimated. At the solar zenith angles of 10° and 50°, the errors in the optical depth retrievals are less than 2% for the cloud with $\overline{\tau} = 1.26$, and less than 1% for the thicker cloud with $\overline{\tau} = 4.0$. This indicates the 2D error is mainly limited to local areas, but these errors cancel upon taking the domain average. The independent pixel calculations IP1 and IP2 agree almost exactly showing that the variable single-scattering albedo field does not degrade the retrieval accuracy in the domain average.

Only the retrievals using 2D reflectances at a solar zenith angle of 75° show significant errors in the domain average. Unlike the RMS errors that are larger towards decreasing scattering angles, these relative domain average errors increase with increasing scattering angle that correspond to backscattering viewing angles. Thus, on average at backscattering viewing angles, the reflectances are enhanced relative to the plane-parallel reflectances. This results in the retrieval of a domain averaged optical depth of up to 10% and 50% larger than the actual optical depth for the $\overline{\tau} = 1.26$ and $\overline{\tau} = 4.0$ clouds respectively. At more forward viewing angles (smaller scattering angles) the errors are locally larger, but fluctuate to the point that there is partial cancellation upon averaging. Overall, for the cloud studied in these simulations the optical depth retrievals are best for solar zenith angles less than 50° and show little sensitivity to the variable single-scattering albedo field. The major cloud structural inhomogeneities appear to affect the retrievals for this cloud more greatly than varying the single-scattering albedo.

3.2.3 Effective Radius Retrieval

In order to evaluate the sensitivities of the effective radius retrievals to the vertical and horizontal inhomogeneities of this cloud, an effective radius is required which is representative of the size distributions present in a given column. Such an effective radius is defined for this analysis here as the column weighted effective radius. The column effective radius is computed analogously to the domain averaged effective radius in equation 2.8 and is expressed as:

$$\langle r_e \rangle_{column} = \frac{\sum_{i=1}^{Nz} N_{o_i} r_{e_i}^3}{\sum_{i=1}^{Nz} N_{o_i} r_{e_i}^2} \tag{3.2}$$

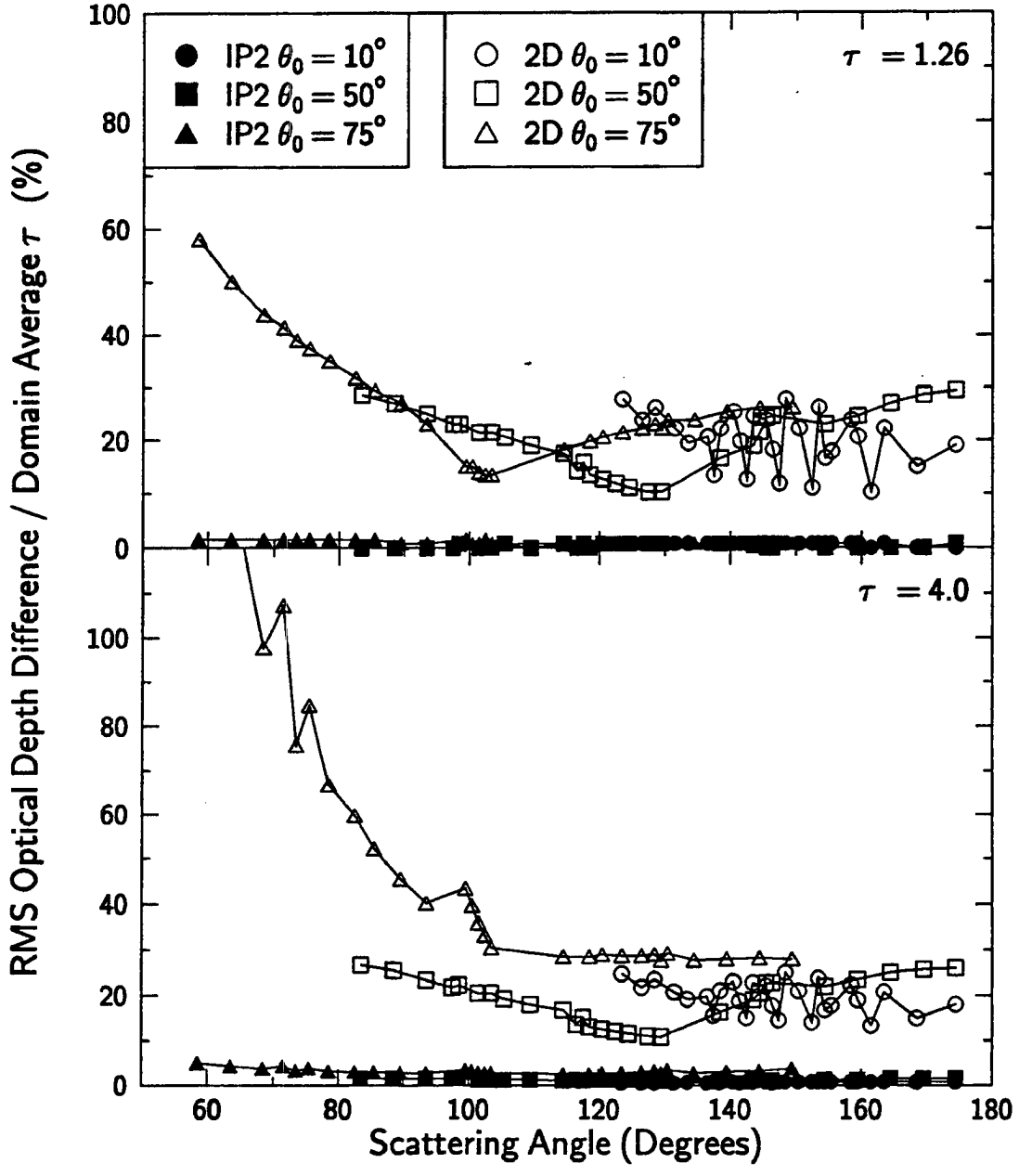

Figure 3.21: RMS differences averaged over all horizontal grid points between optical depth retrievals and actual column averaged optical depths as a function of the scattering angle. The differences are divided by the actual domain averaged optical depth and expressed in terms of a percent. Solid shapes correspond to retrievals from IP2 reflectances and open shapes refer to retrievals using 2D reflectances. The phase function DHG2 is used in all the calculations.

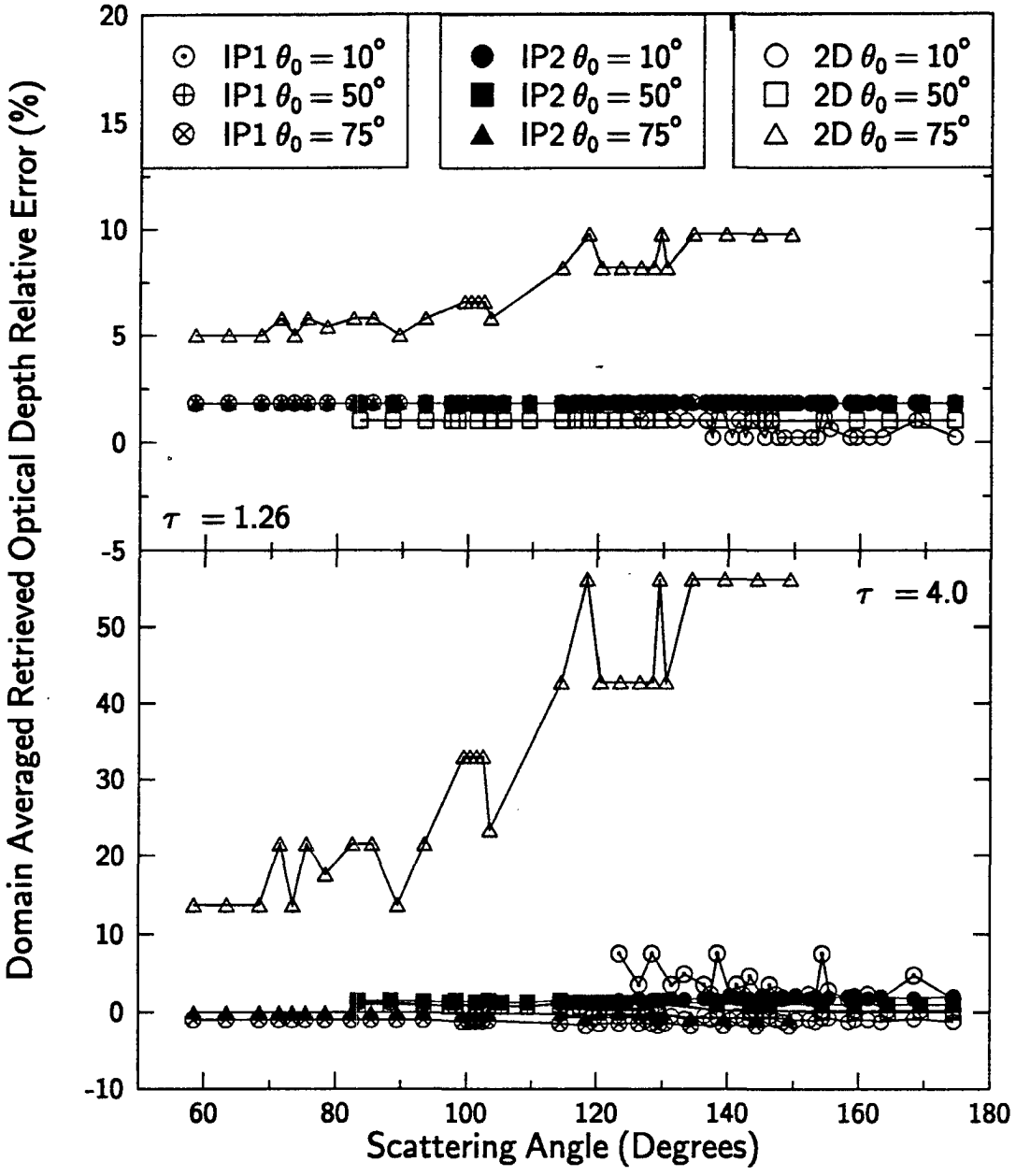

Figure 3.22: Relative errors of the domain averaged IP1, IP2 and 2D retrieved optical depth for the variable ω_0 cloud as a function of the scattering angle. IP1 denotes the independent pixel retrievals using a domain averaged single-scattering albedo and the points are indicated as circles with inserted characters as shown. IP2 and 2D denote independent pixel and two-dimensional retrievals using the variable ω_0 field and are indicated by the solid and open shapes respectively. All calculations use DHG2.

where N_z is the number vertical grid points and N_{o_i} and r_{e_i} are the total concentration and effective radius respectively at each grid point. This column effective radius is chosen to be consistent with the independent pixel method of retrieval which estimates an effective radius for the cloud column from the reflected radiances.

The column effective radius is shown along with retrievals of 2D and IP2 reflectances for the cloud with domain averaged optical depths of 1.26 and 4.0 in Figures 3.23 and 3.24 respectively. Each panel of each figure gives the retrievals at the indicated solar zenith angle viewed at nadir. The phase function DHG2 is used for all the calculations (denoted P22). The bottom panel of each figure contains the horizontal variation of optical depth for each of the clouds. The plots show that the agreement between the IPA and 2D retrievals is good for thinner optical depths and smaller solar zenith angles except at certain locations. As the solar zenith angle and the optical depth become larger, more cloud shadowing effects are observed decreasing the agreement (see Fig. 3.24, $\theta_0 = 75°$).

The agreement between the IP2 retrievals and the column integrated effective radius also deteriorates as the optical depth and the solar zenith angle increase. At the domain averaged optical depth of 4.0, the retrievals appear to be biased high. This bias appears to become larger as the solar zenith angle increases. For instance, at $\theta_0 = 10°$ in Fig. 3.24, the column integrated effective radius at 2 km is 62.97 μm. The IP2 retrieved effective radius at this point is 70.78 μm, representing a bias of about 8 μm. At $\theta_0 = 75°$, the IP2 retrieved effective radius is 76.64 μm. So, the bias at 2 km grows about 75% from solar zenith angle 10° to 75°. Interestingly, the computation of an arithmetic average column effective radius at 2 km gives 69.71 μm which compares much more favorably to the IP2 retrieved effective radius. Thus, in this column, which has an optical depth of 4.15, the reflectances from the IPA are more closely associated with a column effective radius computed by an arithmetic average than one computed using equation 3.2. The arithmetic averaged column effective radii are larger in most locations than those computed with equation 3.2, but are similar to and even less than the weighted average column effective radius in other locations (not shown). Thus, the arithmetic averaged column effective radius is not more accurate in all locations. The fact that the radiation field behaves differently with increasing optical depth is not surprising in that the radiances are nonlinear in optical depth. The thinner optical depths represent a more linear regime where the weighted average is more appropriate. This may not be the case as the optical depth increases due to the nonlinearity. Since the bias of the retrievals observed for these cases is high, the reflectances from the IPA may be influenced by size distributions more deeply in the cloud where the effective radii are larger than the column averaged effective radius indicates. Thus, the reason for the disagreement between IP2 and the column effective radius must ultimately be attributed to the vertical inhomogeneities of particle size throughout the column and the nonlinearity of the relationship between reflectance and optical depth.

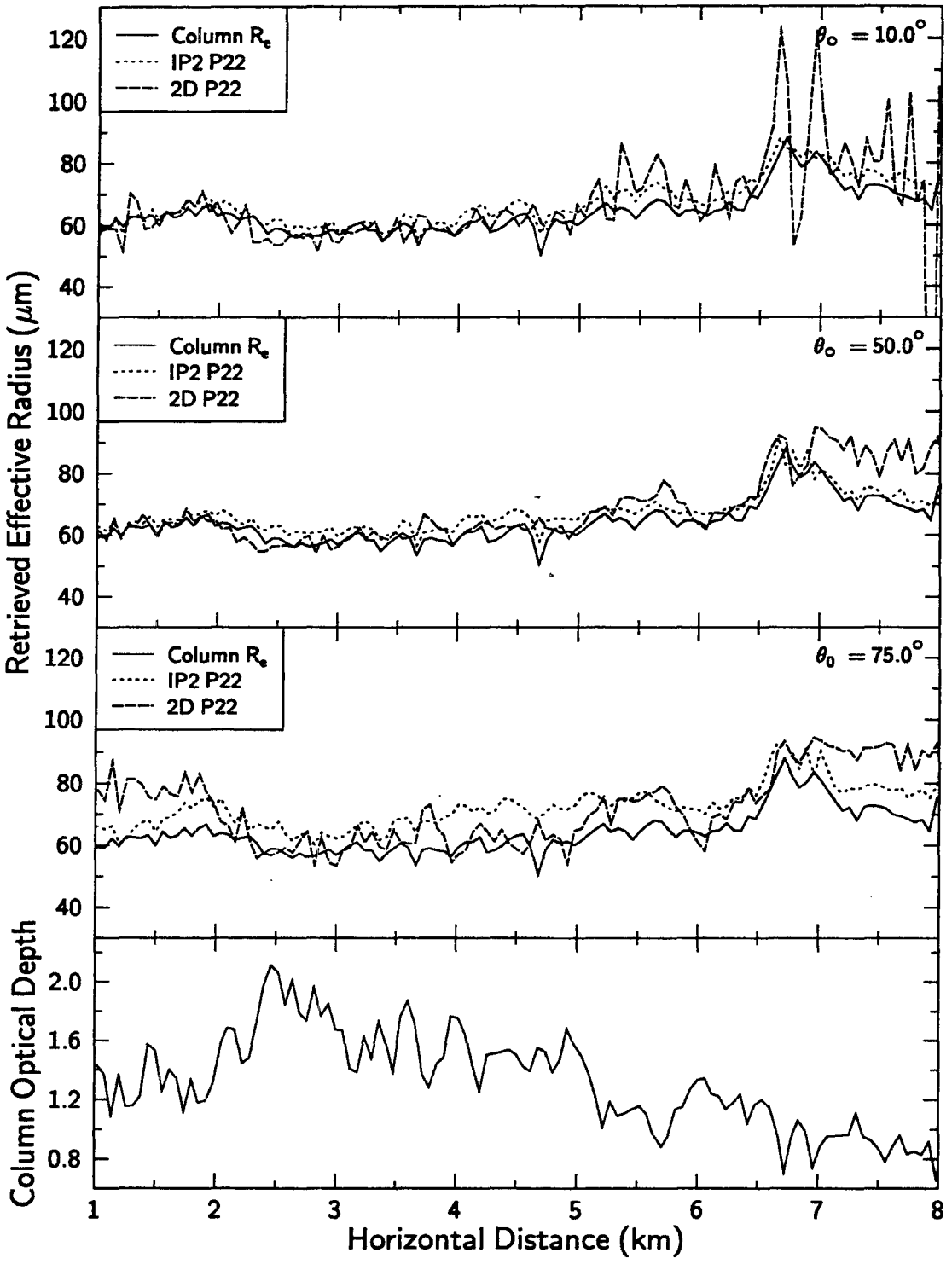

Figure 3.23: Retrieved effective radius from IP2 and 2D reflectances as a function of horizontal distance and a retrieval grid which used the phase function DHG2 for the variable k_{ext} and ω_0 cloud with domain averaged optical depth of 1.26. The top three panels give the retrievals for the different solar zenith angles as indicated. The bottom panel contains the actual column integrated optical depth for comparison.

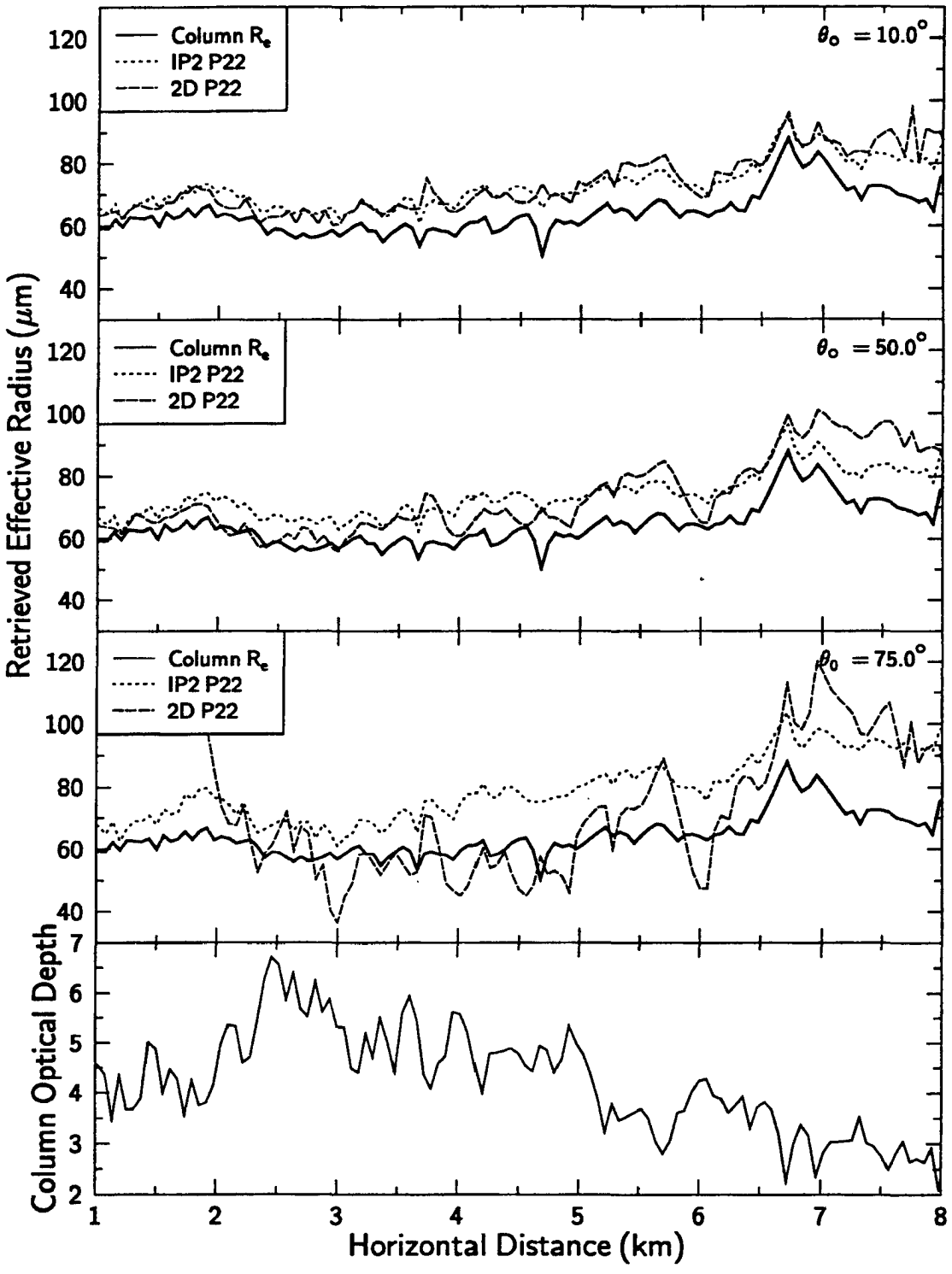

Figure 3.24: Retrieved effective radius from IP2 and 2D reflectances as a function of horizontal distance and a retrieval grid which used the phase function DHG2 for the variable k_{ext} and ω_0 cloud with domain averaged optical depth of 4.0. The top three panels give the retrievals for the different solar zenith angles as indicated. The bottom panel contains the actual column integrated optical depth for comparison.

A better overview of the local differences between the column effective radius and the IP2 and 2D retrievals is given in Figure 3.25. This figure presents the RMS differences between the IPA and 2D retrievals with the column effective radius computed from eq. 3.2 as a percent of the domain averaged effective radius. The RMS relative differences are shown for clouds with domain averaged optical depth of 1.26 and 4.0. The IP2 and 2D RMS differences are given for each of the three solar zenith angles as indicated in the legend. Immediately apparent from this figure is the larger RMS differences from the column effective radius for the 2D retrievals than for the IPA retrievals. For the thinner cloud, the percent RMS differences of the 2D retrievals are up to a factor of two larger than the IPA for the solar zenith angles of 10° and 50°. For the thicker cloud, the percent RMS differences for the 2D retrievals were only about 1/4 to 1/3 larger than that for the IP2 retrievals. This indicates that the effects of the vertical variability upon the plane-parallel retrievals are adding uncertainty to the retrieval comparable to that of the 2D horizontal and vertical inhomogeneity as the optical depth is increased. Note that the percent RMS differences are much higher for both the IP2 and 2D retrievals at 75° than for the smaller zenith angles. This is further evidence that the retrievals at low sun angles add considerable uncertainty to the retrieval process. Finally, the percent RMS differences for this variable ω_0 field cloud can be compared to Figure 3.16 for the clouds with a domain averaged ω_0. Comparison reveals that the percent RMS differences are higher for this stratified cloud with the variable ω_0 than for the stratified cloud 2 of the previous section. Thus, the variable ω_0 does add uncertainty to both the IPA and 2D retrievals.

The domain averaged relative errors of the retrievals for this variable ω_0 cloud are given in Figure 3.26. This figure presents, as a function of the scattering angle, the domain averaged IP1, IP2, and the 2D retrievals. For the thin cloud with $\overline{\tau} = 1.26$, the IP1 retrievals give domain averaged effective radii which slightly underestimate the actual domain averaged r_e by less than 5%. However, the IP2 and 2D domain averaged retrievals give an overestimation of 6-10% depending upon the solar zenith and scattering angles. The 2D relative errors are only a percent or so higher than the IP2 errors. This indicates that the uncertainty added to the domain averaged retrievals by the vertical inhomogeneities are as much as the uncertainty added with two-dimensional variability. The agreement of the magnitude of error between the 2D and IP2 retrievals occurs despite the much larger variability associated with the 2D measurements as shown in Fig. 3.25. Although the 2D variability is larger, the domain average relative errors are not much larger than those for the IP2 retrievals because the error associated with horizontal inhomogeneities partially cancels upon averaging across the domain. Note that even the relative errors of the retrievals at 75° are very close for the thin cloud even though they are 8% higher than errors for the lower solar zenith angles.

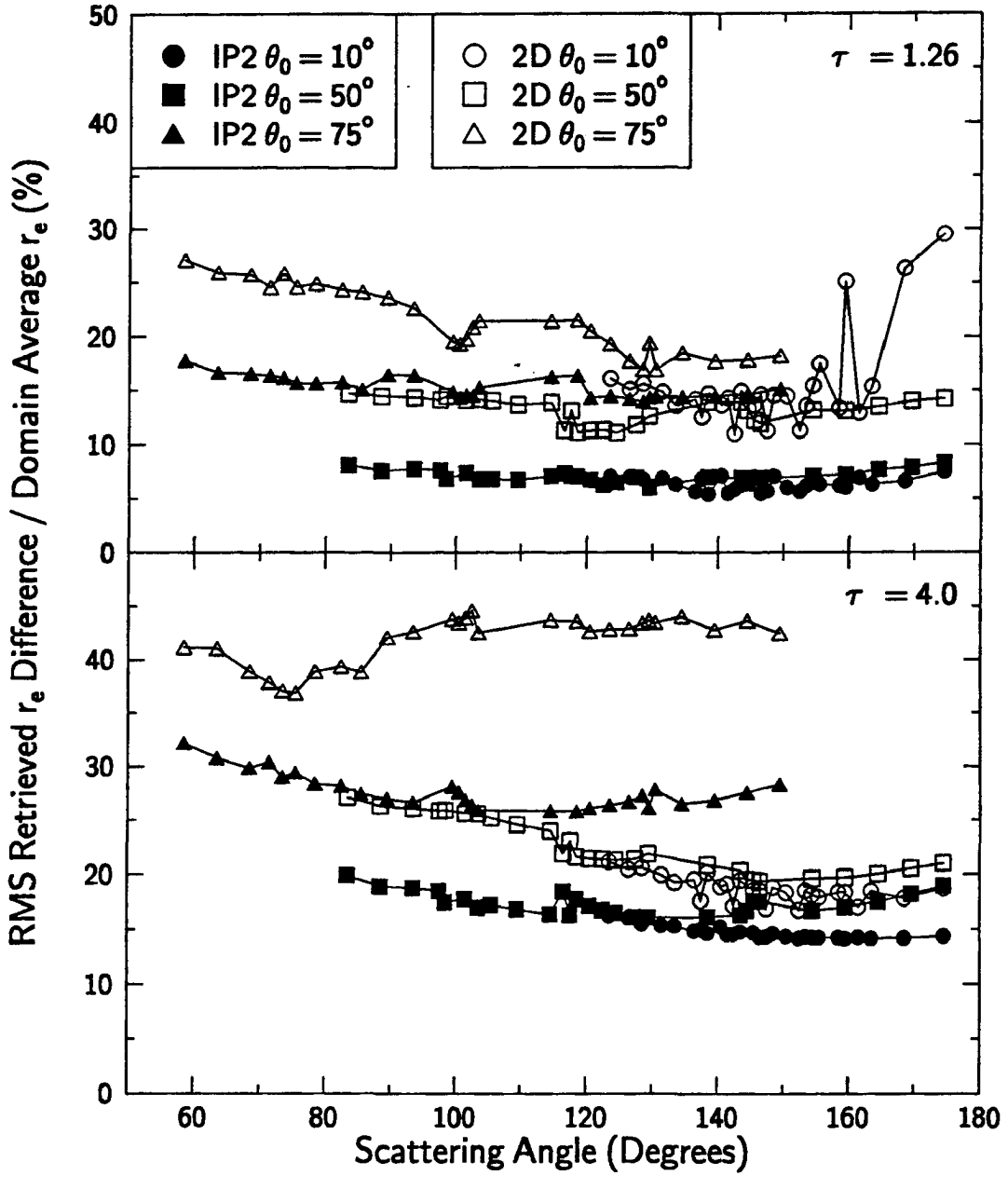

Figure 3.25: RMS differences for the variable ω_0 cloud between the effective radius retrievals using 2D and IP1 reflectances and the column effective radius computed over all horizontal grid points as a function of the scattering angle. The differences are divided by the domain averaged effective radius and expressed in percent. Solid shapes correspond to retrievals using IPA reflectances. Open shapes refer to retrievals using 2D reflectances. All calculations use DHG2.

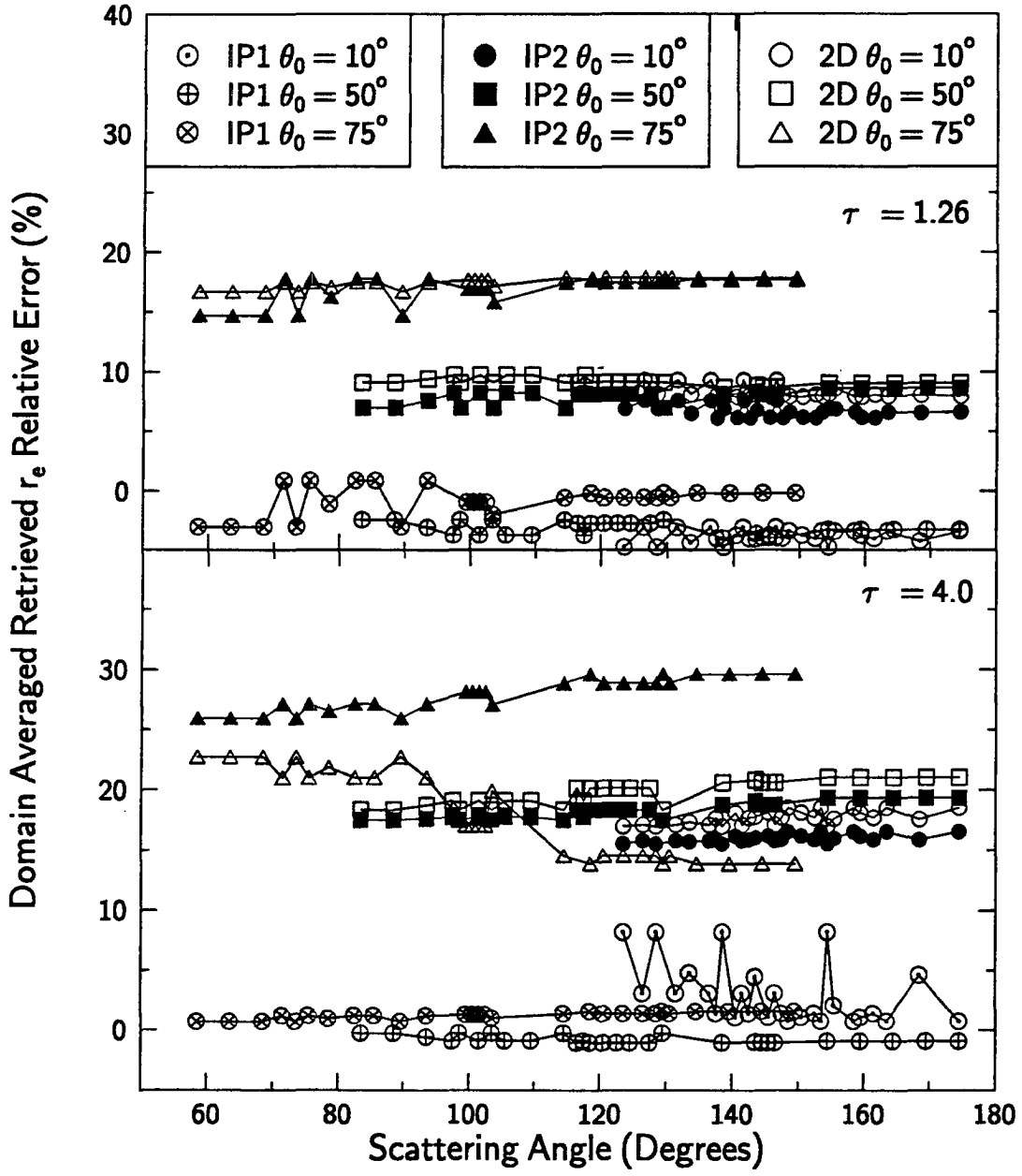

Figure 3.26: Relative errors of the domain averaged IP1, IP2 and 2D retrieved effective radius for the variable ω_0 cloud as a function of the scattering angle. IP1 denotes the independent pixel retrievals using a domain averaged single-scattering albedo and the points are indicated as circles with inserted characters as shown. IP2 and 2D denote independent pixel and two-dimensional retrievals using the variable ω_0 field and are indicated by the solid and open shapes respectively. All calculations use DHG2.

In the bottom panel of Figure 3.26 the retrievals for the thicker cloud are presented. In general, these retrievals have about 8% more error than the error with the thinner cloud. The retrievals show similar agreement between the IP2 and 2D domain averaged retrieved effective radii but the differences are a percent or so worse than for the thin cloud. Interestingly, the 2D retrievals at 75° show less error than those for IP2. At some scattering angles, the IP2 retrievals at 75° have less error than retrievals at 50°. This occurs even though the RMS differences in this case are much higher than RMS differences for the retrievals at all the other solar zenith angles. Presumably, the errors at this solar zenith angle cancel more completely since they are attributed more to the cloud shadowing effects. This figure shows that considerable uncertainty is added to retrieval of effective radius by the presence of a variable ω_0 field. The vertical variability in this field accounts for most of the error. This suggests that corrections for the domain averaged vertical variability of the particle size distributions may dramatically improve retrievals of effective radius. However, this correction is only possible in the case of the stratified clouds considered here. The uncertainty added by extreme variability such as brokenness might overwhelm the uncertainties due to the vertical variability.

3.3 Chapter Summary

In this chapter, the effect of cloud inhomogeneity on the calculation of radiances and microphysical retrievals is studied. These results are divided into two general areas. The first area examined is the radiative transfer properties of clouds that contain variable extinction but constant phase function and single-scattering albedo throughout the domain. Three such clouds are used as derived in Chapter 2 from radar observations of cirrus clouds. One of the clouds, cloud 3, is artificially broken by setting extinction values in a thin part of the cloud to a minimum value. The second part of this chapter shows the sensitivities of more realistic clouds that have variable particle size distributions across the domain. This variability is examined using unbroken clouds with a distribution of single-scattering albedo as well as the distribution of extinction. To ascertain the relative importance of cloud geometry to microphysical properties in both cloud types, a series of calculations are presented in which the domain averaged optical depths, phase function forms (g_{eff} is conserved) and solar zenith angles are varied.

The results of the simulations for the clouds with constant effective radius indicate that the effect of cloud geometry becomes more important in two-dimensional simulations as the cloud becomes thicker, the solar zenith angle increases, and/or the cloud brokenness increases. The dominant cloud effect under these conditions is referred to as cloud shadowing. This cloud shadowing causes locally large differences between IPA and 2D because radiances are enhanced to the sun side of a region of maximum optical depth and decreased to the opposite side. A secondary effect, observed at smaller solar zenith

angles, is a smoothing of the radiance field occurs in which the difference between the minimum and maximum 2D radiances is less than the that of the IPA radiances. Both of effects are the result of the horizontal interaction of radiation inside the cloud and both depend upon the solar geometry and the viewing angle. The difference between IPA and 2D radiances in the domain average is small, as these local effects tend to cancel. This is especially true in the case of the unbroken clouds, but in the case of the broken cloud this cancellation is not complete leaving differences between IPA and 2D in the domain average. The sensitivity to the shape of the phase function is found to depend upon the difference between the shapes of the phase functions at a particular scattering angle as defined by solar and viewing geometry. Unlike the cloud shadowing and smoothing effects, the effect of changing the phase function shape causes a bias in the radiances. The relative difference in this bias is found to decrease as the domain averaged optical depth of the cloud increases.

In the case of the variable single-scattering albedo, simulations are made for two independent pixel cases; one with a domain averaged single-scattering albedo (IP1) and one with the actual varying single-scattering albedo (IP2). Both of these calculations are compared to the 2D radiances. The cloud was unbroken but had more small scale variability. The variable ω_o is found to have little effect on the radiances calculated at the visible wavelength, but large effect on the radiances computed in the absorbing channel. This is simply due to the fact that changes in the size distribution impact the $\omega_o$of the absorbing wavelength much more. The effect of the vertical inhomogeneity decreased the agreement between IP1 and IP2 as the optical depth increased and as the solar zenith angle increased. Both cloud smoothing and cloud shadowing effects were observed in the 2D radiances and these effects where more pronounced in the thicker cloud at larger solar zenith angles.

To better understand the implications of the above radiance sensitivities, a plane-parallel uniform cloud retrieval procedure is developed to determine the errors in the estimate of known cloud properties due to these effects. A bispectral retrieval grid is computed for a uniform cirrus cloud for all the various optical depths, phase functions and solar zenith angles used in the study. The effect horizontal and vertical cloud inhomogeneities are then ascertained by using the 2D and IPA radiances to estimate optical depth and effective radius using the bispectral grid. The results of these calculations are summarized as follows:

- local errors in τ and r_e retrievals due to the smoothing of the radiance field at small solar zenith angles were about $\pm 10\%$ and easily exceed 25% for cloud shadowing errors, especially for the thick cloud at large solar zenith angles;

- RMS relative errors over the domain for each case were usually less than 15%, improving toward the nadir viewing angle, for the τ retrievals at $\theta_o < 50°$ and less 10% improving toward the backscatter angle for r_e retrievals at the same solar zenith angles;
- RMS relative errors for $\theta_o = 75°$ become as much as three times larger than the errors at the smaller solar zenith angles for the clouds with the largest optical depth;
- biases due to the use of the wrong phase function could easily exceed 30% at scattering angles where there was a large difference between the actual and the retrieval phase function;
- the phase function biases decreased in relative sensitivity as the domain optical depth of the cloud increased, but are still the same magnitude of the horizontal inhomogeneity at certain scattering angles;
- variation of the ω_o throughout the cloud field produced errors in τ retrievals due primarily to horizontal inhomogeneities and $5 - 10\%$ larger than the constant ω_o cases;
- variation of the ω_o throughout the cloud field produced errors in column r_e that were $5 - 10\%$ larger than those of the constant microphysics cases that were due to both the vertical inhomogeneity as seen by the IP2 cases and horizontal inhomogeneity as seen by the 2D cases;
- the effects of the vertical inhomogeneities became relatively more important than the horizontal effects as the domain averaged optical depth increased;
- domain averaged error is found to be primarily due to the vertical inhomogeneity effects since horizontal effects cancelled in the unbroken cloud; and finally,
- the broken cloud, despite having a cloud fraction of about 90%, greatly enhanced all retrieval errors, especially in the vicinity of the cloud break, such that the effects of horizontal inhomogeneity would not cancel completely in the domain average.

The results of this chapter not only highlight the effects of cloud inhomogeneity on radiative transfer, but also outline the importance of these effects upon the inverse problem of retrieving cloud microphysical properties. The results indicate that the retrieval of cloud properties in the presence of vertical and horizontal inhomogeneity using a plane-parallel uniform reflectance grid is most reliable for the estimation of τ and r_e in unbroken clouds at a nadir viewing angle and solar zenith angles less than 50°. Retrieval errors are considerably increased in broken cloud fields, larger solar zenith angles and at scattering angles where large differences between the actual and retrieval grid phase function occur.

It is important to note that cirrus clouds probably also contain some variability across the domain in the first moment of scattering phase function (i.e., the effective asymmetry parameter, g_{eff}). This variability adds additional uncertainty to the results presented in this chapter. In the next chapter, the sensitivity of fluxes to horizontal inhomogeneities is examined for all the clouds analyzed in this chapter.

Chapter 4

THE SENSITIVITY OF RADIATIVE FLUXES TO ICE CLOUD STRUCTURE AND OPTICAL PROPERTIES

Radiative flux observations from satellite and/or aircraft are typically used to characterize the bulk radiative properties of clouds and the resulting state of the climate system. Climate models use flux models based upon the plane-parallel theory to derive important radiative quantities such as cloud heating and cloud radiative forcing. The sensitivity of these flux observations and plane-parallel radiative transfer models to cloud inhomogeneity is not well understood. The incorporation of cloud inhomogeneity effects into climate type models is in its infancy. In order to understand the effect of inhomogeneity upon flux properties and build a foundation upon which parameterizations of the radiative properties of inhomogeneous clouds can be based, the sensitivities of flux quantities to cloud inhomogeneities must be studied in terms of the limits of plane-parallel theory.

The purpose of this chapter is to demonstrate the sensitivity of cirrus cloud radiative flux properties to variations in cloud structure and cloud microphysical properties in two dimensions. This sensitivity is compared to plane-parallel theory in order to demonstrate the types of cloud variabilities that result in a break down of this theory. Clouds with both constant and variable microphysical distributions, which were derived in the previous chapter, are used for these flux sensitivities studies. Radiative transfer calculations on these clouds represent the convolution of both the cloud structural effects and the variation of microphysical properties in two dimensions. These effects, along with the effects of variations in the scattering phase function are discussed. Some inferences are then made to the possible effects that cloud inhomogeneities have in the realms of the measurement of ice cloud radiative properties.

4.1 Sensitivities of Radiative Fluxes to Clouds with Constant Effective Radius

In order to isolate the effects of cloud structure on the radiative transfer properties of ice clouds, a series of simulations are performed for the three clouds (see Fig. 2.2a,b,c) assuming a constant microphysical size distribution and thus a constant effective radius. This subsection presents the results of these simulations for the flux computations. Two-dimensional flux calculations are compared to independent pixel approximation calculations to learn about the effects of the multi-dimensional media. The calculations are

performed for three different solar zenith angles; 10°, 50° and 75° respectively. For the purposes of this study, the cloud fields were scaled such that the domain average column optical depths are averaged to 0.5, 1.0, 2.0, 4.0 and 8.0 respectively. The analysis of the three clouds of constant effective radius is presented in terms of the horizontal column by column and domain averaged differences between the two-dimensional (2D) and the independent pixel approximation (IPA) methods. The effect of the cloud variability on the domain average is important for the determination of climatic parameters such as cirrus albedo, transmittance and absorption in the presence of considerable inhomogeneity.

4.1.1 Spatial Flux Sensitivity to Cloud Structure

In the following sections, the fluxes at cloud top and cloud base are examined on a horizontal column by column basis for both 2D and IPA. The effect of the cloud structure on the horizontal variation of these fluxes is discussed in the context of the solar wavelengths at 0.83 μm and 2.21 μm which denote cases for approximate conservative scattering ($\omega_0 = 0.9998$) and weak absorption ($\omega_0 = 0.9020$) respectively. In addition, calculations were performed in the infrared window channel at 11.5 μm in order to understand the effects of inhomogeneity at this wavelength. This analysis not only gives a better understanding of the limits of plane-parallel radiative transfer, but also has important implications for *in situ* aircraft radiative observations and to the remote sensing of clouds.

Horizontal Variations of Boundary Fluxes

The influence of the horizontal dimension on the radiative fluxes is seen in the comparison of the fluxes computed in 2D simulations compared to those computed using IPA. As an example, the 2D and IPA fluxes as a function of the horizontal position for clouds 1, 2, and 3 respectively for the DHG2 phase function are shown in Figures 4.1, 4.2, and 4.3 at 0.83 μm and in Figures 4.4, 4.5, and 4.6 respectively at 2.21 μm. The incident solar flux used for these simulations has been integrated over a bandwidth of the Landsat channels centered at these wavelengths (see Wielicki et al., 1990) and the resulting fluxes are expressed in units of $W\ m^{-2}$. Each figure has three panels showing the variation of diffuse upward flux as a function of the horizontal distance for the three different solar zenith angles: 10°, 50° and 75°. Each panel contains the results for the three different domain averaged column optical depths for 2D and IPA: $\overline{\tau} = 0.5, 2.0$ and 8.0. These figures not only illustrate the relationship between the fluxes and the individual cloud structures, but also how the effects of spatial variabilities depend upon domain averaged column optical thickness and solar zenith angle. Immediately apparent from these figures is the smoothness of the 2D curves compared to the IPA curves. This is a result of the way adjacent pixels influence radiative transfer and the flux. Also apparent in these figures is the way in which the local differences between the 2D and IPA fluxes become larger

with increasing optical depth, indicating that the effects of the cloud spatial variabilities become more important in these situations. Additionally, increasing the solar zenith angle (lowering the sun angle) causes larger differences between the IPA and 2D calculations. This occurs because lower sun angles increase the path lengths of radiation through the cloud and thus increase the number of adjacent cloud pixel columns that influence the radiative transfer compared to the one column of IPA.

At 2.21 μm, the presence of absorption does not significantly change the characteristics observed for the more conservative scattering case. The absorption does appear to cause a smoothing of the fluxes along the horizontal, reducing the prominence of the reflected features. However, the relative differences between the IPA and 2D fluxes at these solar zenith angles are larger than those for the conservative scattering cases as demonstrated later. Comparing the differences between the 2D and IPA of the upward fluxes of each cloud to one another reveals that IPA is much less accurate for the broken cloud. The differences between the broken cloud and the more stratified cloud are vital to the understanding of the conditions which cause a breakdown of the plane parallel theory and are explored in more detail later.

Figure 4.7 presents the upward fluxes (with units $W\ m^{-2}\ \mu m^{-1}$) for all three clouds for the widow channel wavelength of 11.5 μm. Note that at this wavelength the agreement between the 2D and IPA fluxes is very good and improves with increasing domain averaged optical depth. However, in the vicinity of the cloud break in cloud 3 a large disagreement is found and tends to worsen with increasing $\overline{\tau}$. In this instance the IPA greatly overestimates the flux at the top of the cloud layer compared to the 2D flux by about 50%. Since emission from the cloud acts to lower outgoing infrared radiation, this overestimation of flux by the IPA suggests that in the infrared the emission from cloud sides can be very important in determining the flux at a cloud top boundary. These differences will be explored in more detail.

RMS Fractional Differences

In order to illustrate more quantitatively the effects of changing the solar zenith angle and domain averaged column optical depth, the RMS relative differences between the 2D and IPA fluxes are computed according to

$$RMS = \sqrt{\frac{1}{N_x}\sum_{i=1}^{Nx}\left(\frac{F_{2D_i} - F_{IPA_i}}{F_{2D_i}}\right)^2}$$

which is expressed in terms of a fractional difference from 2D. This quantity represents an absolute measure of the pixel by pixel agreement between the 2D and IPA fluxes. The RMS relative differences between 2D and IPA for varying domain averaged optical depths and solar zenith angles are given in the form of contour plots shown in Figures 4.8 and 4.9. For clarity, the horizontal scale of these figures is actually $\log_2 \overline{\tau}$ but is labeled in terms

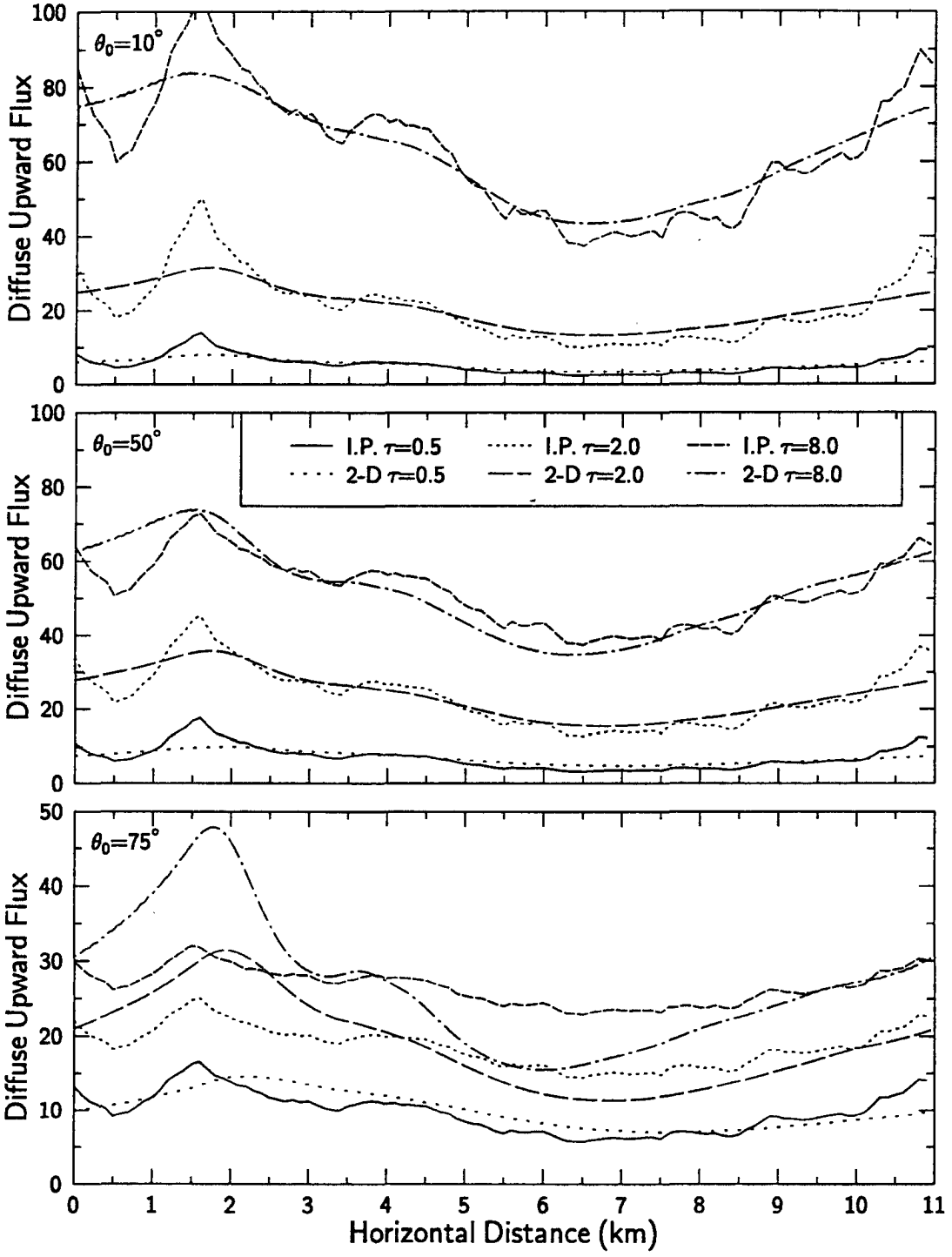

Figure 4.1: Diffuse upward fluxes ($W\,m^{-2}\,ster^{-1}$) at cloud top for $\lambda = 0.83\,\mu m$ as a function of horizontal position for the different solar zenith angles and domain averaged optical depths as indicated for cloud 1.

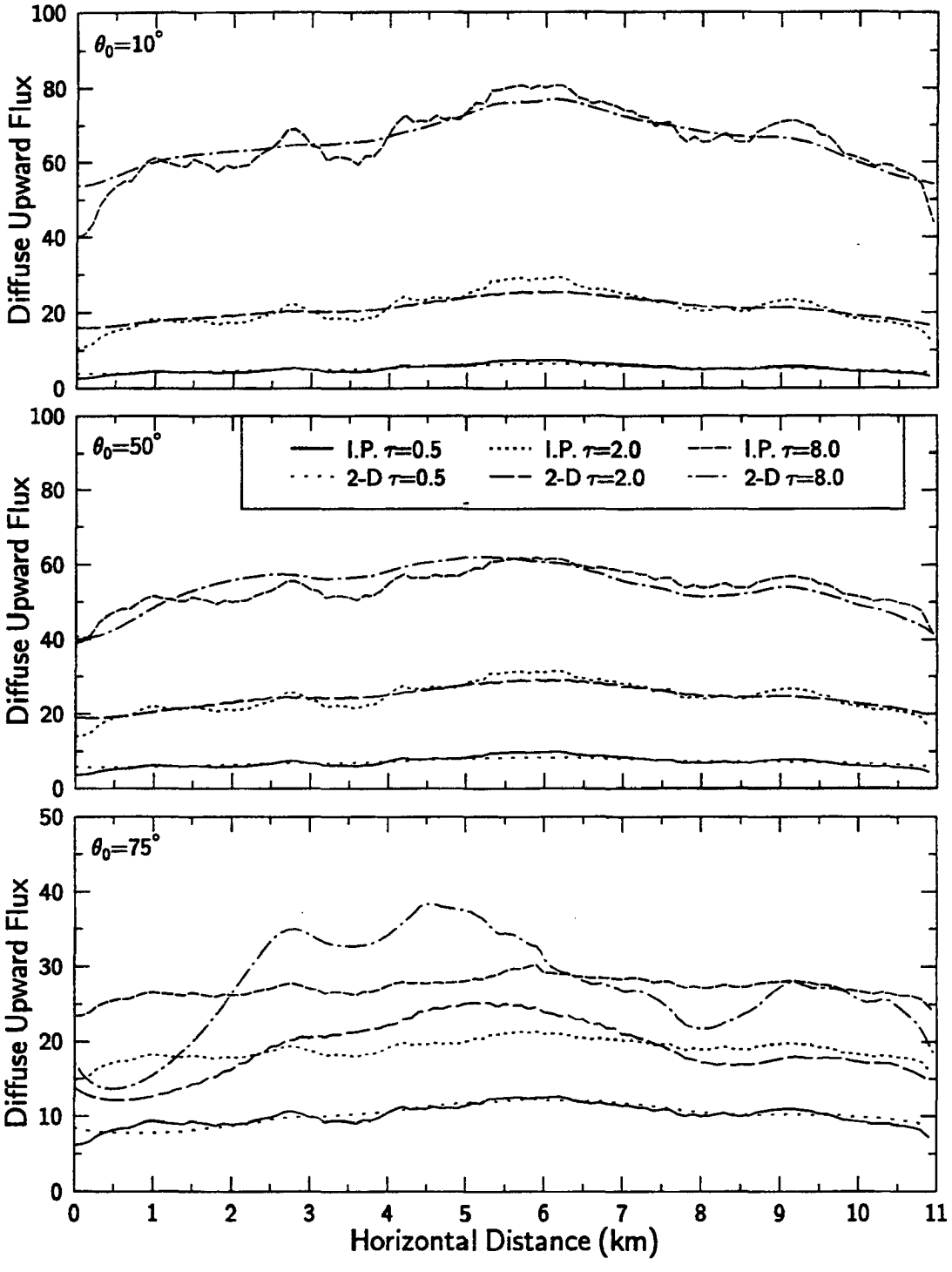

Figure 4.2: Diffuse upward fluxes ($W\,m^{-2}\,ster^{-1}$) at cloud top for $\lambda = 0.83\,\mu m$ as a function of horizontal position for the different solar zenith angles and domain averaged optical depths as indicated for cloud 2.

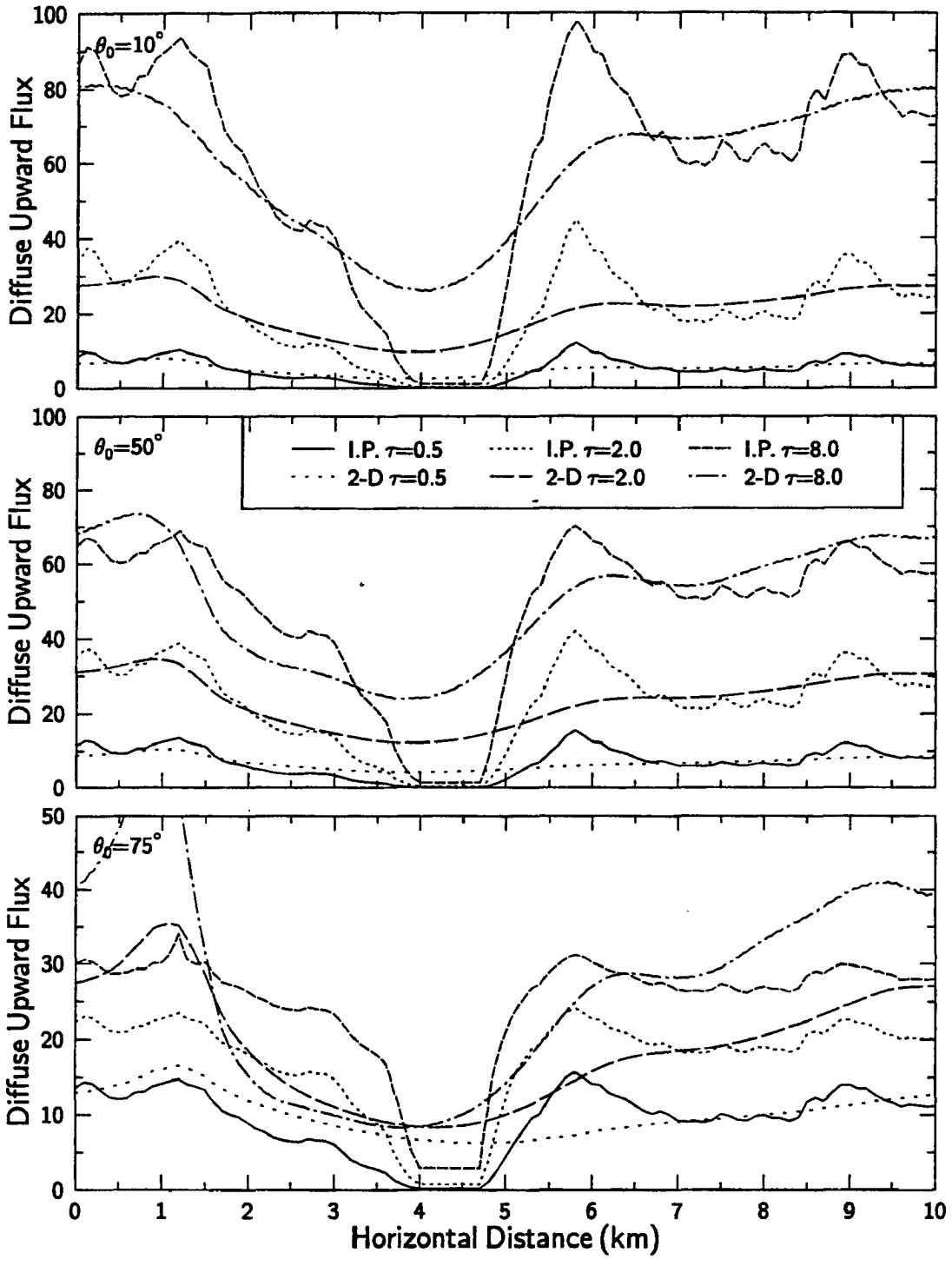

Figure 4.3: Diffuse upward fluxes ($W\,m^{-2}\,ster^{-1}$) at cloud top for $\lambda = 0.83\,\mu m$ as a function of horizontal position for the different solar zenith angles and domain averaged optical depths as indicated for cloud 3.

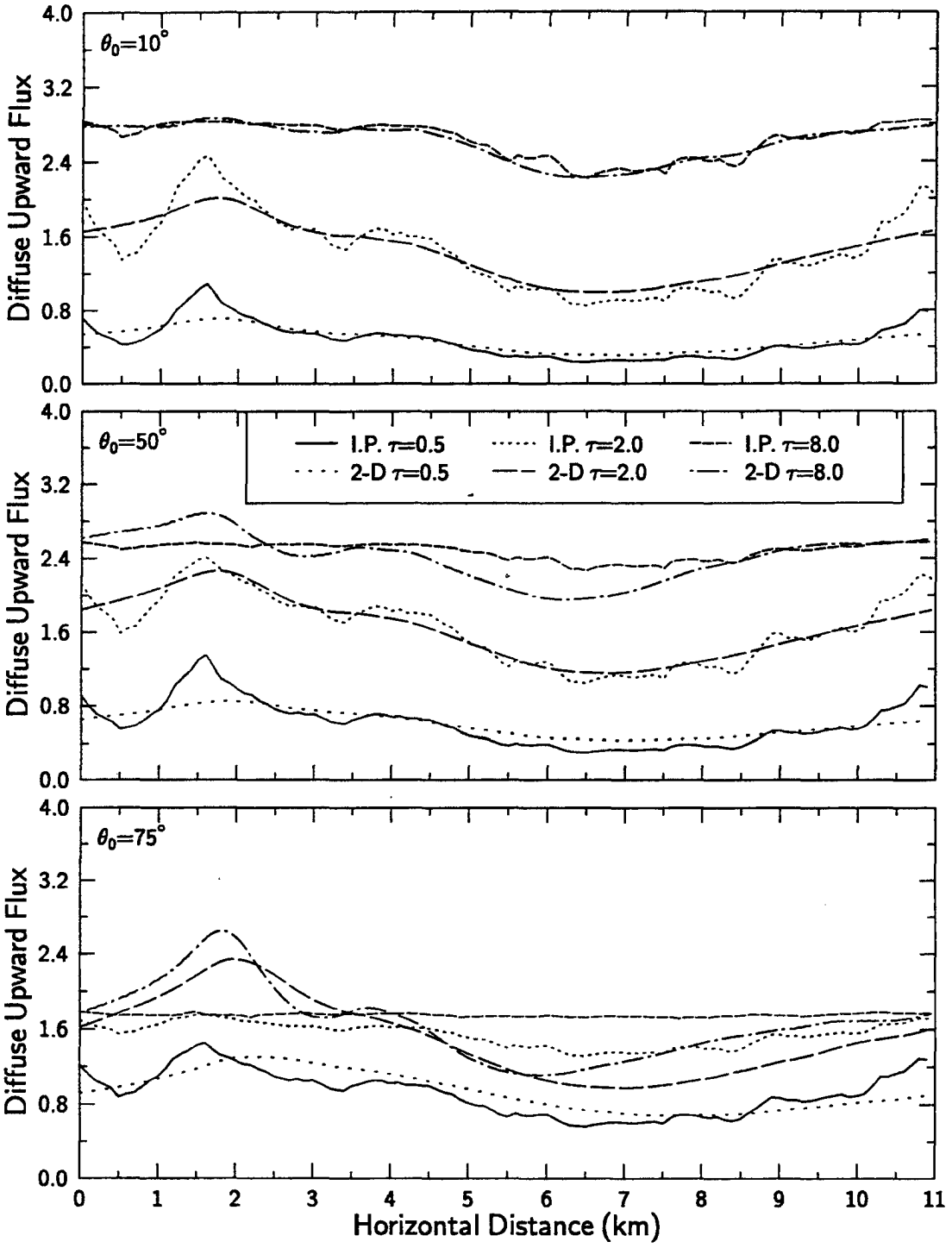

Figure 4.4: Diffuse upward fluxes ($W\,m^{-2}\,ster^{-1}$) at cloud top for $\lambda = 2.21\,\mu m$ as a function of horizontal position for the different solar zenith angles and domain averaged optical depths as indicated for cloud 1.

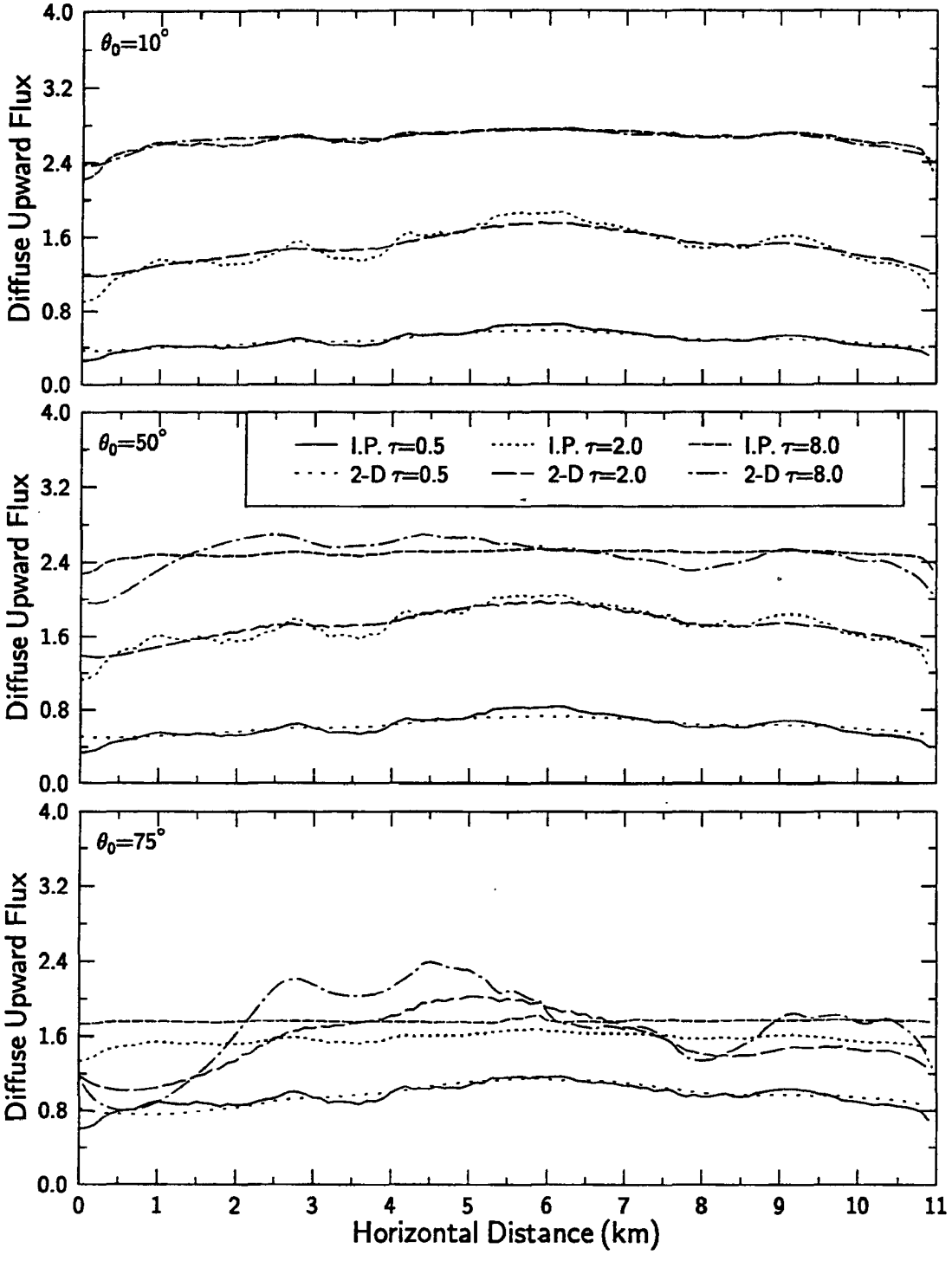

Figure 4.5: Diffuse upward fluxes ($W\,m^{-2}\,ster^{-1}$) at cloud top for $\lambda = 2.21\,\mu m$ as a function of horizontal position for the different solar zenith angles and domain averaged optical depths as indicated for cloud 2.

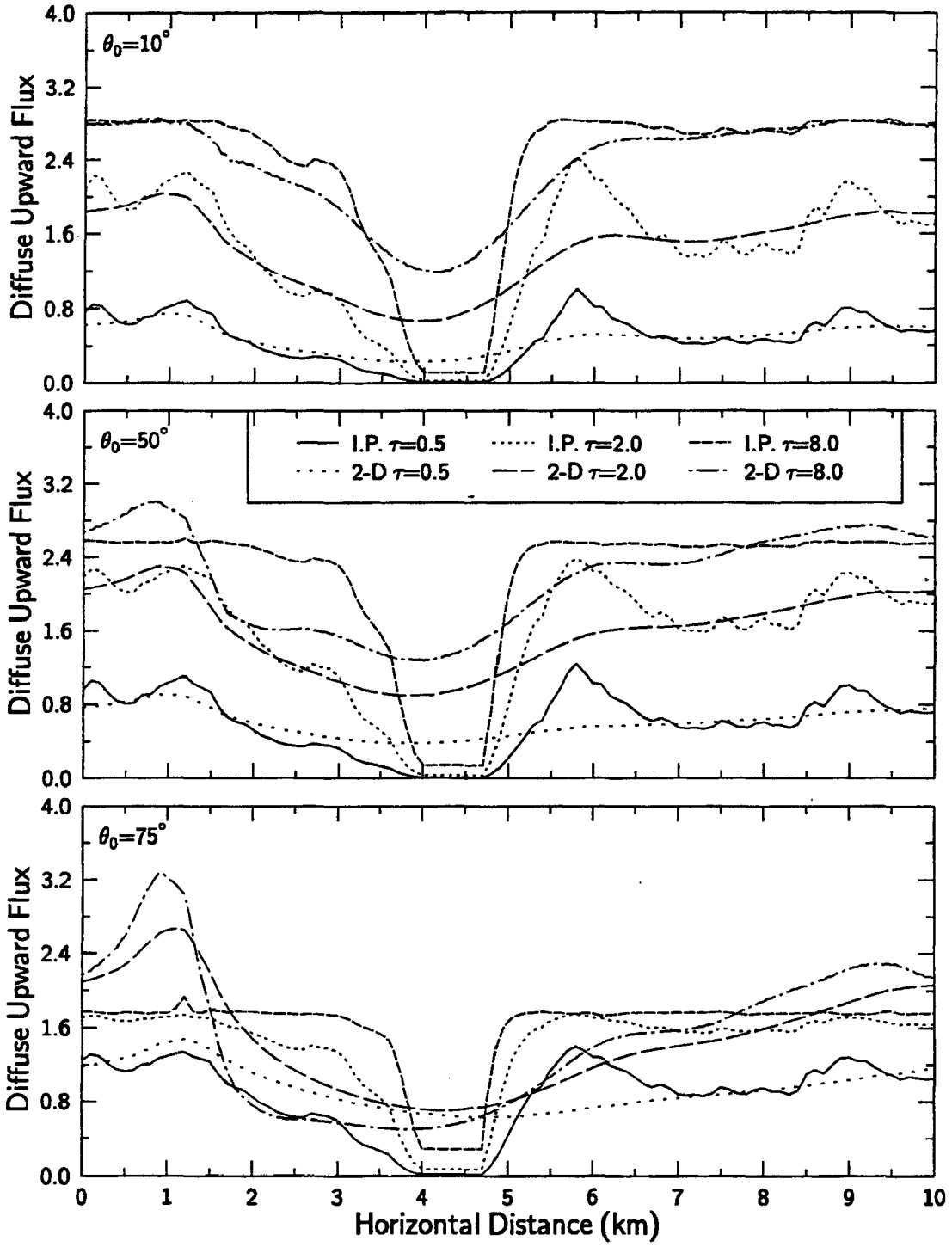

Figure 4.6: Diffuse upward fluxes ($W\,m^{-2}\,ster^{-1}$) at cloud top for $\lambda = 2.21\,\mu m$ as a function of horizontal position for the different solar zenith angles and domain averaged optical depths as indicated for cloud 3.

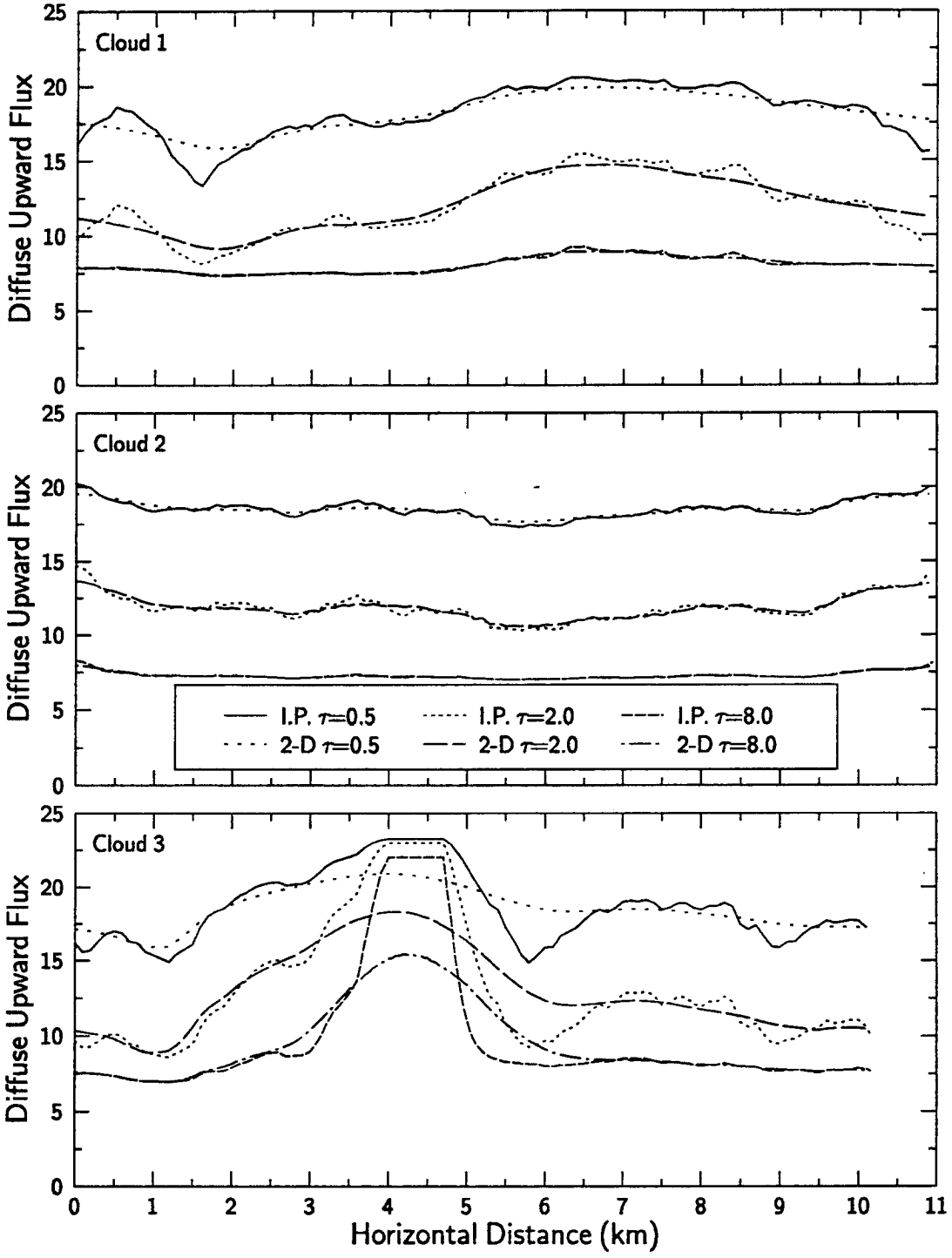

Figure 4.7: Upward fluxes ($W\,m^{-2}\,\mu m^{-1}$) at cloud top for $\lambda = 11.5\,\mu m$ as a function of horizontal position for the three different clouds as indicated.

of the domain averaged column optical depth, $\overline{\tau}$. The figures show the RMS fractional differences for cloud 2 at wavelengths of 0.83 and 2.21 μm. Each diagram consists of three panels containing the differences for diffuse upward flux, diffuse downward flux and total (diffuse + direct) downward flux respectively. Arrows are drawn to indicate the directions of increasing errors. The plots indicate that RMS fractional differences increase as the mean optical depth increases and the solar zenith angle increases. This behavior is common to all the panels of each plot for each wavelength and is observed despite the fact that cloud 2 represents the most horizontally stratified case giving the best agreement between the IPA and 2D calculations. The reason for this is that the longer the path of direct sunlight in the cloud, the more horizontal interactions occur and the worse the IPA performs. The behavior implies that the IPA performs progressively worse than 2D as the sun becomes lower and thus has important implications for studies of clouds at higher latitudes.

Examination of the top panel of Figures 4.8 and 4.9 show that the minimum IPA and 2D diffuse upward flux differences occur at the highest sun and largest optical depth for both wavelengths. This is because most of the energy is reflected near the tops of the optically thick portions of the cloud and the higher sun angles provide less opportunity for horizontal flow and interaction. Note that the minimum difference located at the small solar zenith angles is approximately a factor of two less at 2.21 μm than at 0.83 μm while the maximum difference located at the large solar angles is approximately 30% larger. For the small solar zenith angles (high sun), the increased absorption and forward scattering at 2.21 μm causes the energy to be reflected even closer to cloud top compared to that reflected at 0.83 μm since any radiation that penetrates deeper within the cloud is more likely absorbed and less likely to be reflected backwards. This mechanism might also explain the greater maximum difference at low sun since the energy at a more glancing incidence is more sensitive to the cloud top structure. Another feature that occurs for both wavelengths is a relative maximum fractional difference (just under 11% for 0.83 μm, see Table 4.1) for medium sun (around 50°) and very thin domain averaged optical depth. For the solar zenith angle of 75°, the RMS flux difference at this wavelength was approximately 7%. This feature seems counterintuitive, but increasing the solar zenith angle from 50° for the thinnest clouds enhances the variability of the 2D fluxes relative to that of IPA fluxes such that the standard deviations are virtually identical (see Table 4.1) As a result, the RMS relative differences at 75° are least for optical depths less unity. For optical depths greater than unity the RMS relative differences are always greatest at the solar zenith angle of 75° and decrease as the solar zenith angle decreases. Thus, domain average optical depths just less than unity may represent a type of transition from one type of regime where increasing the solar zenith angle leads to a decreasing relative error of the IPA to a regime where increasing the solar zenith angles lead to a increase in relative error of the IPA.

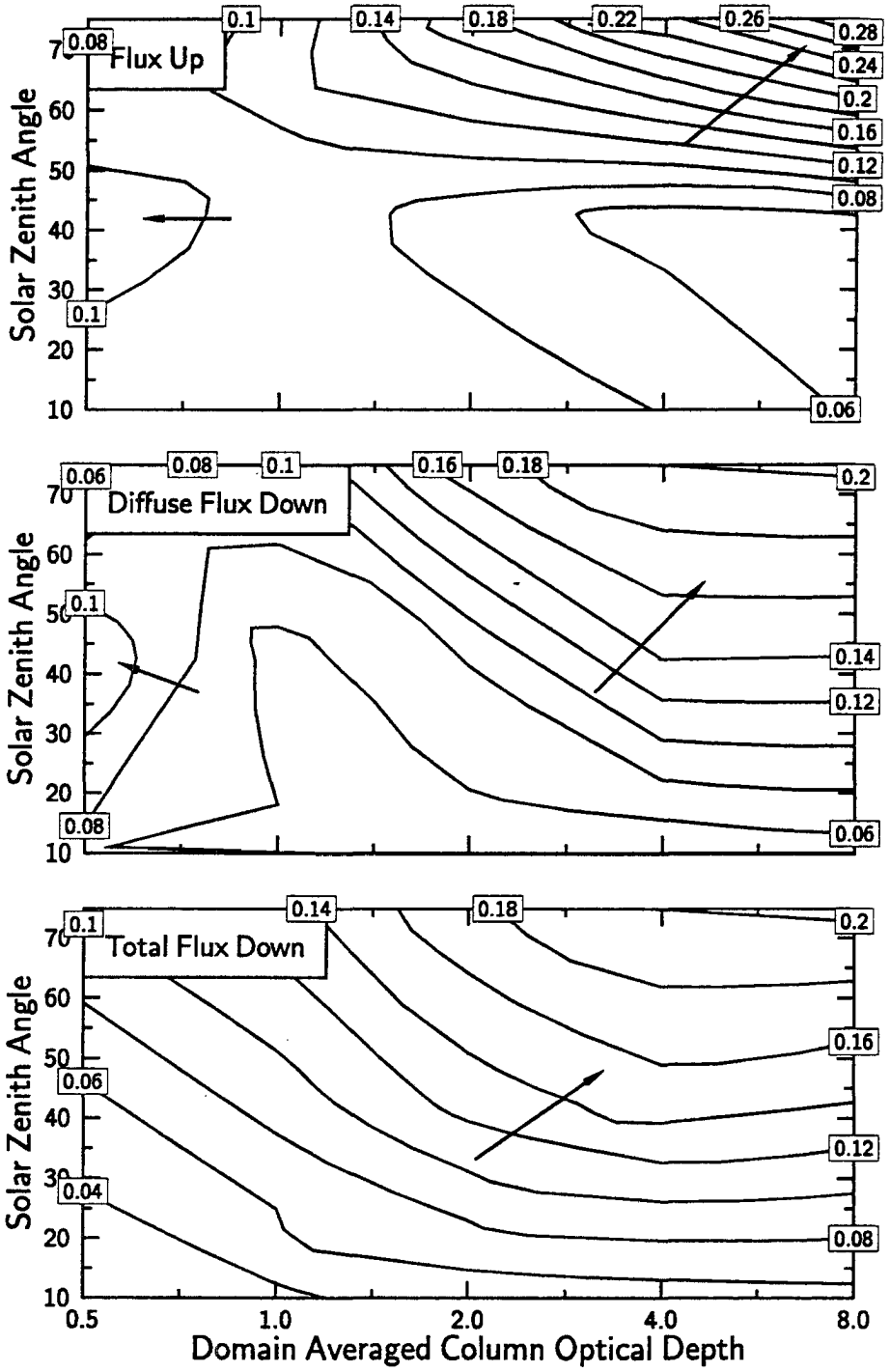

Figure 4.8: RMS fractional differences between 2D and IPA diffuse flux up at cloud top, diffuse flux down at cloud base and total flux down at cloud base for cloud 2 at $\lambda = 0.83\,\mu m$.

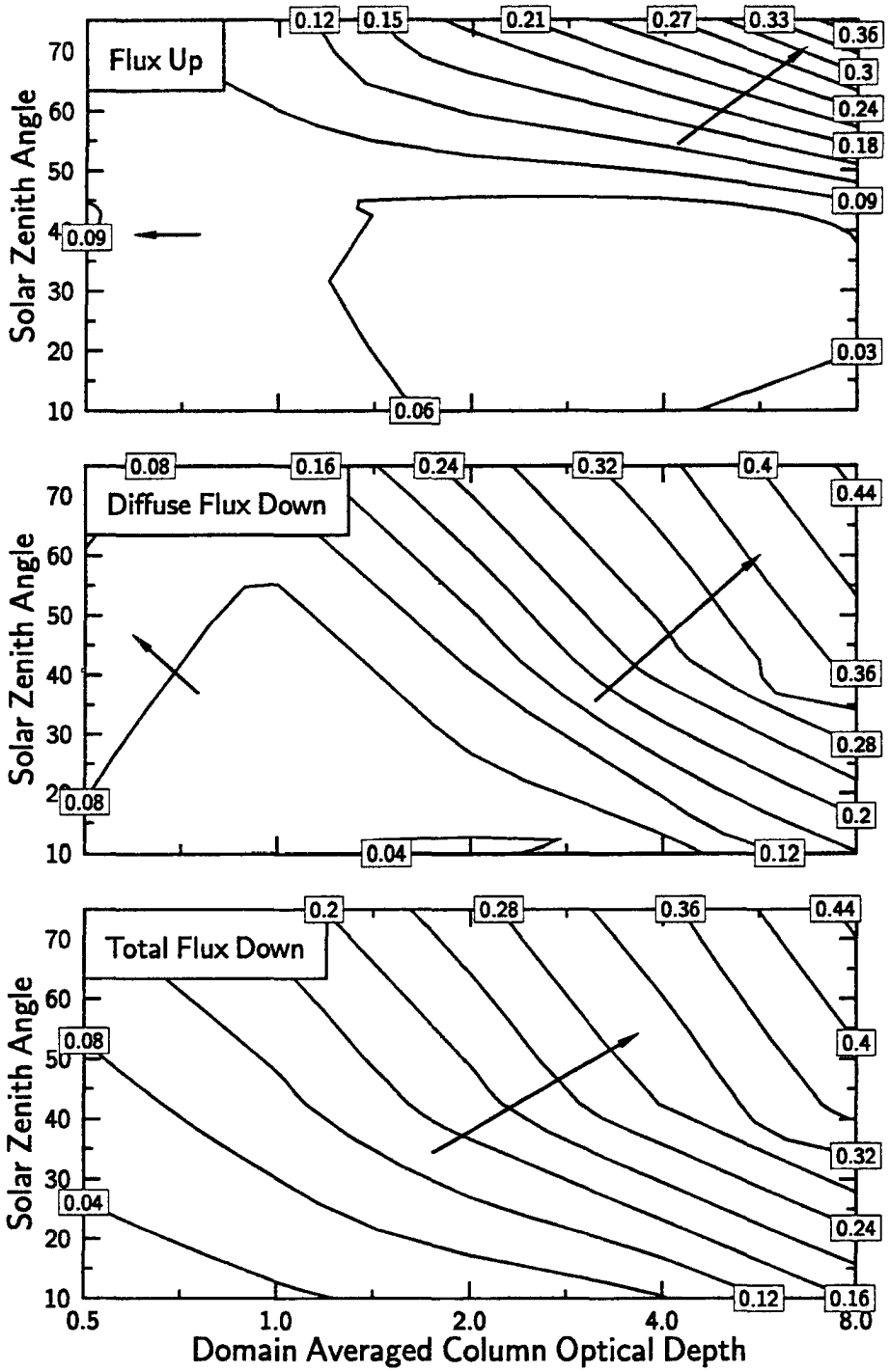

Figure 4.9: RMS fractional differences between 2D and IPA diffuse flux up at cloud top, diffuse flux down at cloud base and total flux down at cloud base for cloud 2 at $\lambda = 2.21\ \mu m$.

Table 4.1: Domain averaged mean fluxes, standard deviations and RMS relative differences for 2D and IPA diffuse upward fluxes at $\lambda = 0.83\mu m$ for cloud 2 with domain optical thickness of 0.5.

Solar Angle (deg)	2D Mean $W \cdot m^{-2}$	2D Standard $W \cdot m^{-2}$	IPA Mean $W \cdot m^{-2}$	IPA Standard $W \cdot m^{-2}$	RMS Relative Difference (%)
10.0	5.16	0.72	5.15	1.09	9.22
50.0	7.03	0.81	7.03	1.44	10.81
75.0	10.18	1.35	10.12	1.40	7.64

Figures 4.8 and 4.9 also show the RMS differences between 2D and IPA downward diffuse and total fluxes. For the downward diffuse fluxes there seems to be two scenarios which give better agreement. The first is for thin clouds at large solar zenith angles and the second for intermediate cloud thickness with small solar zenith angles. The former scenario is peculiar and represents only a relative minimum that is similar to the relative minimum in the diffuse upward fluxes at large solar zenith angles and thin clouds. The agreement between 2D and IPA here is about 5% for both wavelengths. As above, this relative minimum corresponds to a location where the standard deviations of 2D and IPA diffuse downward flux are virtually identical. However, the cloud must be thin enough that the cloud structure does not significantly affect the 2D downward diffuse fluxes relative to the IPA fluxes. As the optical depth of the cloud itself increases, the agreement worsens by factors of 4 and 8 for $0.83\,\mu m$ and $2.21\,\mu m$ respectively (see upper right hand corner of plots). Interestingly, the relative errors in the direct downward flux (not shown) are so large for low sun that the relatively good agreement of the diffuse downward fluxes is overwhelmed in the computation of the total downward flux. The best agreements between 2D and IPA calculations for the total downward flux occur at high sun angles and thin clouds where horizontal interaction is minimized and a localized cloud column dominates the determination of the transmitted fluxes.

Figures 4.10 and 4.11 show the RMS differences between 2D and IPA for cloud 3. A cursory comparison of these figures to Figures 4.8 and 4.9 show how greatly the broken cloud causes a breakdown of the plane-parallel theory. For $0.83\,\mu m$, the maximum error exceeds 55%, 110% and 200% for the upward diffuse, downward diffuse, and downward total fluxes respectively for the thickest cloud and lowest sun. The minimum relative differences are in the 20-30% range. Note that despite the large physical difference between these two clouds, the contours show the same type of features that were observed to occur for the stratified cloud. Also the maximum relative differences at $2.21\,\mu m$ are greater than those at $0.83\,\mu m$ as observed for cloud 2.

The relative RMS differences for all three clouds in the infrared window channel of $11.5\ \mu m$ are presented in Figure 4.12 for both the upward and downward flux at cloud top and base respectively. The figure indicates that cloud 2 gives the best agreement between

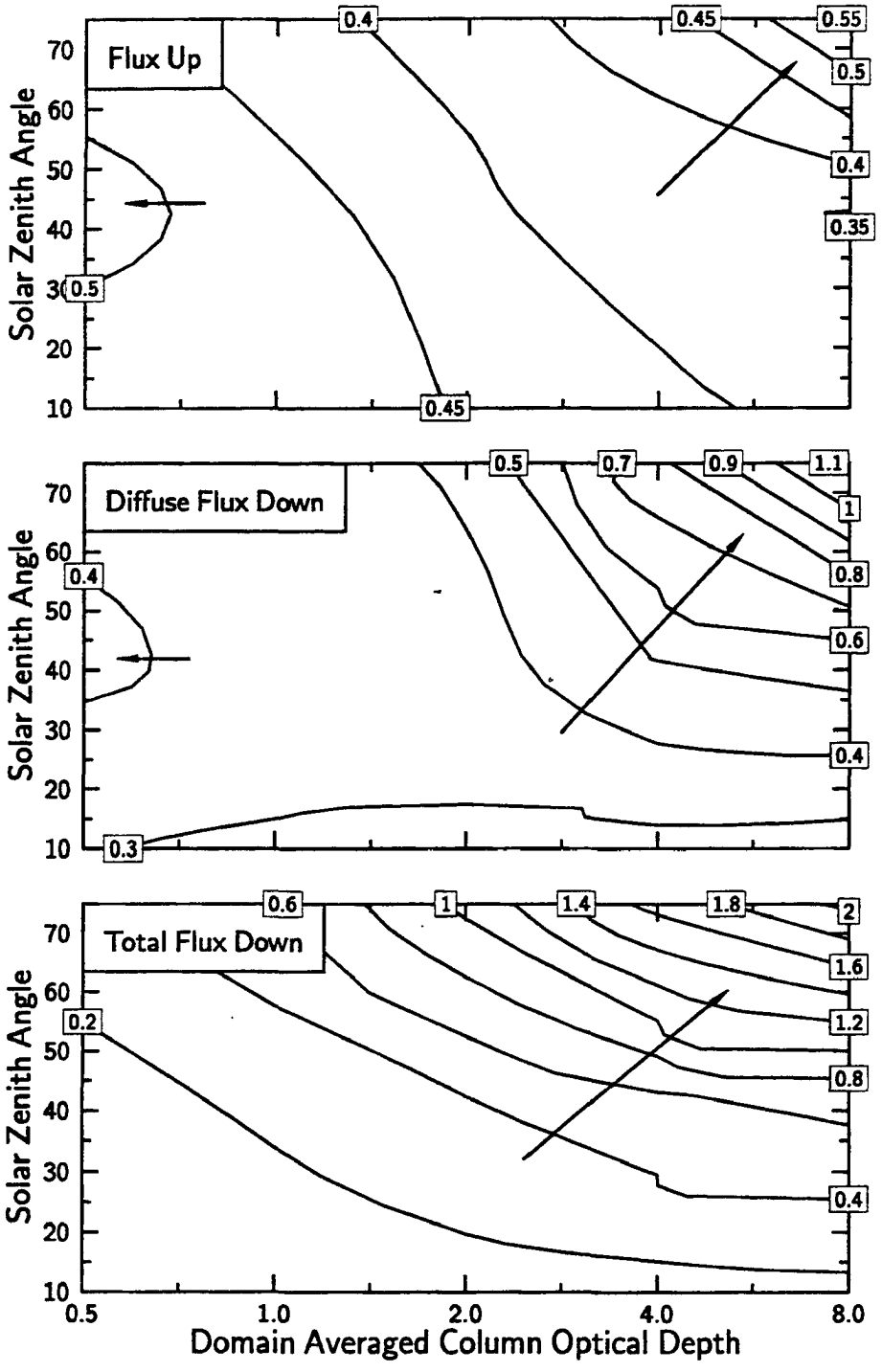

Figure 4.10: RMS fractional differences between 2D and IPA diffuse flux up at cloud top, diffuse flux down at cloud base and total flux down at cloud base for cloud 3 at $\lambda = 0.83\,\mu m$.

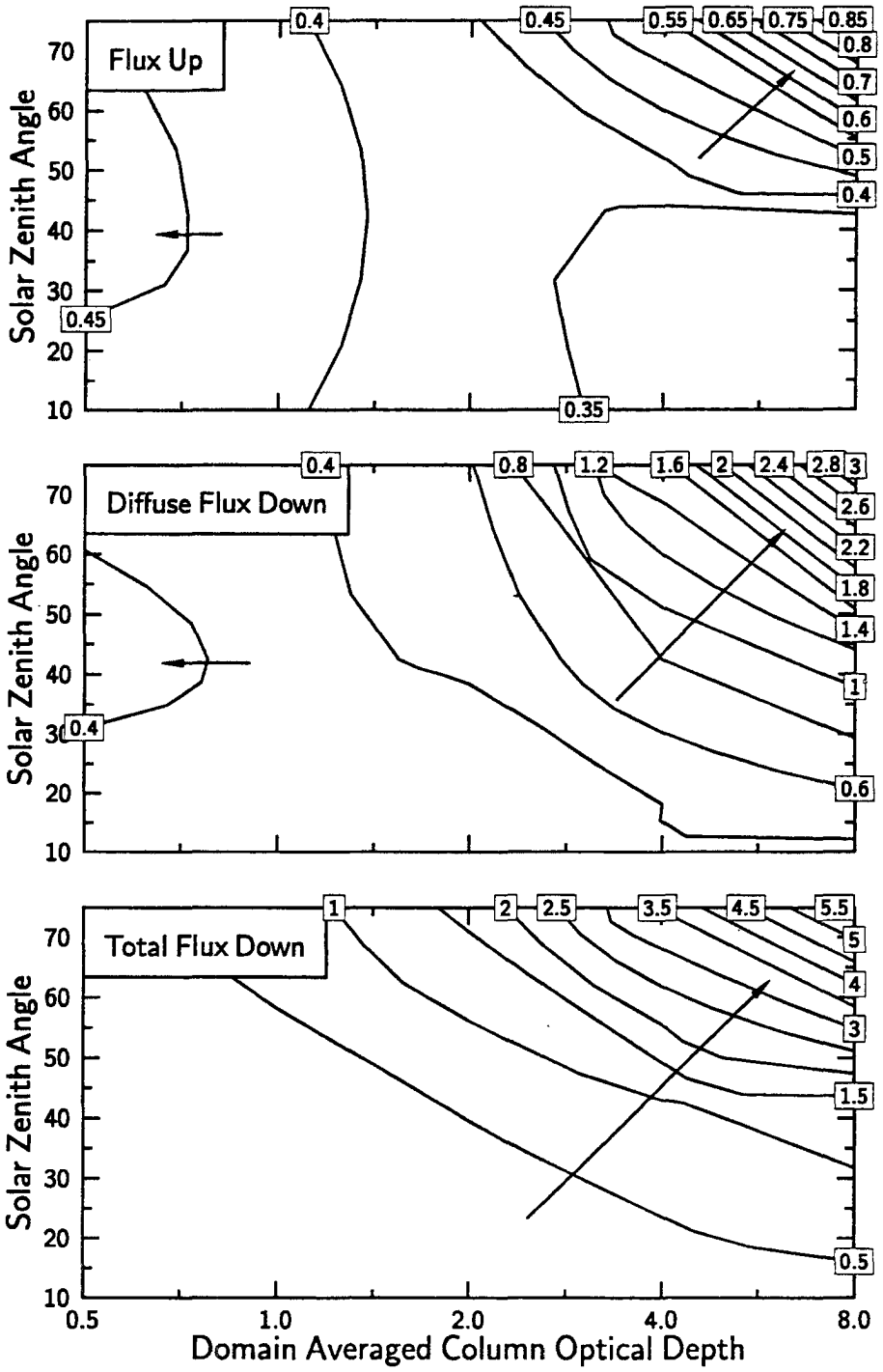

Figure 4.11: RMS fractional differences between 2D and IPA diffuse flux up at cloud top, diffuse flux down at cloud base and total flux down at cloud base for cloud 3 at $\lambda = 2.21\,\mu m$.

2D and IPA for the upward flux followed by cloud 1 and then cloud 3. Both cloud 1 and cloud 2 have the largest RMS differences at an optical depth of unity while the differences in the broken cloud show no such behavior. Note that the relative differences decrease with increasing optical depth for the 100% cloud fraction cases (i.e., clouds 1 and 2), but the reverse is true for the broken cloud. This is probably due to the fact that the emission of the cloud sides increases with increasing optical depth. This increased emission increases the difference between 2D and IPA fluxes. For the downward flux at cloud base, the RMS relative differences decrease with increasing optical depth for all three clouds. For optical depths less than 4.0, the RMS differences are lowest for cloud 2, but are slightly larger than cloud 1 for the largest optical depth. However, at the largest optical depth the differences of both clouds are only about 1%. The magnitudes of these differences are equivalent in magnitude to the differences seen in the solar wavelengths under high sun conditions.

2D vs. IPA Flux Distributions

A more complete picture of the differences between the 2D and IPA fluxes is seen in Figures 4.13, 4.14, and 4.15 which present the 2D and IPA fluxes in terms of the column optical depth of the cloud field from all five of the domain average cases i.e., 0.5, 1.0, 2.0, 4.0 and 8.0. The figures present the flux up, diffuse flux down, and total (direct+diffuse) flux down at the cloud boundaries for all three clouds at 0.83 μm. The IPA fluxes have a nonlinear functional dependence on optical depth (since we have assumed constant effective radius) which is clearly shown by the solid shapes in the figures. The 2D fluxes reveal how the horizontal interaction of radiation within the cloud act to change this relationship. The spread of the 2D fluxes about the IPA fluxes for the stratified cloud (Fig. 4.14), as indicated by the corresponding RMS fractional difference values given in the figures, is much tighter than that for both the cirrus uncinus (Fig. 4.13) and the broken cloud (Fig. 4.15). However, even for this case some of the upward fluxes at the low sun angle show $\pm 50\%$ differences with the IPA fluxes at a given column optical depth. The influence of the extra dimension in the radiative transfer breaks down the one-to-one correspondence between the optical depth and the corresponding fluxes of plane-parallel theory. The extent to which this relationship is violated at this wavelength is dependent upon the cloud structure as shown by comparing the distributions of the fluxes for the three clouds.

Unlike the fluxes of the stratified clouds, the IPA fluxes for both the cirrus uncinus case and the broken cloud case appear to develop biases relative to the 2D fluxes (compare Figs. 4.13 and 4.15). This behavior is more clearly illustrated in Figure 4.16 which shows relationship between fluxes and the column optical depths for cloud 1 with $\overline{\tau} = 8.0$. Interestingly, for large column optical depths (in this instance greater than 12) upward fluxes at the small solar zenith angle are overestimated by IPA while those at the large solar zenith angle are underestimated. This type of behavior is observed to varying degrees

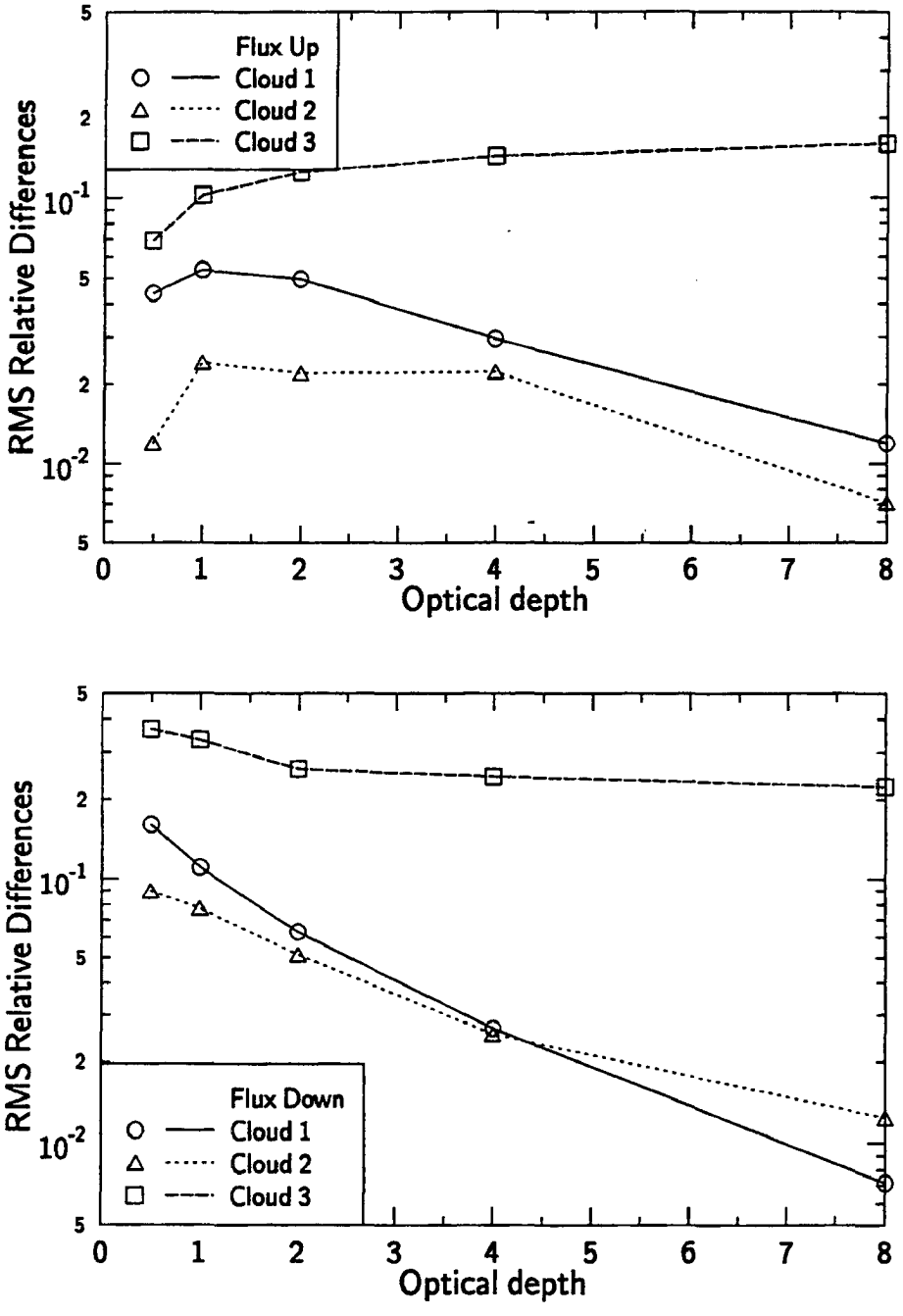

Figure 4.12: RMS fractional differences between 2D and IPA flux up at cloud top and flux down at cloud base for clouds 1, 2 and 3 (as indicated) at $\lambda = 11.5\,\mu m$.

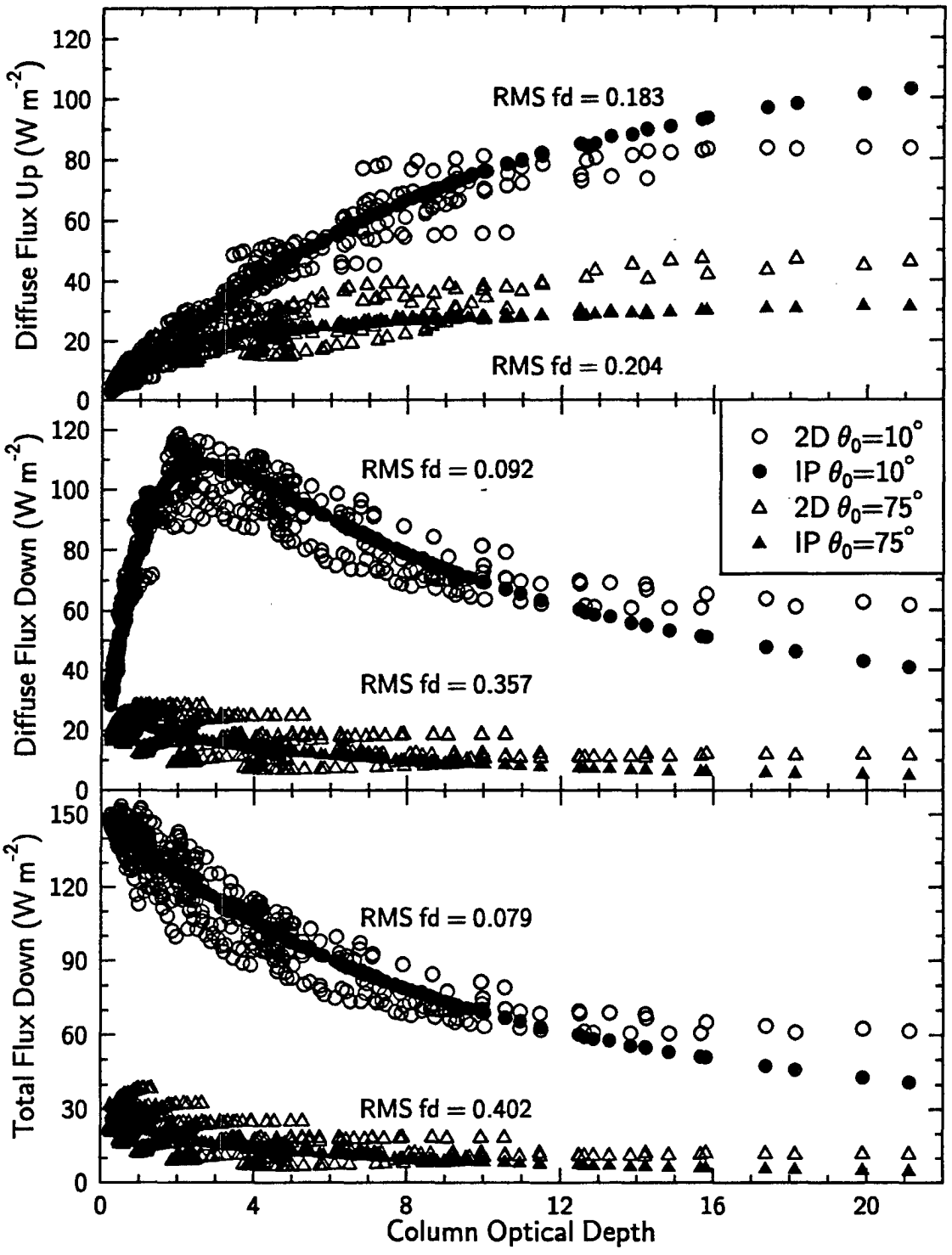

Figure 4.13: The distribution of diffuse upward, diffuse downward, and direct downward fluxes as a function of column optical depth for cloud 1 and $\lambda = 0.83\ \mu m$. Solid shapes represent IPA fluxes and hollow shapes represent 2D fluxes for solar zenith angles 10° and 75° as shown. The RMS fractional difference values are indicated.

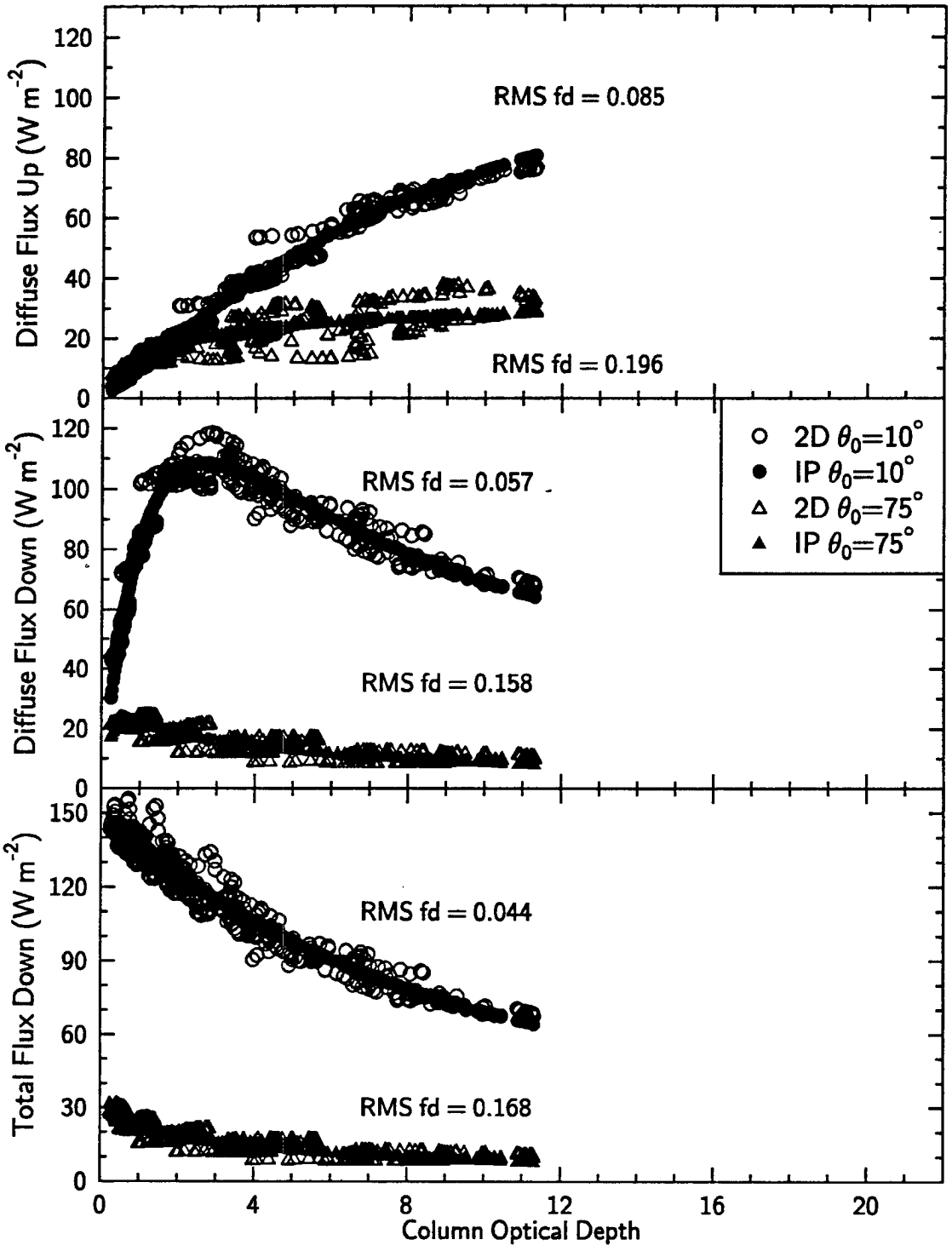

Figure 4.14: The distribution of diffuse upward, diffuse downward, and direct downward fluxes as a function of column optical depth for cloud 2 and $\lambda = 0.83\ \mu m$. Solid shapes represent IPA fluxes and hollow shapes represent 2D fluxes for solar zenith angles 10° and 75° as shown. The RMS fractional difference values are indicated.

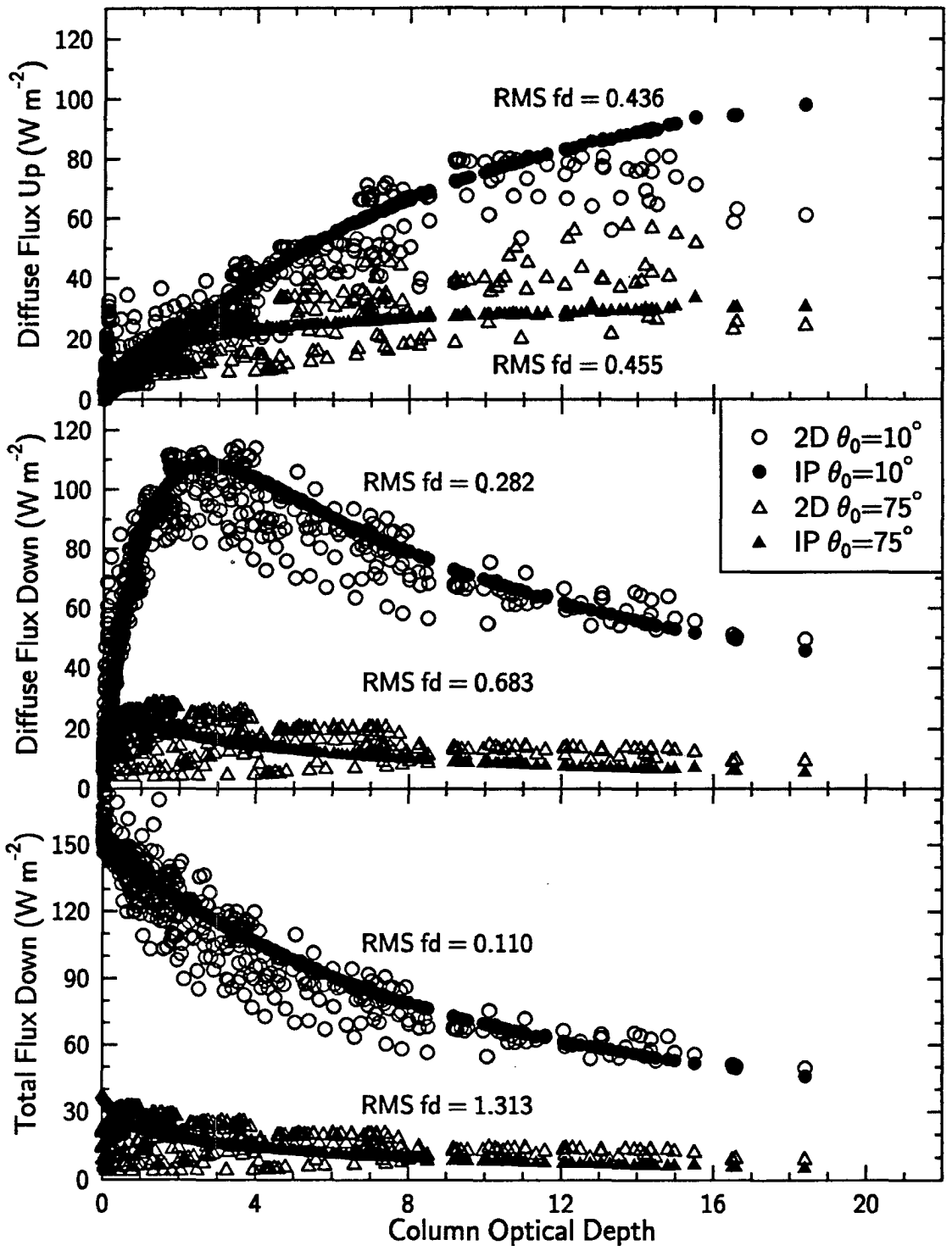

Figure 4.15: The distribution of diffuse upward, diffuse downward, and direct downward fluxes as a function of column optical depth for cloud 3 and $\lambda = 0.83\ \mu m$. Solid shapes represent IPA fluxes and hollow shapes represent 2D fluxes for solar zenith angles 10° and 75° as shown. The RMS fractional difference values are indicated.

for each different domain averaged optical depth case for clouds 1 and 3 and is mostly responsible for the spread of data observed in Figs. 4.13, 4.14, and 4.15. These clouds, unlike the stratified cloud, have generating cells which have optical depth maximums more than factors of 2 greater than the surrounding columns (refer back to Fig. 3.3). In two dimensions at a high sun angle, the horizontal interaction of radiation allows the energy which normally is reflected upward inside the thick column in plane-parallel theory to be scattered aside to a thinner column. This reduces the flux reflected upward and increases the flux transmitted through the cloud relative to IPA. At large solar zenith angles and optical depths, the incident solar radiation encounters areas of enhanced extinction such that more radiation is reflected by these areas upward than plane-parallel would predict. This depends upon the orientation of these optically thick areas relative to the incident radiation and represents a type of "cloud shadowing" effect similar to that described for radiances in Chapter 3.

These processes are illustrated schematically in Figure 4.17a and b which represent the clouds in terms of shaded columns for small (part A) and large (part B) solar zenith angles respectively. The shading represents the optical depth of the column such that the darker the shading the larger the optical depth or density. The left two boxes of parts A and B represent the case of the stratified cloud for IPA and 2D fluxes respectively. The right two boxes of parts A and B represent the case where a column of large optical depth is surrounded by two columns of much smaller optical depth. The vertical boundaries of the IPA flux cases are thickened to represent the prevention of the horizontal flow of radiation. All the energy incident to the column in these IPA cases is either reflected or transmitted (assuming no absorption). In the 2D cases, the horizontal flow of radiation is permitted and the internal arrows designate the net flow across the boundary. The relative thickness of the arrows represent the magnitude of the flow of radiation across the horizontal and vertical cloud column boundaries. Comparison of the IPA and 2D fluxes for the two right most boxes in Figure 4.17a shows a net divergence of energy out of the thick cloud column near cloud top compared to plane-parallel theory. For large solar zenith angles, the IPA and 2D fluxes for the two right most boxes in Figure 4.17b show a net convergence near cloud top for both the thick cloud column and the thin cloud column to the sun side. This convergence occurs as horizontally propagating radiation interacts with the thick cloud column. This is the mechanism responsible for differences between the 2D and IPA fluxes shown in Figure 4.16.

For upward fluxes with optical depths less than the domain averaged optical depth (refer again to Fig. 4.16), these relationships for clouds 1 and 3 are slightly reversed such that IPA underestimates the flux at the small solar zenith angle and overestimates the upward flux at the large zenith angle. At small solar zenith angles, this effect is caused by the scattering of radiation off optically thick areas (or off the sides of the clouds in cloud 3) which results in fluxes at the top of the domain in pixels where there is very little extinction

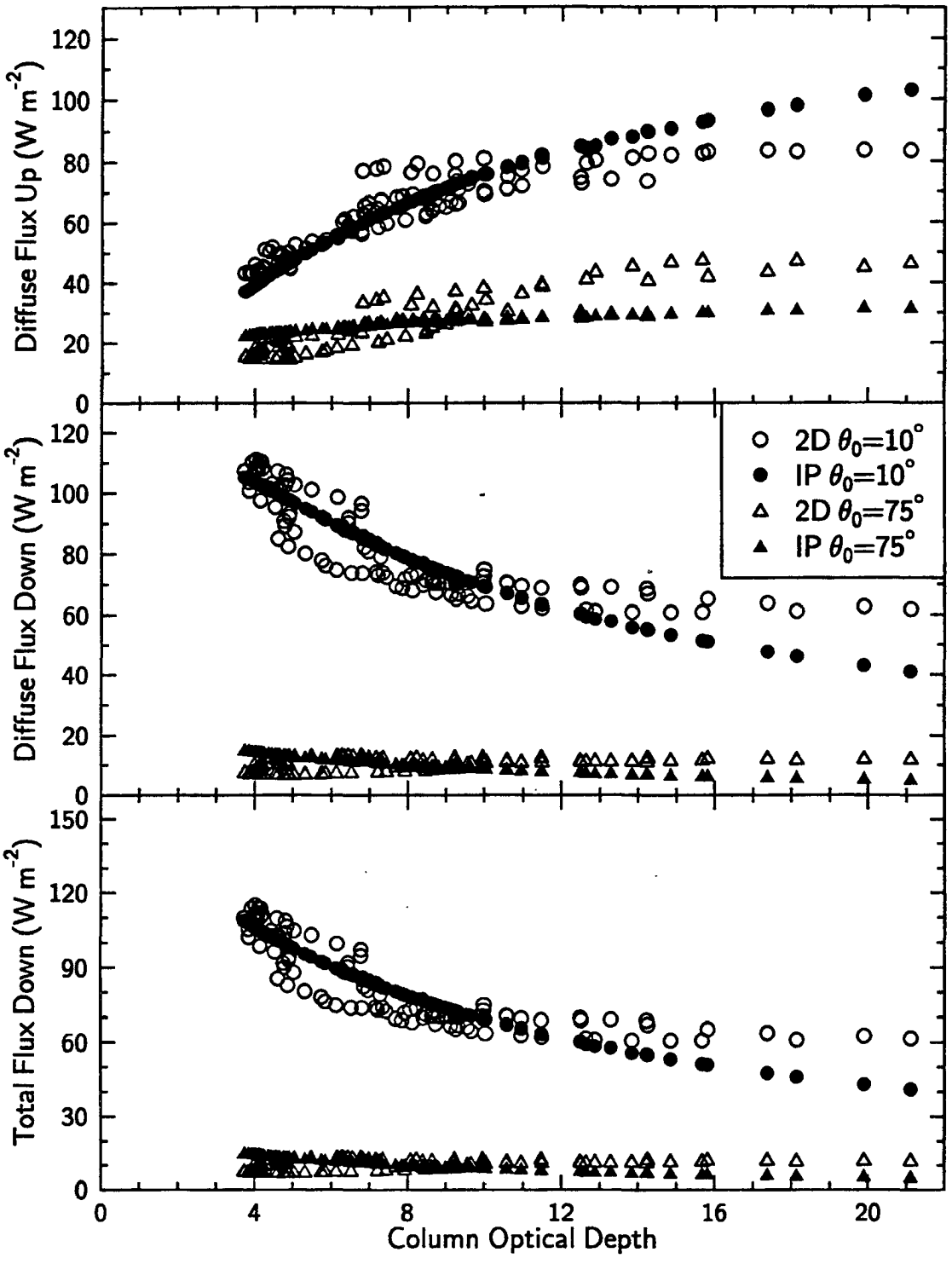

Figure 4.16: The distribution of diffuse upward, diffuse downward, and direct downward fluxes as a function of column optical depth for cloud 1 $\overline{\tau} = 8.0$ and $\lambda = 0.83\ \mu m$. Solid shapes represent IPA fluxes and hollow shapes represent 2D fluxes for solar zenith angles 10° and 75° as shown.

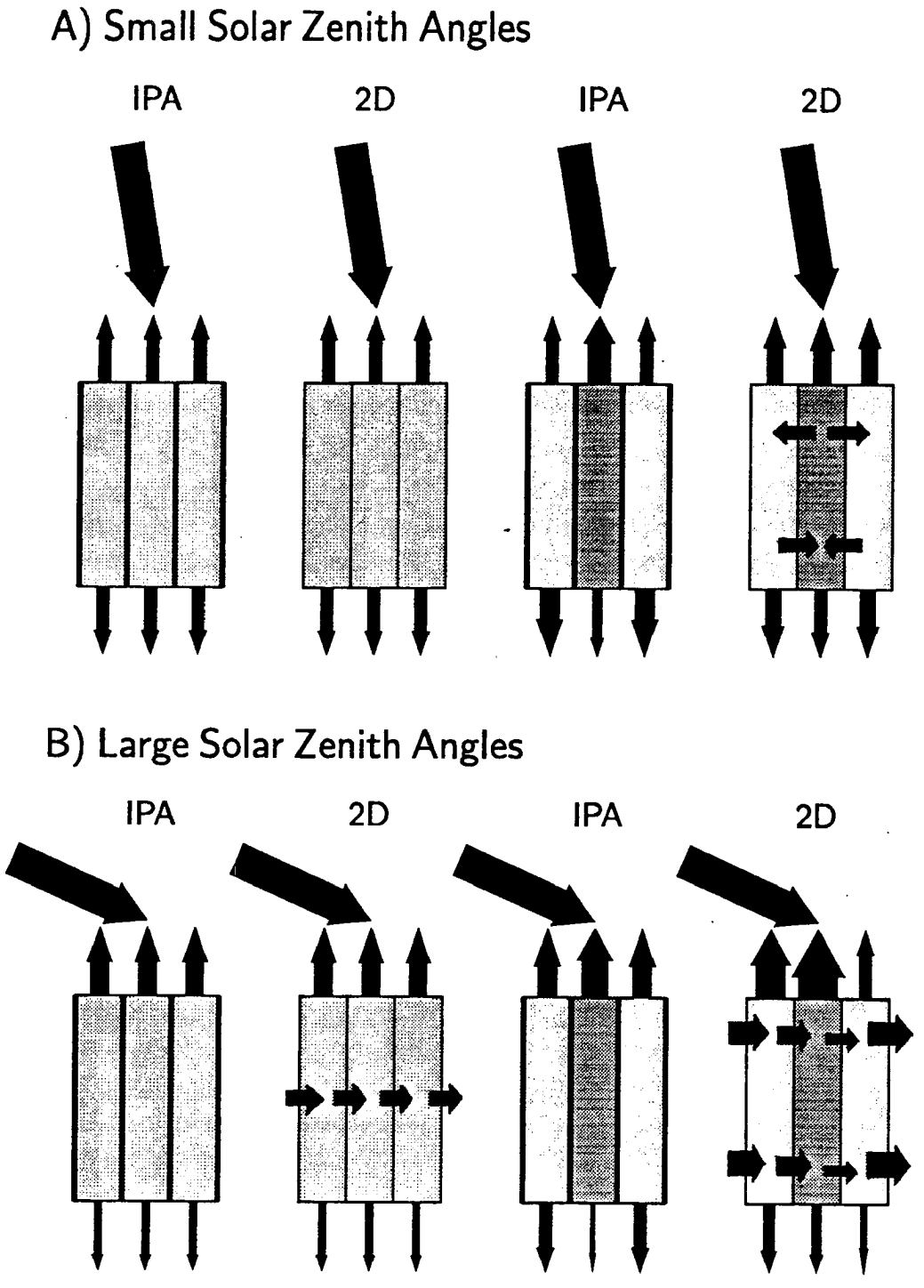

Figure 4.17: A schematic illustration depicting the difference between plane-parallel and two-dimensional radiative transfer for a) high and b) low sun situations with each column representing a physical cloud element and arrows the flow of net radiation. The thickness of the arrows represents qualitatively the relative amounts of radiation entering and escaping the cloud columns.

(Fig. 4.17a). At the larger solar zenith angles, the fluxes over regions of minimal optical depth, such as the cloud breaks of cloud 3, are depressed because the incident radiation tends to propagate horizontally until it encounters the large areas of extinction as noted above and illustrated in Fig. 4.17b. This behavior for columns of optical depths less than the domain average optical depth acts to compensate for the errors produced by the IPA at larger optical depths. The extent to which this compensation occurs determines the agreement between IPA and 2D fluxes over the domain average which is the subject of a later section. Close examination of the upward fluxes in Fig. 4.14 reveals similar behavior but to a much lesser extent making the independent pixel calculations a good approximation to the 2D fluxes for this stratified cloud.

The diffuse and total downward fluxes also reveal the effect of horizontal structure. The tendency at high sun for the IPA to overestimate 2D upward fluxes at large optical depths and underestimate 2D fluxes at smaller optical depths corresponds to the exact opposite differences for the downward fluxes (see Fig. 4.16). The reason for this can also be explained by referring to Fig. 4.17a. Although energy is effectively scattered out of the optically thick column at the top, scattering near the base of the column allows for some energy to be scattered back into the column and then downward as depicted by the figure. It is interesting to note that although the high sun angle upward and downward 2D and IPA flux differences complement in this way, the low sun differences do not. In this case, energy is propagating horizontally until it reaches the area of large optical depth. The larger optical depth in this region provides more opportunity for scattering in the upward and downward directions (see Fig. 4.17b). Thus, both the upward and downward 2D fluxes are underestimated by IPA. This has some important implications on the local conservation of energy which are explored in the next section. As noted in the case of the upward fluxes, Figures 4.13 and 4.15 show downward 2D flux distributions which appear to be centered about the IPA fluxes. This is especially true for fluxes in columns with optical depths less than about 10. Further examination for fluxes with optical depths less than about 4 reveals that IPA underestimations of diffuse downward flux are compensated by overestimations of direct flux (not shown) and vice versa such that the total downward fluxes for the 2D and IPA agree well. This compensation decreases for optical depths greater than about 5 as the direct fluxes decrease to zero explaining why the diffuse and total downward flux distributions for optical depths greater than 5 are virtually identical. These results also indicate that the direct and diffuse downwelling radiation as predicted by IPA differ significantly from 2D theory.

For the case where there is weak absorption (2.21 μm), the spread of the 2D fluxes about the IPA fluxes was much greater in all cases except for the upward fluxes at the smallest solar zenith angle. This is shown by the flux distributions of cloud 3 shown in Figure 4.18 and the RMS fractional differences indicated. At the largest solar zenith angle, the RMS values were the highest and the range of 2D fluxes a factor of ± 2 from the IPA

fluxes. Presumably this is because radiation incident at low sun angles is more likely to be propagated horizontally since the asymmetry factor is slightly higher than the visible case and is, therefore, more easily absorbed by the cloud. The combination of the increased forward scatter and the absorption cause the larger fluctuations from the IPA fluxes and as a result the relative errors of the IPA are larger at this wavelength. Note that at the smallest solar zenith angle, the high bias of the IPA upward fluxes and low bias of the downward diffuse IPA fluxes is also observed as for the case of 0.83 μm even though the fractional differences of IPA from 2D are less.

The flux distributions in the window channel (11.5 μm) are shown for cloud 3 in Figure 4.19. The IPA upward and downward fluxes for this case have smaller RMS fractional differences from 2D than for the same cloud at the other two wavelengths which is found for the other two clouds as well. Thus, the IPA is a better approximation to the 2D fluxes at this wavelength than at the solar wavelengths. However, there are still substantial differences between 2D and IPA at certain locations, especially in the upward fluxes for the optically thick broken cloud as shown in Fig. 4.19. The fractional RMS differences between 2D and IPA fluxes for this case are 44% and 68% for upward and downward fluxes respectively. These differences are ten times as large as for cloud 2 (not shown), but still not as high as the differences found in the solar wavelengths.

Albedos, Transmittances and Absorptances

The pixel by pixel differences between the 2D and IPA upward and downward fluxes at the cloud boundaries have a profound effect on the cloud albedo (α), transmittance (T) and absorptance (a). These three quantities are typically used to describe the radiative properties of clouds and are defined here as

$$\alpha = \frac{F^{\uparrow}_{\text{top}}}{F^{\downarrow}_{\text{top}}},$$

$$T = \frac{F^{\downarrow}_{\text{bot}}}{F^{\downarrow}_{\text{top}}},$$

and

$$a = 1 - \alpha - T$$

where F is the total flux flowing in the indicated direction at cloud top or cloud bottom. Note that these quantities are normalized using the incident flux relative to a horizontal surface which is typically done for plane-parallel clouds. The effects of this assumption are demonstrated upon interpretation of the 2D albedos, transmittances, and absorption. Figures 4.20 and 4.21 show these quantities at 0.83 μm for clouds 2 and 3 respectively. Each figure displays the variation of 2D and IPA albedos, transmittances, and absorptions for the thinnest and thickest clouds and for solar zenith angles of 10°, 50°, and 75°. Note

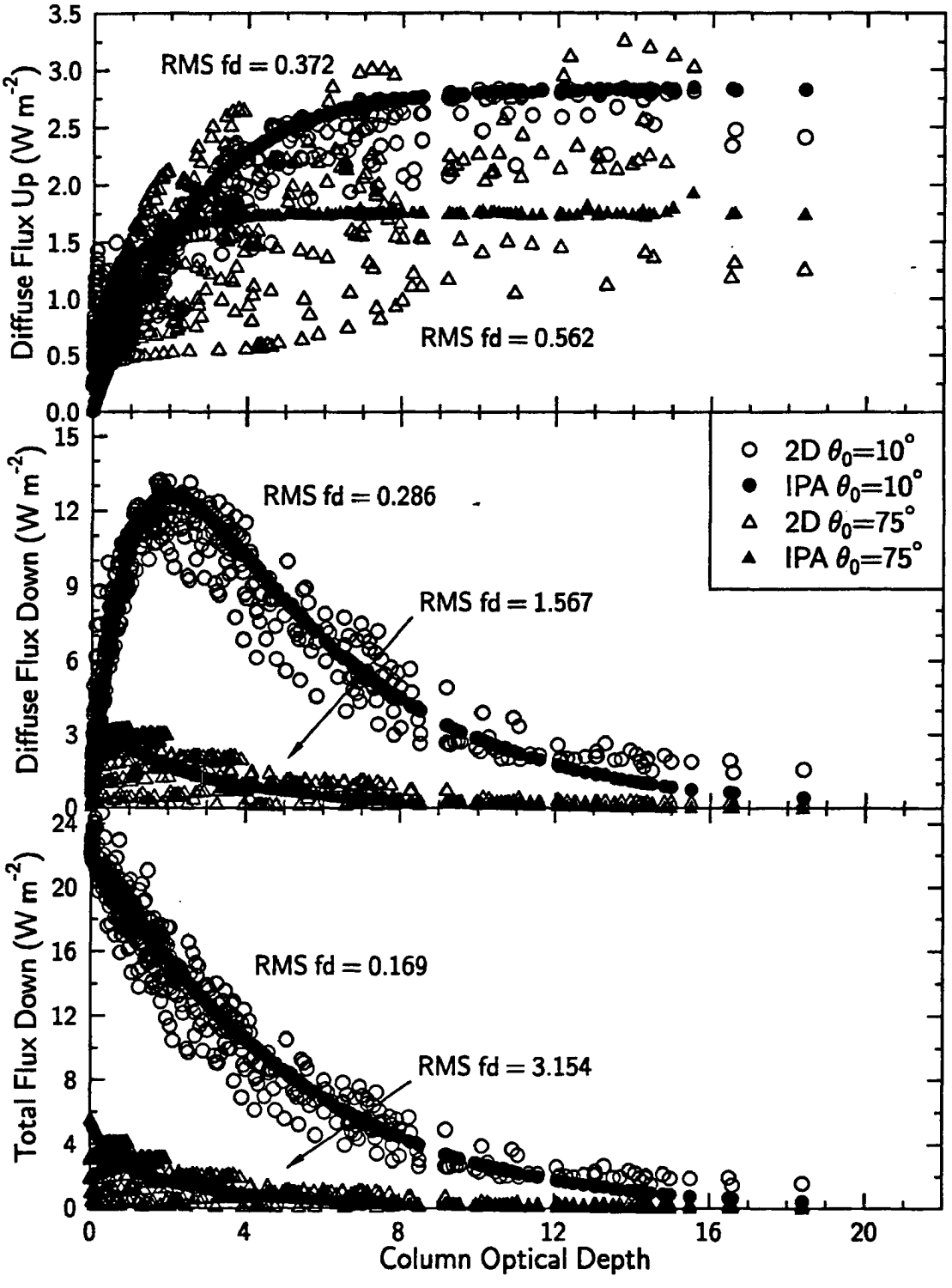

Figure 4.18: The distribution of diffuse upward, diffuse downward, and direct downward fluxes as a function of column optical depth for cloud 3 and $\lambda = 2.21\ \mu m$. Solid shapes represent IPA fluxes and hollow shapes represent 2D fluxes for solar zenith angles 10° and 75° as shown. The RMS fractional difference values are indicated.

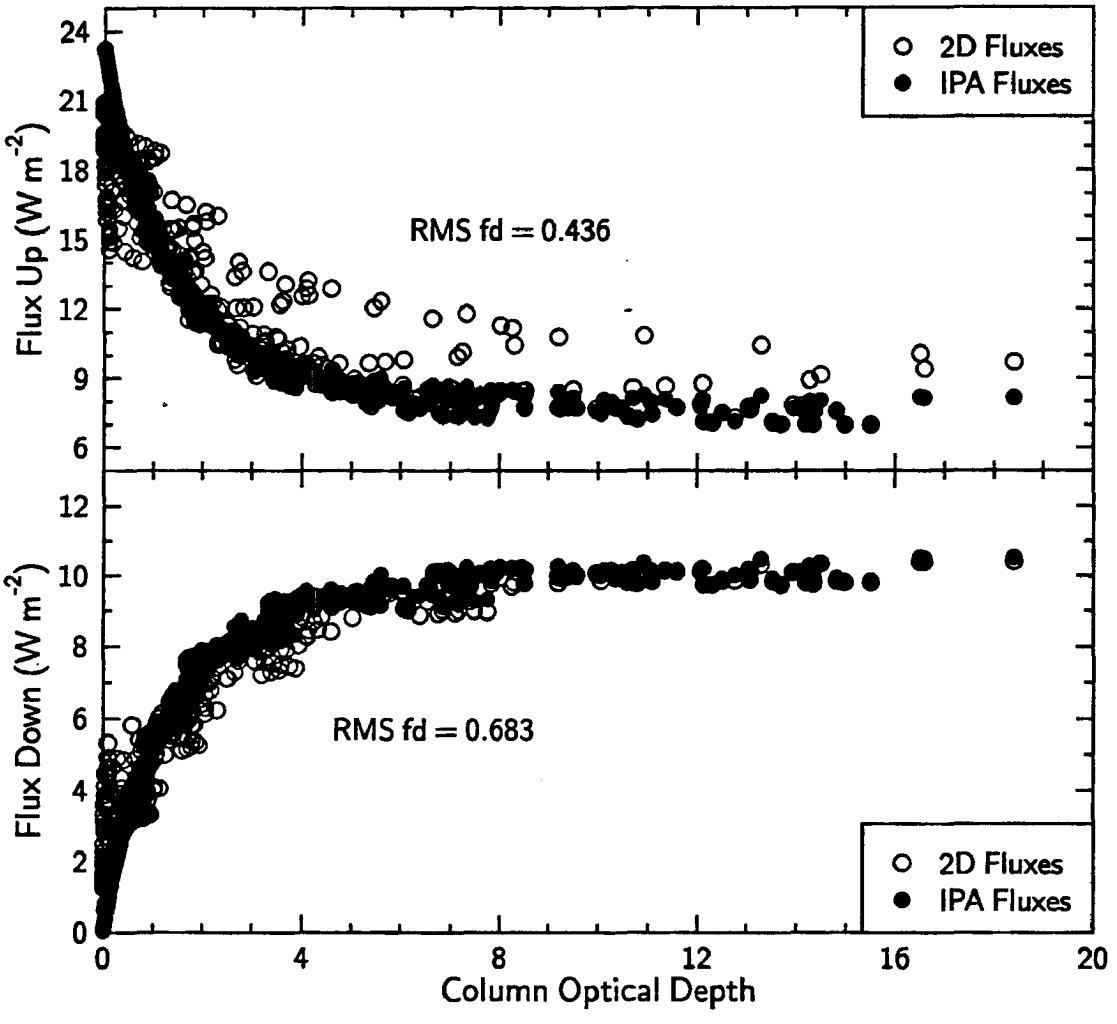

Figure 4.19: The distribution of upward and downward fluxes as a function of column optical depth for cloud 3 and $\lambda = 11.5\ \mu m$. Solid shapes represent IPA fluxes and hollow shapes represent 2D fluxes as shown. The RMS fractional difference values are indicated.

that for this wavelength the single-scattering albedo is 0.9998 so there should be very little cloud absorption (<1%). Thus the quantity "a" is entitled apparent absorption for this wavelength.

Figure 4.20 shows that the differences between 2D and IPA are less for the very thinnest cloud than for the thick cloud where it is expected that cloud structure matters more in the computation of flux. The differences are also small for the high sun angles and progressively increase with increasing solar zenith angle. Even at a solar zenith angle of 50° there is overall excellent agreement. However, the apparent absorption shows values which are slightly negative for the thick cloud at 50°. These regions occur where the sum of the albedo and the transmittance derived from 2D fluxes exceed one relative to the incident source at cloud top. The 2D calculations conserve energy relative to a plane–parallel source in a domain average sense, but not locally. This is because there can be propagation of energy horizontally within the cloud field and the total energy input to a given locality may not only be that incident at cloud top, but also flux incident from the side. This side illumination demonstrates the weakness and eventual breakdown of the independent pixel approximation. Note that as the solar zenith angle decreases to 75°, the differences between 2D and IPA become larger as the IPA breaks down. This breakdown causes the anomalously large positive and negative apparent absorptions. These anomalies occur because the 2D fluxes are interpreted with plane–parallel theory i.e., the only source incident at any given locality is that relative to a horizontal surface at cloud top. If the internal side illuminations were taken into account in the computation of albedos and transmittances, these apparent absorption anomalies would not occur.

The cloud properties of the broken cloud show more clearly these effects which are presented in Figure 4.21. The break in the cloud is clearly shown by examining the IPA curves in the figure. Note that even at the 10° solar zenith angle, the 2D albedos for the cloud of $\overline{\tau} = 8$ appear to smooth over the break in the cloud. This is a direct result of the scattering off the sides of the cloud. The transmittances for this thick cloud at this solar zenith angle exceed unity inside the cloud break. Cannon (1970) noted that radiation tends to flow from regions of greater opacity to regions of smaller opacity and named this behavior "channeling". The enhanced transmittances through the cloud break may be partially attributed to a type of channeling behavior along with the scattering of the direct beam off the sides of the clouds. As the solar zenith angle becomes larger, the effect of the brokenness becomes as the IPA breaks down. Note that at 75° the albedos even exceed unity for the $\overline{\tau} = 8$ case. The direct beam at low sun angles cannot flow through the cloud break without entering the sides of the cloud. Instead, much of the direct beam that enters the cloud through the side is converted to diffuse radiation and is horizontally transported as diffuse radiation until it interacts with areas of maximum extinction embedded within the cloud. The enhanced horizontal advection of radiation coupled with the areas of maximum extinction result in anomalously high albedos. Finally,

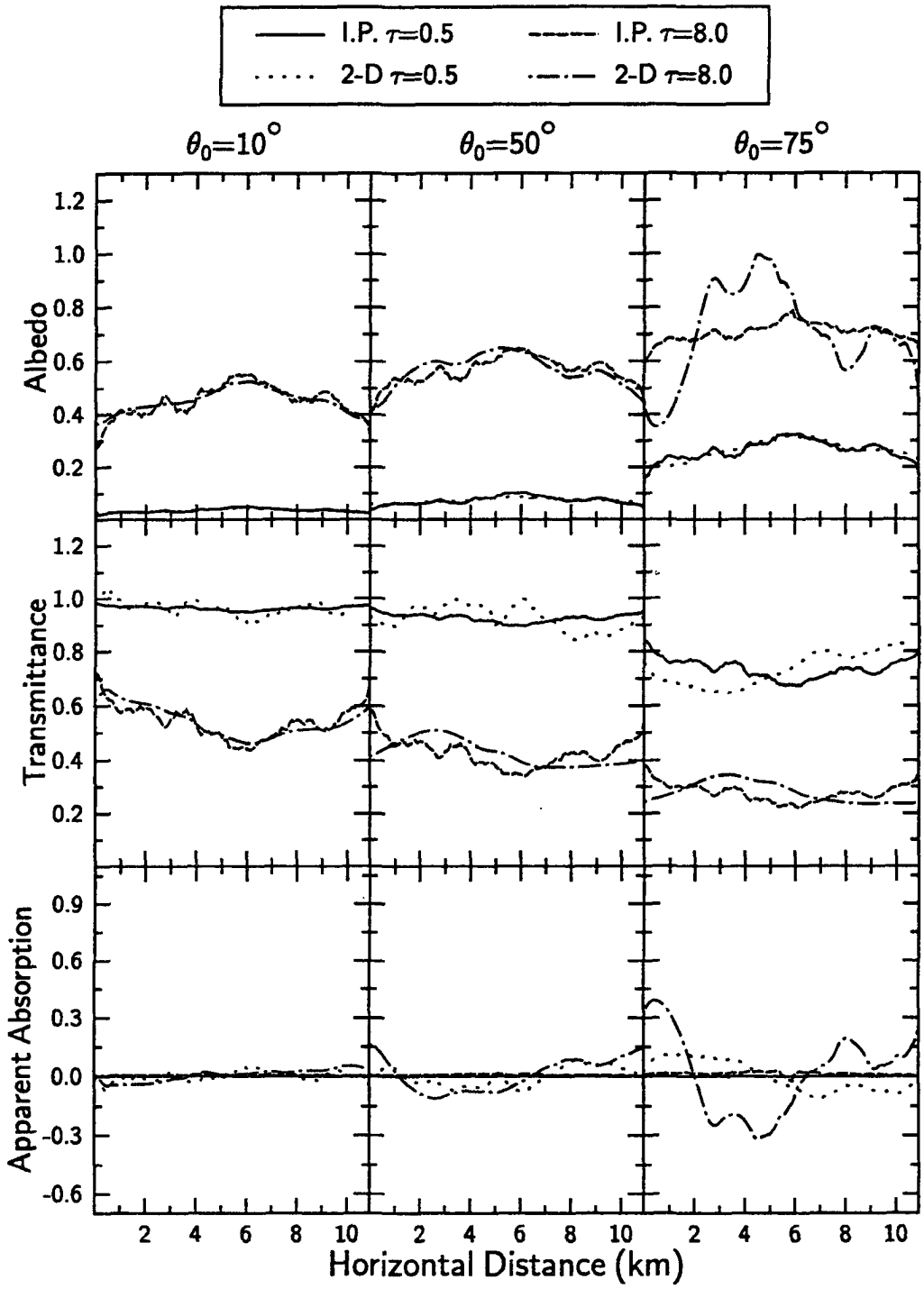

Figure 4.20: Albedo, transmittance, and absorptance as a function of horizontal distance for cloud 2 for 0.83 μm. Each column of the plots contains the results for solar zenith angles 10°, 50°, and 75° respectively.

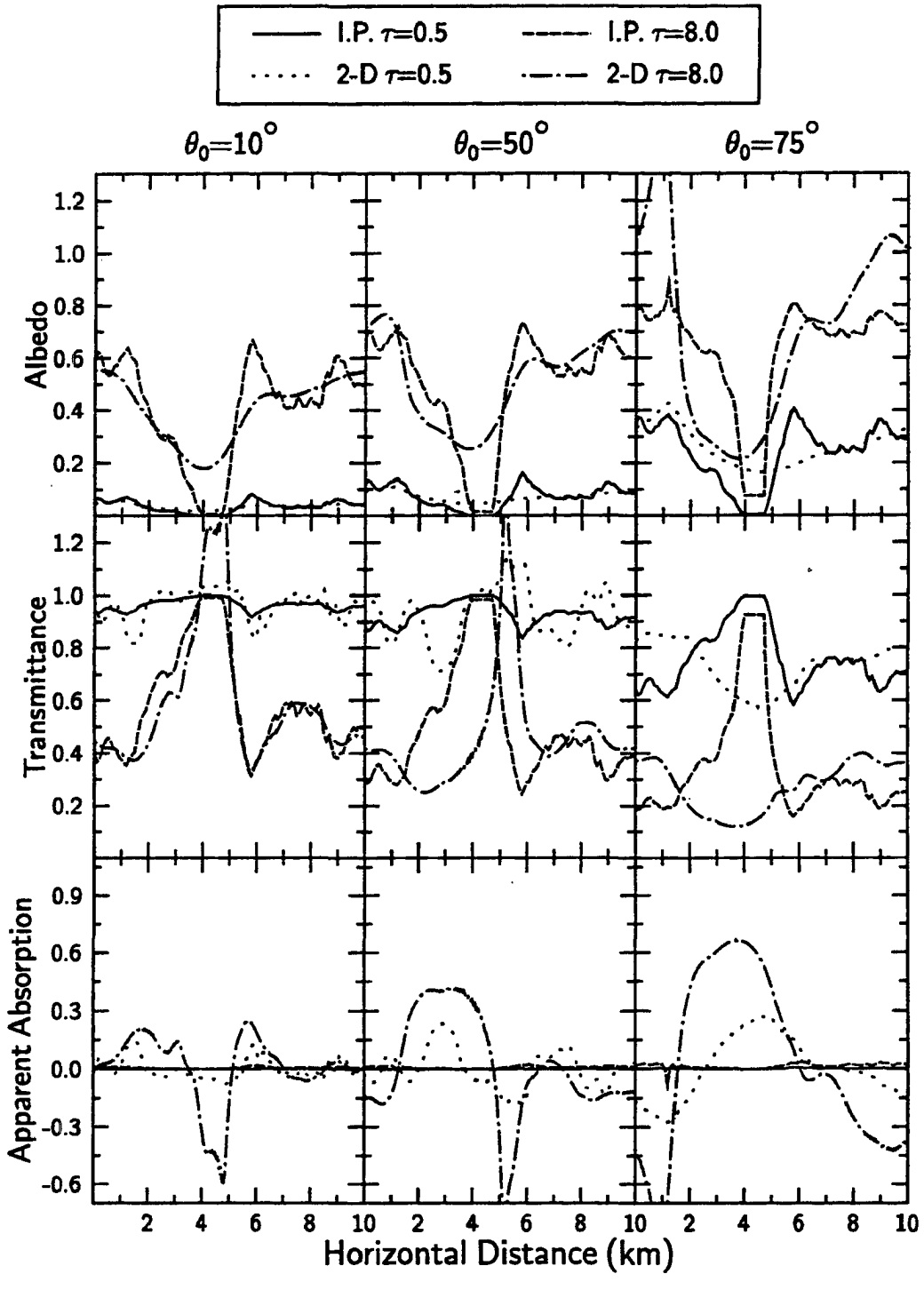

Figure 4.21: Albedo, transmittance, and absorptance as a function of horizontal distance for cloud 3 for 0.83 μm. Each column of the plots contains the results for solar zenith angles 10°, 50°, and 75° respectively.

significant positive and negative apparent absorptions, which are a result of the anomalous transmittances and albedos, are observed especially for the lowest sun. These anomalous absorptions exceed ±30% even for the thinnest cloud.

Figure 4.22 illustrates the horizontal variation of albedo, transmittance, and absorption for cloud 3 at 2.21 μm. The behavior at this wavelength is essentially the same as that described above although the extremes in transmittances and albedos are not seen due to the presence of the absorption. Despite the absorption, there are still some localities where the 2D fluxes interpreted in plane-parallel terms give slightly negative absorptions and large absorptions are still present in the region of the cloud break.

At a wavelength of 11.5 μm, the upward and downward emittances are computed instead of the albedo, transmission and absorption. The emittances show the radiative effect of a cloud compared to a black body and are derived formally by Cox (1976). The upward and downward emittances respectively are defined here as:

$$\epsilon_\lambda^\uparrow = \frac{\pi B_\lambda(T_{surf}) - F_{top}^\uparrow}{\pi \left[B_\lambda(T_{surf}) - B_\lambda(T_{cld})\right]}$$

and

$$\epsilon_\lambda^\downarrow = \frac{F_{bot}^\downarrow - \pi B_\lambda(T_{sky})}{\pi \left[B_\lambda(T_{cld}) - B_\lambda(T_{sky})\right]}$$

where $B_\lambda(T)$ represents the Planck function evaluated at λ and a temperature T. The temperatures T_{surf}, T_{sky}, and T_{cld} represent the surface, sky and cloud temperatures which are set to 285 K, 100 K, and 233 K respectively for these simulations and analyses. All the fluxes have units $W \cdot m^{-2} \cdot \mu m^{-1}$.

The upward and downward emittances relative to the cloud midpoint temperature T_{cld} and as functions of the horizontal distance are shown in Figure 4.23. The agreement between IPA and 2D emittances is much like that for fluxes at this wavelength in that the 2D emittances appear smoothed relative to the independent pixel calculations. Note that both the upward and downward emittances are greater than zero inside the cloud break. Thus for this case, inhomogeneities cause an apparent cloud emittance in the clear sky between clouds. Finally, the thickest cloud case with domain averaged optical depth 0.8 has both upward and downward emittances exceeding unity. Referring back to the emittance definitions above, this implies that the actual cloud emitting temperature is warmer than the cloud midpoint temperature and so the cloud is effectively emitting from a region near cloud base. This is not surprising because the thickest part of the cirrus cloud in these calculations is located near cloud base.

The climatological effects of cirrus cloudiness are often shown in terms of the albedo-emittance relationship (Stephens et al., 1990). These relationships are often derived from radiometric observations from aircraft (Stackhouse, Jr. and Stephens, 1991). The albedo-emittance relationships for all three clouds are shown in Figure 4.24. At the solar

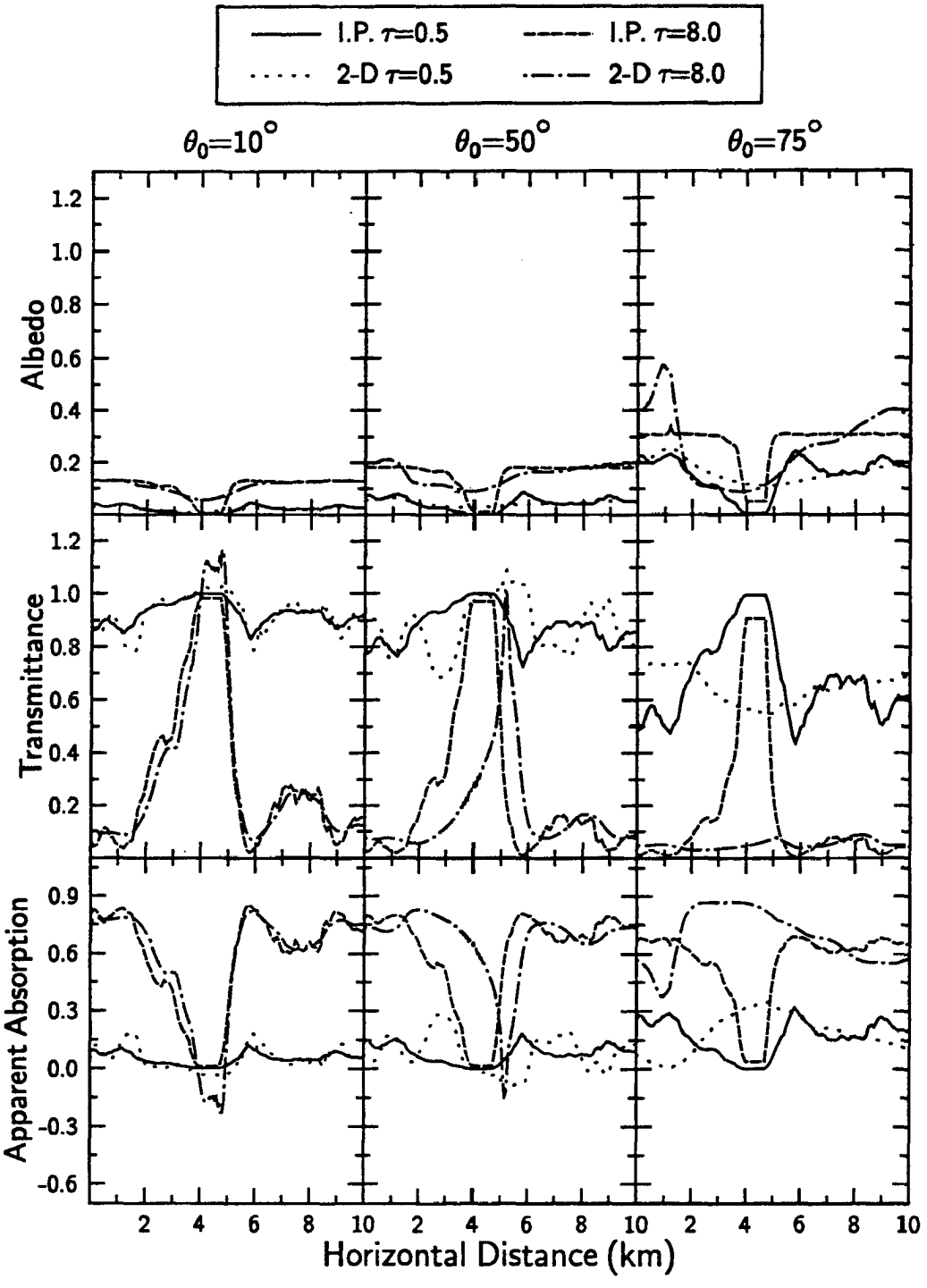

Figure 4.22: Albedo, transmittance, and absorptance as a function of horizontal distance for cloud 3 for 2.21 μm. Each column of the plots contains the results for solar zenith angles 10°, 50°, and 75° respectively.

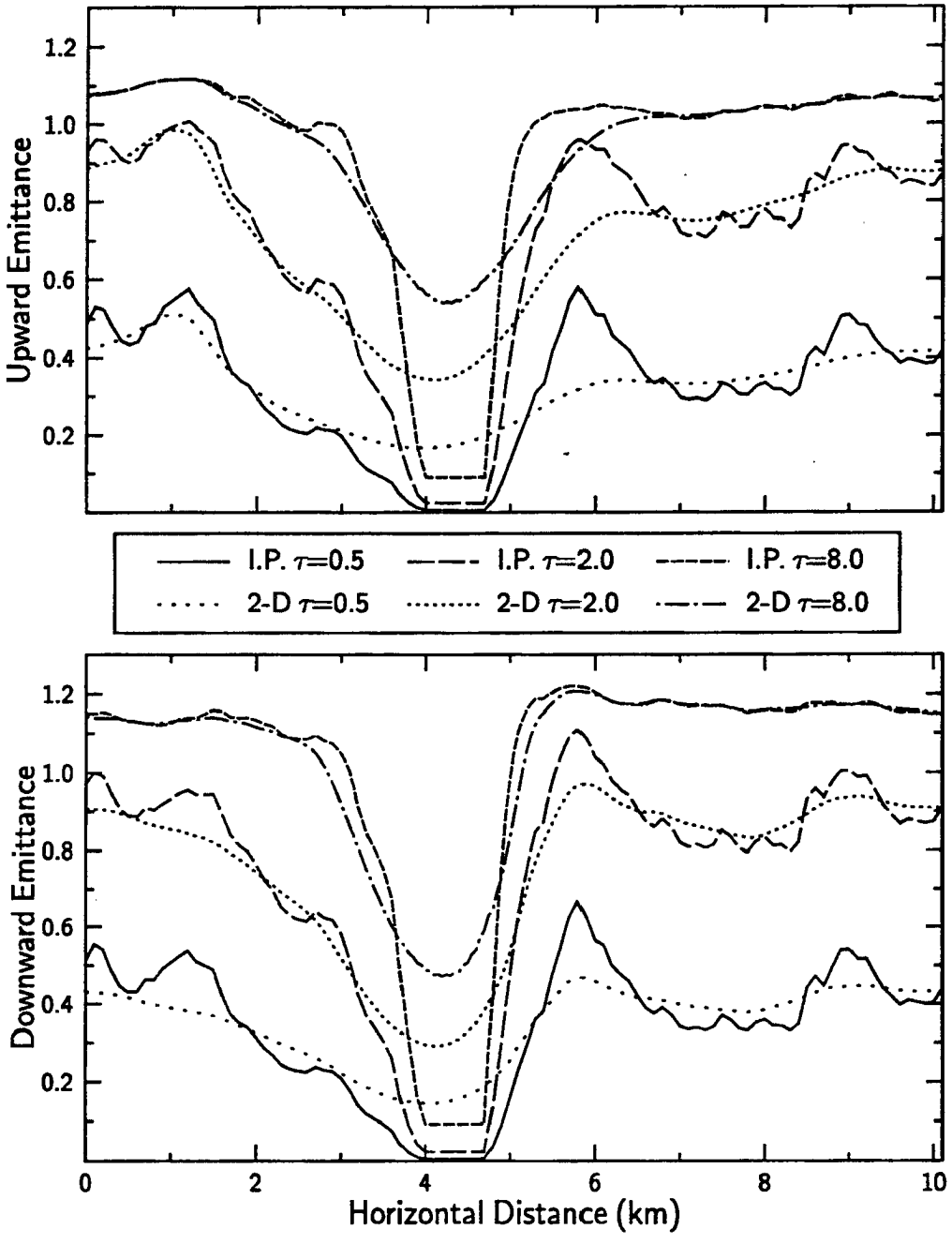

Figure 4.23: Upward and downward emittances as a function of horizontal distance for cloud 3 and 11.5 μm.

zenith angle of 10°, the 2D and the IPA albedo-emittance relationships follow very closely especially for the unbroken clouds 1 and 2. Note that the broken cloud yields 2D albedos which are slightly larger at times than the IPA albedos at the same emittance. However, this agreement deteriorates significantly for the smaller solar zenith angle of 75°. Here the one-to-one correspondence breaks down due to the horizontal interaction of the flux field. Fortunately, only the bulk albedo-emittance relationships as derived from domain average fluxes are most relevant to cloud-climate studies. Comparison of the domain averaged fluxes for these cases between IPA and 2D calculations are presented later.

The anomalous transmittances, albedos, absorptances, and emittances for the cloud cases presented here clearly show the potential effects of cloud inhomogeneities upon the local measurements and subsequent interpretation of cloud radiative properties. Although these calculations are performed at specific wavelengths, past *in situ* field experiments have yielded apparent positive and negative absorptions in the visible wavelengths (see Stephens and Tsay, 1990 and references therein). Recognizing the large uncertainties in the calculation of bulk cloud absorptances, several authors have proposed corrections to broadband measurements to account for radiation that leaks from the sides of the clouds (Ackerman and Cox, 1981; Rawlins, 1989). These simulations show that local cloud inhomogeneities may not only bias cloud absorptances, but also the albedos, transmittances, and emittances. The important issue then becomes whether the averaging process can properly account for the influences of cloud inhomogeneity. This subject is left to future study.

The Sensitivity to Phase Function

To this point only the sensitivities of the fluxes to the spatial distribution of cloud structure have been presented. One of the largest uncertainties in the optical properties of cirrus clouds is the form of the phase function. As discussed in Chapter 3, the radiance calculations exhibit a very large sensitivity to the form of the phase function. As in the case of radiances, the possible effect of this uncertainty is examined here using the three forms of the Double Henyey-Greenstein function as denoted in Table 3.1 and illustrated in Figure 3.4. Figure 4.25 gives the 2D upward fluxes from cloud 2 for all three of the phase functions for the domain averaged optical depth cases of 0.5, 2.0 and 8.0. There are a variety of differences in given situations, but none ever exceed about 4 $W \cdot m^{-2}$. The maximum relative differences between phase functions DHG1 and DHG3 occur in the clouds with domain average optical depth of 0.5 and for the solar zenith angles of 10°. Since the sun is in the plane of the cloud and is located to the left of the figures (i.e., $\phi_o = 180°$), the scattering angle relative to the vertical for this solar zenith angle is 170°. Referring back to Fig. 3.4, the difference between the phase DHG1 and DHG3 at this scattering angle is almost an order of magnitude. Despite the fact that fluxes are an integrated quantity, the enhanced backscatter of DHG3 relative to DHG1 is evidently

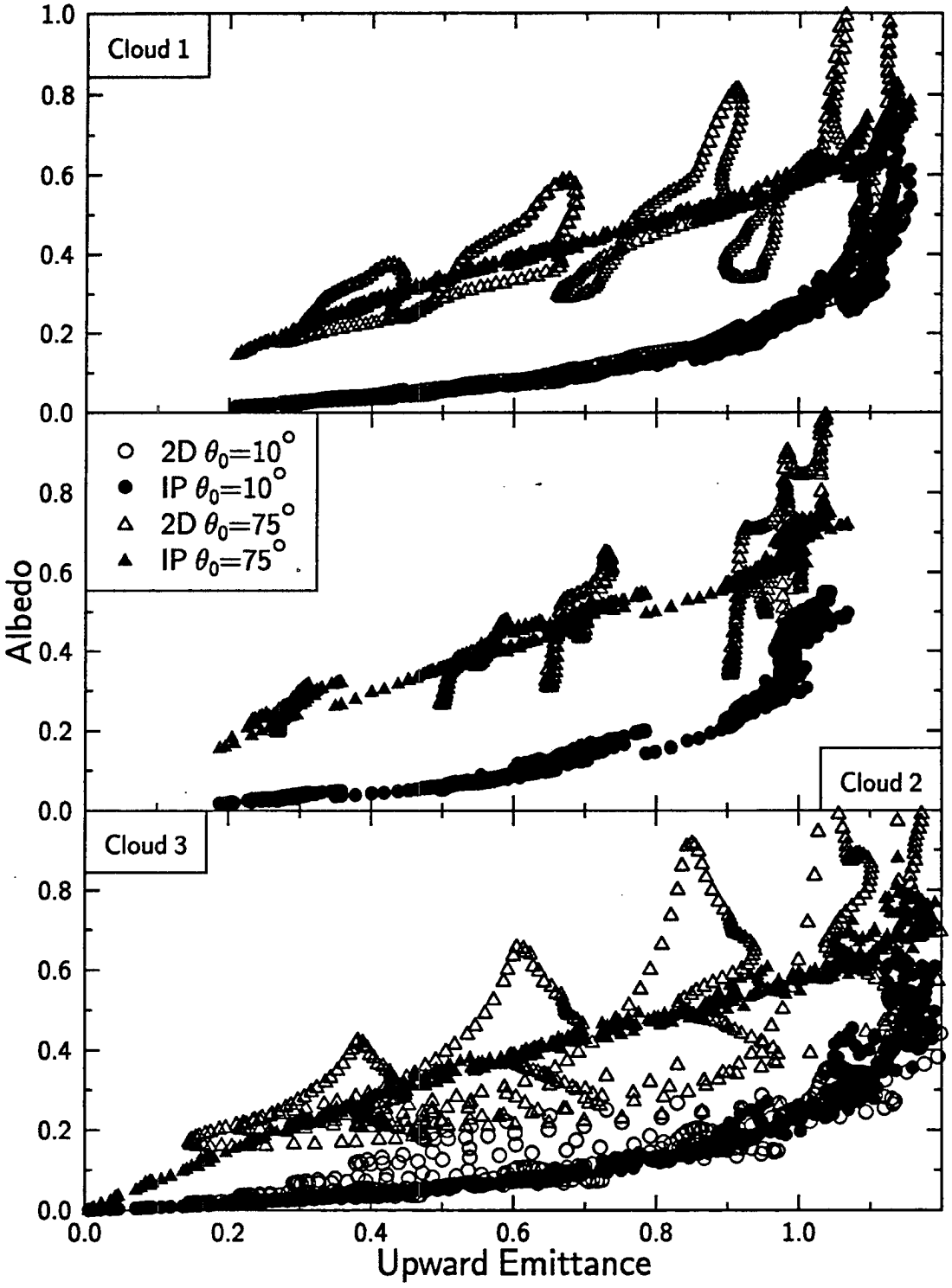

Figure 4.24: Albedo (0.83 μm) as a function of emittance (11.5 μm) for all three clouds as indicated.

significant enough to bias the fluxes upward from 4.6 to 6.5 $W \cdot m^{-2}$ or increase the albedo from 3% to 4.5%. At an optical depth of 2.0, the difference between the DHG3 and the DHG1 fluxes is 3.2 $W \cdot m^{-2}$ and corresponds to an increase in the albedo from 13.8% to 16.0%. At the largest domain average optical thickness there is practically no difference between the fluxes from the two phase functions. The reason for this decrease is attributed to the large multiple scattering which occurs at large optical depths. This multiple scattering will tend to average out the differences in the phase functions forms since each of these phase functions have the same asymmetry parameter.

This situation becomes more complicated as the solar zenith angle increases since the effects of the two-dimensional interaction become more important. Close examination of the curves for the thickest cloud at both the solar zenith angles of 50° and 75° reveal that DHG1 fluxes alternate between being greater and less than DHG3 fluxes. The reason for this involves the actual cloud structure since IPA fluxes show no such alternating behavior (not shown). The localities where DHG1 flux exceeds the DHG3 flux and vice versa tend to cancel such that average fluxes for each of these phase functions are virtually identical. The smallest optical depth cloud for the largest solar zenith angle case does produce a bias in the fluxes similar to that at the lowest solar zenith angle but in the opposite sense. For this case, the scattering angle is 105° relative to the vertical and at that angle the magnitude of the phase function for DHG1 exceeds that for DHG3. Thus the thin cloud biases in the fluxes between the forms of the phase functions are in the same sense as the differences in the magnitudes of their respective phase functions. These thin cloud biases disappear or are changed to alternating local biases as the optical depth and the solar angle increase.

4.1.2 Domain Averaged Fluxes

The importance of the local effects of horizontal radiative transfer also carries over to the domain averaged cloud radiative properties under certain conditions. The purpose of this section is to explore the conditions under which plane-parallel radiative transfer breaks down in a domain averaged sense. These situations are important since they define circumstances where present radiation parameterizations in global circulation models break down. For clouds 2 and 3, the agreement between 2D and IPA fluxes in the domain averaged sense is shown by Figures 4.26 and 4.27 respectively in terms of the fractional difference from the 2D fluxes for 0.83 μm. Negative differences indicate that the IPA flux overestimates the more realistic 2D flux and vice versa for positive differences. The differences are shown in terms of domain averaged optical depth and solar zenith angle. The stratified cloud 2 shows excellent agreement between the IPA and 2D fluxes for all domain averaged optical depths and all solar zenith angles. In all cases, for this cloud and wavelength, the relative errors of the IPA fluxes are much less than 1%. This result should not be surprising since the effective radius of the cloud is assumed constant

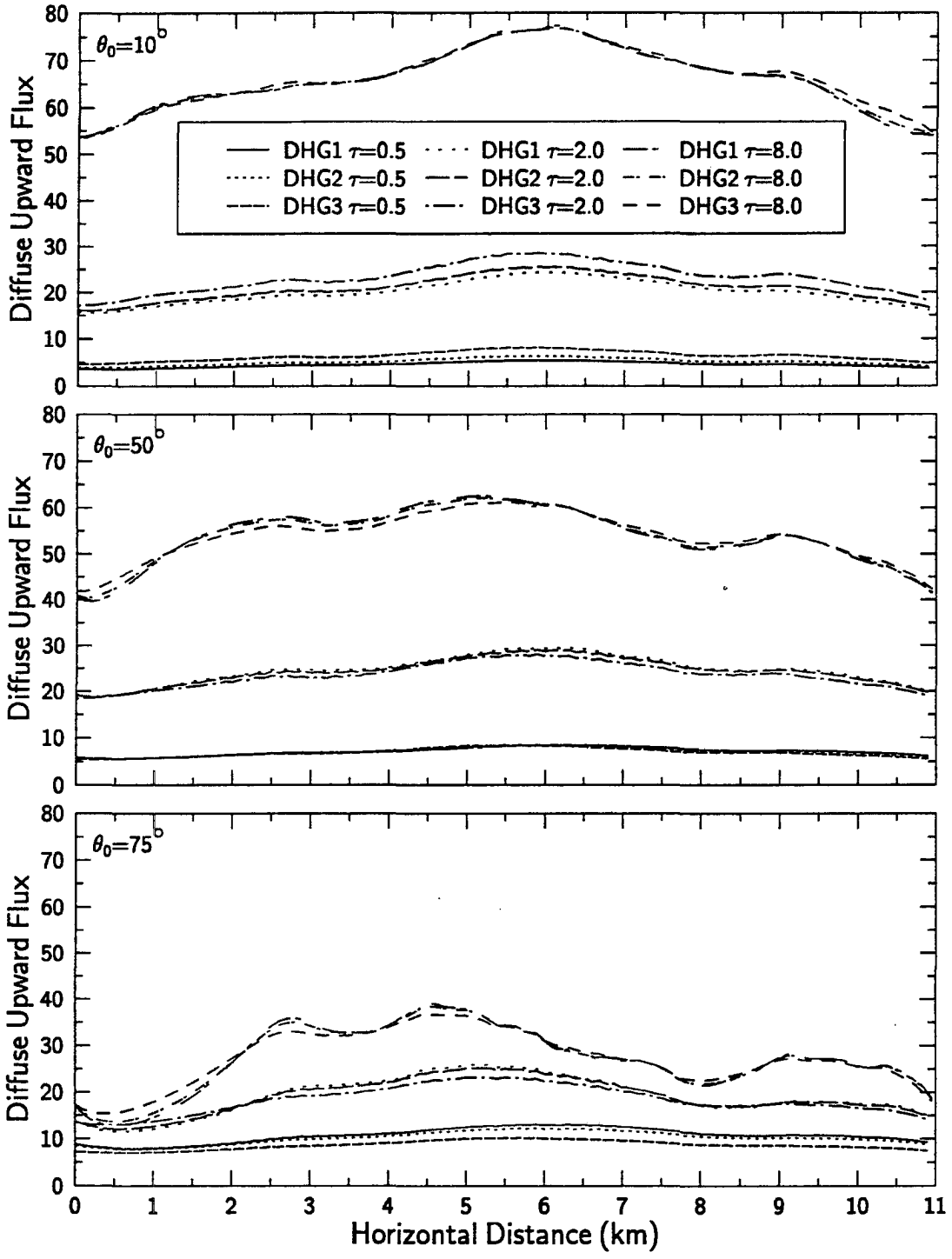

Figure 4.25: 2D diffuse upward fluxes ($W\,m^{-2}\,ster^{-1}$) at cloud top for $\lambda = 0.83\,\mu m$ as a function of horizontal position for the different sun angles, domain averaged optical depths, and phase functions as indicated for cloud 2.

throughout and the cloud is stratified horizontally. Indeed, this is the best situation for plane-parallel theory to approximate the true fluxes with accuracy. On the other hand, the broken cloudiness gives quite different results. The relative differences for the upward fluxes indicates that the IPA fluxes underestimate the 2D fluxes by up to 9% at the largest solar zenith angles (lowest sun). Note this error seems to be more dependent upon the solar zenith angle than the optical depth, but does increase with optical depth for solar zenith angles between 20° and 50° degrees. Since the relative error as shown here is exactly analogous to the albedo, the results indicate that the IPA underestimates the albedos of this cloud by an amount which approaches 10% for larger solar zenith angles and optical depths.

Figure 4.27 also shows the relative difference between the IPA and 2D transmitted fluxes. Note that for the diffuse flux the errors are largest (approaching 15%) for small optical depths and large solar zenith angles. This occurs as a result of the interaction of the direct beam with the 2D medium. In two dimensions, the direct beam interacts with the radiation along a path that contains the information about the horizontal variability of the cloud. By contrast, the direct beam for the IPA only encounters the extinction in a given cloud column. Thus when the penetration depths of the direct beam are longer, the discrepancy between the diffuse and direct 2D and IPA fluxes is increased. As optical depths increase, the penetration of the direct beam becomes much less and this effect diminishes which is shown in the figure by the decreasing errors with increasing optical depths at large solar zenith angles. Note for $\theta_0 < 50°$, the errors reverse this trend and become larger with optical depth. This occurs because at these smaller solar zenith angles, the solar penetration into the cloud is more vertically oriented. However, as the optical depth is increased the multiple scattering increases and the so does the horizontal interaction of radiation.

The total transmitted fluxes as shown in Figure 4.27 show a significant trend of increasing difference between 2D and IPA with increasing optical depths and solar zenith angles. Consistent with the fact that IPA underestimates the upward fluxes at cloud top, the IPA total downward fluxes are overestimated relative to the 2D fluxes. As a result the IPA overestimates that amount of radiation transmitted through the cloud as the optical depths and solar zenith angles become large. The reason for this is that in the independent pixel approximation, direct flux is transmitted through the clouds at the cloud break, while in 2D the sun is sufficiently low that no direct path through the cloud exists. Consequently, the IPA fluxes for broken cloud presented here tends to overestimate the transmittance causing the albedos at cloud top to be underestimated. Although not shown the domain averaged absorptances are well under 2% even at very large optical depths and both the 2D and IPA agreed almost exactly at this wavelength. The wild fluctuations in apparent absorption that occurred locally disappear in the domain averages.

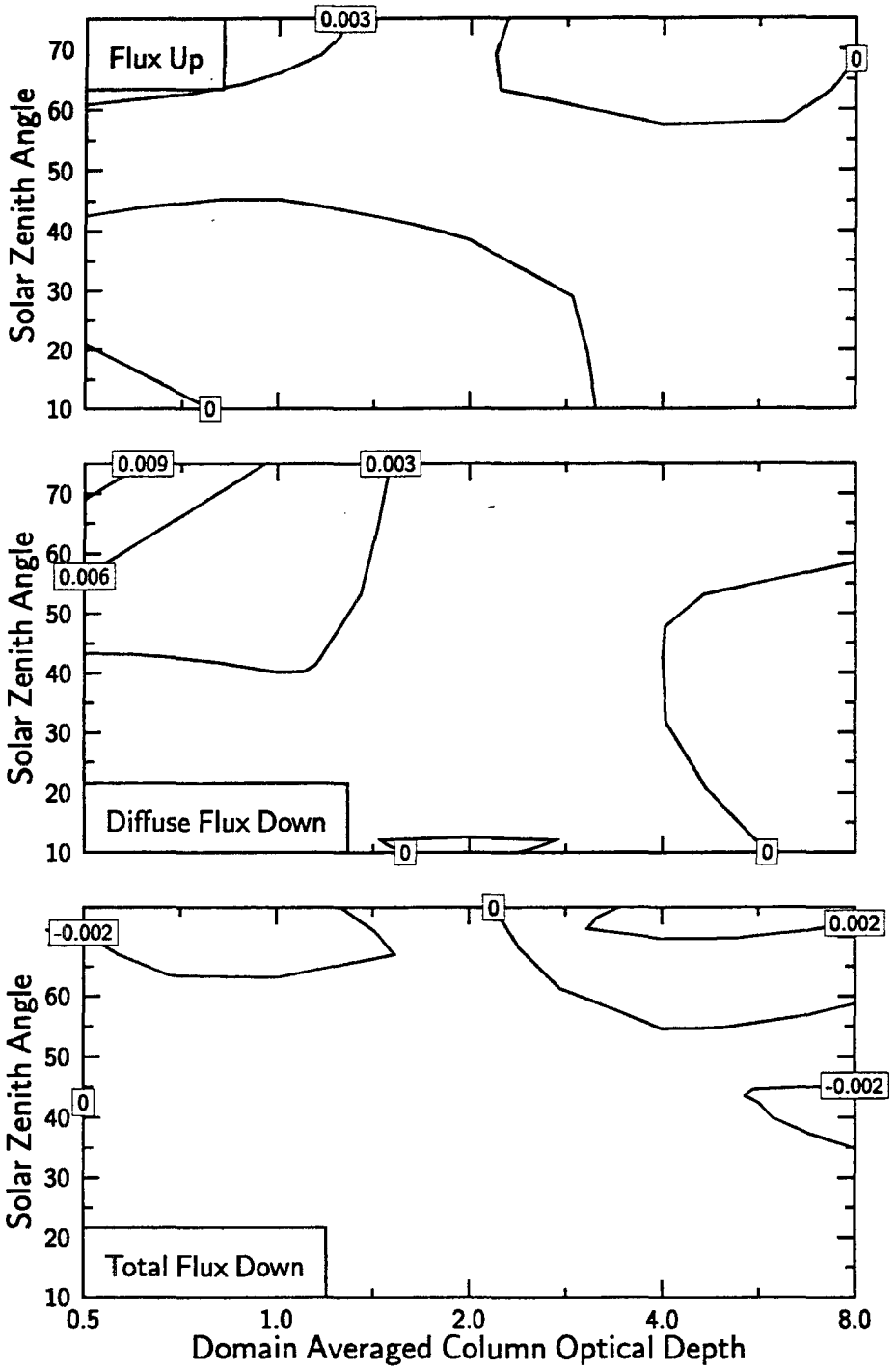

Figure 4.26: Fractional differences between 2D and IPA for domain averaged fluxes for cloud 2 at 0.83 μm.

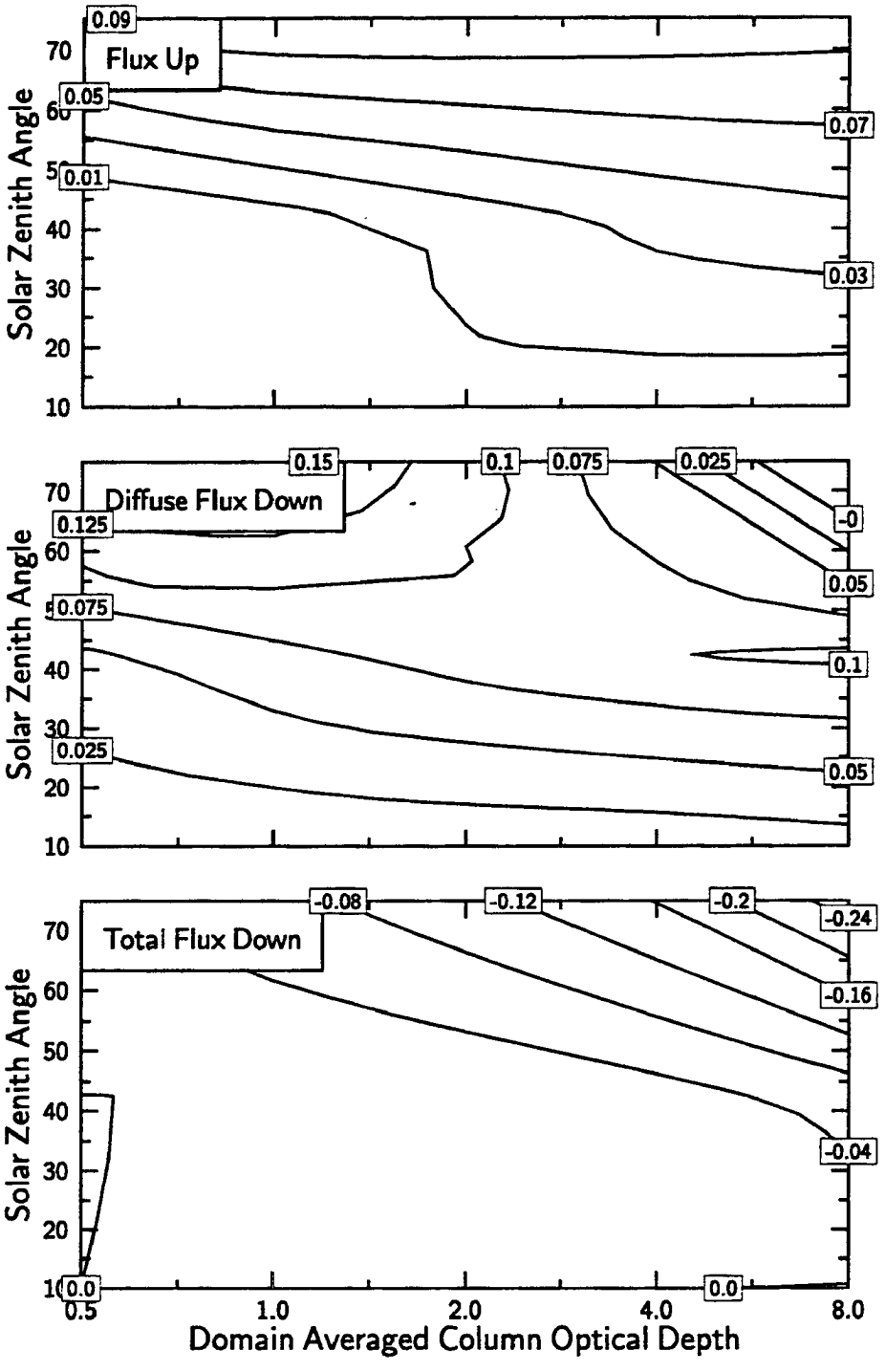

Figure 4.27: Fractional differences between 2D and IPA for domain averaged fluxes for cloud 3 at 0.83 μm.

Table 4.2: The fractional relative difference between 2D and IPA fluxes at the wavelength 11.5 μm relative to the 2D flux. Quantities greater than zero are underestimated by IPA and vice versa.

Domain Averaged	2D–IPA Relative Flux Differences					
	Cloud 1		Cloud 2		Cloud 3	
τ	Up	Down	Up	Down	Up	Down
0.5	-0.001	0.002	-0.000	0.001	-0.005	0.019
1.0	-0.001	0.001	-0.001	0.002	-0.010	0.021
2.0	-0.000	0.000	-0.001	0.000	-0.018	0.021
4.0	0.001	-0.001	-0.001	0.000	-0.027	0.022
8.0	0.001	-0.000	-0.000	-0.000	-0.033	0.021

Figure 4.28 shows the fractional differences for the broken cloud at 2.21 μm. The relative differences are much larger than the visible wavelength illustrating the effect of absorption along a horizontal slant path as compared to the column. It must be noted however, that despite the much larger relative errors the amount of flux at this wavelength is much less and this may partially account for the very large fractional differences. The behavior of the total downward fluxes is quite similar to that of the visible wavelength with the differences increasing with large optical depths and solar zenith angles. The transmittance is still overestimated by the independent pixel approach. In this case the large relative differences are a result of the increased absorption along the slanted path through the cloud. The IPA underestimates the total absorption (not shown) of the cloud by almost 19% relative to the 2D absorption at this wavelength. This indicates that the differences in domain averaged cloud heating for this broken cloud are significant. This underestimation of absorption at the large optical depths and large zenith angles is the reason that the diffuse downward fluxes and diffuse upward fluxes are significantly overestimated by IPA. With this exception the shape of the contours in Fig. 4.28 indicate a similar behavior to that of the visible wavelength.

The agreement between the 2D and IPA domain averaged fluxes at 11.5 μm is much better than that for the solar wavelengths as shown in Table 4.2. This table gives the fraction difference between 2D and IPA fluxes relative to the 2D mean. The table shows that differences are much less than 1% for the clouds without breaks and vary between 1-3% for the broken cloud case. These errors are much smaller in comparison than those errors associated with the solar wavelengths which range up to 10% in some instances. Consequently, despite obtaining large local differences at the infrared wavelength, the domain averages are very close. Since this agreement occurs when averaging over the entire domain, even the clear areas, the exclusion of this area from the average will bias the IPA upward flux higher and the downward flux lower relative to the 2D fluxes. Therefore, the importance of the averaging method should not be overlooked in the process of determining bulk cloud properties.

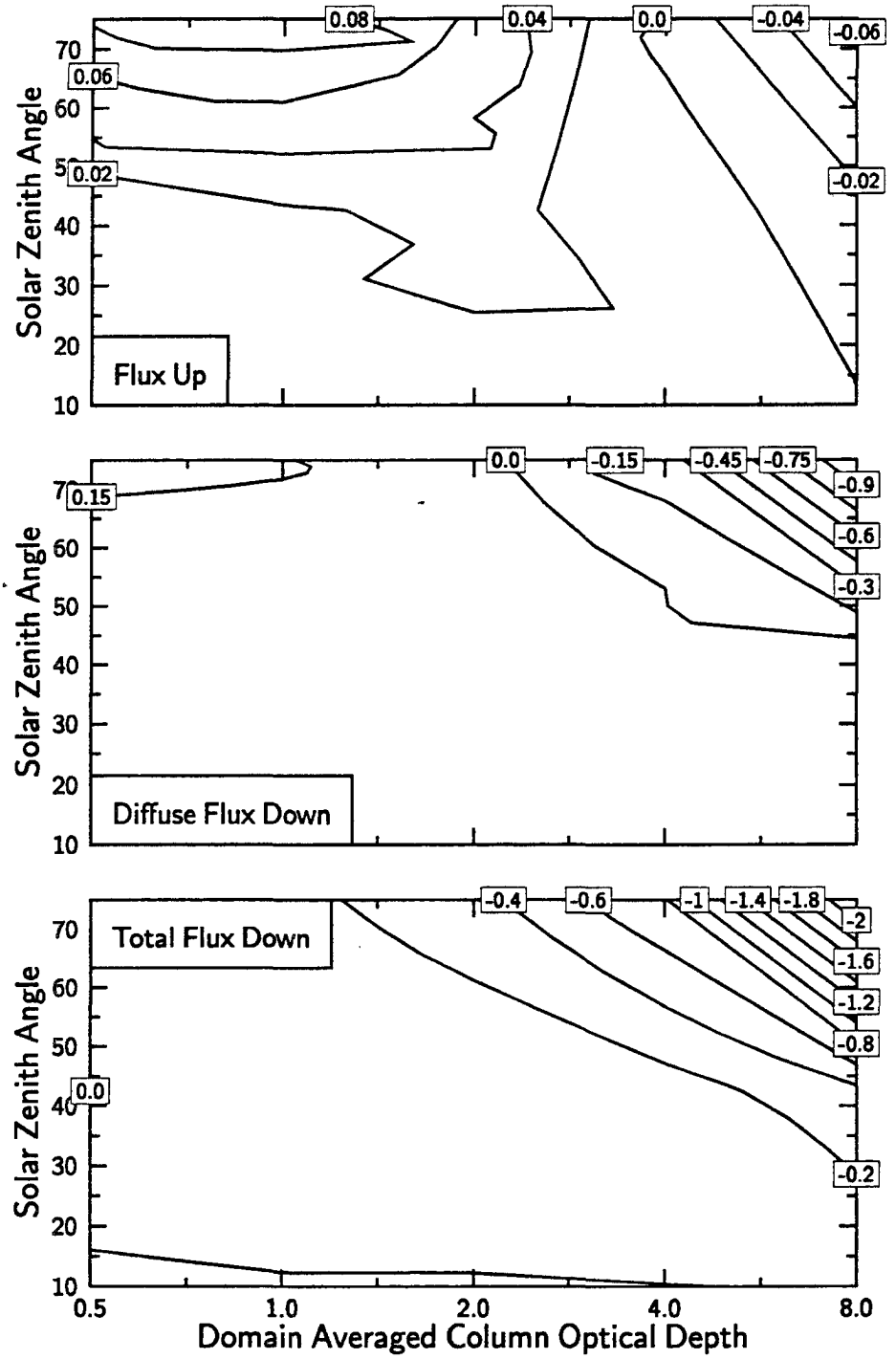

Figure 4.28: Fractional differences between 2D and IPA for domain averaged fluxes for cloud 3 at 2.21 μm.

4.2 Flux Sensitivities of Inhomogeneous Clouds with Variable Microphysics

In addition to the simulations studying clouds with constant microphysics, simulations are performed investigating the effect of varying the total concentrations (extinction) and size distributions (single-scattering albedo) on the fluxes of cirrus clouds. In chapter 3, the effects of the variable single-scattering albedo on the radiance fields is discussed. The effects of this variability upon the flux fields are examined in this chapter. These issues are explored in this section by comparing 2D and IPA flux simulations using a variable single-scattering albedo to IPA flux simulations using a domain averaged single-scattering albedo as specified in Section 2.1.2. The goal of this analysis is to ascertain for fluxes the importance of vertical inhomogeneities compared to the combined influence of both horizontal and vertical inhomogeneities at several difference wavelengths.

4.2.1 Sensitivity of Spatial Fluxes to Cloud Structure

In this section, the flux quantities are examined for the variable microphysics cloud having domain averaged optical depths of 1.26 and 4.0 at the wavelengths 0.83 μm, 2.21 μm, and 11.5 μm. In section 4.1.1, the horizontal distribution of boundary fluxes was presented for the upward flux, and both the diffuse and total downward fluxes for these wavelengths. Here these sensitivities are examined only in terms of albedo, transmittance, and absorption since these represent normalized quantities with respect to the incident solar flux. The 11.5 μm simulations are analyzed in terms of emittances in order to compare to earlier simulations at this wavelength. The plots in this section present curves labeled as IP1, IP2, and 2D. The curves labeled IP1 present the albedo, transmittance, absorptance, or emittance from independent pixel simulations using a domain averaged ω_0. The curves labeled IP2 and 2D present the same quantities using the variable ω_0 field for independent pixel and two-dimensional calculations respectively. For reference, the RMS fractional differences between curves IP1, IP2, and 2D are given in Table 4.3 for all three wavelengths.

Figures 4.29 and 4.30 give the albedo, transmittance, and absorptance at wavelength 0.83 μm for variable ω_0 clouds with domain averaged optical depth of 1.26 and 4.0 respectively as a function of the horizontal distance. Curves for the solar zenith angles of 10° and 75° are presented. The two IPA curves agree almost exactly for both domain averaged optical depths (many times to the fourth significant digit for $\overline{\tau} = 1.26$) indicating that the effect of the vertical inhomogeneities for this cloud are not significant. The RMS fractional differences at this wavelength between IP1 and IP2, as shown in Table 4.3, are much less than 0.01 for both upward and downward fluxes. Comparison of the 2D albedos, transmittances, and absorptances to those calculated using the IPA for both cloud cases does reveal significant local differences. As in the case of the constant microphysics clouds, the 2D fluxes appear smooth compared to the IPA fluxes especially for the albedos in the top

Table 4.3: RMS fractional upward and downward flux differences between IP1, IP2, and 2D simulations of the variable ω_0 cloud for domain averaged optical depths of 1.26 and 4.0. The RMS values are unitless.

λ (μm)		θ_0 (deg)	$\overline{\tau} = 1.26$		$\overline{\tau} = 4.0$	
			RMS $F^{\uparrow}$	RMS $F^{\downarrow}$	RMS $F^{\uparrow}$	RMS $F^{\downarrow}$
0.83	IP2 vs IP1	10	0.00007	0.00003	0.00624	0.00228
		75	0.00221	0.00174	0.00248	0.00356
	2D vs IP1	10	0.19679	0.05820	0.14737	0.06584
		75	0.11948	0.09620	0.17276	0.08206
	2D vs IP2	10	0.19681	0.05820	0.14724	0.06606
		75	0.11957	0.09650	0.17195	0.08148
2.21	IP2 vs IP1	10	0.03354	0.00813	0.08528	0.02906
		75	0.06105	0.02562	0.12630	0.07899
	2D vs IP1	10	0.15552	0.06273	0.09770	0.11601
		75	0.12463	0.15650	0.27127	0.19099
	2D vs IP2	10	0.16524	0.06197	0.08877	0.10861
		75	0.12783	0.13965	0.24577	0.16817
11.5	IP2 vs IP1	—	0.01243	0.00430	0.00138	0.00257
	2D vs IP1	—	0.05801	0.08363	0.04750	0.03358
	2D vs IP2	—	0.05861	0.08410	0.04800	0.03360

panel. The exception to this is the transmittances for $\overline{\tau} = 1.26$ at $\theta_o = 10°$ which show large variations about IPA transmittances. This is possible evidence for the "channeling" type effect mentioned in the discussion concerning constant microphysics clouds. The variable ω_0 cloud with $\overline{\tau} = 4.0$ shows less of the channeling effect, but greater cloud shadowing effects especially at the 75° solar zenith angle. As a result of the cloud channeling and shadowing, there are areas of both positive and negative apparent absorption that are largest for the thick cloud and approach 20% at some locations. The RMS fractional differences between 2D and IP1 calculations and the 2D and IP2 calculations are virtually identical (see Table 4.3). This indicates that the disagreement between the independent pixel and two-dimensional fluxes is primarily due to the horizontal interaction of radiation within the given cloud structure and not the variable single-scattering albedo field. The reason for this, as discussed in Chapter 3, is that the single-scattering albedo shows little sensitivity to the changing effective radius in the visible wavelengths.

The insensitivity of the single-scattering albedo to the variable effective radius of this cloud field results in the preservation of the one-to-one relationship between column optical depth and independent pixel fluxes. This is shown in Figure 4.31 that presents distributions of the albedos, and both the diffuse and total transmittances at 0.83 μm as a function of column optical depth. The distributions are shown for the same solar zenith angles as the previous figures for IP1, IP2, and 2D fluxes. The albedos and transmittances from each of the two domain average clouds are plotted together and are separated as indicated. This figure shows clearly that IP2 fluxes maintain the plane-parallel monotonic relationship between fluxes and column optical depth despite the vertical variation of the single-scattering albedo. The figure also shows that the effects in the horizontal transport

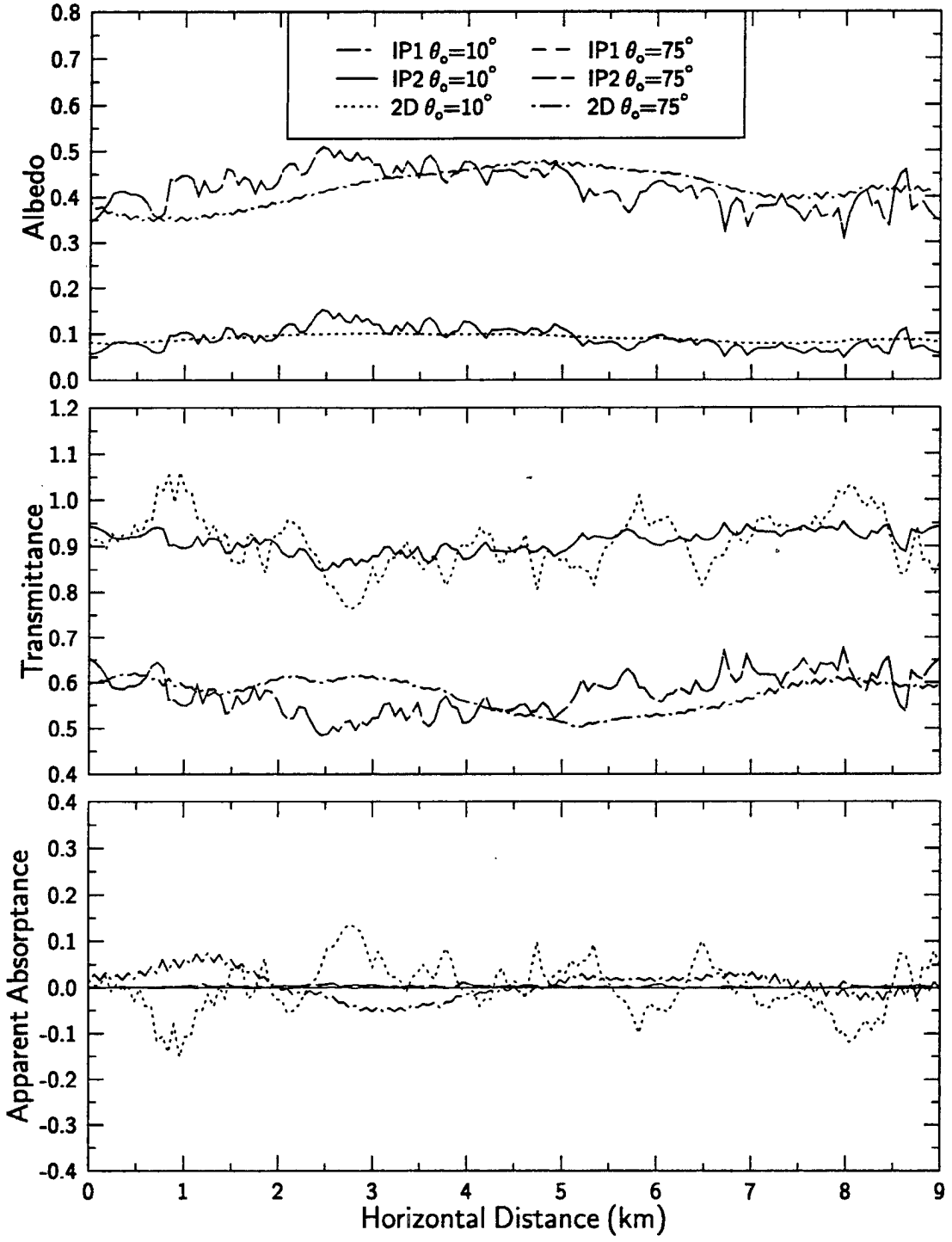

Figure 4.29: Albedo, transmittance, and apparent absorptance as a function of horizontal distance at 0.83 μm for the variable ω_0 cloud with $\overline{\tau} = 1.26$. Each panel contains the results for solar zenith angles 10° and 75°. IP1 and IP2 refer to independent pixel calculations performed using a domain averaged ω_o and variable ω_o respectively.

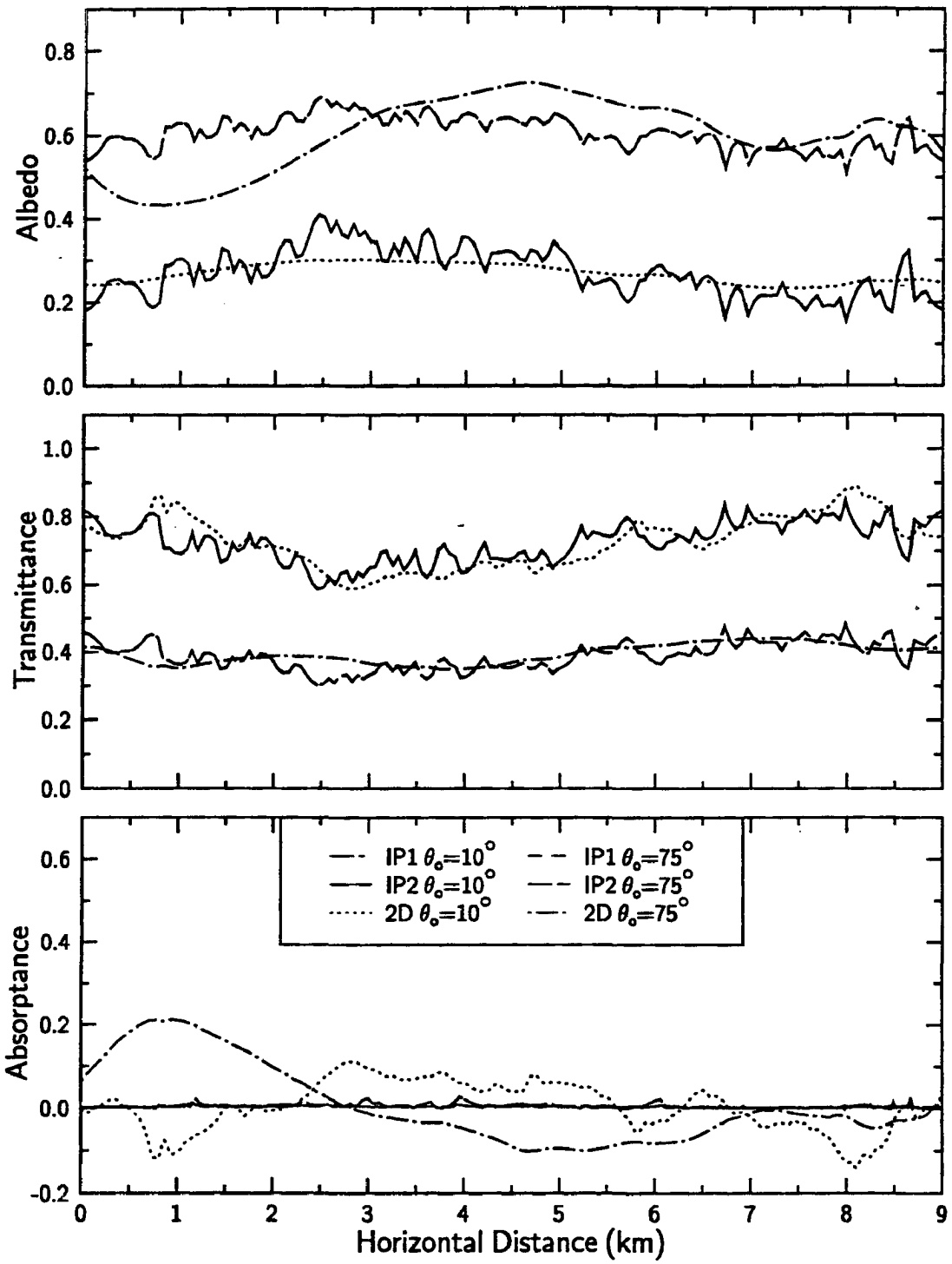

Figure 4.30: Albedo, transmittance, and apparent absorptance as a function of horizontal distance at 0.83 μm for the variable ω_0 cloud with $\overline{\tau} = 4.0$. Each panel contains the results for solar zenith angles 10° and 75°. IP1 and IP2 refer to independent pixel calculations performed using a domain averaged ω_0 and variable ω_0 respectively.

of radiative flux, inherent in the 2D albedos and transmittances, introduce much more scatter than the vertical inhomogeneity in the IP2 curves. The scatter of the 2D albedos and transmittances about the IPA simulations show trends similar to the distribution of fluxes for the constant microphysics clouds at 0.83 μm. For instance, relative to the domain averaged optical depth of the cloud, the IP2 albedos are greater than the 2D albedos at large optical depths and large solar zenith angles. However, this trend reverses for small optical depths. This behavior is the result of the "smoothing" of the 2D fluxes relative to the IPA fluxes. At the small solar zenith angle this behavior is reversed for the albedos. The trends for the transmittances mirror those for the albedos. This behavior was discussed previously in section 4.1.1 and shows the importance horizontal inhomogeneities for this stratified cloud.

At 2.21 μm, the sensitivity of the single-scattering albedo to the variation of the effective radius is much larger and this effects the characteristics of the flux fields. Figures 4.32 and 4.33 give the albedos, transmittances, and absorptances at 2.21 μm for the variable ω_0 cloud with domain averaged optical depths of 1.26 and 4.0 respectively. For $\overline{\tau} = 1.26$, the two IPA curves agree well, but differences do arise at various places along the domain especially at the large solar zenith angle. The RMS fractional differences from Table 4.3 between the IP1 and IP2 fluxes at this $\overline{\tau}$ never exceed 0.03 for the downward fluxes but vary from 0.034 at $\theta_o = 10°$ to 0.061 at $\theta_o = 75°$ for the upward fluxes.However, Figure 4.33 shows that the difference between IP1 and IP2 becomes noticeably larger for the thick cloud, especially at the large solar zenith angle. The largest differences are found in the absorptances in the bottom panel of Fig. 4.33 for $\theta_0 = 75°$. Here the column absorptance of IP2 is almost 10% higher than IP1 at certain locations. In this instance, the RMS fractional differences are 0.126 and 0.079 for the upward and downward fluxes respectively and are at least a factor of two larger than the RMS differences for the thin cloud (see Table 4.3). The 2D absorptances at this solar zenith angle again show sensitivity to cloud structure but agree more with the IP2 results beyond the influence of cloud shadowing from about 7 to 9 km. The RMS fractional differences between 2D and IP1 are 0.271 and 0.191 for the upward and downward fluxes respectively. Since the differences between the two independent pixel methods are about a factor of two less than these values, the vertical inhomogeneities appear to account for about one half of the RMS differences from 2D fluxes at this absorbing wavelength and solar zenith angle. The horizontal interaction of the radiation field in this stratified cloud at $\overline{\tau} = 4.0$ accounts for the remaining differences. Also Table 4.3 reveals that the RMS differences in downward fluxes (or transmittances) at this wavelength always become larger as the optical depth and solar zenith angle increase. This trend corresponds to cases where the optical path through the medium increases. Therefore, the assumption of a domain averaged single-scattering albedo causes the greatest error in these cases.

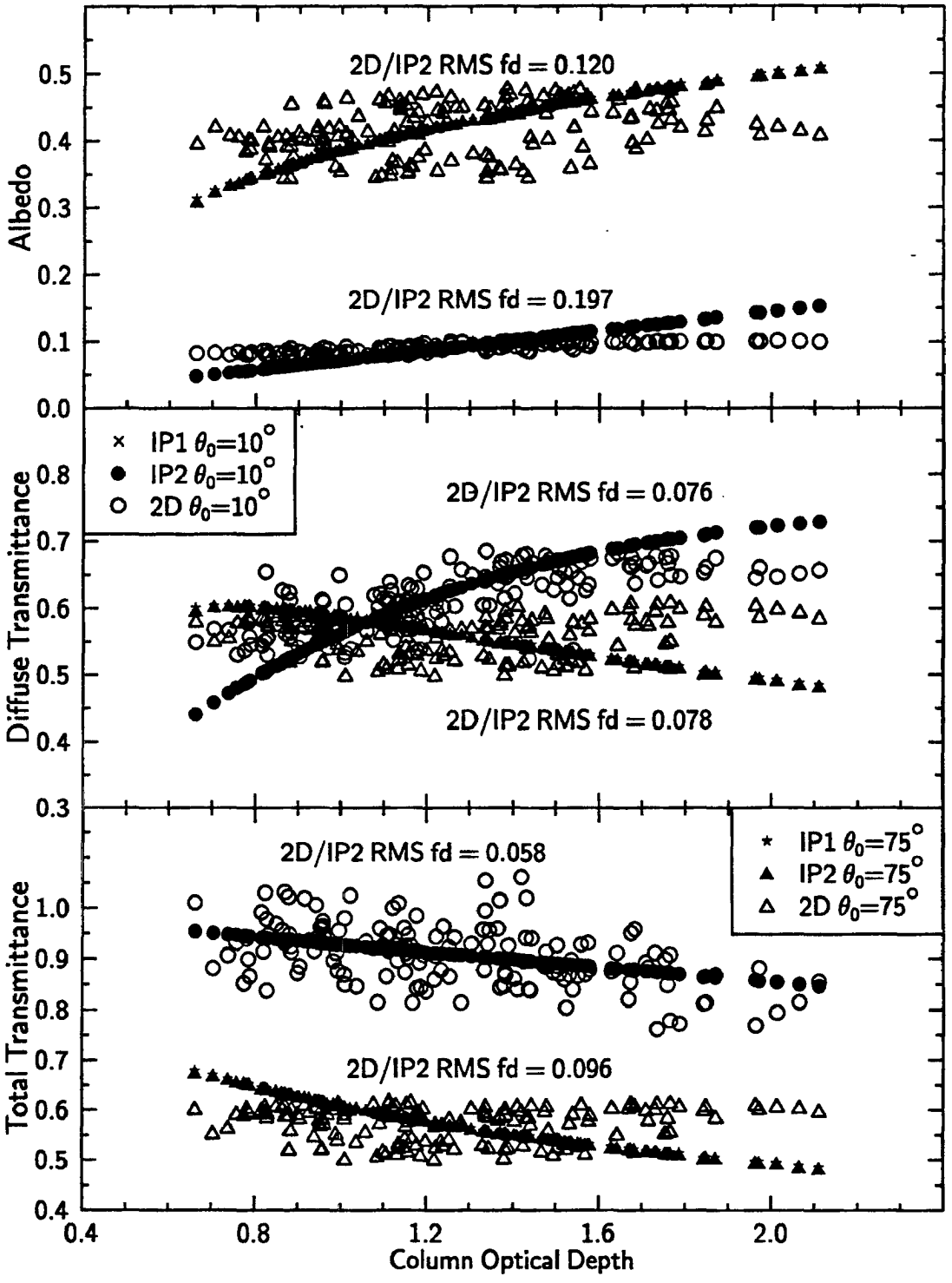

Figure 4.31: Albedo, diffuse transmittance, and total transmittance as a function of column optical depth at 0.83 μm for the variable ω_0 cloud with domain averaged optical depths of 1.26 and 4.0. Each panel contains the results for solar zenith angles 10° and 75°. IP1 and IP2 refer to independent pixel calculations performed using a domain averaged ω_0 and variable ω_0 respectively.

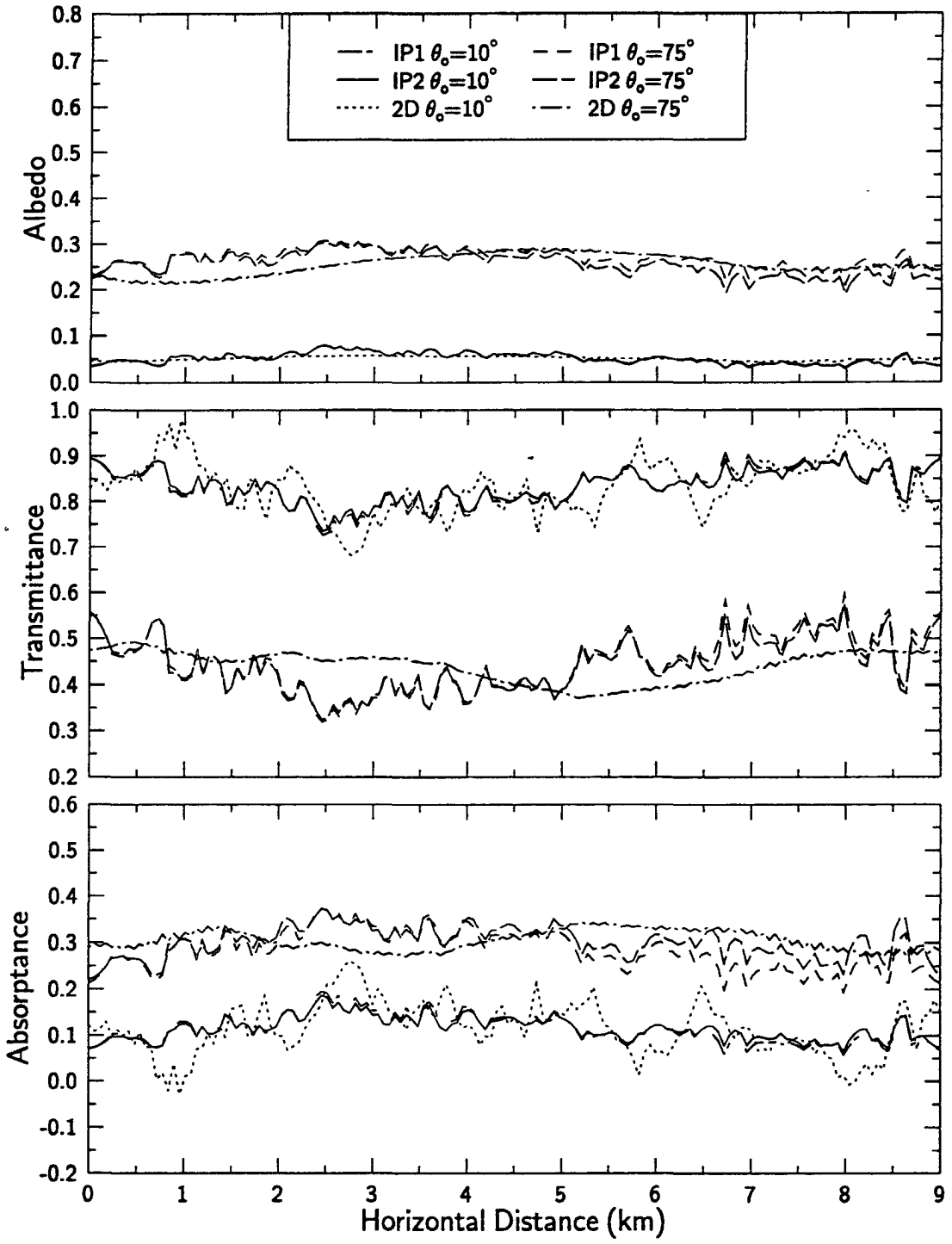

Figure 4.32: Albedo, transmittance, and absorptance as a function of horizontal distance at 2.21 μm for the variable ω_0 cloud with $\overline{\tau} = 1.26$. Each panel contains the results for solar zenith angles 10° and 75°. IP1 and IP2 refer to independent pixel calculations performed using a domain averaged ω_0 and variable ω_0 respectively.

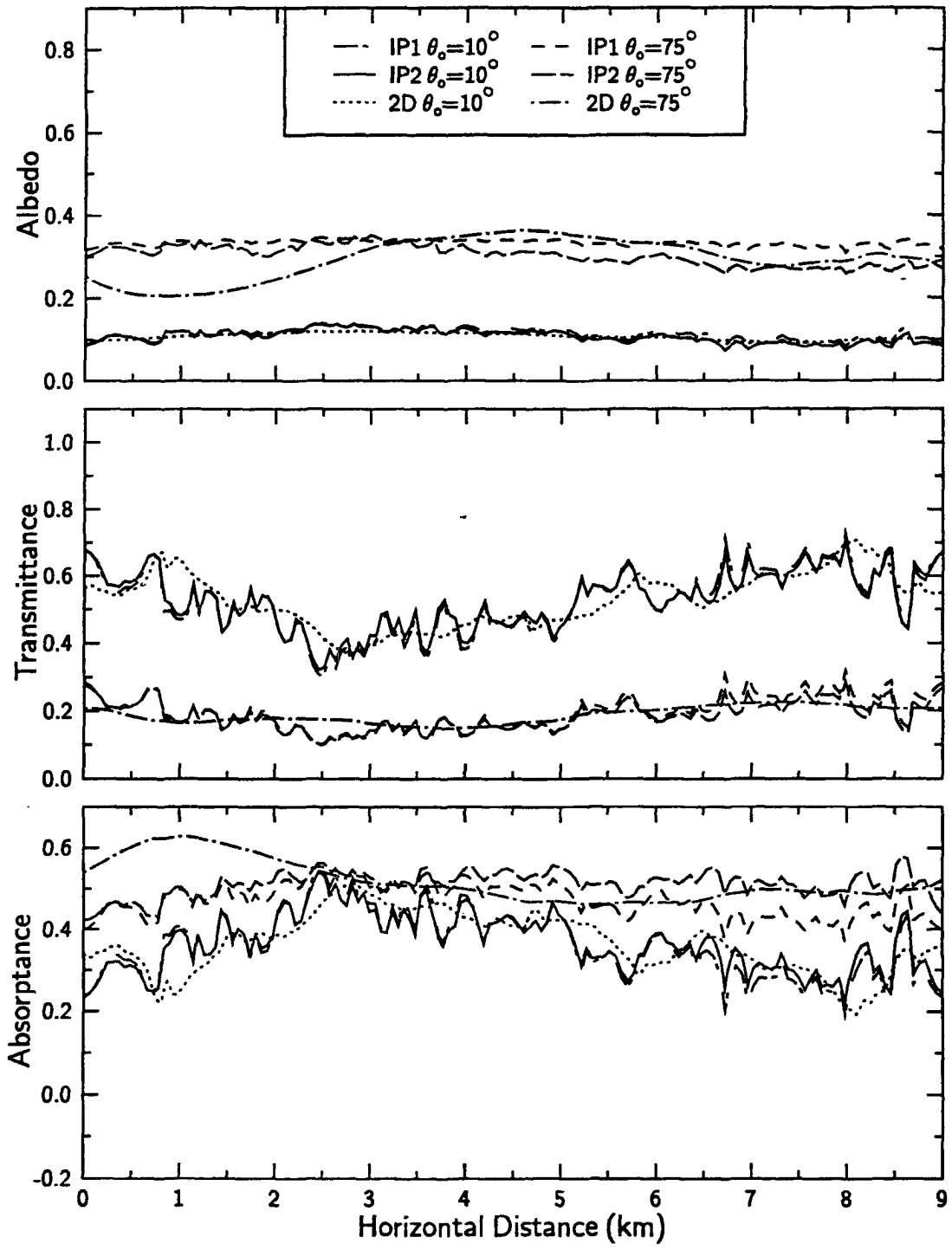

Figure 4.33: Albedo, transmittance, and absorptance as a function of horizontal distance at 2.21 μm for the variable ω_0 cloud with $\overline{\tau}$=4.0. Each panel contains the results for solar zenith angles 10° and 75°. IP1 and IP2 refer to independent pixel calculations performed using a domain averaged ω_0 and variable ω_0 respectively.

Figure 4.34 shows the distributions of albedo, and both the diffuse and total transmittance for this cloud with domain optical depths of 1.26 and 4.0 at 2.21 μm. A careful examination of this figure shows the increase in scatter of the IP2 albedos and transmittances relative to those of IP1. This scatter is most prevalent for the albedos at the largest solar zenith angle as evidenced by the difference between the IP1 and IP2 simulations given in Table 4.3. Comparing back to Figure 4.33, the effect is most likely due to enhanced absorption at this large solar zenith angle inside the column with the variable ω_0 compared to the column with the constant ω_0. This absorption causes a break down of the one-to-one relationship between column optical depth and plane-parallel albedos which is important for the interpretation of flux measurements. The transmittances also show some scatter between the IP1 and IP2 calculations, but to a much lesser extent. Consequently, for this stratiform cloud the transmittances are comparatively insensitive to the vertical variation of particle size regardless of optical depth. Nevertheless, the sensitivity in the independent pixel cases for both the albedos and transmittances is still small compared to the scatter of the 2D fluxes which change the one-to-one relationship between fluxes and column optical depth.

The sensitivity of single-scattering albedo to changes in the effective radius at 11.5 μm is not as large as at 2.21 μm. As a result, the independent pixel fluxes at 11.5 μm are not sensitive to the vertical variation of the effective radius. This is shown in Figure 4.35 which gives the upward and downward emittances at 11.5 μm for IP1, IP2, and 2D simulations at domain averaged optical depths of 1.26 and 4.0. The cloud midpoint temperature for these quantities is assumed to be 238 K. The figure shows the same "smoothing" effect for the 2D emittances relative to both independent pixel emittances that was observed in the visible wavelength. The IP1 and IP2 upward and downward emittances are almost identical and the RMS fractional flux differences are less than 0.005 in all cases (see Table 4.3). By contrast, the RMS fractional differences between the 2D and IP1 fluxes and the 2D and IP2 fluxes are more than an order of magnitude larger. Therefore, the interaction of radiation in two dimensions determines the differences between the 2D and IPA calculations. Since there is little sensitivity of the albedos at 0.83 μm and the emittances at 11.5 μm for the distribution of effective radius found in this cloud, the emittance-albedo relationships for the IP2 calculations follow very closely to the relationships predicted using plane-parallel theory and are, therefore, not shown. Consequently, if the effects of the multi-dimensional cloud structure can somehow be minimized, the albedo-emittance relationship at 0.83 μm and 11.5 μm can be estimated regardless of the vertical distribution of effective radius with an appropriate single-scattering albedo. The major remaining uncertainty is the asymmetry parameter of the ice clouds which can fundamentally affect this albedo-emittance relationship, as shown by Stackhouse, Jr. and Stephens (1991).

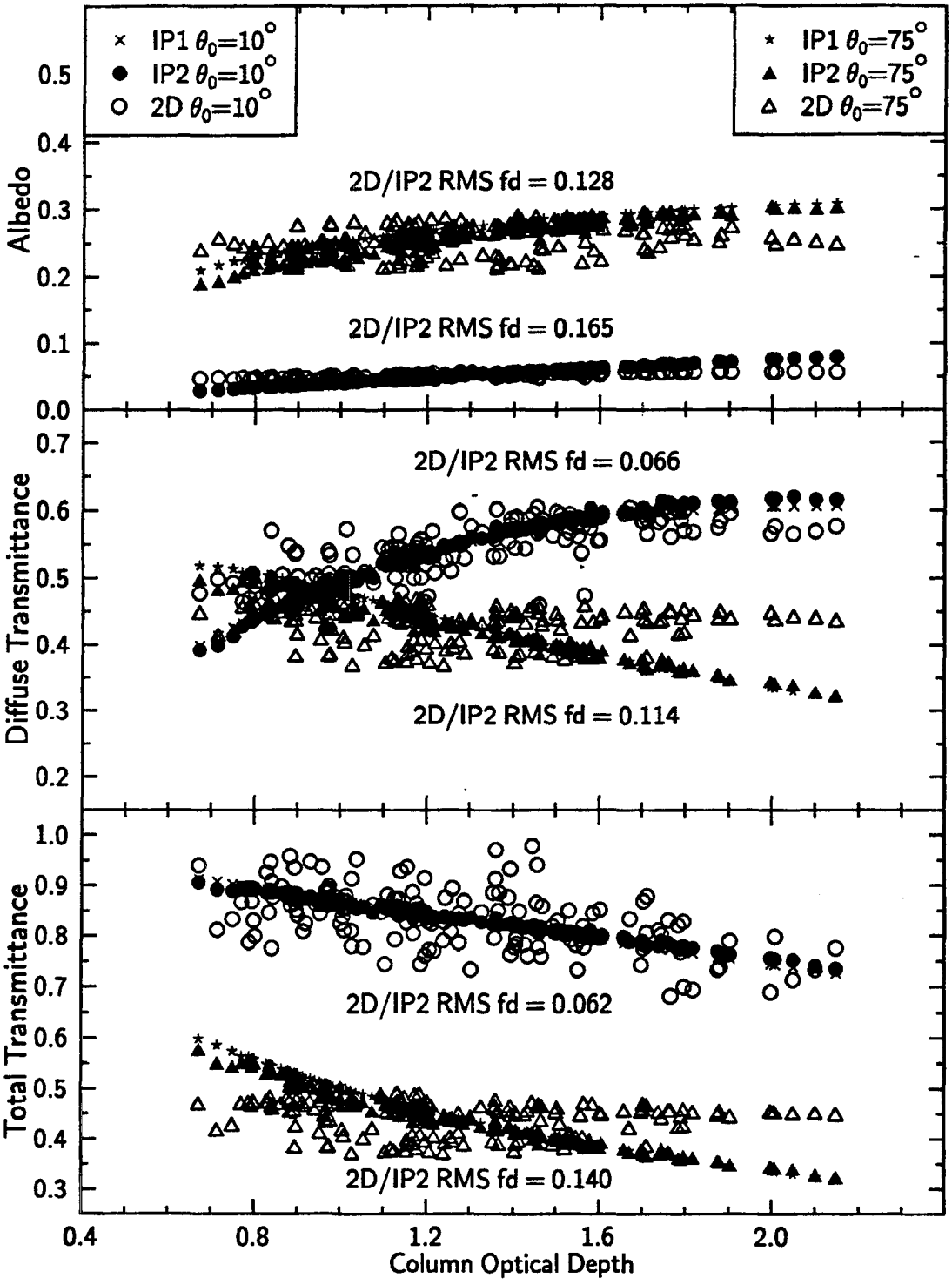

Figure 4.34: Albedo, diffuse transmittance, and total transmittance as a function of column optical depth at 2.21 μm for the variable ω_0 cloud with domain averaged optical depths of 1.26 and 4.0. Each panel contains the results for solar zenith angles 10° and 75°. IP1 and IP2 refer to independent pixel calculations performed using a domain averaged ω_o and variable ω_o respectively.

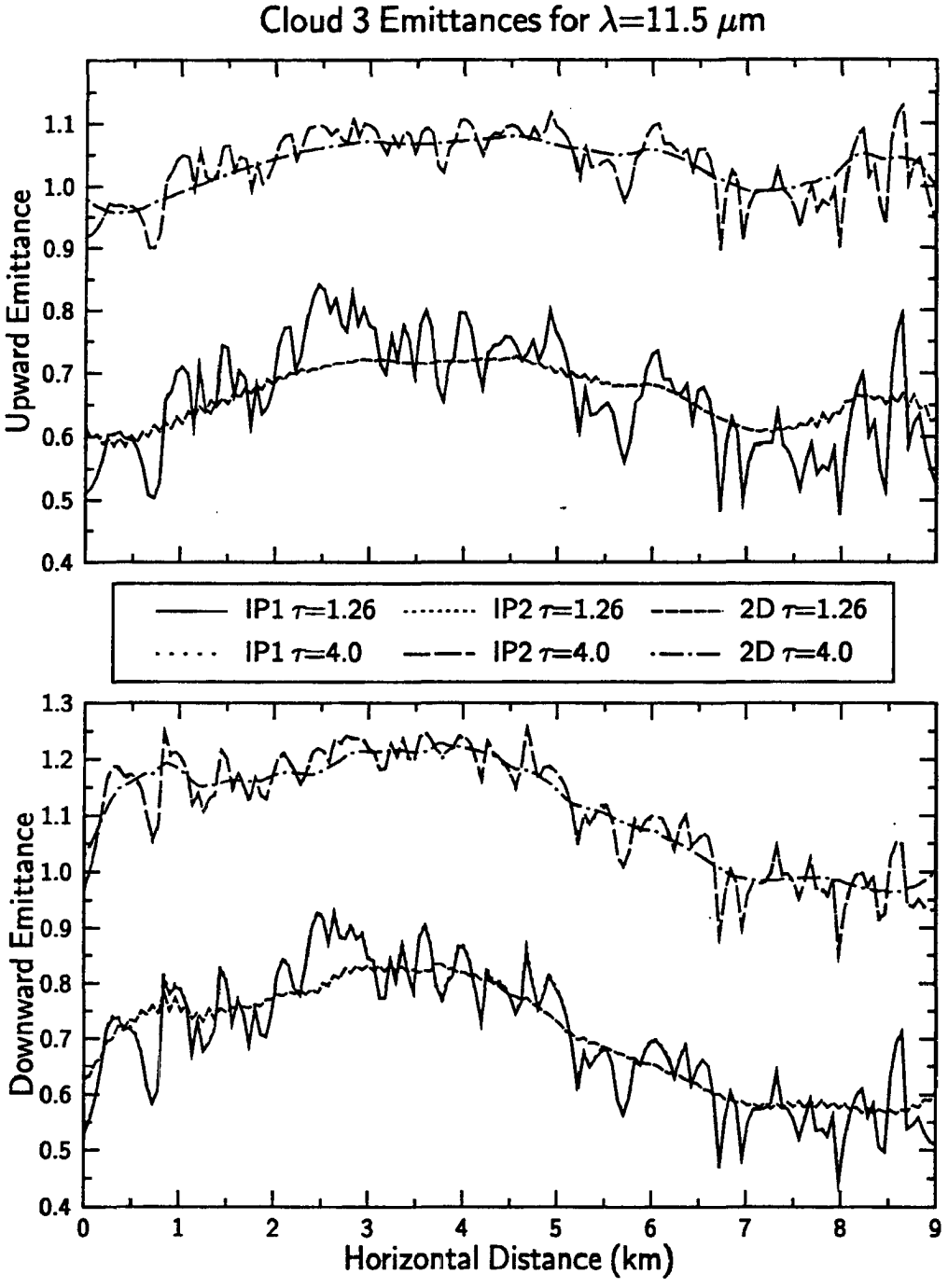

Figure 4.35: Upward and downward emittances as a function of horizontal distance at 11.5 μm for the variable ω_0 cloud with $\overline{\tau} = 1.26$ and $\overline{\tau} = 4.0$. Each panel contains the results for solar zenith angles 10° and 75°. IP1 and IP2 refer to independent pixel calculations performed using a domain averaged ω_0 and variable ω_0 respectively.

4.2.2 Domain Averages

In section 4.1.2, the domain average fluxes from 2D and IPA agreed nearly exactly for the stratified unbroken cloud corresponding to cloud 2 at 0.83 μm. This agreement is also observed in the case with variable microphysics and is shown in Table 4.4. The domain

Table 4.4: Domain averaged albedo, transmittance and absorptance for IP1, IP2, 2D simulations of the cloud with the variable ω_0 for domain averaged opticals of 1.26 and 4.0.

λ	$\overline{\tau}$	θ_0	Albedo			Transmittance			Absorptance		
(μm)		(deg)	IP1	IP2	2D	IP1	IP2	2D	IP1	IP2	2D
0.83	1.26	10	0.091	0.091	0.090	0.909	0.909	0.908	0.000	0.000	0.002
		50	0.174	0.174	0.175	0.825	0.825	0.823	0.001	0.001	0.002
		75	0.420	0.420	0.418	0.577	0.577	0.576	0.003	0.003	0.005
	4.0	10	0.272	0.270	0.269	0.725	0.726	0.726	0.003	0.004	0.005
		50	0.404	0.402	0.403	0.591	0.592	0.590	0.005	0.006	0.008
		75	0.606	0.604	0.598	0.388	0.389	0.393	0.006	0.007	0.009
2.21	1.26	10	0.052	0.051	0.051	0.834	0.835	0.834	0.114	0.114	0.115
		50	0.098	0.096	0.096	0.730	0.731	0.729	0.172	0.173	0.175
		75	0.268	0.256	0.254	0.450	0.444	0.441	0.282	0.300	0.305
	4.0	10	0.114	0.107	0.106	0.526	0.529	0.529	0.360	0.364	0.365
		50	0.179	0.165	0.165	0.372	0.371	0.366	0.449	0.464	0.469
		75	0.333	0.303	0.294	0.196	0.187	0.188	0.471	0.510	0.518

averages of IP1 and IP2 are nearly identical, agreeing many times to the fourth significant digit. The 2D domain averaged albedo, transmittances, and absorptances agree with both the IP1 and IP2 quantities by much less than 1% even for the thicker cloud case with $\overline{\tau} = 4.0$.

However, at 2.21 μm there are significant errors incurred by using the domain averaged single-scattering albedo. Table 4.4 shows that these errors increase with both the domain averaged optical depth and the solar zenith angle. Furthermore, the independent pixel calculations overestimate the domain averaged albedo and transmittance and underestimate the cloud absorptance in all cases. These error trends agree with those found in the simulations for clouds with constant microphysics. In fact, the relative errors between IP1 and 2D for the variable effective radius cloud are much larger than those for the unbroken clouds of constant microphysics. For example, the albedos of clouds 1 and 2 are overestimated in the IPA calculations by 2% and 4% respectively for the solar zenith angle of 75° and the domain averaged optical depth of 4.0. However, this overestimation of the albedos for this variable microphysics cloud is over 13%. The domain averaged absorptances for the same solar zenith angle and domain averaged optical depth are underestimated by IPA in clouds 1 and 2 by 2% and 6% respectively while the underestimation for the variable microphysics cloud is about 9%. Interestingly, the simulations for IP2 give much better results. These results indicate that at 2.21 μm information regarding the vertical distribution of single-scattering albedo is necessary to improve estimates of the domain averaged cloud properties for clouds with variable effective radius. Without this information the albedos of the cloud can be overestimated and the absorptance can be

underestimated by significant amounts approaching 10%. This has important implications not only for the calculation of cloud albedo, but also for the distribution of heating within the cloud. The later may play an important role in the growth or decay of the cloud itself.

As for 0.83 μm, the flux quantities for 11.5 μm agree to much less than 1% for all cases, even those cases with $\overline{\tau} = 4.0$. This is not surprising given that the horizontal interactions of flux, which cancel upon averaging over the domain, determine the variability at this wavelength. Therefore, the dependence of the domain averaged properties upon variation of the effective radius within a given cloud is a spectrally dependent process. The fact that the fluxes at particular wavelengths are more or less sensitive to changes in the effective particle size results in the use of spectral data to resolve such cloud properties.

4.3 Summary and Conclusions

This chapter demonstrates the effects of cloud structure on two-dimensional radiative transfer through clouds composed of ice particles with constant and variable effective radius. The flux simulations for two-dimensional clouds with constant and variable effective radius represent the first step towards calculating the bulk radiative properties of clouds with more realistic features. Simulations of the radiative fluxes in inhomogeneous clouds are performed for cloud structures derived from K_a-band radar observations as described in Chapter 2. Radiative flux simulations for the case of the constant effective radius are presented for three clouds, two of which are unbroken and one which is broken having a cloud fraction of 90%. These cases, especially the two unbroken clouds, represent situations where the plane-parallel approximation is expected to estimate the bulk cloud properties well since only the extinction varies throughout the cloud. The complexities of the broken cloud case test the limits of the plane-parallel theory. The simulations of clouds characterized by a variable effective radius further test the plane-parallel independent pixel theory due to the increased complexity in the cloud optical properties. The results are analyzed in terms of the differences between IPA and 2D fluxes both at the pixel by pixel and at the domain average spatial scales to infer the conditions under which the independent pixel approximation breaks down.

The results of the simulations indicate that the best agreement between IPA and 2D simulations occurs in more stratified clouds than in broken clouds. In the stratified clouds, IPA and 2D upward fluxes agree best at small solar zenith angles and large optical thicknesses while IPA and 2D total downward fluxes agree best at small solar zenith angles and small optical thicknesses . Overall, the agreement between IPA and 2D become worse under those conditions for which the horizontal interaction of radiation within the cloud increases. This is illustrated most clearly for the broken cloud case when the incident radiation enters the side of the cloud and horizontal radiative interaction occurs between the cloud sides. Since albedos and transmittances are calculated relative to a horizontal

surface by ignoring the incident flux to the cloud side, local transmittances exceed unity for the small solar zenith angles and local albedos exceed unity for large solar zenith angles. As a result of this behavior, local areas of positive and negative apparent absorptances are found. Despite these apparently nonphysical local albedos, transmittances, and absorptances, the domain averages of the 2D fluxes conserve energy relative to a horizontal surface. Additionally, the one-to-one correspondence that exists between IPA fluxes and column optical depth for clouds of constant effective radius breaks down in the 2D simulations when the horizontal interaction of radiation is allowed. The 2D fluxes in this case can vary by as much as $\pm 50\%$ of the IPA fluxes and biases are obtained in cloud regions of large optical depths.

Finally, comparison of domain averages between 2D and IPA reveal excellent agreement for the stratified cloud and much larger disagreement for the broken cloud example which was characterized by a 90% cloud coverage. Maximum errors for this broken cloud case approach 10% in the upward fluxes and over 24% in the total downward fluxes for large optical depths and large solar zenith angles. Also it was found that the IPA transmitted too much energy through the cloud and reflected too little compared to the two-dimensional simulations. This is especially true for the absorbing wavelength where errors in the transmission at large optical depths and large solar zenith angles approach a factor of 2.

The effects of the variable effective radius represented through the single-scattering albedo are found to be wavelength dependent. At 2.21 μm, where the single-scattering albedo is very sensitive to the changing effective radius, knowledge of the vertical variability of this parameter is crucial for the estimation of the bulk cloud properties, especially as the solar zenith angle and optical depths increased. For the thickest cloud and largest solar zenith angle, IPA calculations using a domain averaged single-scattering albedo result in a 10% bias of the domain average fluxes compared to 2D simulations. These errors are significantly larger than the errors found for the unbroken clouds with constant effective radius. Independent pixel calculations with the variable column single-scattering albedos produce errors compared to 2D which were several factors less. In all of these cases, the independent pixel calculations underestimate the absorptance at this wavelength which implies that the domain average cloud heating is underestimated by IPA. At the wavelengths of 0.83 μm and 11.5 μm, the sensitivity of the single-scattering albedo to the changes in the effective radius is much less and as a result the fluxes are relatively unaffected. Independent pixel calculations with both a domain averaged single-scattering albedo and the variable single-scattering albedo give domain averages which are virtually identical with each other and nearly identical to the 2D simulations. For these cases, the cloud structure in the form of the variable extinction produce the local disagreements between IPA and 2D fluxes that cancel upon averaging across the domain.

The results of the sensitivity studies indicate the regimes within which independent pixel plane-parallel theory will cause error. These regimes include instances when the solar zenith angle is large and the clouds are broken. The results of this chapter and those of Chapter 3 will be used as a framework to interpret the observations of radiances and fluxes measured during the FIRE Cirrus experiment. These observations were made in cirrus clouds at large solar zenith angles and at times were broken. Comparison of plane-parallel and two-dimensional radiative transfer calculations to these observations is made in Chapters 5 and 6.

Chapter 5

RADIATIVE AND MICROPHYSICAL OBSERVATIONS OF INHOMOGENEOUS CIRRUS CLOUDS DURING FIRE II

In the previous two chapters, the sensitivities of cirrus cloud radiative properties to cloud inhomogeneities are shown to become more important as solar zenith angles and optical depths increase. Although cirrus clouds are observed to be relatively thin (i.e., $\tau < 3$), the solar zenith angles at middle latitudes tend to be relatively large (i.e., $\theta_0 \geq 50^\circ$). Thus, the observations of bulk cloud radiative properties and the relation of these properties to the microphysical properties of these clouds are subject to uncertainties due to the inhomogeneous nature of cirrus clouds. Since the relationship between the microphysical and optical properties of cirrus clouds is of importance not only to the life cycle of these clouds but also to the effect of these clouds on the climate, the effect of the spatial variability upon the estimation of cloud radiative properties needs to be better understood.

In this chapter, the FIRE Cirrus II experiment and the instrumentation placed on board the Sabreliner aircraft are described. Then the cirrus case observed by the afternoon flight of the Sabreliner on 26 November 1991 is described. Methods are derived to infer the optical and radiative properties of cirrus clouds and the results are shown for this specific case with large solar zenith angles. The sensitivity studies of the previous chapter indicate that despite the large solar zenith angles, thin optical depths like those of this case ($\tau < 1$) give RMS agreement with independent pixel calculations to about 10% to 14%. As a result, the cloud transmittances from this case are expected to give good agreement with plane-parallel theory. In anticipation of this agreement a procedure that is based on plane-parallel theory, is then developed to estimate the asymmetry parameter of the cloud using the inferred radiative properties. The disagreement of the measurements with plane-parallel theory gives insight into the effects of inhomogeneity on the downwelling fluxes as observed in this case.

5.1 ISCCP and FIRE Cirrus IFO II

In conjunction with the objectives of the International Satellite Cloud Climatology Program (ISCCP), the First ISCCP Regional Experiment (FIRE) was devised in order to study the relationship between cloud structure, microphysics, and radiative properties for

both stratocumulus and cirrus clouds (Starr, 1987; Fire Cirrus Working Group, 1991). These clouds are important to climate because of their aerial coverage and persistence. To determine the climatology and climatological significance of cirrus clouds the relationship between the large scale satellite measurements and small scale microphysical and radiative measurements must be better understood. To this end intensive field observations (IFO) were made of cirrus clouds during FIRE Cirrus IFO Phase I and Phase II.

In IFO II, which was centered in Coffeyville, Kansas during a 4 week period between November 17 and December 7, 1991, observations of cirrus clouds were made simultaneously from ground based to satellite platforms. During this time the NCAR Sabreliner flew 17 missions, 11 of which sampled cirrus cloudiness with all systems running properly. The cirrus clouds sampled during the experiment ranged from thin orographic cirrus formations to thicker middle latitude cirrus associated with cyclonic development. One case involved the sampling of thin tropical cirrus. The missions were mostly flown parallel to the mean wind at the altitude of the cirrus cloud system. A few cases involved the sampling of mixed phase clouds where ice crystals were predominant at cloud top and supercooled droplets at cloud base. The general flight plan consisted of flying along a straight and level path at several different altitudes within the cloud usually starting at cloud top and working down towards cloud base and then returning to cloud top.

Many of the flights were coordinated with flights from several other aircraft involved in this experiment (i.e., NASA ER-2, NCAR King Air and the University of North Dakota Citation) and still other flights were coordinated with local satellite overpass times with the Landsat, AVHRR and NOAA-9 satellites. Besides the many aircraft and satellite observations, an extensive array of ground based sensors were deployed in and around the central hub site in Coffeyville, Kansas. These included various types of radiation instruments such as radiometers, interferometers, lidars, and radars. There were also many other instruments deployed which measured atmospheric state variables. These instruments included wind profilers, acoustical sounders, and various rawinsondes.

The flight plans of the various aircraft were devised in part to support the arrays of ground based sensors. One Sabreliner flight in particular (Nov. 26 p.m.) was centered at the FIRE II hub site which contained the Ka-band radar. This flight contained a time series of measurements that can be co-located with radar reflectivities. This case and the resulting analysis is the subject of the remainder of this chapter. The remainder of this section is dedicated to the description of the various measurements required for the analysis of this unique case study.

5.1.1 Sabreliner Instrumentation Package

To reach the objectives of the FIRE Cirrus experiment, the NCAR Sabreliner Aircraft was specially equipped to measure atmospheric, microphysical, and radiative properties of *in situ* cirrus cloudiness that can be subsequently compared to other observing systems.

The instruments on board the Sabreliner along with the quantities measured pertinent to this case study are presented in Table 5.1. As indicated by the table, the atmospheric conditions measured were the temperature, moisture and winds. Microphysical measurements included a PMS 2D probe as well as a video camera to measure small particles. The radiation instrumentation included the standard Eppley broadband radiometers, NASA Ames Research Center's Total Direct-Diffuse Radiometer (TDDR), and the CSU-CSIRO Spectrally Scanning Radiometer (SPERAD). Each of these three types of instruments and their measurements are briefly discussed in the following subsections.

Aircraft and Atmospheric State Instruments

Information regarding the state of the aircraft and the environment in which cirrus clouds occur is vital to the interpretation of the measurements collected in flight. Additionally, information regarding the exact location and the speed of the aircraft is essential to co-locating the aircraft with other observing platforms. The essential aircraft state variables of location, heading, speed and acceleration are measured by the inertial navigation system of the aircraft (INS). The INS is calibrated before and after flight and is known to be subject to a degradation of data quality that is oscillatory in nature. This in flight degradation affects the estimation of aircraft location the most and so backup systems are provided to estimate the position of the aircraft. The backup system used in this case study is the Global Position System (GPS) which is described later during description of the co-location between the aircraft and the radar. Knowledge of the exact heading and orientation of the aircraft relative to the mean wind and the sun is important for the correction and interpretation of the aircraft radiative measurements discussed below. Additionally, many of the other atmospheric state variables depend upon the INS measurements as noted in Table 5.1. The precision of the INS measurements of position and orientation are 0.0014° (corresponding to about 156 m) and 0.0028° respectively (Miller and Friesen, 1989).

The aircraft is also equipped with a variety of instruments that measure quantities required to infer atmospheric state variables. A calibrated pressure transducer corrected for flow distortion measures the static air pressure outside the aircraft. This pressure is used to infer the aircraft altitude using the hypsometric approximation and the NACA standard atmospheric lapse rate (Miller and Friesen, 1989). For this reason, the altitude estimations from the aircraft are subject to errors based upon the actual atmospheric lapse rate of the atmosphere.

The ambient air temperature outside the aircraft is computed from the combination of a variety of instruments including total temperature sensors, calibrated and differential pressure sensors and the INS (Miller and Friesen, 1989). The measurement of moisture at low temperatures has been one the problems that has hampered research into the development of cirrus cloudiness. For this experiment, the Sabreliner was not only equipped with

Table 5.1: The instrumentation package on board the NCAR Sabreliner aircraft during FIRE Cirrus Phase II used in this research.

Instrument Name (Acronym)	Quantity Measured (Description)
Aircraft State	
Inertial Navigation System (INS)	Latitude and Longitude ($\approx 156m$ resolution)
INS	Pitch, Heading and Roll Angles (0.0028° resolution)
INS	Ground Speed (0.012 m/s resolution)
Global Position System (GPS)	Latitude and Longitude ($\approx 111m$ resolution)
Atmosphere State	
Calibrated Pressure Transducer (CPT)	Ambient Air Pressure
Total Temperature Sensor (TTS), INS, CPT, and Differential Pressure Transducers (DPT)	Ambient Air temperature
INS, CPT, DPT, TTS, Gust Probe Differential Pressure Sensors	Horizontal and vertical wind components (quality affected by INS degradation)
Dew-Point Hygrometer	Frost point temperature below 0°C adjusted to dew point temperature
Cryogenic Hygrometer	Dew point and frost point temperatures
Microphysics	
Particle Measuring System 2D-C Probe	Particle cross-sectional areas (100 to 5000 μm with 50 μm resolution)
Video Ice Particle Sampler (VIPS)	Video images of particles (particles greater than 10 μm in diameter)
Radiation	
Eppley Infrared Radiometer	Upwelling and downwelling broadband infrared irradiance (3.0 to 50 μm).
Eppley Shortwave Radiometer	Upwelling and downwelling broadband solar irradiance (0.3 to 3.0 μm).
Eppley Shortwave Radiometer w/ Red Dome	Upwelling broadband near infrared irradiance (0.7 to 3.0 μm).
CSIRO/CSU Spectrally Scanning Radiometer (SPERAD)	Downwelling visible irradiance and upwelling visible radiance (48 channels, 15–25 nm resolution from 0.4 to 1.1 μm)
Total-Direct-Diffuse Radiometer (TDDR)	Spectral downwelling irradiance at 7 visible channels (0.380, 0.412, 0.500, 0.675, 0.862, 1.064 and 1.600 μm)

the standard dew point sensor (which cannot measure dew points less than -54°C), but also with a cryogenic hygrometer. The hygrometer measurements should greatly improve the estimation of the water vapor concentrations inside the cirrus clouds. The sampling rates for all of these aircraft and atmospheric state variables is averaged to 1 Hz.

Information regarding the horizontal and vertical components of the winds is inferred from measurements by a variety of sensors; the most importantly of which are the differential pressure sensors located in the gust probe. These sensors are used to derive the aircraft true air speed (also a function of the ambient temperature) and the aircraft attack and sideslip angles. Coupled with position and velocity information from the INS, this information is sufficient to derive the ambient horizontal and vertical wind components (Miller and Friesen, 1989). Since the INS is known to suffer degradation during the flight, these wind component estimates are subject to a time dependent uncertainty. According to Lenschow and Spyers-Duran (1989) the error for each of the horizontal wind components is given by

$$\epsilon_{u,v} = \pm(1.0 + 0.5t) \tag{5.1}$$

where t is the elapsed flight time in hours and the units are m s^{-1}. The vertical velocities can be estimated to within ± 10 cm s^{-1} but are subject to offsets which must be corrected. The information regarding the horizontal wind components will become very important to the co-location of aircraft and radar measurements discussed later in this chapter.

Microphysical Instrumentation

Table 5.1 also shows the microphysical instruments included on the Sabreliner. In particular, the PMS 2D-C probe and the Video Ice Particle Sampler (VIPS) are used to derived the microphysical information for this study. The 2D-C probe is a laser spectrometer that measures cross-sectional area of particles passing through a sampling area. The areas are used to infer microphysical information such as maximum dimension, cross-sectional area, and size distributions. The integrated size distributions are used to infer ice water content (IWC) and other mass related quantities. This particular probe measured particles with maximum dimensions of 100 μm to 5000 μm with a resolution of 50 μm. The particles are typically counted for 5 seconds to produce reliable size distribution information. At a ground speed of 180 m/s, sampling rate gives a size distribution for every 900 m.

The VIPS instrument consisted of a continuously moving film coated with an oil substrate that is exposed directly to the air stream. Particles impacting the film are subsequently videotaped. The subsequent films are analyzed to measure particle dimensions and cross-sectional areas. The advantage of this instrument is its ability to measure particles down to a size of 10 μm. Size distributions can also be inferred over a collection time interval, chosen to be 7 seconds for this research (2D-C measurements can also be integrated over the identical period for comparison). Size distributions including such small

ice particles have not been measured reliably in the past and these measurements combined with the 2D-C probe measurements provide much needed information concerning the entire the size distribution. At this time, the VIPS data set is available only sparsely during flights on November 26 and December 5. The data from both the 2D-C probe and the VIPS instruments is provided by NCAR.

Radiation Instrumentation

The radiation package included on the Sabreliner is designed to provide measurements of cirrus cloud radiative properties that have not been previously observed from aircraft. The NASA Ames' TDDR measures the downwelling solar radiation irradiance at the seven different channels as indicated in Table 5.1 (Valero et al., 1989). Each channel has a bandpass of approximately 10 nm. The instrument is mounted on the top of the aircraft and has an arm designed to periodically shadow the detector from the disk of the sun. At this point in time, the radiometer measures purely diffuse radiation and this information can be used to compute the direct component of the solar radiation. The attenuation of the direct beam of radiation as the aircraft passes underneath the cloud is used to compute the optical depths of the clouds at the wavelengths corresponding to the channels of the instrument. The sampling rate for this instrument was maintained at about 3 Hz. Some of preliminary processing of the data from this instrument is performed at NASA Ames Research Center. Unfortunately for this case study, processing revealed that the 1.6 μm channel malfunctioned during the experiment and information from this channel is irretrievable.

The SPERAD instrument measures the spectral flux throughout the visible and near infrared wavelengths (Stephens and Scott, 1985). Although the instrument had two filter wheels capable of measuring from 0.4 - 2.4 μm, the data from the NIR filter (1.2 to 2.4 μm) was unusable. The calibration of SPERAD is presented in detail in appendix A. The instrument itself was mounted in the nose of the aircraft and measured the upwelling spectral radiance and downwelling spectral flux. With an average of 20 nm resolution throughout the visible spectrum, this instrument is used to obtain spectrally detailed information of the transmittance and reflectance properties of cirrus clouds. The spectral bandpass of each channel varied from about 10 nm to 20 nm. Because of some timing differences due to modifications of the instrument since (Stephens and Scott, 1985), the channels observing upwelling radiation were shifted relative to those measuring downward radiation. The instrument's channels and bandpasses as estimated from the calibration are given in Appendix A. SPERAD was configured to run in either high frequency or low frequency modes. High frequency observations gave a sampling rate of approximately 3 Hz which corresponds to a spatial variability at a ground speed of 180 m/s of 60 meters. The low frequency observations were collected at 1/3 to 1/4 Hz. The rate varied depending upon the filter wheel motor which tended to slow down at the extremely low temperatures.

The high frequency mode provides useful information as to the spatial variability of the radiation field within the cirrus cloud.

Finally, broadband Eppley radiometers were attached to the aircraft to measure irradiance in the solar and infrared wavelengths. As shown in Table 5.1, an Eppley radiometer with a red dome was also flown to measure reflected flux in the near infrared wavelengths. These radiometers are typically used for field experiments such as FIRE Cirrus IFO II, but these measurements combined with TDDR and SPERAD measurements should give more insight into the radiative properties of cirrus. The sampling rate for these measurements is 1 Hz, identical to the sampling rate for all the other state instruments on the aircraft. The calibration of these radiometers is performed at the National Center for Atmospheric Research in the Research Aviation Facility (NCAR RAF).

5.1.2 K_a-band Radar Observations

The radar reflectivity measurements are a vital part of this study. The NOAA Wave Propagation Laboratory (WPL) 8.66 mm K_a-band radar was already discussed in Chapter 3 for the adaptation of RHI scanning data to 2D extinction fields. For this case study, the radar reflectivity time series generated when the radar was vertically pointing are used to determine cloud structure and infer ice water contents which are then compared to aircraft microphysical and radiative observations. In this vertically pointing mode, a 3 second dwell time is required to obtain the appropriate signal to noise ratio (Uttal et al., 1994). The full beam width of the radar is 0.5° and this corresponds to a spatial resolution at 8 km of about 70 m. In addition to the height above the radar, the horizontal spatial resolution of the radar depends upon the mean wind of the specific cloud case. For example, if the mean wind is 30 m s^{-1} the horizontal resolution is approximately 90 m given the 3 second dwell time and subject to the wind shear throughout the cloud layer. The vertical resolution is dependent upon the pulse width of the radar and is 37.5 m for the reflectivity data used in this study. These and other properties of this radar are summarized in Table 5.2.

The vertical profile of the wind speed and direction is also required for this study. Estimation of the winds above Coffeyville were also obtained from the K_a-band radar Velocity Azimuth Display (VAD) scans. The radar was set at an elevation angle of 75° and 360° azimuthal scans were made. Doppler velocities from the cloud particles are obtained and converted to wind vectors. The accuracy of the wind speeds computed in this manner is ± 0.5 m s^{-1}. During the FIRE II experiment, the radar operated in vertically pointing mode for a 20 minute period before the mode was changed to collect RHI and VAD mode data. As a result, estimates of the winds from VAD scans are made twice per hour. All the radar data is analyzed and provided by NOAA at the Wave Propagation Laboratory in Boulder, CO.

Table 5.2: Summary of the characteristics of the doppler radar used for this study (adapted from Kropfli *et. al.*, 1994).

Radar Characteristic	Specification
Wavelength (mm)	8.66
Peak Power (kW)	100
Pulse Width (m)	37.5
Beam Width (deg)	0.5
Dual Polarization	yes
Scannable	yes
Doppler accuracy (4 sec dwell time)	< 5 cm s^{-1}
Sensitivity with 4 s dwell (minimum reflectivity at 10 km)	-31 dBZ

5.1.3 Other FIRE II Data Sources

Besides the radar data, the FIRE II operations plan provided for a dense network of rawinsondes. Of specific importance to this work, (CLASS) rawinsondes. were launched at every three hours at various sites within the operations hub during designated intensive operation periods (IOPs). The soundings give atmospheric altitude, pressure, temperature, relative humidity, and horizontal wind components that are averaged to 5 mb pressure intervals. These soundings are used to correct the aircraft estimations of altitude and verify wind and temperature measurements at the flight altitude. The soundings from Coffeyville launch site were used in the study presented here. The data was collected by the NCAR and distributed through the Langley Distributed Active Archive Center (DAAC).

5.2 Case Study: November 26, 1991 (p.m.)

The afternoon flight of the Sabreliner on November 26 of the FIRE Cirrus IFO II experiment was flown through a developing upper tropospheric cloud system centered over a location in the vicinity of the K_a-band radar. The flight occurred during the middle to late afternoon period and profiled the cloud starting at cloud top and working toward cloud base. As such this case offers a good opportunity to assess the effects of inhomogeneities upon cloud properties inferred from downwelling radiation. This case also offers the unique opportunity to obtain microphysical and radiative measurements in a portion of the cloud with structural information provided by the radar that constitutes the focus of following chapter. This section describes the synoptic situation of this case and the Sabreliner observations obtained during the flight.

5.2.1 A Synoptic Overview

The development of cirrus and eventual development of multi-layered cloud for the November 26 case was associated with an upper level trough propagating through the

central United States. The surface analysis on this date at 7:00 am E.S.T. (or 5:00 am C.S.T., 1100 UT) is shown in the top panel of Figure 5.1 (U.S. Daily Weather Maps, November 26, 1991). The map indicates the position of a cyclone located on the U.S.-Canadian border with its associated cold, warm and occluded fronts. Associated with this system is an upper level trough which is indicated by the thick solid line in the bottom panel of Fig. 5.1.

The upper level trough in the mid-western United States was located at an exit region of a strong northwesterly jet. The dynamics associated with this feature are closely related to the subsequent development of the cloud system observed in this case (Mace and Ackerman, 1993). Cold air advection occurred as the jet core moved southeastward toward the FIRE hub region. The system amplified as it moved eastward in time, especially between 18 UTC and 21 UTC between 8 and 12 km (Mace and Ackerman, 1993). The amplification of this dynamically active system as it propagated through the Coffeyville area is responsible for the westerly shift in the horizontal winds which will complicate the co-location analysis described below. The magnitude of this amplification is shown by the adiabatic vertical velocity fields at 7.5 km from 18 UTC to 21 UTC in Figure 5.2a and b (Mace and Ackerman, 1993). At 21 UTC, which roughly corresponds to the time of the Sabreliner flight leg, a strong area of upward motion to the north and corresponding area of subsidence had developed to the west of the radar site. The area upward motion corresponded to the thickening of cirrus throughout the region which subsequently cleared as area of subsidence passed through.

The propagation of this feature through the FIRE hub site in Coffeyville, Kansas produced thick cirrus along the leading edge. The first influence of the approaching trough system was observed as a region of cirrus spissatus spread over the area around local noon (18 UTC) (Starr, Daily Mission Summary). The development in time of this cloud system at the radar site is shown by the time series of radar reflectivities from 19 UTC to 23 UTC in Figure 5.3. This figure shows that the cloud deck over the hub area increased in thickness and the cloud base lowered throughout the afternoon. At 20 UTC (2:00 p.m. local time) a broken cirrus layer was observed between 8.5 and 9.5 km. By about 22 UTC (4:00 p.m. local time), there were multi-layered clouds with cloud bases as low as 3 km. The flight of the Sabreliner aircraft during this time is described in the next section.

5.2.2 The Sabreliner Flight

The NCAR Sabreliner flew two missions on November 21, 1991. The latter flight, between 19:42 UT to 22:15 UT (1:42 to 4:15 p.m. local time), corresponds to the passage of the upper level disturbance described above. The aircraft flight track was centered just south of the FIRE hub site, which is where the radar was located. The flight plan consisted of race track and figure 8 straight and level flights legs located at various altitudes working

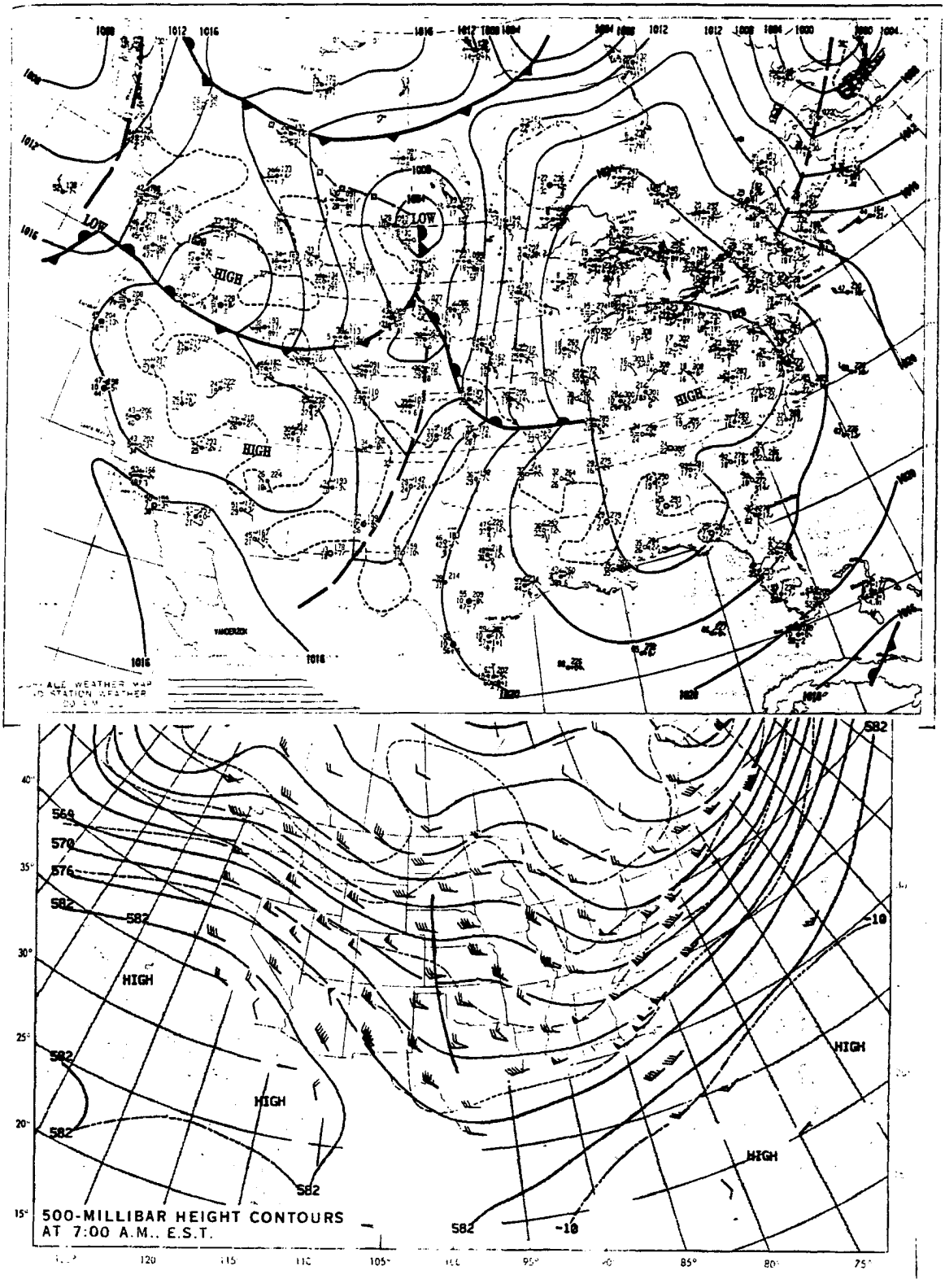

Figure 5.1: Surface analysis (a) and upper level heights (b) at 12 UTC (7 am E.S.T.) on November 26, 1991. The upper level trough axis is in (b) is indicated by the dark line.

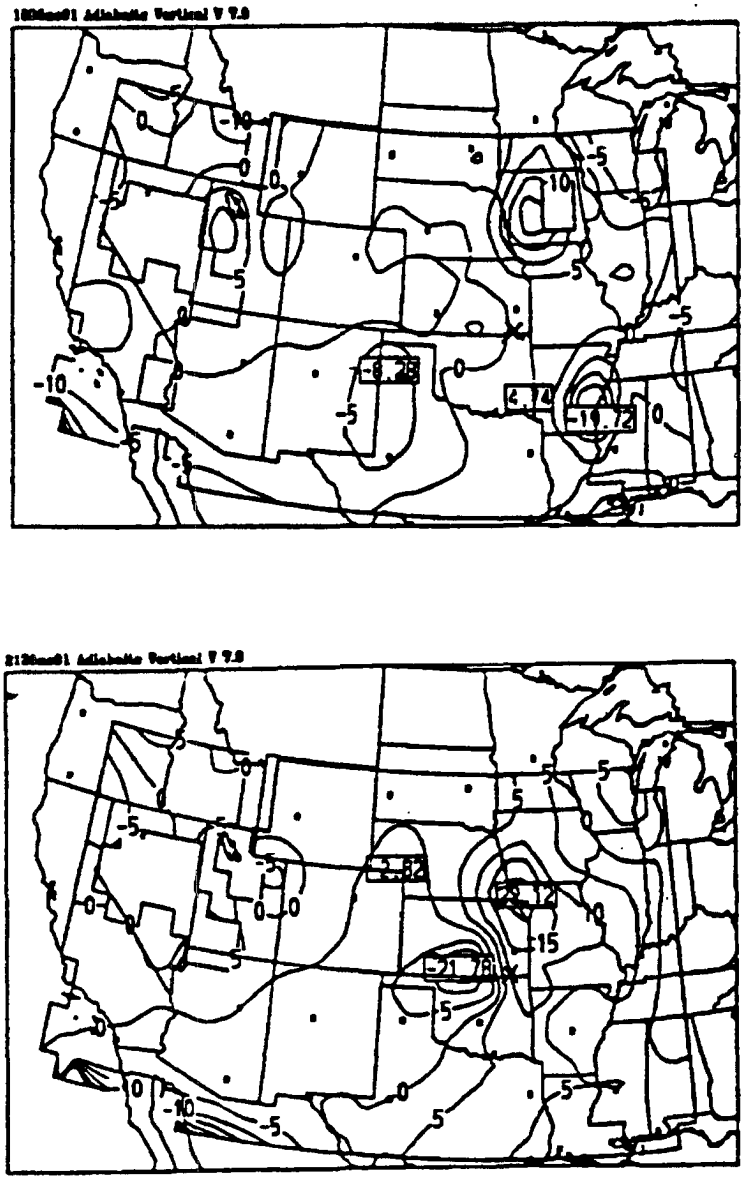

Figure 5.2: Adiabatic vertical velocity for (a) 18 UTC and (b) 21 UTC on November 26, 1991 after Mace and Ackerman (1993). The units are cm s^{-1} and upward velocities are positive. The location of the FIRE hub site in Coffeyville, Kansas is indicated by an 'X' in both plots.

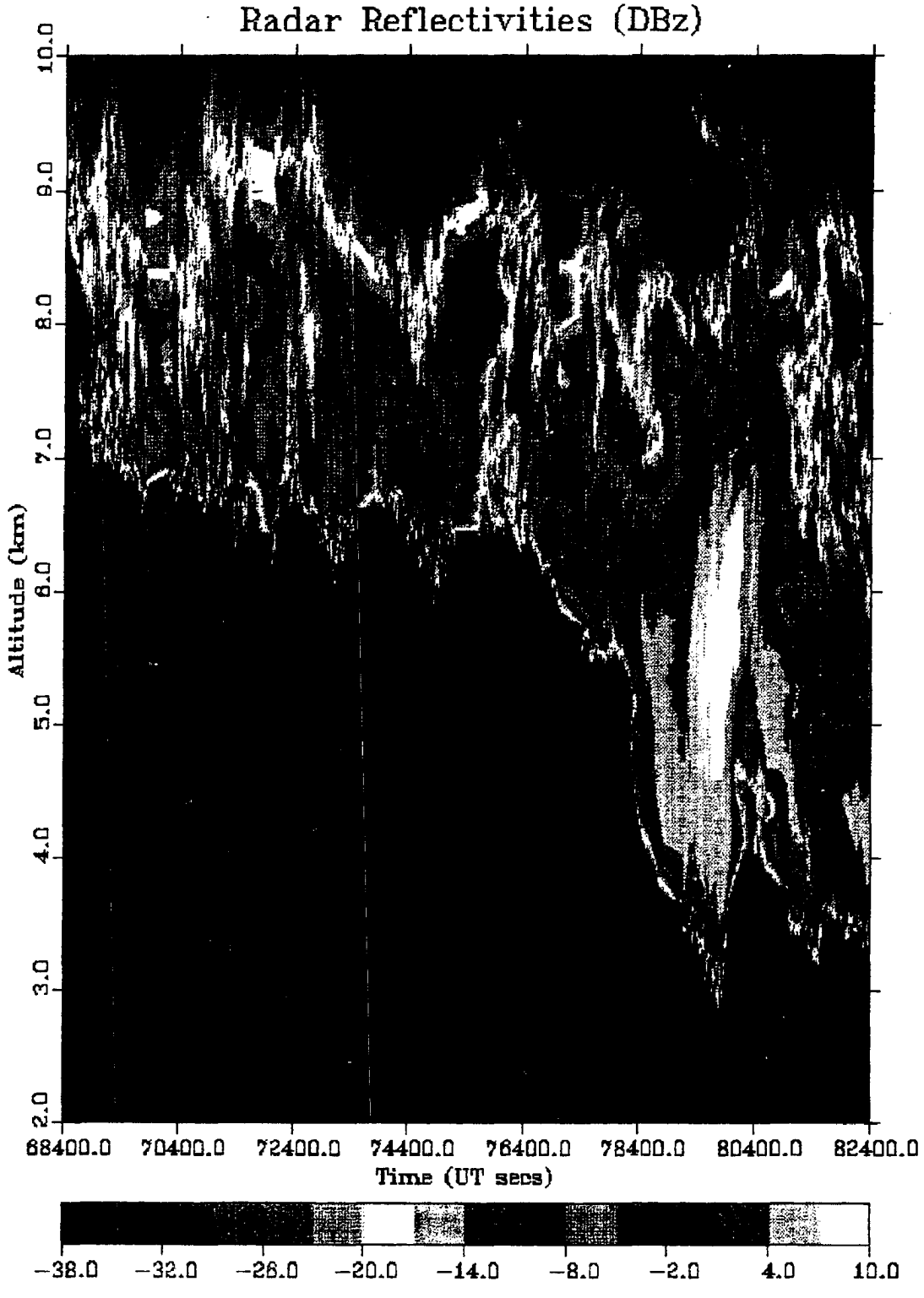

Figure 5.3: Time series of radar reflectivity from the K_a band radar between 18 UT and 23 UT on November 26, 1991.

down from cloud top. The flight track of the aircraft in this case is shown in Figure 5.4. Note, that many of flight legs were flown with a west-southwest to east-northeast directed orientation. The direction of these flight legs roughly corresponded with the direction of the mean wind which although shifting throughout the period mainly blew from west-southwest to east-northeast ($\sim 250°$). These will be the most useful legs for co-locating aircraft and radar observations since the radar time series represents clouds advecting with the mean wind.

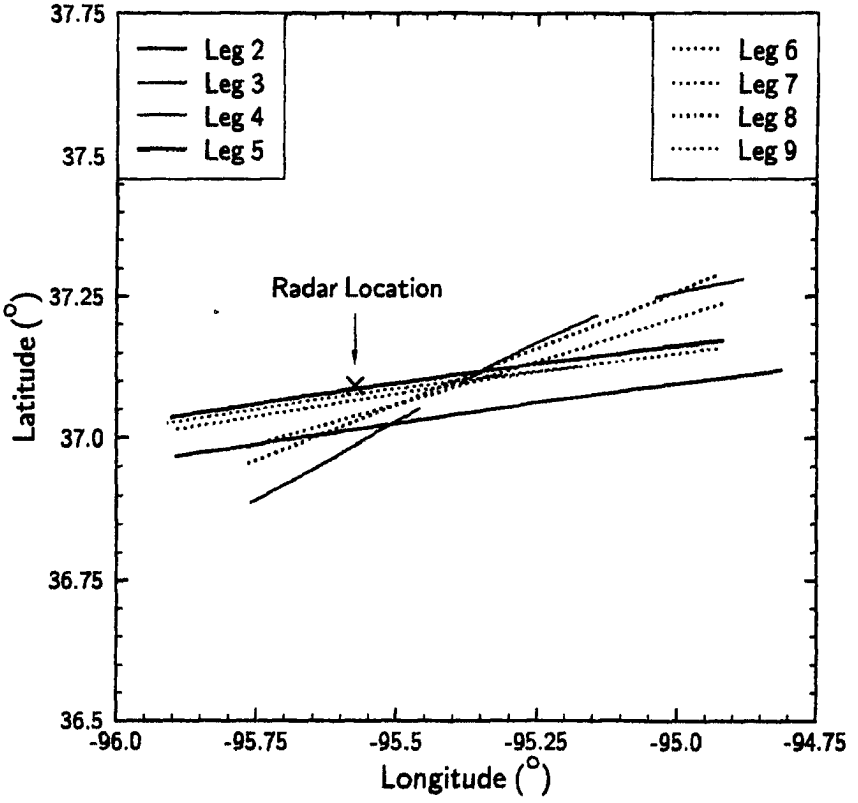

Figure 5.4: Latitude and longitude position plot of the aircraft during each of the straight and level flight legs during the flight in the afternoon of November 26, 1991.

Figure 5.5 schematically illustrates the times and altitudes at which the Sabreliner flew straight and level flight legs. Flight legs 1 and 2 represented cloud top flight legs at 9.5 km. However, referring to Figure 5.3 reveals that not only were cloud bases lowering during this period, but so were the cloud tops. For this reason, despite the fact that the aircraft was flying at lower altitudes the cloud was still sparse and thin until the aircraft reached a level of about 8.2 km. These properties of the observed clouds have important implications in regards to the co-location of the aircraft and radar and the interpretation of the downwelling radiative quantities.

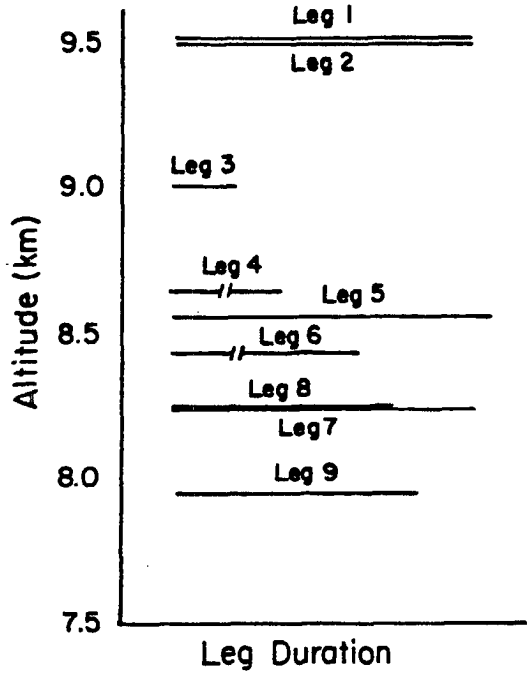

Figure 5.5: Schematic of the altitudes for each of the straight and level flight legs of the Sabreliner for the afternoon flight on November 26, 1991.

5.3 The Estimation of Spectral Solar Cloud Properties from Flux Measurements: Assessing the Effects of Variability

The estimation of intrinsic cloud optical properties such as cloud optical depth and the asymmetry parameter and the relation of the these properties to the cloud transmittance and albedo in the presence of heterogeneity is vital to understanding the effect of cloud inhomogeneity on cloud radiative properties and incorporating these effects in various cloud models. The observations from the Eppley radiometers and TDDR provide information to infer these properties based on retrieval methods that depend in large part on the plane-parallel assumption. Thus, the extent to which the observations can be explained by plane-parallel theory reflects the importance of the cloud inhomogeneities.

The TDDR instrument is used to derive spectral cloud optical depths, direct-to-total ratios and transmittances. The Eppley radiometers are used to calculate broadband cloud properties such as albedos. Deriving a relationship between the broadband and spectral flux allows the estimation of a spectral albedo. The optical depth, direct and diffuse parts of the cloud top downwelling spectral irradiance, total transmittances and albedos provides sufficient information for the estimation of an idealized asymmetry parameter. In this section, the spectral cloud properties for the 26 November afternoon flight and a procedure using the plane-parallel assumption to estimate an asymmetry parameter. Although this particular case has large solar zenith angles which tend to increase sensitivity

to cloud structure as shown in Chapter 4, the thin optical depths observed are expected to mediate this effect. As a result, the procedure gives insight into the importance of cloud structure in determining the transmittance properties of cirrus cloudiness.

Determining the Direct and Total Flux Components from TDDR

The TDDR instrument is uncalibrated for this experiment so the raw voltages are used as a proxy for the flux. This inherently assumes that the flux is related to the voltage by a multiplicative constant and may be a source of uncertainty. Each channel voltage is corrected for a dark current bias which was measured on the ground during the experiment. Two time series of the 0.5 μm voltage at cloud top (flight leg 2) and 1 km below cloud top (flight leg 5) observed during the 26 November afternoon flight are shown in Figure 5.6. Clearly the baseline at cloud top has a much higher signal than that from the lower flight leg indicating the reduction of the total radiation with decreasing altitude. Note also that the spikes at cloud top are longer than those within the cloud. Since each spike occurs when the shadowband arm blocks the solar disk, the longer the spike the more the direct beam contributes to the total radiation. Thus, a reliable estimation of the direct beam length is required to estimate the components of the total flux. A sophisticated technique is used by NASA Ames (see,Valero et al., 1989) to deduce this direct beam voltage. The technique accounts for the forward scattered diffuse radiation blocked by the shadowband arm and is accurate to within a percent or so, especially at cloud top where the pulses are very clearly defined. Considering these uncertainties and the sensitivity of the instrument, the uncertainty in the direct beam length measurements is taken to $\pm 1\%$ at cloud top and $\pm 3\%$ within the cloud.

In principle, comparison of the direct beam length to the baseline voltage gives the fraction of the total downwelling radiation which is composed of the direct beam. This fraction is referred to as the direct-to-total ratio hereby denoted as $R_{D/T}$. To estimate $R_{D/T}$ the total flux at the time of the direct beam measurement is required. Broadband Eppley flux measurements are used to estimate the total flux since this data provides a smooth continuous sampling of the total downwelling flux over the time when TDDR is shaded by the shadowband. Figure 5.7 shows the Eppley downwelling total flux plotted with the TDDR spectral flux for a shadowing event during Leg 5. Although there are some differences between the sensitivities of these measurements (i.e., the broadband flux is sensitive to water vapor absorption), the two measurements track well. Since TDDR measures an approximate total flux (the shadowband is always present and blocks some diffuse radiation) when the shadowband does not block the disc of the sun, the flux of TDDR can be related to the total broadband flux. The time required for the shadowband to move in and out of the disk of the sun depends upon the aircraft tilt and solar zenith angles (see Fig. 5.7). During this flight the average time required was approximately 6 seconds. The central time corresponding to the direct beam measurement in this 6 second

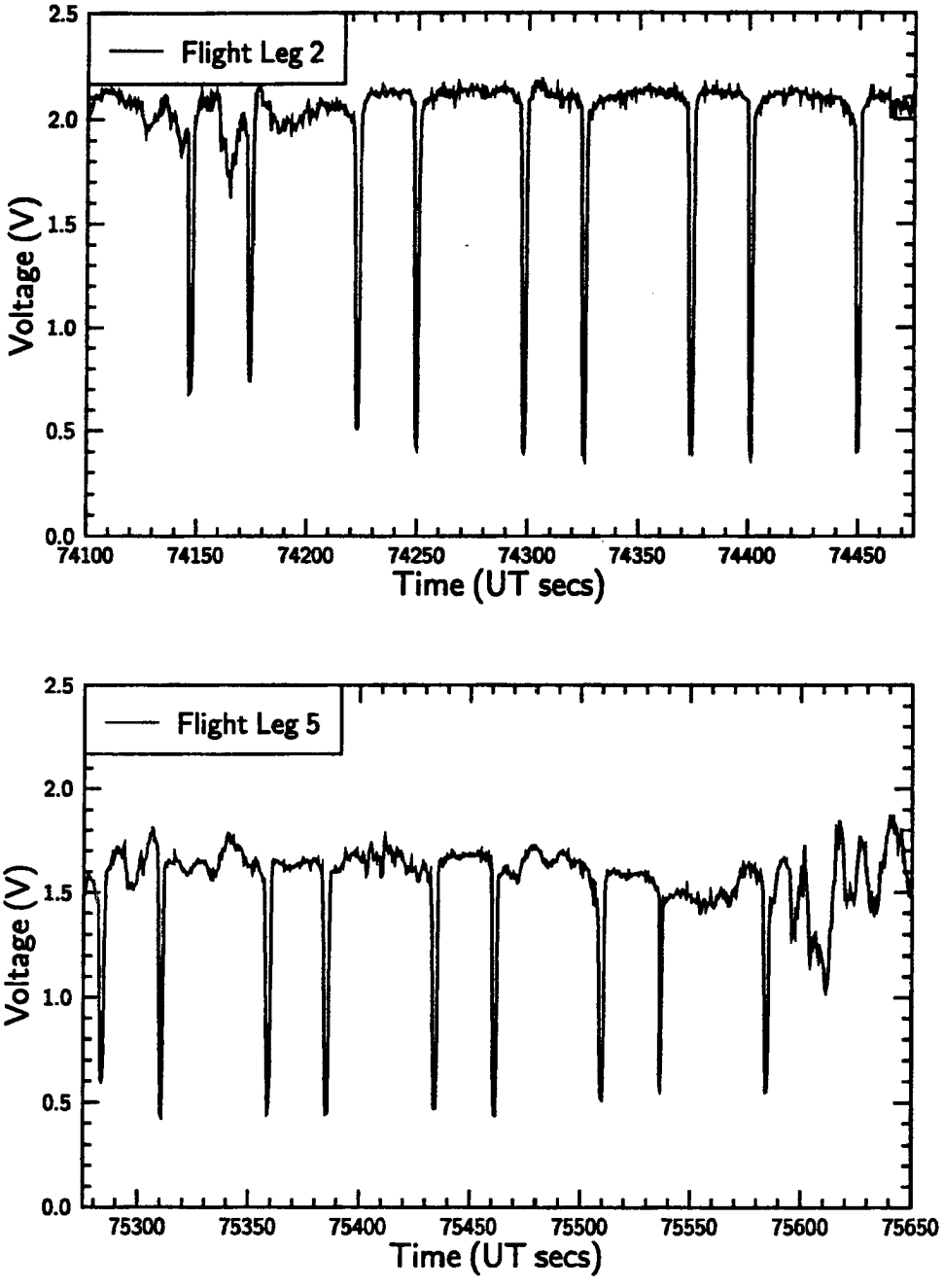

Figure 5.6: Two TDDR voltage time series at a wavelength of 0.5 μm at cloud top and 1 km below cloud top.

window is provided by NASA Ames. To estimate the total spectral TDDR voltage at the time when the direct radiation from the sun is blocked, the TDDR and Eppley fluxes 10 seconds to the left and right of the window are averaged and ratioed (see the bounding box shown in the Fig. 5.7). This ratio is then used to relate the broadband Eppley fluxes to the spectral TDDR voltages at the time when the shadowband arm is blocking the disk of the sun. In this way, an estimate of the TDDR total spectral voltage is obtained. Figure 5.7 also shows the estimate of the total voltage using this simple method (see the filled circle). The diffuse voltage, as depicted in Fig. 5.7 by the filled square, is computed as the difference between the total and the direct beam voltages. The uncertainties of the total voltage estimates depend upon the sensitivity of the Eppley radiometers and the variability of flux field. Because the Eppley radiometers have a response time on the order of a second, high frequency variations in the flux field are smoothed. However, as evidenced in the figure the 3 Hz TDDR measurements do not contain significantly greater variability than the Eppley measurements. Another source of error may be caused by the shadowband arm which blocks diffuse radiation from the detector. This may be a problem deeper within a cloud system as the diffuse flux becomes isotropic. However, the clouds sampled here are very thin and most of the diffuse energy should be near the direction of the sun. As a result the uncertainty in this method of estimating the total voltage is taken to be ±3%.

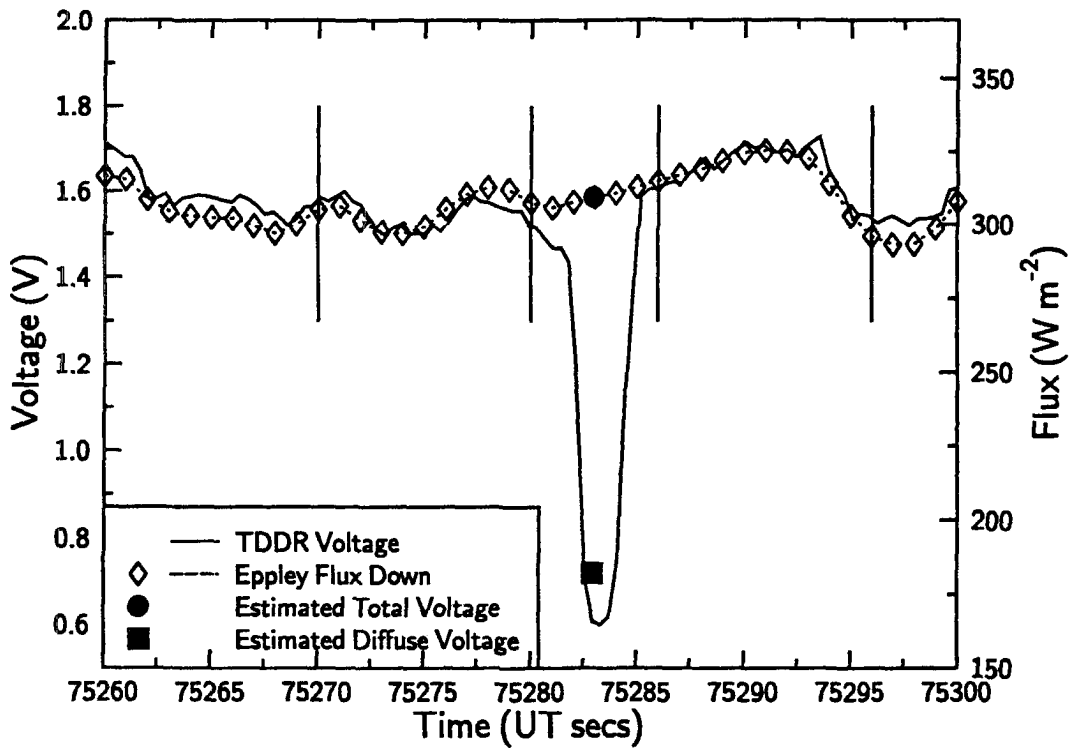

Figure 5.7: TDDR flux time series at a wavelength of 0.5 μm

Once the total spectral flux is estimated, then the direct-to-total flux ratio is found at that time by

$$R_{D/T} = \frac{\frac{\mu_o(t)}{\mu_p(t)} V_{dir,\lambda}(\tau^*_\lambda, t)}{\frac{\mu_o(t)}{\mu_p(t)} V_{dir,\lambda}(\tau^*_\lambda, t) + V_{dif,\lambda}(\tau^*_\lambda, t)}$$

where $V_{dir,\lambda}(\tau^*, t)$ and $V_{dif,\lambda}(\tau^*, t)$ are the direct and diffuse voltages at a given spectral channel λ, time t and total atmospheric optical depth τ^*_λ. The ratio of the cosine of solar zenith angle μ_o and the cosine of the angle between the normal of the aircraft platform and the sun μ_p is used to correct the direct flux for aircraft tilt relative to the horizontal. The solar zenith angle and the aircraft-sun angle are determined from the absolute time of the observation, the location of the aircraft, and the aircraft heading, pitch and roll (see, Walraven, 1978, Iqbal, 1983).

Estimation of Optical Depth from TDDR

Using the direct beam lengths as described above, optical depths of the cloud at the time of the direct beam measurement are possible to derive. However, because the solar zenith angles are so low for this particular cloud case (<65°), the usual method of using a normalized form of Lambert's law of extinction to estimate optical depth (e.g.,Valero et al., 1989) requires modification. At these solar zenith angles, small changes of a few degrees become large changes in the cosine. As a result, the influence of these angles on the measured downwelling spectral irradiance is required to derive reliable optical depths from the cloud top to a given layer.

To account for these effects, the downwelling direct flux incident to a plane parallel to the aircraft platform at cloud top and at some time t_o is written using Lambert's law as

$$F^{\downarrow}_{dir,\lambda}(\tau_{o_\lambda}, t_o) = \mu_p(t_o) F_{o,\lambda} \exp\left(\frac{-\tau_{o\lambda}}{\mu_o(t_o)}\right) \tag{5.2}$$

where $F_{o,\lambda}$ is the direct beam spectral flux incident at the top of the atmosphere and $\tau_{o\lambda}$ is the total optical depth from the top of the atmosphere to cloud top. At some lower level inside the cloud (τ^*_λ) and at some later time t, the expression of the direct downwelling component of radiation is given by

$$F^{\downarrow}_{dir,\lambda}(\tau^*, t) = \mu_p(t) F_{o,\lambda} \exp\left(\frac{-\tau^*_\lambda}{\mu_o(t)}\right). \tag{5.3}$$

Here we assume that the optical depth from the top of the atmosphere (TOA) to the cloud top level does not change when t is on the order of 1 to 2 hours. As a result the optical depth from TOA to the current level inside the cloud is represented by $\tau^*_\lambda = \tau_\lambda + \tau_{o_\lambda}$ where τ_λ is the optical depth from cloud top to the current level within the cloud. Taking ratio of equations 5.3 and 5.3 and solving for τ_λ gives

$$\tau_\lambda = \tau_{o_\lambda}\left(\frac{\mu_o(t) - \mu_o(t_o)}{\mu_o(t_o)}\right) - \mu_o(t) \ln\left(\frac{\mu_p(t_o) F^{\downarrow}_{dir,\lambda}(\tau^*, t)}{\mu_p(t) F^{\downarrow}_{dir,\lambda}(\tau_o, t_o)}\right). \tag{5.4}$$

This expression gives the optical depth of the atmosphere between these two levels. The cloud optical depth is estimated by subtracting the optical depths due to scattering absorbing processes in the clear sky. For the TDDR optical depths, these processes are confined to Rayleigh scatter and ozone absorption at 0.5 and 0.675 μm.

In circumstances where the solar zenith angle is not changing appreciably with time, equation 5.4 reduces to the simple Lambert's law between two layers. However, since the cosine of the solar zenith angle is changing rapidly during this flight (>25% in the time between cloud top and cloud base flight legs), this approximation is not justified. The disadvantage of equation 5.4 is the requirement of knowing an estimate the optical depth between TOA and cloud top. However, this optical depth is multiplied by the percent change of the cosine of the solar zenith angle which although not negligible is small enough to reduce the sensitivity to τ_o, especially for flight legs relatively close to the cloud top leg. Figure 5.8 shows the sensitivity of τ to τ_o when the percent change in the cosine of the solar zenith angle is 17.5% for a variety of direct beam ratios as shown. Note that τ is most sensitive to the ratio of the direct beams and the relative importance of τ_o decreases as the ratio of the direct beams increases.

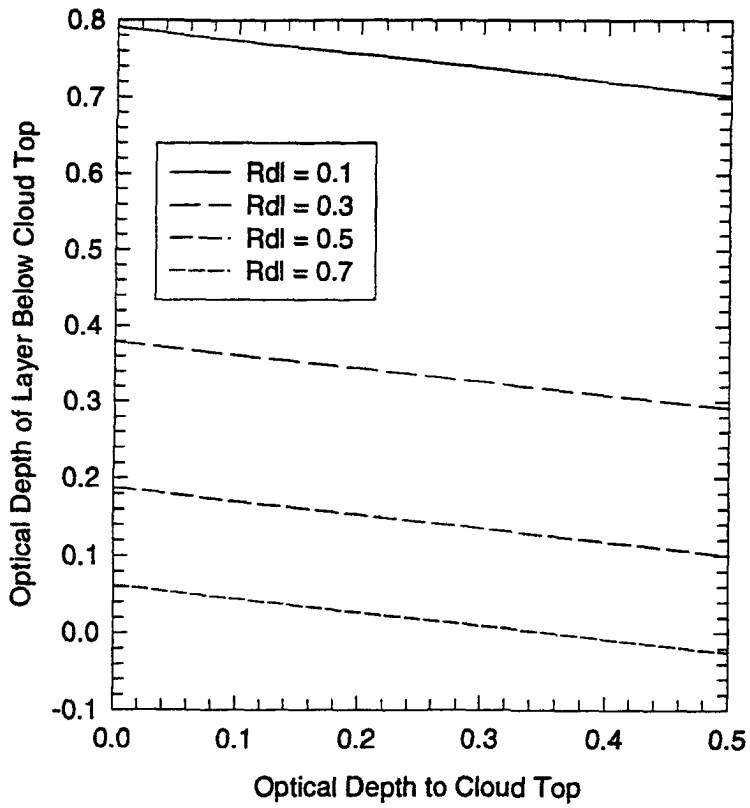

Figure 5.8: The sensitivity of the optical depth from cloud top to a level within the cloud as a function of the optical depth from TOA to cloud top. The ratio of the solar zenith angles is 17.5% and the aircraft is assumed to be horizontal (i.e., $\mu_p = 1.0$). Each curve represents a different ratio of the direct beam fluxes as shown.

The optical depth from top of atmosphere to cloud top is estimated by considering the processes at each wavelength that attenuate the direct beam and produce downwelling

diffuse flux. The processes considered are Rayleigh scatter, Ozone absorption and extinction due to the scattering and absorption from aerosols in the stratosphere. The Rayleigh scatter optical depth is estimated using the parameterization of Dutton et al. (1994) in which

$$\tau_{Rayleigh} = \frac{p}{p_o} 0.00877 \lambda^{-4.05}$$

where p represents the pressure at altitude, p_o is the standard surface pressure of 1013.25 mb, and the wavelength λ is specified in μm. The absorption of radiation by ozone is only significant at the TDDR wavelengths 0.500 and 0.675 μm. The amount of radiation attenuated by this absorption is computed using the two-stream model of Stackhouse, Jr. and Stephens (1991). This model includes the parameterization for Rayleigh scatter above and also gaseous absorption including ozone. The model requires an atmospheric sounding with an Ozone profile. A sounding released from Coffeyville at 20:25 UT on 26 November is used with upper level data taken from the McClatchey et al. (1972) middle-latitude winter sounding. The Ozone profile from the McClatchey profile is interpolated to the levels of the sounding below 10 km. Ferrare et al. (1992) give the Ozone profiles as measured on 26 November 1991 between the altitudes of 10 and 20 km. These measurements are used to adjust the McClatchey ozone concentrations between these levels. The atmospheric temperature, water vapor and ozone amounts are shown in Fig. 5.9.

The aerosol optical properties are determined by comparing radiative observations in a clear region at cloud top with two-stream simulations of the upper atmosphere. During the experiment, volcanic aerosol in the stratosphere advected over the field experiment location from the June 1991 Mount Pinotubo volcanic eruption (see,Sassen et al., 1995). Profiles of the extinction for this aerosol as determined by lidar measurements on 26 November 1991 are given as a function of wavelength by Ferrare et al. (1992). They determined that the extinction scaled according to $\lambda^{-0.6}$ between 0.351 and 0.694 μm from 15 to 25 km. This relationship is assumed to hold out to 1.064 μm and is used to estimate the extinction due to aerosol from the top of the atmosphere to cloud top. The panel of Figure 5.10 gives the direct-to-total ratio from TDDR as observed in a clear region near cloud top. Two-stream simulations for clear sky with and without aerosol extinction. The spectral optical depths from each radiative component are shown in the bottom panel of Figure 5.10. The aerosol optical depths required to approximate the observed direct-to-total ratios are consistent with those found by Ferrare et al. (1992), especially when accounting background aerosol optical depths from McClatchey et al. (1972). The single-scattering albedos and asymmetry parameters are 0.9999 and 0.7 for wavelength channels 0.38 μm through 0.675 μm respectively assuming that the aerosol is made primarily of sulfuric acid droplets (seeToon and Pollack, 1976) typical of volcanic aerosol. At 0.864 μm and 1.062 μm, the single-scattering albedos are assumed to be 0.9999 and 0.999 and the asymmetry parameters are 0.65 and 0.6 respectively.

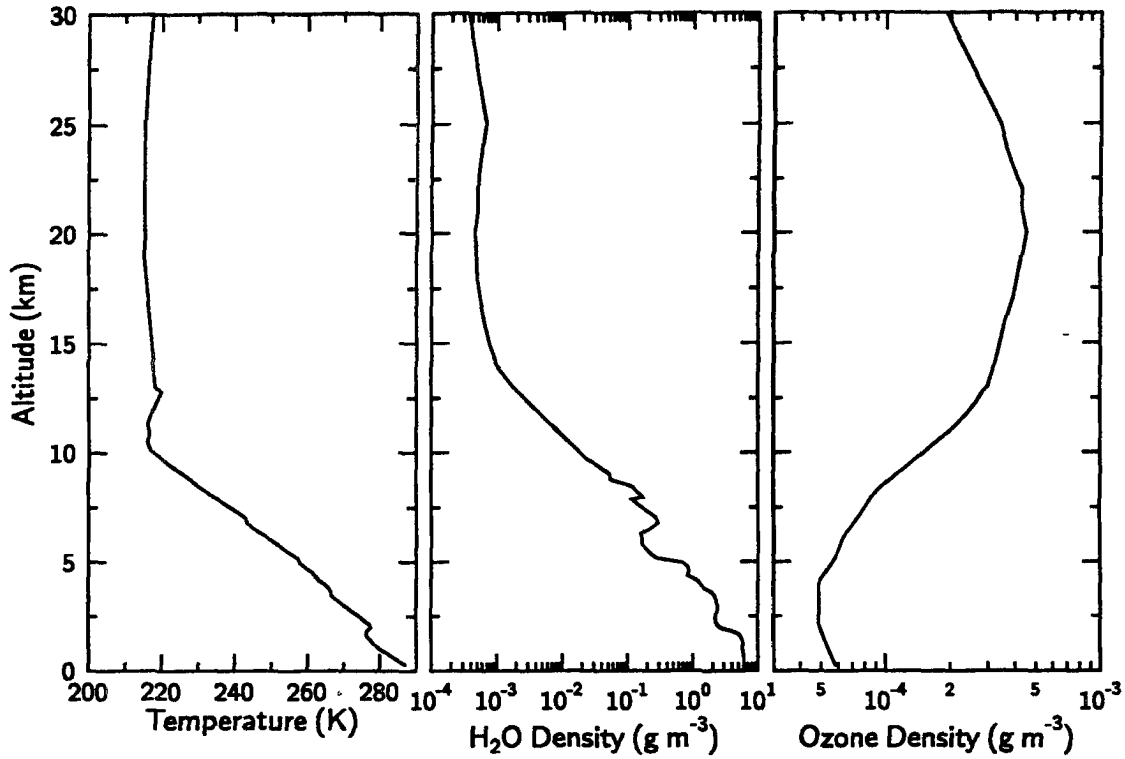

Figure 5.9: The atmospheric temperature, water vapor and ozone profiles used to estimate clear sky radiative properties on 26 Nov. 1991.

The uncertainties associated with the computation of τ_λ come from the estimate of the top of atmosphere to cloud top optical depth τ_{o_λ} and the estimation of the direct beam voltages from TDDR as discussed above. In Figure 5.10, the uncertainties in the estimates of the τ_{o_λ} are shown by the vertical error bars. These uncertainties are derived from the uncertainty of the Rayleigh scatter approximation, the ozone amount and the variability of the volcanic aerosol extinction profiles. The largest uncertainty is associated with the aerosol amounts since Ferrare *et al.* give the extinction profiles only from 13 to 23 km using their lidar method. Measurements of the extinction at 0.864 μm and 1.062 μm are not given. However, the scaling relationship as shown in Figure 5.10 does produce direct-to-total ratios in the two-stream that show good agreement with the measured direct-to-total ratios from TDDR. The uncertainties in the atmospheric optical depth above the cloud and the direct beam voltages are carried through the calculations are represented as error bars.

Estimation of Cirrus Cloud Transmittances

In addition to estimating the cloud optical depth, combining the TDDR measurements with those of the Eppley radiometers and using the two-stream model allows the estimation of cloud transmittances. The diffuse and total transmittances are found relative to the total flux at cloud top. These are defined accordingly

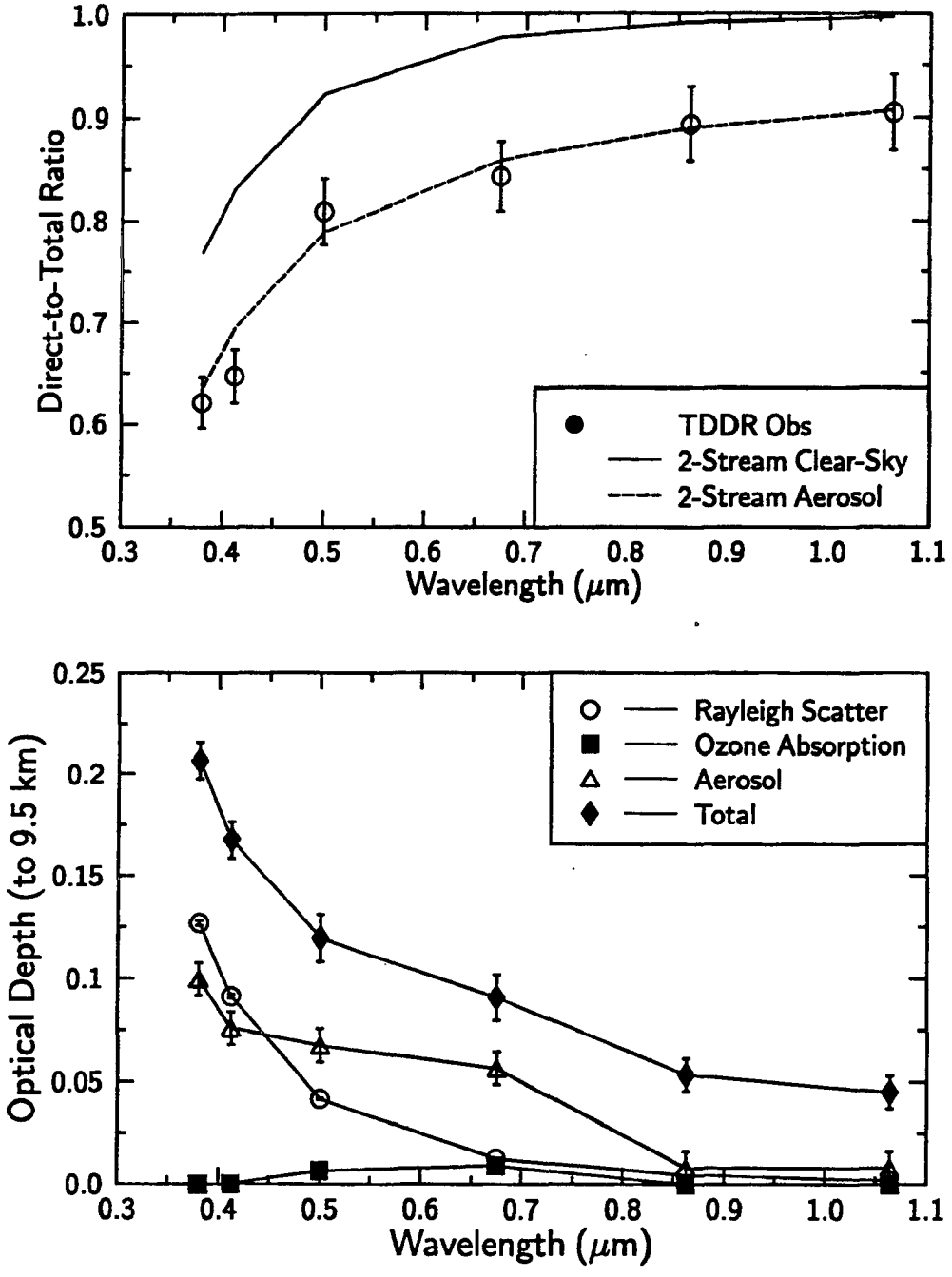

Figure 5.10: The observed and computed atmospheric spectral direct-to-total ratios (top panel) and the spectral components of the optical depths with and without aerosol (bottom panel). The lines in the top panel represent the results of two-stream calculations using the optical depths shown in the bottom panel and optical properties as noted in the text.

$$T_{dif,\lambda} = \frac{F^{\downarrow}_{dif,\lambda}(\tau^*, t)}{C_{dir} F^{\downarrow}_{dir,\lambda}(\tau_o, t) + C_{dif} F^{\downarrow}_{dif,\lambda}(\tau_o, t)}$$

and

$$T_{dif,\lambda} = \frac{\frac{\mu_o(t)}{\mu_p(t)} F^{\downarrow}_{dir,\lambda}(\tau^*, t) + F^{\downarrow}_{dif,\lambda}(\tau^*, t)}{C_{dir}(\mu_o(t)) F^{\downarrow}_{dir,\lambda}(\tau_o, t_o) + C_{dif}(\mu_o(t)) F^{\downarrow}_{dif,\lambda}(\tau_o, t_o)}$$

where C_{dir} and C_{dif} are correction factors for the direct and diffuse fluxes respectively that adjust the cloud top fluxes measured at $\mu_o(t_o)$ to $\mu_o(t)$. The correction of the diffuse flux for small solar zenith angles is normally negligible. However, it is important for the large solar zenith angles in this case. Both of these factors are determined from the two–stream radiative transfer code using the optical properties of the aerosol above the cloud. The model is setup to compute the direct and diffuse downwelling fluxes from the top of the atmosphere to cloud top at two different solar zenith angles, $\mu_o(t_o)$ to $\mu_o(t)$. The bottom boundary condition is the albedo as determined by the Eppley radiometers at the aircraft level. The broadband albedo is related to the spectral albedo using a series of two-stream calculations with the model atmosphere at a 70° solar zenith angle. The curves relating spectral albedo to broadband albedo are shown in Figure 5.11.This approximation does not impact the calculation of C_{dir}, and will only slightly affect the calculation of C_{dif} because the atmosphere above the cloud is very thin.

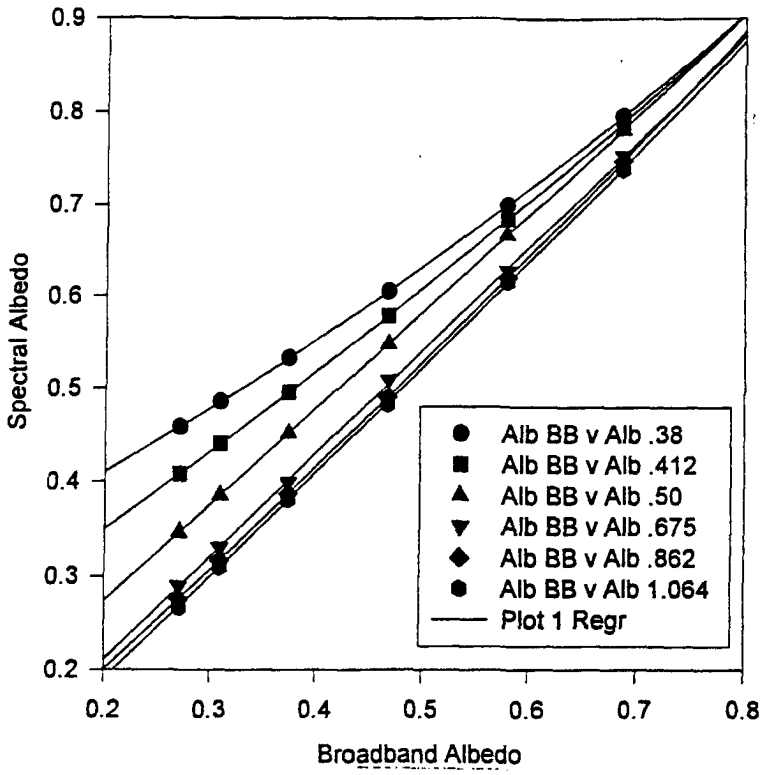

Figure 5.11: The curve fit of spectral albedo to broadband albedo as computed by the two-stream model.

An example of the results from the previous two sections are shown in Figure 5.12 which gives the variation of the atmospheric direct-to-total ratio, the diffuse transmittance and the total transmittance as a function of the atmospheric slant path optical depth (i.e., τ/μ_o) from the TDDR measurements. The measurements shown are taken from flight legs at 8.56 km, 8.24 km and 7.95 km at the wavelengths of 0.412 μm and 0.862 μm. Note that the bottom panel has an enlarged vertical scale relative to the other two panels to increase clarity. Immediately apparent is the general trend of the data for the direct-to-total ratio and the total transmittance to decrease with increasing slant path optical depth. However, the atmospheric diffuse transmittance, shown in the center panel, increases with increasing optical depth. This is because the optical depths are small enough in these cases that the conversion of direct to diffuse radiation is larger than the extinction processes. These trends are predicted by plane-parallel theory.

Note the scatter about the trends for both the diffuse and total transmittances. The source of this scatter is probably due to the combination of instrument noise and the extreme inhomogeneity at these very low sun angles. The inhomogeneity affects the observations by introducing larger error in to the computation of the flux components and breaking down the one-to-one correspondence between optical depth and transmittance. The former effect has been minimized here by scrutinizing the flux components computed from each observation to ensure quality. The latter effect is consistent with the scatter in the fluxes produced by cloud inhomogeneities in the two-dimensional radiative transfer model as discussed in Section 4.1 (see especially the 75° curves in Figures 4.13 - 4.18) and shall examined further in the subsequent section. Another source of a which should be mentioned here is the possibility that of cloud developing above cloud top. The cloud top height flight leg was located at about 9.46 km. The aircraft did fly through a some area of cloud at this level. Radar observations do not show much cloud above this level at the radar site. Cloud developing above the level taken as cloud top will skew the estimates of the cloud top fluxes and will increase the optical depths and change the transmittances inferred from the observations.

The observations in Figure 5.12 also show the wavelength dependence of these cloud and atmospheric properties. The direct-to-total ratio are much larger at 0.862 μm than at 0.412 μm. This is due solely to the Rayleigh scattering at 0.412 μm which is roughly a factor of 20 greater than at 0.862 μm. This Rayleigh scatter effect also is seen in the differences between the two wavelengths in the diffuse transmittances. However, note that the total transmittances do not show this effect as clearly due to the relatively large scatter of the points.

Toward Estimating an Asymmetry Parameter in Cirrus

As noted above, the dependence of the diffuse and total transmittances on optical depth is predicted from simple plane-parallel theory. The relation of the observations above

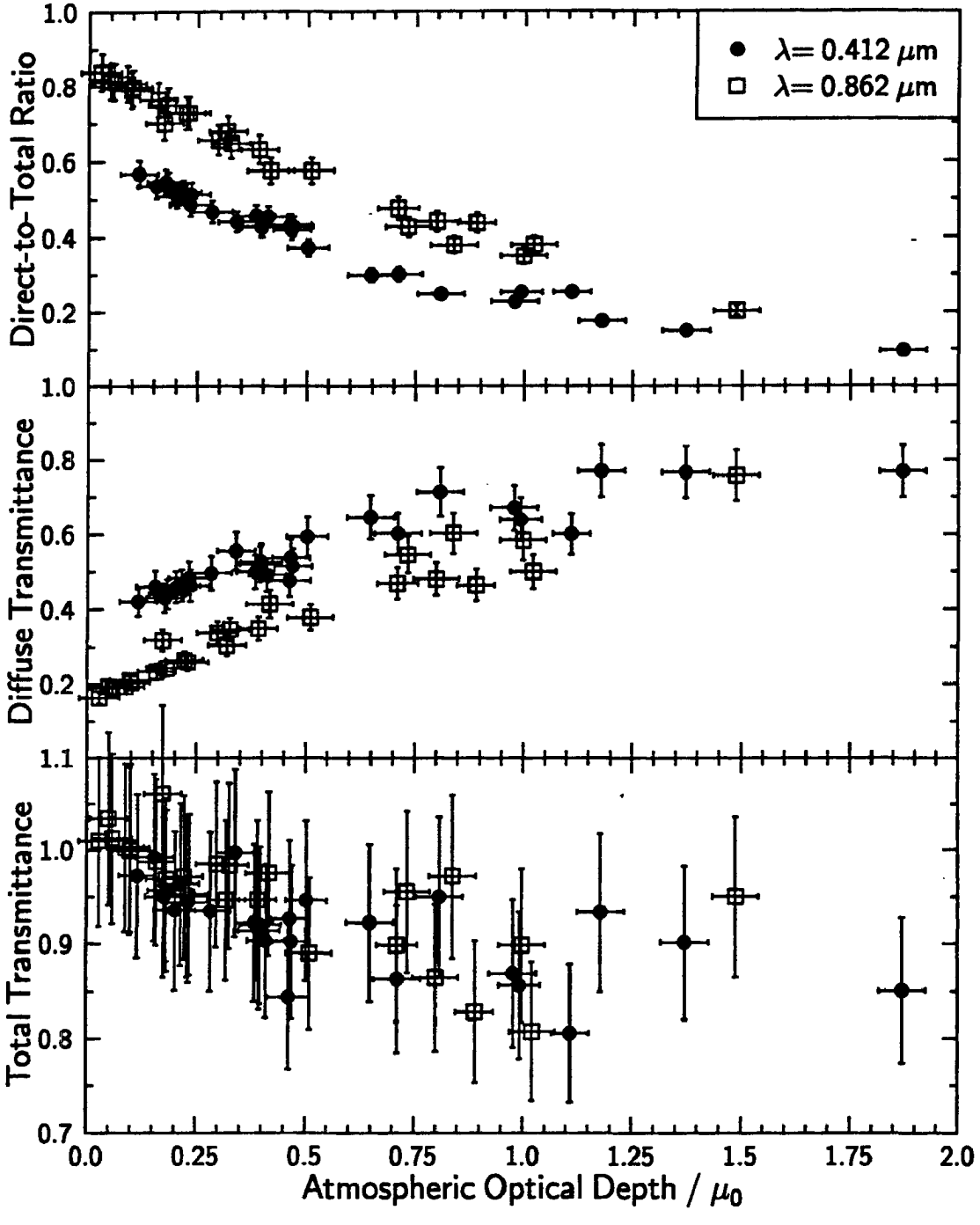

Figure 5.12: The atmospheric direct-to-total ratios, diffuse transmittances and total transmittances at 0.412 μm and 0.862 μm as estimated from TDDR observations.

to plane-parallel theory indicates the effect that inhomogeneity produces on the observed fluxes. The TDDR observations and broadband Eppley radiometers afford the opportunity to use plane-parallel radiative transfer theory to investigate this inhomogeneity effect and to learn about the cloud properties.

At the visible wavelengths of TDDR the single scattering albedo is virtually unity, so the transmittance becomes a function of the total direct and diffuse flux at cloud top, the albedo of the atmosphere (cloud + ground) at the aircraft level, the optical depth and the scattering phase function. All these quantities with the exception of the scattering phase function can be inferred from the observations. For simplicity, the two-stream model mentioned above is used here to estimate the direct-to-total ratios, diffuse transmittances and total transmittance of the atmosphere and cloud given the optical depths and boundary conditions provided by TDDR and the Eppley radiometers. Since fluxes are an integrated quantity, the details of the phase function are not as important as the first moment of the phase function, the asymmetry parameter (refer to Fig. 4.25). In the two-stream plane-parallel model, the scattering phase function is represented by the asymmetry parameter. As a result, if the observations are adequately explained by plane-parallel under certain conditions, then information regarding this two-stream asymmetry parameter can be inferred from the observations.

In order to perform these calculations the boundary conditions to the two-stream are required. Both the downwelling direct and diffuse fluxes and the spectral albedos are determined as in the previous section. The retrieved optical depths from TDDR are used and the single-scattering albedo is assumed to be 0.9999 at all wavelengths. To assess of the sensitivity of the two-stream model to changes in the asymmetry parameter a series of calculation are performed at various solar zenith angles and optical depths. The diffuse and total transmittances that result from these calculations are shown in Figures 5.13 and 5.14. Each figure contains three panels which represent the same series of calculations performed at the different albedos. All the data is normalized to the slant path for clarity. The diffuse transmittances show the trend that the observations show, namely an increase in the diffuse transmittance for small optical depths. Note that between at the slant path of about optical depth 3, the diffuse transmittance is at a maximum. For optical depths larger than 3 the diffuse transmittance decreases with increasing optical depth. Between the optical depths of 2 and 4 the diffuse transmittance is most sensitive to the asymmetry parameter. However even at a slant path optical depth of 1, the diffuse transmittance varies from about 0.4 to 0.6 for an asymmetry parameter change from 0.5 to 0.9. This result implies that the method works best as the slant path optical depth increases. Ultimately, the uncertainty of the TDDR measurements will determine the slant path optical depths required for the best results. It is important to note that TDDR's sensitivity to the direct beam is lost for slant path optical depths larger than about 3.0. So this represents a practical limit to the method. Comparing the three panels representing different albedos

shows that the diffuse transmittance increases only about 5% for an increase of the albedo from 0.2 to 0.6. This implies that the method is not overly sensitive to the albedo.

In order to understand how inhomogeneity might affect this method a series of two-dimensional radiative transfer calculations are performed using the optical properties described in detail in Chapter 3. Figure 5.15 presents the diffuse transmittances resulting from these calculations for two solar zenith angles (30° and 71°) as a function of slant path optical depths. This figure illustrates the scatter about the plane-parallel solution (denoted IPA here) that occurs when allowing horizontal interaction in the radiation field. However, despite this large variability the retrieval of the asymmetry parameter does improve with increasing optical depth. If the boundary fluxes from the simulations are used as input to the two-stream and the asymmetry parameter is changed until the two-stream transmittances match the computed two-dimensional transmittances, then the effective asymmetry parameter can be deduced. The results of such a procedure are performed for two cases presented in Figure 5.16 having domain averaged slant paths of 0.6 and 1.8 as indicated. The results show that the retrievals for the thin case are completely unreliable compared to those for the thicker case. The important thing to note from this diagram is that the retrievals of the asymmetry parameter are centered about the correct value used for the two-dimensional simulation, namely 0.79. This implies that a large number of retrievals are required for reliable estimation of the asymmetry parameter.

As a result of the discussion above, only those TDDR inferred total and diffuse transmittance corresponding to slant path optical depths in the vicinity of unity are analyzed here. Slant paths of this magnitude occurred during Leg 9 of the Sabreliner flight. This flight leg corresponded to a height of 7.95 km nearly 1.5 km below cloud top. The solar zenith angle for this leg is about 76°. The TDDR inferred observations of transmittances and $R_{D/T}$ along with two-stream simulations are shown in Figures 5.17 and 5.18 for wavelengths 0.412 μm and 0.862 μm respectively. The top panels of both figures reveal very good agreement between the direct-to-total ratios and the two-stream calculations. Although not sensitive to g, this implies that the plane-parallel theory the observations is sufficient to compute conversion from direct to diffuse radiation for these clouds of thin optical depth. On the other the hand, the transmittances show much larger scatter. These figures show large scatter centered within the range of the two-stream asymmetry parameters. There are far too few points with too large of uncertainties to conclude anything about the nature of g other than it most likely falls between about 0.6 and 0.9. The range is approximately the same for both wavelengths. This is within the range which current theories predict for the asymmetry factor of nonspherical ice crystals. The inhomogeneity and instrument uncertainties account for the scatter.

This retrieval procedure illustrates using observations the departure from plane-parallel theory that cloud inhomogeneities may cause. However, the fact that a simple

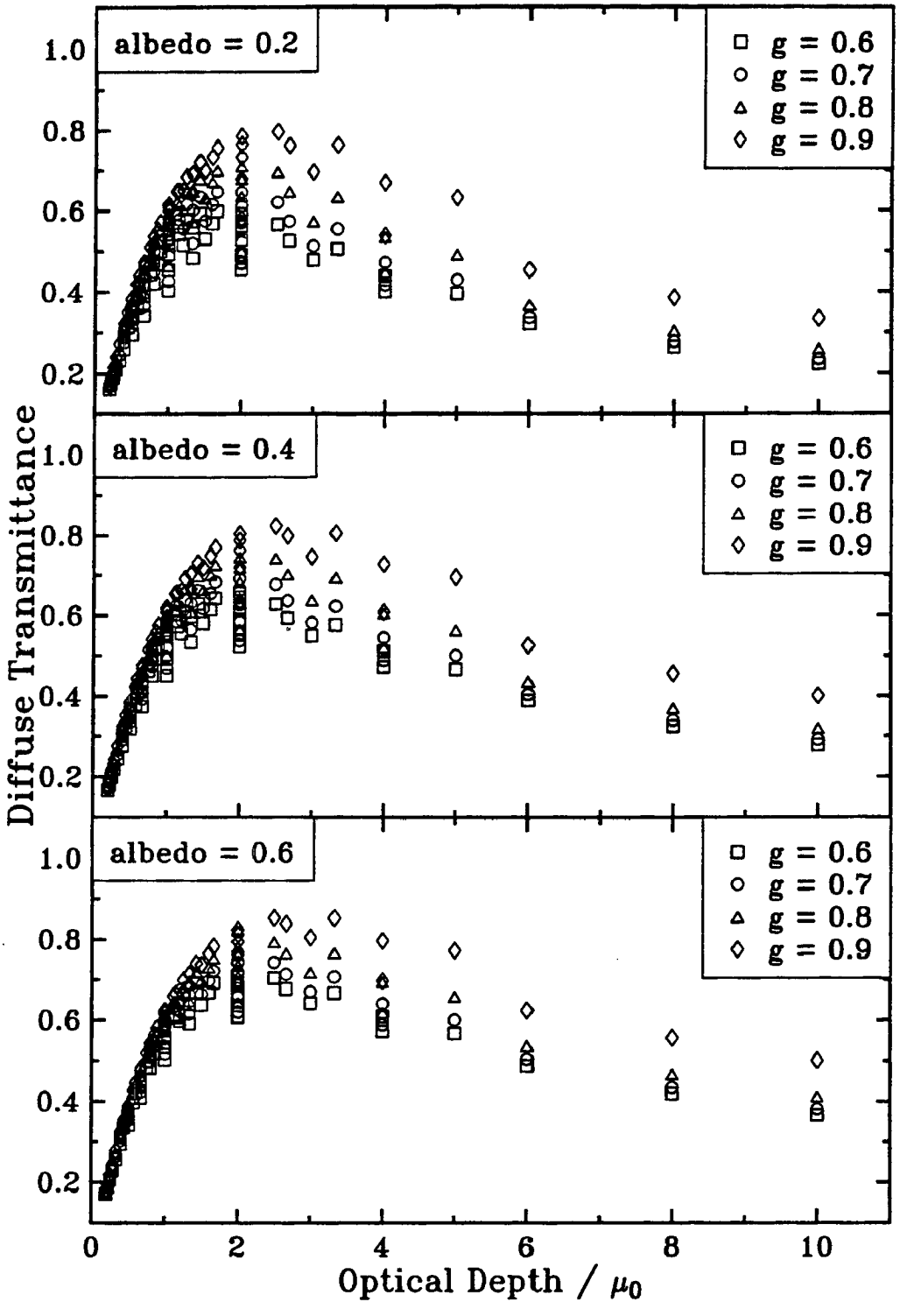

Figure 5.13: The diffuse transmittances computed from a two-stream model as a function of slant path optical depth for a range of asymmetry parameters. Each panel represents the results using a different albedo.

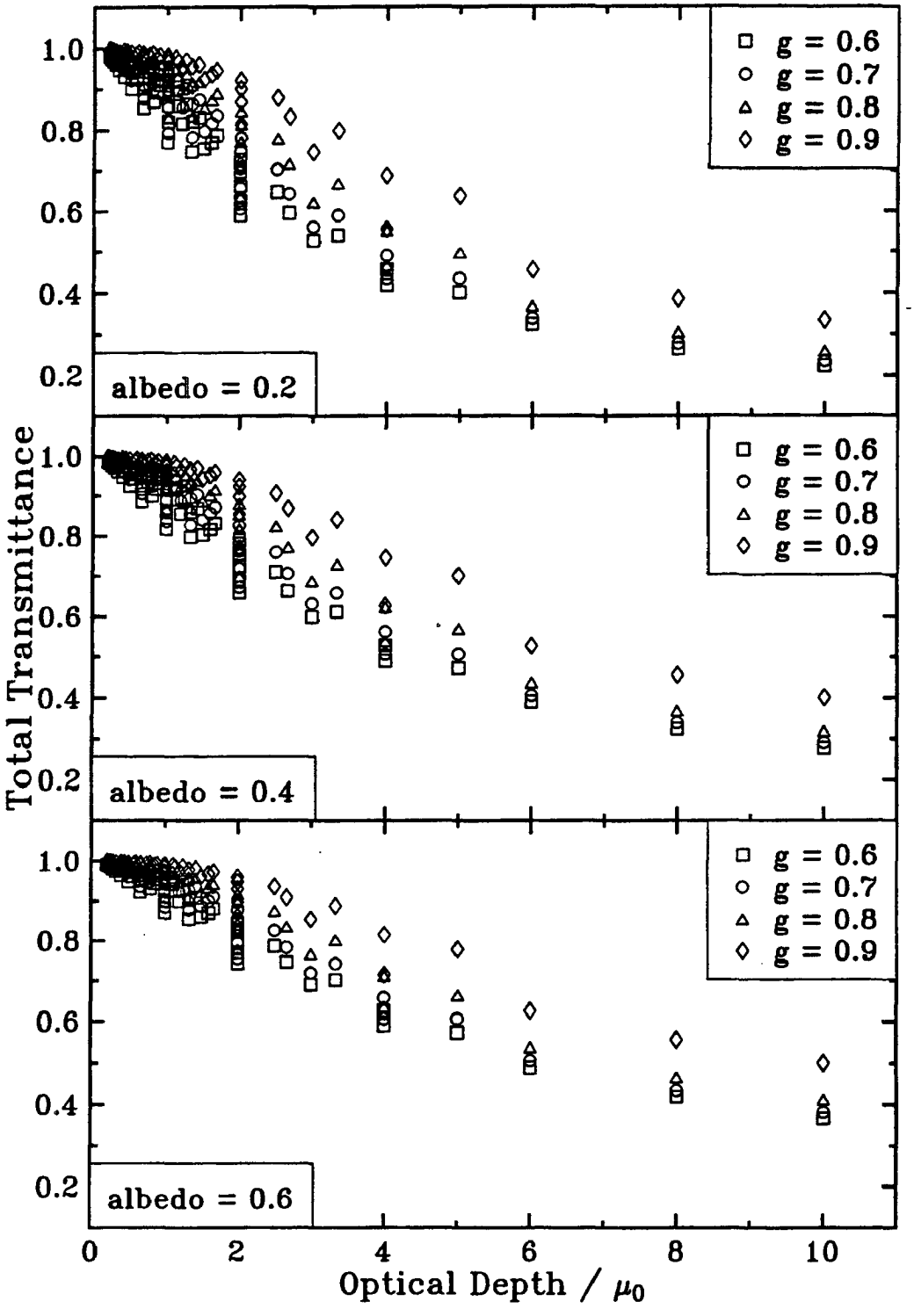

Figure 5.14: The total transmittances computed from a two-stream model as a function of slant path optical depth for a range of asymmetry parameters. Each panel represents the results using a different albedo.

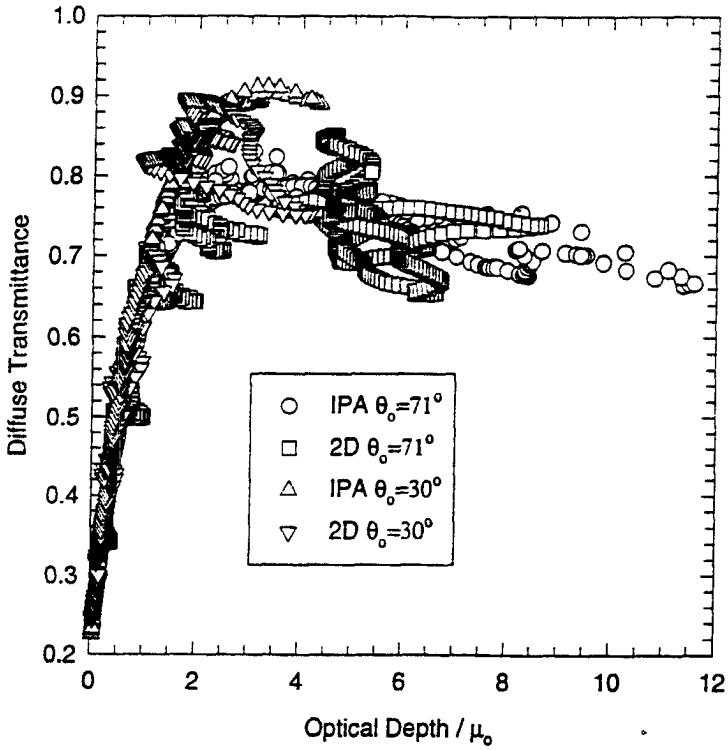

Figure 5.15: The diffuse transmittances computed from a two-dimensional model as a function of slant path optical depth for two solar zenith angles as indicated.

two-stream model was able to simulate an envelope within which many of the observations lie is encouraging especially given the very small optical depths. As a result, this procedure might be usable in the future to deduce information regarding the asymmetry parameter. The results suggest some improvements to the experimental procedure that should ensure better estimates of the asymmetry parameter. First, the instrument should be carefully calibrated. This instrument is left uncalibrated because the original intent was to only estimate optical depths. However, a reliable estimate of total radiation signal is very important to begin to understand more about the intrinsic cloud properties than just their optical depths. Unknown instrument biases greatly affect the estimation of the total downwelling flux. It is possible that these unknown biases are the reason that data from the other channels (0.380, 0.500 and 0.675) could not be analyzed in this way. Second, independent estimates of the total downwelling and upwelling fluxes at the identical channels would enhance the reliability of the procedure. Finally, the arm speed of the TDDR should be increased to provide more data. This would require an increase in the data rate collection rate, but should be possible with the given the properties of the instrumentation. Increasing, the number of observations would give a larger sample and a better chance of producing a good estimate of the asymmetry parameter.

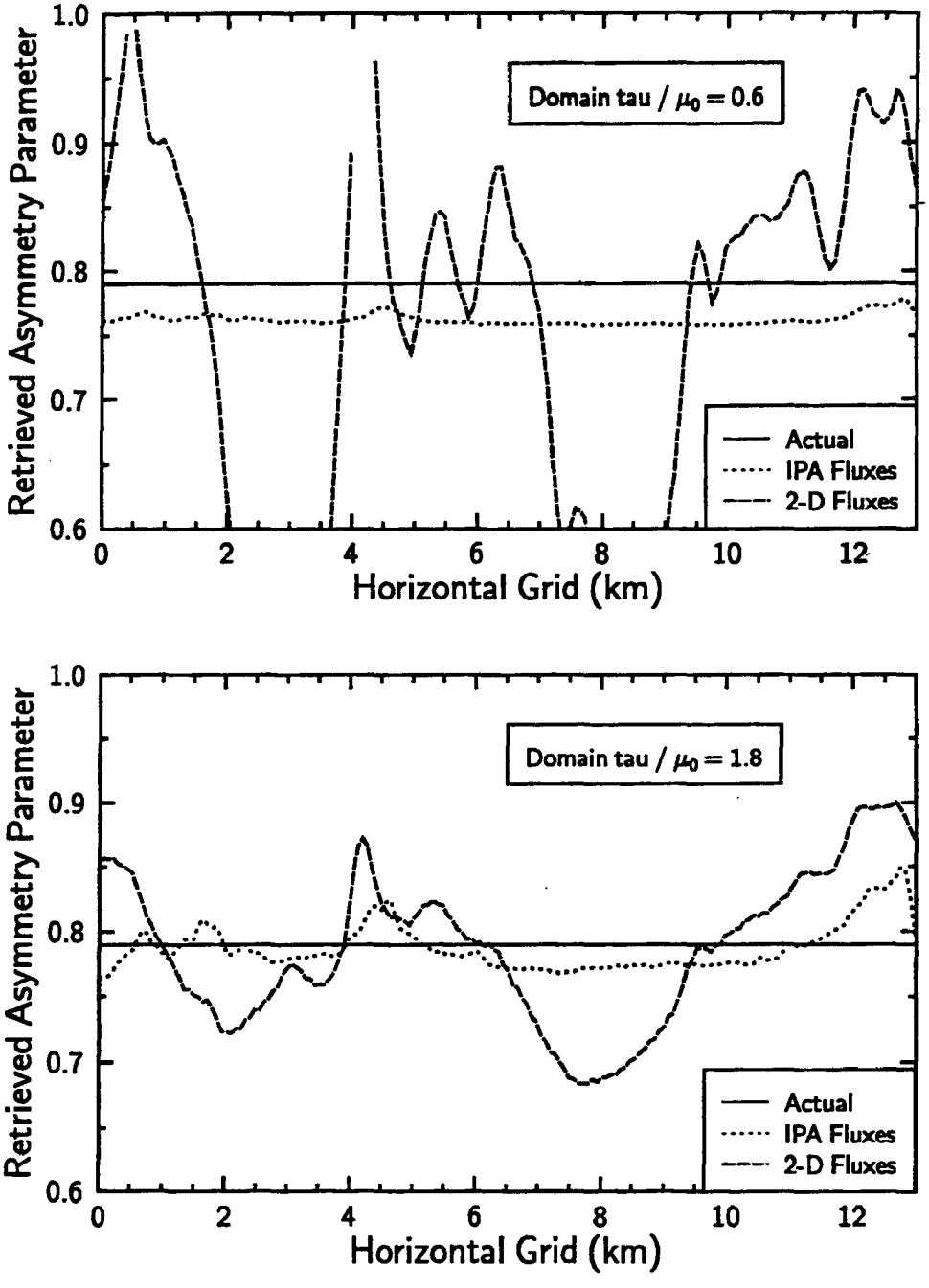

Figure 5.16: The retrieved asymmetry parameter from the two-stream model from the transmittances of the two-dimensional model as a function of the horizontal grid point. The top and bottom panels have domain averaged slant path optical depths of 0.6 and 1.8 respectively.

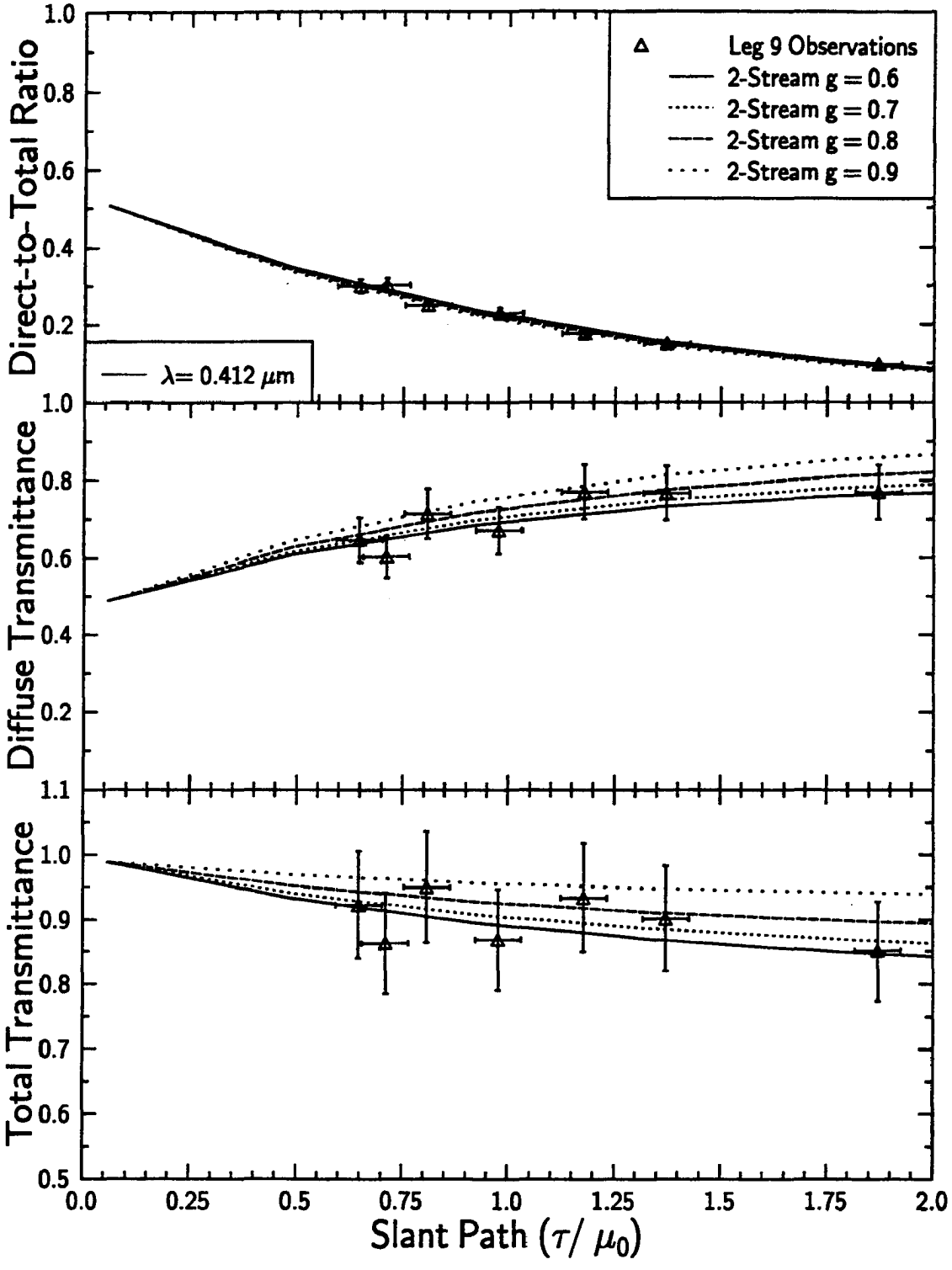

Figure 5.17: The direct-to-total ratio, diffuse transmittance and total transmittance from TDDR as a function of slant path plotted along with two-stream calculations using a large range of asymmetry parameters. The observations and calculations are at a wavelength of 0.412 μm.

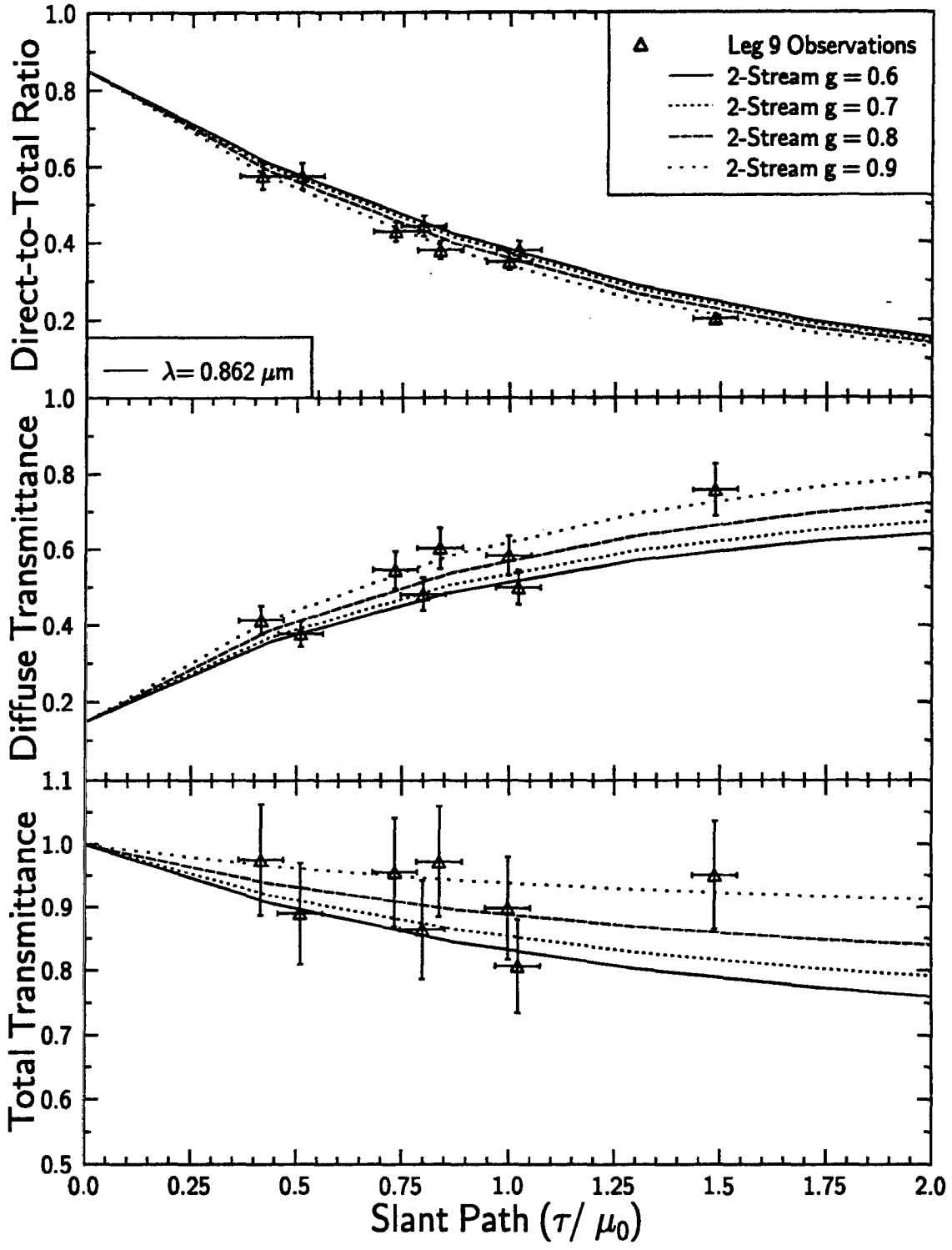

Figure 5.18: The direct-to-total ratio, diffuse transmittance and total transmittance from TDDR as a function of slant path plotted along with two-stream calculations using a large range of asymmetry parameters. The observations and calculations are at a wavelength of 0.862 μm.

5.4 Chapter Summary

In this chapter, an overview of the FIRE Cirrus IFO II field experiment is given including the instrumentation included on board the Sabreliner aircraft. The flight on 26 November 1991 is chosen for case study analysis because the aircraft worked from cloud top towards cloud base and the flight is centered about location of the K_a-band radar. Due to the time of the flight (middle to late afternoon), the radiative observations are made at very large solar zenith angles. This represents a situation in cirrus in which the radiative properties become more sensitive to horizontal heterogeneity as deduced from the sensitivity studies in Chapter 4. However, the small optical depths of the cloud in this case should act to reduce these effects. Thus, the comparison of these measurements to plane-parallel theory gives insight into the role of the inhomogeneity.

Using TDDR and Eppley flux measurements, the spectral optical depths of the cirrus during this case are inferred from the attenuation of the direct beam from cloud top to the current aircraft level. Additionally, using an estimate of the diffuse flux, the direct-to-total ratio, the diffuse transmittance and the total transmittance of the cloud are estimated. A two-stream model is used to compute the plane-parallel relationship between optical depth and transmittance using a range of asymmetry parameters and initialized with the measured optical depths and boundary conditions. Although the error bars from the measurements are too large and the number of samples is too small to make conclusions about the value of g, the plane-parallel theory provides an envelope within which most of the observations lie.

These results seem to indicate that there is hope of retrieving an approximate range of g using this scheme if clouds of optical depth larger than those for this case are observed and if the experimental setup is altered to reduce the uncertainties in the measurements. The results also indicate that the three-dimensional flux observations produce scatter about the plane-parallel theory similar to the scatter resulting from the two-dimensional fluxes compared to independent pixel as predicted from SHSG in Chapter 4. In the next chapter, two-dimensional simulations are performed to test the ability of the SHSG with two-dimensional cloud structure to account for three-dimensional radiance and fluxes.

Chapter 6

SIMULATIONS OF CLOUD INHOMOGENEITY USING CO-LOCATED AIRCRAFT AND RADAR OBSERVATIONS

In the previous chapter, downwelling flux observations were used to compute the radiative properties of cirrus clouds from the 26 November 1991 afternoon case. These radiative properties plotted as a function of optical depth produced scatter around plane-parallel simulations similar to that produced from two-dimensional fluxes by SHSG in Chapter 4. This indicates that the despite the large solar zenith angles, the effects of cloud inhomogeneity for the thin cirrus cloud studied do not appear to behave radically differently from the two-dimensional theory. To verify this result, simulations of two-dimensional clouds are performed to determine to what extent the two-dimensional theory can account for the observed variability in radiances and fluxes. To this end, a co-location of the aircraft and the radar is pursued to compare the radiative simulations using the radar derived cloud structure with actual observed radiative quantities.

This chapter first presents the method that is used to determine the co-location between the radar and aircraft during the 26 November afternoon flight case. The results of this co-location are presented and the microphysical and optical properties of the cloud are described. Lastly, two-dimensional simulations using SHSG are performed and compared to the observed reflected radiances and fluxes during the co-located time frame. These results highlight the differences between radiances and fluxes and have important implications as to the amount of cloud structural information required to properly simulate these quantities.

6.1 The Co-location of Radar and Aircraft Observations

The co-location of the Sabreliner flight legs and the radar observations became an arduous task due to the many uncertainties with the aircraft position and the advection speed of the cloud. The procedure used to co-locate the aircraft data with the radar reflectivity time series is outlined in this section. The objective of the co-location is to find a period of time during the aircraft flight in which the cloud observed by the aircraft eventually advected over the radar site. Such a co-location would enable the comparison of radiometric observations with information of the cloud structure as observed by the radar. Ultimately, the goal is to estimate the cloud optical properties from the combination of

aircraft and radar observations in order to model the radiometric properties of the clouds. Thus, the co-location process becomes very important to reach the goals of this research.

The co-location requires knowledge of the radar position and the aircraft location along the flight path. Additionally, the mean wind speeds of the cloud between these positions must also be estimated. The estimations of these quantities are subject to many uncertainties not only due to the precision and accuracy of the aircraft measurements, but also due to the changing wind fields associated with this particular cirrus event. As a result, the co-location scheme was designed to account for these uncertainties by comparing different aircraft quantities and considering the constraints of the radar itself.

6.1.1 Relative Positions Between Aircraft and Radar

In order to establish the co-location between aircraft and radar, the horizontal and vertical positions of the aircraft relative to the radar must be determined. The degradation of the INS during the flight can affect the aircraft estimation of the horizontal position adversely. The characteristics of this behavior are understood (Lenschow and Spyers-Duran, 1989), but the exact error at any given time is dependent upon the INS calibration and initialization before the flight and is unpredictable. Fortunately, the aircraft data system provided by NCAR also had access to the GPS satellite navigation for comparison to the on board INS measurements. Comparison between these measurements revealed differences which increased during the flight in an oscillatory manner. However, the absolute accuracy of the GPS is also unknown. Therefore, the horizontal position of the aircraft is considered to be either at the INS coordinates or at the GPS coordinates with uncertainty boxes determined by the difference between the two different locations. At times, the differences between the INS and GPS locations grew to 1.5 km thus, adding considerable uncertainty to the actual horizontal position of the aircraft relative to the radar. Figure 6.1 shows an hypothetical example of the difference between the INS and GPS and the assigned error boxes to each.

Another uncertainty associated with the aircraft position is its altitude above sea level. As noted earlier, the altitude of the aircraft is calculated from the static pressure assuming a standard lapse rate. With no redundant measurements of the altitude during this flight, the magnitude of the error associated with this altitude estimate is also required. One independent method of determining the error in the aircraft altitude is to compare the altitude estimate to rawinsonde measurements. Fortunately, a rawinsonde balloon was launched at 20:25 UT from the hub site. The balloon rose through the altitudes flown by the aircraft allowing for a comparison between aircraft altitudes and the balloon altitudes at a given pressure level. This comparison revealed that the estimate of the altitude provided by NCAR was approximately 40 m too low. Due to both the uncertainties in the relative positions of these instruments at different times and the change in pressure height

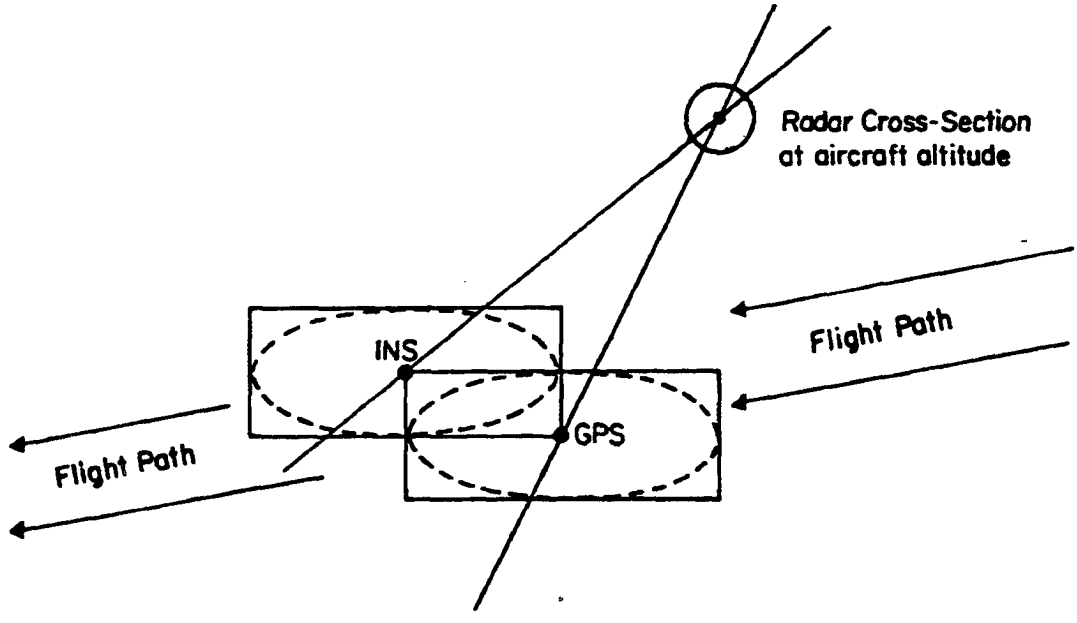

Figure 6.1: Schematic of the relative INS, GPS and radar positions. An example of aircraft position error boxes are shown as well as the radar cross-section at the aircraft altitude.

fields over the period of the aircraft flight a reasonable uncertainty in the estimation of the aircraft altitude is taken to be ±20 m.

Figure 6.1 also shows the radar cross-section at the aircraft altitude. Thus, a cloud element anywhere within the indicated circle is considered observed by the radar. The cross-sectional radius of the radar is easily calculated by

$$r_{crs} = h \tan(\frac{1}{2} FOV)$$

where h is the height above ground level and FOV is the full beam width of the radar which according to Table 5.2 is 0.5°. The estimation of the aircraft altitude (adjusted for the elevation of the radar site) determines the horizontal cross-sectional area of the radar used in the co-location scheme. The radar cross-section also has a vertical extent determined by the range gate resolution which is 37.5 m. This vertical smoothing of the cloud microphysics might contribute to the differences between aircraft microphysics measurements and radar reflectivities discussed later.

6.1.2 The Estimation of the Cloud Advection Wind Components

Once the horizontal and vertical positions of the aircraft relative to the radar are determined within the uncertainties described above, the co-location of aircraft to radar depends upon the cloud advection from the aircraft position to the radar (refer to Fig.

6.1). The uncertainties in the position of the aircraft determine a range of possible cloud advection directions that can result in the cloud sampled by the aircraft advecting into the cross-sectional area of the radar. The determination of this range of wind directions is a geometric problem which is simplified by approximating the position error boxes as approximated by error ellipses (as shown in Fig. 6.1).

After the range of acceptable wind directions are estimated, the actual mean wind between the aircraft and the radar is required to determine whether a co-location is possible for a given portion of the cloud. To estimate this mean wind it is assumed that over a short time period ($\sim$ 15 min.) the wind at any given location in space can be represented as the sum of its mean and perturbation components. Since there is not enough information available regarding these wind components over the distance between the aircraft and radar, the vector mean between the aircraft and radar is used to estimate the mean wind. The computation of this vector mean wind is estimated using both the winds measured on board the aircraft and the winds measured by the radar itself in VAD mode every 30 minutes.

The wind at the aircraft location is estimated by using the measurements provided by the aircraft sensors as previously discussed. Since these measurements are subject not only to noise from the instruments, but also perturbations in the wind field these measurements were smoothed with a 5 point running average. Since the measurements have a sampling frequency of 1 Hz and the ground speed of the aircraft was in the vicinity of 175 m/s, the smoothing occurs over an approximate distance of 875 m. The uncertainties associated with the measurement of the horizontal wind components on the aircraft were discussed in Chapter 5. Due to the usage of the INS to derive these wind components, the uncertainties of these measurements increase linearly with time (see eqn. 5.1). These uncertainties are used to determine the range of possible horizontal wind components at the aircraft given the measurements.

The wind at the radar is given by the VAD mode scans. The wind speed and direction are estimated for each range gate with an estimated uncertainty in the wind speed of ± 0.5 m/s. Since VAD scans were only obtained once every 30 minutes the horizontal wind components were interpolated to the time of the aircraft observation. This assumption can lead to errors if the winds change abruptly at a given time between radar observations. Fortunately, in the case analyzed here, the winds at the flight altitudes did not change significantly relative to the radar uncertainty between each observation.

The measurement and the uncertainty of the aircraft derived winds are vectorally averaged with the interpolated measurement and uncertainty of the radar observation to derive the estimate of the mean wind within a total uncertainty range. The resulting wind directions are then compared to the range of allowable wind directions to determine whether a given portion of the cloud could have been advected over the radar. If the directions of the mean wind fall within the range of possible wind directions then a minimum

and maximum time required for the cloud to be advected from the aircraft position to the radar is determined. In this way, the times of the cloud observed by the radar are mapped to the times in which the Sabreliner flew through that portion of the cloud.

6.1.3 Results of the Co-location Scheme

Upon applying the co-location scheme as outlined above to the aircraft data, segments of two different flight legs were found to advect over the hub. Unfortunately, one of these cases was predicted to advect over the hub during a time period in which the radar was down. The other case, flight leg 5, gives a cloud segment that passed over the radar in a 10 minute period starting about 5 minutes after the aircraft passed through the cloud. This case will become the focus of the remainder of this chapter as the cloud optical properties are developed for this case for modeling within SHSG.

The resulting co-location between the aircraft and radar is shown in the comparison of the measured 2D-C probe IWC and inferred radar reflectivity with the observed radar reflectivity and inferred IWC. These quantities are shown in Figure 6.2 as a function of cloud distance. The aircraft measurements appear as step functions because each measurement represented an average over 5 seconds. The estimate of the IWC from the radar reflectivity is derived using the relationship of Sassen, 1987. Although large differences between the radar and 2D-C derived IWC occur, both the radar and 2D-C probe quantities have same main features. The agreement between the derived and inferred radar reflectivities gives a much better indication of the degree of agreement between the aircraft and radar time series despite the many uncertainties.

As a further evidence of the coincidence of the aircraft and radar time series, Figure 6.3 shows the measured upwelling radiative properties from the cloud compared to radar inferred IWP estimates from the aircraft level to cloud base. The top panel is the raw SPERAD reflected radiance at 0.5 μm. Note that this radiance quantity with a small field of view agrees better with the IWP than the hemispheric broadband quantities shown in the remaining panels. The upwelling measured irradiances are smoothed relative to the SPERAD radiance. These differences between the radiance and flux properties of the cloud have implications regarding remote sensing and the estimation of bulk cloud properties, and are explored in the subsequent section.

Unfortunately, the agreement between the downwelling solar and infrared fluxes and the radar-inferred IWP to cloud top (or more appropriately the slant path to cloud top) did not produce such good agreement (not shown). This is due to the thin and tenuous nature of the clouds above the aircraft during this flight leg. Another factor is the changing wind speeds aloft at this time which increase the error of the cloud advection assumptions. As a result, only the upwelling radiative quantities are used in the comparison of the aircraft radiative properties to radar inferred cloud structure. However, the instantaneous downwelling radiative quantities during the flight will be used to derive cloud properties vital to our characterization of the bulk optical properties of this cirrus cloud.